

INFORMATION TO USERS

The most advanced technology has been used to photograph and reproduce this manuscript from the microfilm master. UMI films the text directly from the original or copy submitted. Thus, some thesis and dissertation copies are in typewriter face, while others may be from any type of computer printer.

The quality of this reproduction is dependent upon the quality of the copy submitted. Broken or indistinct print, colored or poor quality illustrations and photographs, print bleedthrough, substandard margins, and improper alignment can adversely affect reproduction.

In the unlikely event that the author did not send UMI a complete manuscript and there are missing pages, these will be noted. Also, if unauthorized copyright material had to be removed, a note will indicate the deletion.

Oversize materials (e.g., maps, drawings, charts) are reproduced by sectioning the original, beginning at the upper left-hand corner and continuing from left to right in equal sections with small overlaps. Each original is also photographed in one exposure and is included in reduced form at the back of the book.

Photographs included in the original manuscript have been reproduced xerographically in this copy. Higher quality 6" x 9" black and white photographic prints are available for any photographs or illustrations appearing in this copy for an additional charge. Contact UMI directly to order.

U·M·I

University Microfilms International
A Bell & Howell Information Company
300 North Zeeb Road, Ann Arbor, MI 48106-1346 USA
313/761-4700 800/521-0600



Order Number 9111309

**Seismic analysis of the sun from intermediate and high-degree
p-modes**

Korzennik, Sylvain Gereon, Ph.D.

University of California, Los Angeles, 1990

U·M·I
300 N. Zeeb Rd.
Ann Arbor, MI 48106



UNIVERSITY OF CALIFORNIA
Los Angeles

Seismic Analysis of the Sun from Intermediate and High Degree p-Modes

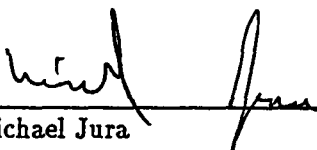
**A dissertation submitted in partial satisfaction of the
requirements for the degree Doctor of Philosophy
in Astronomy**

by


Sylvain Gereon Korzennik

1990


The dissertation of Sylvain Gereon Korzennik is approved.



Michael Jura



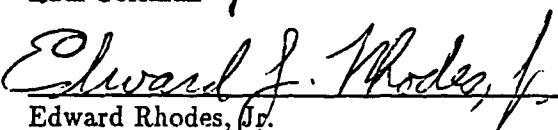
Ferdinand Coroniti



Walter Gekeimian



Paul Coleman



Edward Rhodes, Jr.



Roger K. Ulrich, Committee Chair

University of California, Los Angeles

1990

*A la mémoire mon oncle, Samuel Korzennik, et de mes grand-parents Sara
Braun-Korzennik et Salomon Korzennik, victimes de la barbarie nazie.*

A mes parents, Eugenia et Henryk.

Contents

List of Figures	viii
List of Tables	xiv
Acknowledgments	xv
Vita	xviii
Publications and Presentations	xviii
Abstract	xxi
1 Introduction	1
1.1 Background	3
1.2 Present Study	9
2 Instrument	11
2.1 Solar Telescope	13
2.2 MOF Doppler Analyzer	14
2.3 Optical Layout	17
2.4 1024×1024 CCD Camera and Data Acquisition System	19
2.5 Observation Procedure	20
3 Data Reduction	26
3.1 Dopplergram Computation	27
3.2 Calibration Procedures	37

3.2.1	Spatial Calibration	39
3.2.2	Temporal Calibration	40
3.2.3	Non-Linear Calibration	42
3.2.4	Comparison	46
3.3	Spatial Decomposition	48
3.3.1	Theory	48
3.3.2	Practical Considerations	50
3.4	Spectral Analysis	53
3.5	Power Spectra Analysis	57
3.5.1	Frequency Splittings	58
3.5.2	Mode Frequency, Amplitude and Width	59
4	Frequency Splittings	61
4.1	Tesseral Measurements	62
4.1.1	Results from the High-Resolution Spectra	62
4.1.2	Results from the Low-Resolution Spectra	73
4.1.3	Comparison of High- and Low-Resolution Results	73
4.1.4	Sources of Systematic Errors	78
4.1.5	Correction for Systematic Errors	105
4.2	Sectoral Measurements	113
4.2.1	Results from the High-Resolution Spectra	114
4.2.2	Results from the Low-Resolution Spectra	114
4.2.3	Comparison of High- and Low-Resolution Sectoral Splittings	115
4.2.4	Source of systematic errors	118
4.2.5	Correction for systematic errors	120
4.3	Comparison with Previous Measurements	122

4.3.1	Low- and Intermediate-Degree Modes	122
4.3.2	High-Degree Modes	127
5	Mode Frequency, Width and Amplitude	128
5.1	Results of the High-Resolution Spectra	129
5.1.1	Systematic Effects	135
5.1.2	Uncertainties	136
5.2	Results from the Low-Resolution Spectra	137
5.2.1	Correction for Systematics: Frequencies	138
5.2.2	Correction for Systematics: Widths	142
5.2.3	Correction for Systematics: Amplitudes	144
5.2.4	Uncertainties	148
5.3	Comparisons with Previous Measurements	152
5.3.1	High-Resolution Results	152
5.3.2	Low-Resolution Results	152
5.4	Comparison with Theory	157
6	Internal Rotation Rate	165
6.1	Theoretical Background	166
6.1.1	Rotational splittings	166
6.1.2	Inversion Techniques	168
6.2	“Equatorial” Rotation Rate	182
6.2.1	MWO Measurements Alone	184
6.2.2	MWO and BBSO Measurements Combined	204
6.3	Conclusions	216
	Bibliography	220

A	Frequency Splittings	224
A.1	Tesseral Values from the High-Resolution Spectra	224
A.2	Sectoral Results from the Low-Resolution Spectra	227
B	Modal Frequencies, Widths and Amplitudes Estimated from the High-Resolution Spectra	228
C	Modal Frequencies, Widths and Amplitudes Estimated from the Low-Resolution Spectra	237

List of Figures

1.1	Power density distribution as a function of degree and frequency of the solar acoustic spectrum for $20 \leq \ell \leq 600$ and $1 \leq \nu \leq 8$ mHz	5
1.2	Schematic description of the ray path of an acoustic wave	6
1.3	Selection of spherical harmonic functions	8
2.1	Schematic diagram of the instrument.	12
2.2	Typical variation as a function of time for the ambient temperature and the cells pits	18
2.3	Schematic diagram of the data acquisition system.	21
3.1	Typical “red” filtergram	29
3.2	Typical “blue” filtergram	30
3.3	Typical dopplergram, corresponding to Figures 3.1 and 3.2	31
3.4	Difference of two dopplergrams obtained two minutes apart	32
3.5	Typical “red” images statistics	33
3.6	Typical “blue” images statistics	34
3.7	Typical dopplergram statistics	34
3.8	Typical North-South scan of a filtergram image	38
3.9	Typical East-West scan of a filtergram image	38
3.10	Temporal calibration curve	41
3.11	Temporal calibration regression curve	41

3.12	Matrices $K(i, j)$ and $V(i, j)$ and the regression coefficient.	44
3.13	Matrices $K'(i, j)$ and $V'(i, j)$ and the regression coefficient.	45
3.14	Comparison of calibration coefficients.	46
3.15	Time series for a selection of spherical harmonic coefficients	54
3.16	Window function, in the time domain.	56
3.17	Window functions, in the frequency domain for the high-resolution and low-resolution spectra.	56
4.1	Even-index Legendre polynomials expansion coefficients, estimated from the high-resolution spectra	63
4.2	Odd-indexed Legendre polynomials expansion coefficients, estimated from the high-resolution spectra	64
4.3	Portion of the $\ell = 50$ and $m = 0$ high-resolution spectrum.	66
4.4	Portion of the collapsed, $\ell = 50$ and $\langle m = 0 \rangle$ high-resolution spectrum.	66
4.5	Cross-correlation functions between the collapsed $\langle m = 0 \rangle$ and the indi- vidual $m = 20$, $m = 0$ and $m = -20$ high-resolution spectra, for $\ell = 50$	67
4.6	Portion of the $\ell = 140$ and $m = 0$ high-resolution spectrum.	67
4.7	Portion of the collapsed, $\ell = 140$ and $\langle m = 0 \rangle$ high-resolution spectrum.	68
4.8	Cross-correlation functions between the collapsed $\langle m = 0 \rangle$ and the indi- vidual $m = 80$, $m = 0$ and $m = -80$ high-resolution spectra, for $\ell = 140$	68
4.9	Even-indexed Legendre polynomial expansion coefficients, estimated from the smoothed and unsmoothed high-resolution spectra	70
4.10	Odd-indexed Legendre polynomial expansion coefficients, estimated from the smoothed and unsmoothed high-resolution spectra	71
4.11	Even-indexed Legendre polynomials expansion coefficients, estimated from the low-resolution spectra	74
4.12	Odd-indexed Legendre polynomial expansion coefficients, estimated from the low-resolution spectra	75
4.13	Comparison of the even-indexed Legendre polynomial expansion coefficients	76
4.14	Comparison of the odd-indexed Legendre polynomials expansion coefficients	77

4.15 Leakage matrix for $\ell = 90$	81
4.16 Leakage matrix for $\ell = 150$	82
4.17 Leakage matrix for $\ell = 300$	83
4.18 Perturbed leakage matrix for $\ell = 90$	85
4.19 Perturbed leakage matrix for $\ell = 150$	86
4.20 Perturbed leakage matrix for $\ell = 300$	87
4.21 Total power in the 5-minute band as a function of m/ℓ for $\ell = 50$	88
4.22 $\langle Q_l \rangle_n$ as a function of spherical harmonic degree ℓ	91
4.23 $\langle \partial \bar{\nu} / \partial \ell \rangle_n$ as a function of spherical harmonic degree ℓ	92
4.24 Individual terms on the right-hand-side of Equation (4.21) for $\beta = 1 - 0.75(m/\ell)^2$	94
4.25 Individual terms on the right-hand-side of Equation (4.21) for $\beta = 1 - 0.5(m/\ell)^2$	95
4.26 Numerical simulations for $\ell = 90, 150$ and 300	99
4.27 Numerical simulations using $P = B_o = 0$ and $P = 12, B_o = 3$	101
4.28 Analytical simulations for $\ell = 90, 150, 300,$ and $600.$	103
4.29 Observed frequency shifts	104
4.30 Functions $\varepsilon = \delta(\Delta\nu)/L$ as a function of m/L	107
4.31 Overall averaged function ε	108
4.32 Correction coefficients, q_i , plotted as a function of the spherical harmonic degree ℓ	109
4.33 Even-indexed Legendre polynomial expansion coefficients, estimated from the low-resolution spectra, after being corrected for systematics introduced by mode blending.	111
4.34 Odd-indexed Legendre polynomial expansion coefficients, estimated from the low-resolution spectra, after being corrected for systematics introduced by mode blending.	112
4.35 Scaled frequency splittings, $\Delta\nu/2\ell$, estimated from cross-correlation of high-resolution sectoral spectra	115

4.36	Scaled frequency splittings, $\Delta\nu/2\ell$, estimated from ridge fitting to the low-resolution sectoral spectra	116
4.37	Comparison of the scaled frequency shifts estimated from the high-resolution cross-correlation with the low-resolution ridge fitting results	116
4.38	Comparison of sectoral and tesseral equivalent (11th order) splittings	118
4.39	Simulated sectoral splitting systematic error	120
4.40	Even-indexed coefficients compared with BBSO measurements	124
4.41	Odd-indexed coefficients compared with BBSO measurements	125
4.42	Sum of the odd-indexed coefficients compared with BBSO measurements	126
4.43	Sum of the odd-indexed coefficients compared with 1984 Mt Wilson measurements at low- and intermediate-degrees.	126
5.1	ℓ - ν diagram for the modes obtained from the high-resolution spectra	130
5.2	FWHM for the modes obtained from the high-resolution spectra	131
5.3	Total modal power for the modes obtained from the high-resolution spectra	132
5.4	Set of modes sensitive to spatio-temporal sidelobe contamination	134
5.5	Partial regression plots	140
5.6	Total regression plot	141
5.7	Comparison of m -averaged leakage matrices with a Gaussian profile	142
5.8	ℓ - ν diagram for the modes obtained from the low-resolution spectra	143
5.9	Ridge FWHM computed from the low-resolution spectra	145
5.10	Modal FWHM computed from the low-resolution spectra	146
5.11	Limb Fourier transforms and resulting MTF	149
5.12	Total modal power estimated from the low-resolution spectra	150
5.13	Modal frequency differences with BBSO 1988 set	153
5.14	Modal frequency difference with BBSO high-degree measurements	155
5.15	Comparison of observed frequencies with theoretical frequencies computed with a standard solar model	159

5.16	Total energy per mode	161
5.17	Lifetime correlations plots	163
6.1	Rotational kernels for $\ell = 10, 20, 50, 100, 200$ and 500 and selected radial orders, n	169
6.2	Initial inverted rotation rate profiles, function of target radii	186
6.3	Initial inverted profiles, function of kernel centroids	187
6.4	Resolution kernel corresponding to the initial inverted profiles	188
6.5	ISE solution profile after adjustment of the discretization grid through an iterative process	193
6.6	Set of resolution kernels corresponding to the ISE solutions	194
6.7	Solution obtained with the CLS1d method using MWO n -averaged splittings	196
6.8	Solution obtained with the CLS2d method using MWO n -averaged splittings	197
6.9	Solution obtained with the OAK method using MWO n -averaged splittings	197
6.10	Selection of resolution kernels corresponding to the solution presented Figure 6.7	198
6.11	Selection of resolution kernels corresponding to the solution presented Figure 6.8	199
6.12	Selection of resolution kernels corresponding to the solution presented Figure 6.8	200
6.13	Direct comparison of inverted rotation rate profiles based on the MWO set alone	201
6.14	Comparison of profiles obtained using the MWO set alone, but with and without high-degree modes	202
6.15	Resolution kernels corresponding to the CSL1d solution obtained using solely the MWO low and intermediate degree	203
6.16	Comparison of inverted profile using MWO and combined n -averaged BBSO-MWO splittings, using the CLS1d method	205
6.17	Comparison of inverted profile using MWO and combined n -averaged BBSO-MWO splittings, using the CLS2d method	206

6.18	Comparison of inverted profile using MWO and combined n -averaged BBSO-MWO splittings, using the OAK method	206
6.19	Comparison of resolving widths obtained using MWO and combined n -averaged BBSO-MWO splittings	207
6.20	Inverted profiles using the CLS1d method modified to allow for a discontinuity	209
6.21	Resolution kernels associated with the inverted profile using the CLS1d method modified to allow for a discontinuity	210
6.22	Resolving widths associated with the profile inverted using the CLS1d method modified to allow for a discontinuity	211
6.23	Inverted profile computed with the OAK method and obtained using the singlet BBSO set consolidated by the MWO set	212
6.24	Selection of resolution kernels associated with the solution presented Figure 6.23 that uses only the singlet BBSO set	213
6.25	Selection of resolution kernels associated with the solution presented Figure 6.23 that uses the singlet BBSO set combined with the intermediate-degree MWO set	214
6.26	Selection of resolution kernels associated with the solution presented Figure 6.23 that uses the singlet BBSO set consolidated by the MWO intermediate- and high-degree set	215
6.27	Resolving widths associated with solutions presented Figure 6.23	216
6.28	Equatorial rotation rate as a function of depth inferred from rotational frequency splittings, measured for degree $5 \leq \ell \leq 600$	217

List of Tables

3.1	Image size comparison for 88-07-12	37
3.2	Comparison of calibration coefficients	47
4.1	Comparison of Legendre polynomial fitting coefficients, computed for $\ell = 50$ with different methods	72
4.2	Comparison of Legendre polynomial fitting coefficients, computed for $\ell =$ 160 with different methods	72
4.3	Correction coefficients q_i	106
5.1	Comparison of high-degree modal frequencies with BBSO measurements . .	156
6.1	Azimuthal extension of $\bar{\Omega}$ as a function of spherical harmonic degree ℓ , and typical corresponding inner turning point	171
A.1	Legendre polynomials fitting coefficients resulting from the frequency split- ting analysis of the tesseral high resolution spectra	224
A.2	Scaled frequency splittings ($\Delta\nu/2\ell$) estimated from the low resolution sec- toral spectra	227
B.1	Modal frequency, width and total power estimated from the high resolution collapsed spectra	228
C.1	Modal frequency, width and total power estimated from the low resolution collapsed spectra	237

ACKNOWLEDGMENTS

I thank my advisor, Roger K. Ulrich, for providing guidance and support throughout my years at U.C.L.A. Roger managed to achieve the fine balance between superb scientific support and guidance, excellent direction and motivation, and exceptional tolerance for independent research. I also thank Roger for providing me steadfast financial support during my graduate study career.

I am grateful to Edward J. Rhodes, Jr., from the department of Astronomy at U.S.C. and principal investigator of the Mount Wilson 60-foot tower project, for entrusting me with access to the data and resources associated with the 60-foot tower. During these years of close collaboration, Edward gave me not only access to a unique set of exceptional data, but complete access to all the resources associated with the project, data and resources without which this dissertation would not have been possible. I also thank Edward for providing remarkable support and guidance throughout my work on the project, and for complementing my financial support when possible.

I am also grateful to Alessandro Cacciani, for providing the know-how regarding the magneto-optical filters, heart of the project's instrument. I thank Jan van Amersfoort, from the Space Physics and Astrophysics at the Jet Propulsion Laboratory (J.P.L.), for building, under the supervision of Alessandro Cacciani, most of the magneto-optical filter units used for this project. I also extend my thanks to Edward J. Smith, supervisor of the Magnetic Fields and Plasma Waves Group of the Space Physics and Astrophysics at J.P.L., for supporting our activities at the Mt Wilson 60-foot tower.

I thank Steven Tomczyk, whose work on the project during his graduate studies at U.C.L.A. contributed largely to the feasibility of this dissertation. Steven played also a key role in my understanding of the 60-foot tower instrumentation and observing procedures by sharing with me his unique experience on the project.

I am very much grateful to Maynard Clark and John Boyden, whose contribution to the project's instrumentation and software are immense and in turn made this project possible. I also thank Tony Misch, Martin Iedema, Tim Purdy, and Victoria Alten for providing the project with a dedicated observing crew, and wish to extend my thanks to Larry Webster and the staff and residents of Mt Wilson for their generous support and assistance to this project.

I am also very much grateful to Zdenka Plavec and Jonathan Eisenhamer, from the U.C.L.A. Astronomy department, for providing me with an exceptional in house support with computer hardware and software, and tailoring the departmental computer environment to accommodate some of the needs specific to this dissertation. I also thank Dennis Smith, from the U.S.C. University Computing Services, for his superb support and assistance in our use of the supercomputing facilities made available to this project; Robert Tooper, from U.S.C. University Computing Services, for porting to the IBM 3090-160E most of the computer intensive reduction procedures and for his excellent assistance in making use of that facility; the supporting staff from the University Computing Center at U.S.C. for providing such an excellent support of the computing facilities and for accommodating some of the specific requirements of this project; the crew of operators at U.S.C., known as the "cube" operators, for carrying the burden of mounting and dismounting the numerous tapes and cartridges. I also extend my thanks to Richard E. Kaplan, U.S.C.'s Vice-Provost for Research and Academic Computing for his support of this project by providing the assistance of Dennis Smith and Robert Tooper and by providing us with access to both the Alliant FX/80 and the IBM 3090 computers of the University Computing Center. I am also grateful to the supporting staff of the J.P.L. Cray X-MP supercomputer, and the supporting staff of the Numerical Aerodynamics Simulation (N.A.S.) Program of the Ames research center for providing such excellent support of their supercomputing facilities, including their Cray 2 and Cray Y-MP supercomputers.

I thank Ken G. Libbrecht for providing his results to me prior to their publication.

Last, but not least, I am very much grateful to my sister, Nourit H. Korzennik-Brunner, my brother-in-law, Elliott H. Brunner, and my nephew Jaron K. Brunner, for their support, love, and care. I wish also to express my infinite gratitude towards Elliott who has patiently proof-read the numerous incarnations of this manuscript. I am grateful to my parents, Eugenia Geller-Korzennik and Henryk Korzennik, for their boundless support, love and care during my undergraduate and graduate studies, and for all the efforts and sacrifices they made to give me a proper education. Finally, amongst my fellow U.C.L.A. graduate students, I shall single out Joel Kastner and Dave Weintraub. Joel became a close friend and confidant throughout these years of life as a graduate student in a foreign country, while Dave, with whom I had the pleasure to share my office, entrusted me with his friendship; both have through their generous support contributed in many ways to make this endeavor possible.

This research was supported by the NASA grant NAGW-472 at U.C.L.A. and NAGW-13 at U.S.C., and by the NSF grant ATM-8009469 and INT-8400213 at U.S.C.. Additional financial support was provided by the Jet Propulsion Laboratory's Director's Discretionary Fund and the California Institute of Technology's President's Fund.

VITA

- June 15, 1959 Born, Brussels, Belgium
- 1982 Engineer, Applied Physics (*Ingénieur Civil Physicien*)
Université Libre de Bruxelles
Brussels, Belgium
- 1983–1985 Research Fellow
European Space Agency, Space Science Department
Noordwijk, The Netherlands
- 1985–1986 Teaching Assistant
Department of Astronomy
University of California, Los Angeles
- 1986–1990 Research Assistant
Department of Astronomy
University of California, Los Angeles

PUBLICATIONS AND PRESENTATIONS

- Anderson, B., Domingo, V., Jimenez, A., Jones, A., Korzennik, S. G., Pallé, P. L., Pérez Hernández, F., Régulo, C., Roca Cortés, T., and Tomás, L., 1988: "Diurnal Photometric Conditions at Teide Solar Observatory and Long-term Solar Irradiance Variations," *Solar Phys.*, **116**, 391–399.
- Anderson, B., Domingo, V., Jones, A., Korzennik, S. G., Jimenez, A., Pallé, P. L., Régulo, C., Roca Cortés, T., and Tomás, L., 1988: "Solar Luminosity Oscillation Telescope (SLOT)," in *Seismology of the Sun and Sun-like Star*, E. J. Rolfe (Ed.), Paris: ESA SP-286, 175–176.
- Crommelynck, D., Domingo, V., and Korzennik, S. G., 1984: "Determination of the Variation of the Total Solar Irradiance over a Five Month Interval," at 25th COSPAR Plenary Meeting, Graz, Austria.
- Goode, P. R., Dziembowski, W. A., Korzennik, S. G., and Rhodes, E. J., Jr., 1990: "What We Know about the Sun's Internal Rotation from Solar Oscillations," *Astrophys. J.*, in press.
- Goode, P. R., Dziembowski, W. A., Rhodes, E. J., Jr., and Korzennik, S. G., 1990: "Has the Sun's Internal Rotation Changed through this Activity Cycle?," to appear in *Progress of Seismology of the Sun and Stars*, Y. Osaki and H. Shibahashi (Ed.), in press.

- Hathaway, D. H., Rhodes, E. J., Jr., Cacciani, A., and Korzennik, S. G., 1987: "Spectrum, Lifetime and Rotation Rate of Supergranules," at A.A.S. Solar Division Meeting, Hawaii.
- Jiménez, A., Pallé, P. L., Pérez Hernández, F., Régulo, C., Roca Cortés, T., Domingo, V., and Korzennik, S. G., 1988: "Earth Based Observations of Solar Luminosity Oscillations," in *Advances in Helio- and Asteroseismology*, I.A.U. Symp. 123, J. Christensen-Dalsgaard and S. Frandsen (Ed.), Reidel: Dordrecht, 71-74.
- Jiménez, A., Pallé, P. L., Régulo, C., Roca Cortés, T., Domingo, V., and Korzennik, S. G., 1986: "Variations in the Luminosity of Integral Sunlight," at 26th COSPAR Plenary Meeting, Toulouse, France.
- Jiménez, A., Pallé, P. L., Roca Cortés, T., Domingo, V., and Korzennik, S. G., 1987: "Ground-Based Measurements of Solar Intensity Oscillations," *Astron. Astrophys.*, **172**, 323-326.
- Korzennik, S. G., Cacciani, A., Rhodes, E. J., Jr., Tomczyk, S., Ulrich, R. K., and Woodard, M. F., 1988: "Inversion of Solar Rotation Rate vs. Depth and Latitude," in *Seismology of the Sun and Sun-like Star*, E. J. Rolfe (Ed.), Paris: ESA SP-286, 117-124.
- Korzennik, S. G., Cacciani, A., Rhodes, E. J., Jr., and Ulrich, R. K., 1990: "Contribution of High Degree Frequency Splittings to the Inversion of the Solar Rotation Rate," to appear in *Progress of Seismology of the Sun and Stars*, Y. Osaki and H. Shibahashi (Ed.), in press.
- Korzennik, S. G. and Ulrich, R. K., 1989: "Seismic Analysis of the Solar Interior I.: Can Opacity Changes Improve the Theoretical Frequencies?," *Astrophys. J.*, **339**, 1144-1155.
- Korzennik, S. G., Yaari, A., and Ulrich, R. K., 1986: "Inversion of Perturbed Solar Models for Improved Solar Oscillation Frequencies Agreement," at 169th A.A.S. Meeting, Pasadena, California.
- Rhodes, E. J., Jr., Cacciani, A., Garneau, G., Korzennik, S. G., and Smith, D., 1988: "Video Movies of 1987 Magneto-Optical Filter Observations Recorded with the J.P.L. 1024x1024 CCD Camera," at 172nd A.A.S. Meeting, Kansas City, Missouri.
- Rhodes, E. J., Jr., Cacciani, A., and Korzennik, S. G., 1988: "Initial High Degree p-Mode Frequency Splittings from the 1988 Mt Wilson 60-Foot Solar Tower Oscillation Program," in *Seismology of the Sun and Sun-like Star*, E. J. Rolfe (Ed.), Paris: ESA SP-286, 81-86.
- Rhodes, E. J., Jr., Cacciani, A., and Korzennik, S. G., 1990: "Evidence for Radial Variations in the Equatorial Profile of the Solar Internal Angular Velocity," to appear in *Progress of Seismology of the Sun and Stars*, Y. Osaki and H. Shibahashi (Ed.), in press.

- Rhodes E. J., Jr., Cacciani, A., and Korzennik, S. G., 1990: "Observations of Intermediate- and High-Degree p-Modes Oscillations During Sunspot Cycles 21 and 22," at 29th COSPAR Plenary Meeting, The Hague, the Netherlands.
- Rhodes, E. J., Jr., Cacciani, A., Korzennik, S. G., Tomczyk, S., Ulrich, R. K., and Woodard, M. F., 1988: "Radial and Latitudinal Gradients in the Solar Internal Angular Velocity," in *Seismology of the Sun and Sun-like Star*, E. J. Rolfe (Ed.), Paris: ESA SP-286, 73-80.
- Rhodes, E. J., Jr., Cacciani, A., Korzennik, S. G., Tomczyk, S., Ulrich, R. K., and Woodard, M. F., 1990: "Depth and Latitude Dependence of the Solar Internal Angular Velocity," *Astrophys. J.*, **351**, 687-700.
- Rhodes E. J., Jr., Cacciani, A., Korzennik, S. G., and Ulrich, R. K., 1990: "Further Evidence for Radial Variations in the Solar Equatorial Angular Velocity Profile," at 167th A.A.S. meeting, Albuquerque, New Mexico.
- Rhodes, E. J., Jr., Cacciani, A., Woodard, M. F., Tomczyk, S., Korzennik, S. G., and Ulrich, R. K., 1987: "Estimates of the Solar Angular Velocity Obtained with the Mt Wilson 60-Foot Solar Tower," in *The Internal Solar Angular Velocity: Theory, Observations and Relationship to Magnetic Fields*, B. R. Durney and S. Sofia (Ed.), Dordrecht: Reidel, 75-82.
- Rhodes, E. J., Jr., Cacciani, A., Woodard, M. F., Tomczyk, S., Korzennik, S. G., and Ulrich, R. K., 1988: "Measurements of Solar Internal Rotation Obtained with the Mt Wilson 60-Foot Solar Tower," in *Advances in Helio- and Asteroseismology*, I.A.U. Symp. 123, J. Christensen-Dalsgaard and S. Frandsen (Ed.), Dordrecht: Reidel, 41-44.
- Rhodes, E. J., Jr., Tomczyk, S., Woodard, M. F., Cacciani, A., Korzennik, S. G., and Ulrich, R. K., 1986: "Evidence for Radial Gradients in the Solar Internal Rotational Velocity," at 169th A.A.S. Meeting, Pasadena, California.
- Rhodes, E. J., Jr., Woodard, M. F., Cacciani, A., Tomczyk, S., Korzennik, S. G., and Ulrich, R. K., 1988: "On the Consistency of Intermediate Degree p-Mode Frequencies during the Declining Phase of Solar Cycle 21," *Astrophys. J.*, **326**, 479-485.
- Rhodes, E. J., Jr., Woodard, M. F., Cacciani, A., Tomczyk, S., Korzennik, S. G., and Ulrich, R. K., 1987: "On the Consistency of Intermediate Degree p-Mode Frequencies during the Declining Phase of Solar Cycle 21," at A.A.S. Solar Division Meeting, Hawaii.
- Tomczyk, S., Cacciani, A., Korzennik, S. G., Rhodes, E. J., Jr., and Ulrich, R. K., 1988: "Measurements of the Rotational Frequency Splittings of the Solar Five-Minute Oscillations from Magneto-Optical Filter Observations," in *Seismology of the Sun and Sun-like Star*, E. J. Rolfe (Ed.), Paris: ESA SP-286, 141-147.
- Woodard, M. F., Rhodes, E. J., Jr., Tomczyk, S., Korzennik, S. G., Cacciani, A., and Ulrich, R. K., 1987: "Angular Velocity of the Solar Interior Obtained by an Asymptotic Inversion of p-Modes Frequency Shifts," at A.A.S. Solar Division Meeting, Hawaii.

ABSTRACT OF THE DISSERTATION

Seismic Analysis of the Sun from Intermediate and High Degree p-Modes

by

Sylvain Gereon Korzennik

Doctor of Philosophy in Astronomy

University of California, Los Angeles, 1990

Professor Roger K. Ulrich, Chair

Solar oscillations provide a unique tool to investigate the internal structure and dynamics of the Sun. While accurate measurements of the solar acoustic spectrum characteristics have been performed for low- and intermediate-degree modes, only a limited set of short time baseline measurements for high-degree modes has been available ($\ell > 120$). The purpose of this work is to provide an accurate and more reliable set of measurements for these high-degree modes.

High spatial resolution (2.2 arcsec per pixel) full-disk dopplergrams of the solar surface have been acquired at the Mt Wilson 60-foot solar tower during the summer of 1988, using a doppler analyzer based on the sodium magneto-optical filter. Twenty consecutive days of observations have been reduced to spherical harmonic coefficient time series, for degrees $\ell \leq 600$. The time series were then Fourier transformed in order to estimate the corresponding power spectra.

From these power spectra, frequency splittings have been estimated for degree $20 \leq \ell \leq 600$. At low and intermediate degree ($\ell \leq 120$), individual modes could be isolated, and

hence reliable tesseral measurements have been obtained. At high-degree ($\ell > 120$), the presence of mode blending introduced systematic errors in the tesseral frequency splitting determination. The nature of these systematics has been carefully studied, but our simulations were unable to reproduce in detail the observed systematics, and therefore, an *ad hoc* procedure was developed to correct for them. Alternatively, sectoral frequency splittings, shown to be less sensitive to mode blending systematics, have provided a more reliable estimate of the frequency splitting for these high-degree modes.

From collapsed $\langle m = 0 \rangle$ spectra modal frequencies, amplitudes and lifetimes have been estimated for $20 \leq \ell \leq 600$. The required corrections for mode blending, point spread function attenuation, and finite observing run have been applied. These new measurements are compared with previous determinations and theoretical predictions.

Finally, based on the frequency splittings obtained from the present study, as well as contemporaneous independent measurements, we have inferred the internal rotation rate as a function of depth in the equatorial regions, and discuss some of the implications of such a profile in relation to solar dynamo, global circulation and evolutionary models of rotating stars.

Chapter 1

Introduction

Since the early observation, more than three decades ago, of a peculiar oscillatory behaviour at the solar surface, that is now known as the 5-minute oscillation, helioseismology has emerged today as a powerful diagnostic tool to probe and understand the solar structure and its dynamics, and beyond the Sun, some of the key aspects of astrophysics.

The Sun, our nearest star, has always provided astrophysicists with the unique opportunity of testing or challenging our understanding of stellar structure and evolution and, by extension, our understanding of galaxies and the universe. Yet, most of this knowledge has been gained from the study of the visible part of the Sun, namely the surface and the outer atmosphere. On the basis of these observations, a wide range of conclusions have been drawn on the solar interior, whose predicted structure is governed by our understanding of nuclear energy generation and nucleosynthesis in the core, the composition, equation of state and energy transport throughout the interior. This structure depends also on the transport of energy in the envelope by convection, and its dynamics hold the key to our the understanding of large-scale flow patterns, the solar dynamo, and ultimately the solar cycle.

While the observation of the solar neutrino flux has provided a new diagnostic tool for the deep solar interior structure, with a particular sensitivity to the nuclear energy generation in the core, the analysis of the solar acoustic spectrum provides a unique access to the study of a wide variety of properties of the Sun's interior. Indeed, the solar interior stratification creates an acoustic cavity whose depth and latitudinal extent varies with frequency and horizontal wavenumber. Moreover, the solar acoustic spectrum is rich with perhaps more than ten million modes excited, and the solar cavity has overall a high quality factor within which some modes are observed to have lifetimes exceeding one month. Since each individual mode, i.e. each resonant frequency, is constrained by the structural and dynamical properties that prevail throughout the extent of its resonant cavity, specific information on the Sun's internal properties can be extracted from the analysis of the solar acoustic spectrum.

Solar oscillations is today a mature subject, described in detail in any modern solar textbook (see for instance Noyes, 1982; Brown *et al.*, 1986; Zirin, 1988 or Unno *et al.*, 1989). The "embarrassing extent" (Deubner, 1975) to which early observations matched theoretical predictions has since been replaced, due to the exceptional accuracy of modern observations, with puzzling discrepancies that, like the neutrino problem, indicate the incomplete nature of our understanding of the physical processes and conditions that govern the solar structure.

In the following sections, we briefly review some of the key points of solar oscillation theory followed by the precise context of the present study. We present the motivations behind our attempt to extend the accurate measurement of the properties of the solar acoustic spectrum to high-degree modes. Finally, let us point out that we have limited ourselves to the study of p-modes, and f-modes (i.e. modes whose restoring force is dominated by pressure, and the fundamental modes), since the small surface amplitude and the long period of g-modes (i.e. the modes whose restoring force is dominated by gravity) place

them most probably beyond the reach of the doppler analyser used for the present study.

1.1 Background

The first detection of an oscillatory pattern in the Sun's surface velocity field was made as early as 1960 (Leighton *et al.*, 1962). For over a decade, these quasi-periodic variations seen in high spatial resolution Doppler observations of small portions of the solar disk, were thought to be a localized resonant response of the solar atmosphere to local excitation from convection cells. In fact, these observations showed bursts of quasi-periodic velocity signals, of some 1000 m s^{-1} in amplitude and with a period around 5 minutes that would last for some 6 or 7 periods, and showed a spatial coherence length of about 30 Mm.

The existence of an acoustic resonant cavity below the solar surface was first suggested by Ulrich (1970) and demonstrated a few years later by Deubner (1975) and Rhodes *et al.* (1977). The unequivocal demonstration of the global nature of the 5-minute oscillations as acoustic resonant modes came from the power distribution of the observed velocity signal as a function of frequency and spatial wavenumber. Actually, from the dispersion relation of the acoustic spectrum, which is the relation between the temporal frequency and the spatial wavenumber that guarantees radial propagation of the wave, the precise location of the power distribution as a function of frequency and spatial wavenumber could be predicted on the basis of a model of the solar interior stratification. This is illustrated in Figure 1.1, where the power distribution as a function of spherical harmonic degree, ℓ , (corresponding to the horizontal wavenumber) and frequency, ν , resulting from the present study, is presented for $20 \leq \ell \leq 600$ and $1 \leq \nu \leq 8 \text{ mHz}$. The remarkable agreement between the predicted and observed power distribution of very early measurements in a totally new aspect of solar physics can be viewed in retrospect as a clear indication of the strength of helioseismology as a diagnostic tool. The apparent quasi-periodic behaviour

of the localized oscillatory pattern and its apparent short spatial coherence length result from the beating of some 10^7 modes simultaneously excited, each at different frequency and spatial wavenumber, and of some $20\text{--}50\text{ cm s}^{-1}$ in amplitude.

The solar acoustic oscillations can be characterized as small perturbations of pressure and density about the equilibrium. Since the Sun's oblateness is small, the equilibrium model can be considered as spherically symmetric and the angular dependence of the perturbation decomposed as a sum of spherical harmonic functions, which form a complete basis of orthonormal functions on the sphere. The angular dependence of the wave function will be characterized by the spherical harmonic degree ℓ and azimuthal order m ($|m| \leq \ell$), while its radial dependence will be characterized by the number of radial overtone, or the radial order, n of the wave.

From a ray path point of view, a wave of a given horizontal wavenumber, k_h , and frequency, ν , will be reflected at the surface by the very steep density gradient present there. The downward wave will then be progressively refracted since the deeper portion of the wave front will propagate faster as the sound speed increases with depth in the solar interior, as schematically illustrated in Figure 1.2. At some given depth the wave will be traveling horizontally, and is thus turned around or reflected and will propagate back towards the surface. This reflection will occur at a depth where the wave's horizontal velocity $2\pi\nu/k_h$ equals the local sound speed, c . Hence, for a larger horizontal wavenumber (or larger spherical harmonic degree ℓ , since $k_h = \sqrt{\ell(\ell+1)}/R$) but a similar frequency, reflection will occur at lower local sound speed, hence at a shallower depth. Indeed, since wave fronts are proportionally more tilted from the horizontal for larger wavenumber, they will be refracted faster and penetrate less deeply in the Sun's interior, as illustrated in Figure 1.2.

Resonance (i.e. standing waves) will only occur if there is an integral relation between the wave's travel time along the ray path between each reflection and the wave frequency.

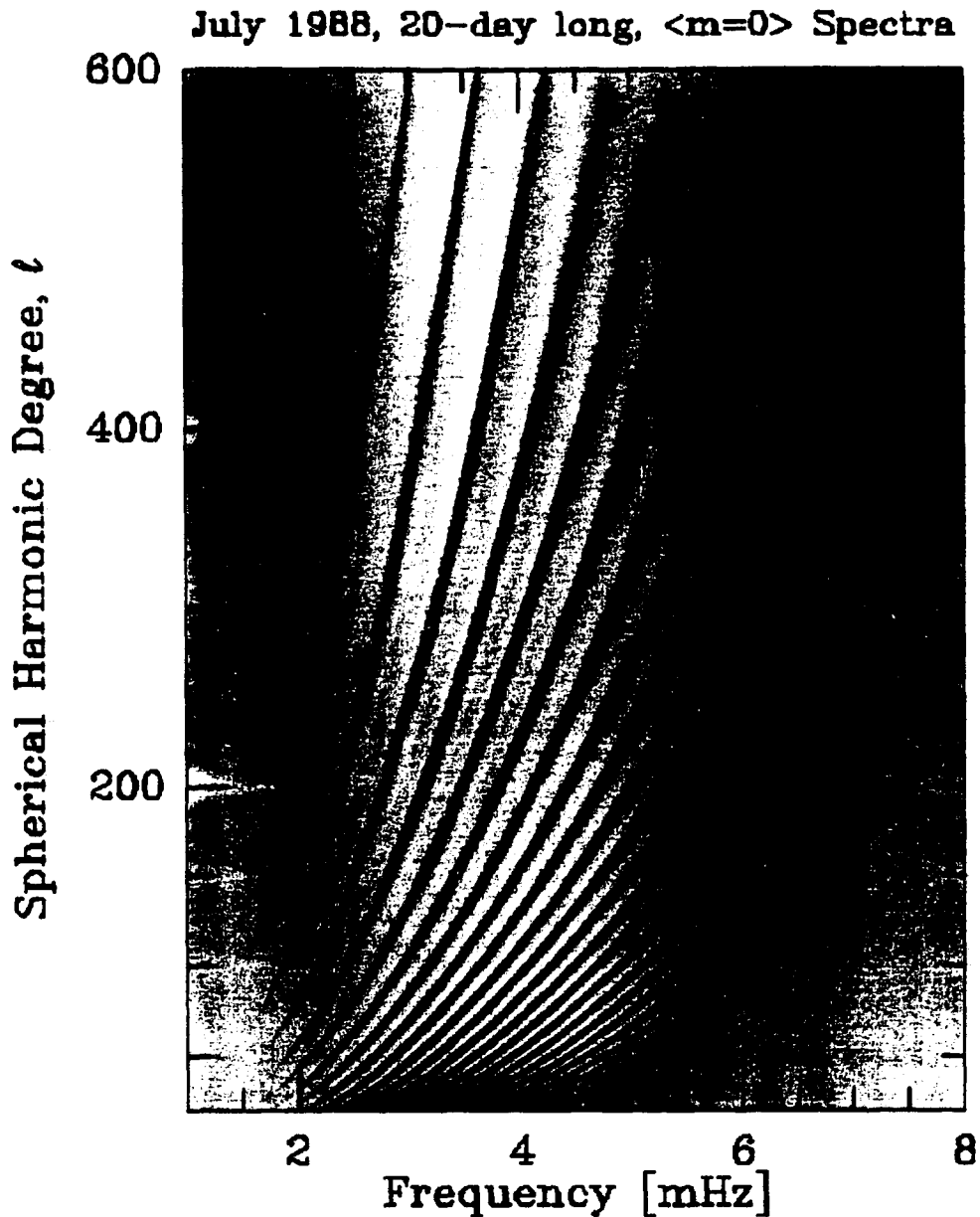


Figure 1.1: Power density distribution, in scaled logarithmic units, as a function of degree and frequency, of the solar acoustic spectrum for $20 \leq \ell \leq 600$ and $1 \leq \nu \leq 8$ mHz. Namely, low frequency resolution $\langle m = 0 \rangle$ average power spectrum corresponding to 20 days of full-disk doppler observations. Note that the f-mode is clearly visible in the upper left corner of the figure, while power ridges at lower degree can be seen up to the Nyquist frequency (8.3 mHz). (In order to reduce the dynamical range required to display this figure, the logarithm of the power density was divided by its frequency averaged ℓ dependence and then by the ℓ -averaged frequency dependence. Thus, the contrast in this figure does not reflect the observed envelope of the power distribution, but only the local signal-to-noise ratio)

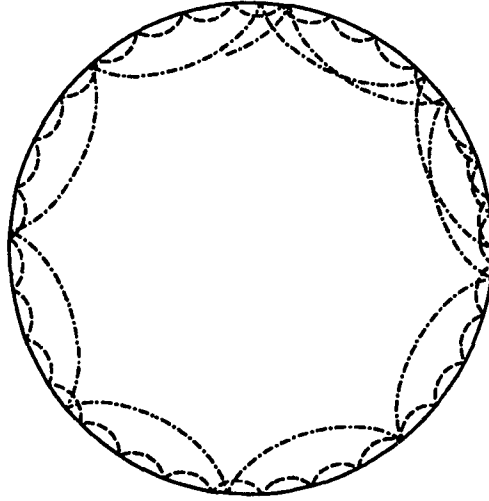


Figure 1.2: Schematic description of the ray path of an acoustic wave in a radially stratified medium. Notice that for a mode with a large horizontal wavenumber (i.e. a large degree, dashed curve), the wave is reflected at a shallower depth than for a mode with a smaller wavenumber (i.e. smaller degree, dot dashed line). For this particular figure, a power law with depth for the sound speed stratification was used and the ray path of a sound wave was computed in a cylindrical geometry.

Therefore, for a given horizontal wavenumber (or spherical harmonic degree ℓ), there will be a discrete set of resonant modes, or resonant frequencies, for each possible radial overtone, n .

In a spherically symmetric model, since there is no preferential axis to define the azimuthal direction, the acoustic spectrum will be degenerated in the azimuthal order m . In reality, non-spherically symmetric perturbations are present on the Sun, like the solar rotation for instance, and the $2\ell + 1$ azimuthal degeneracy will be lifted. There will be a specific resonant frequency for each spherical harmonic degree, ℓ , azimuthal order m and radial order n . The radial extent of the resonant cavity associated with each mode will be characterized by the location of the inner turning point, function of ℓ and n , while the latitudinal extent will be characterized by the angular dependence of the spherical harmonic

functions and will be a function of the ratio m/ℓ . Figure 1.3 illustrates the angular dependence of the spherical harmonic functions, and shows the concentration of the mode around the equator for the sectoral modes (i.e. $m = \pm\ell$), while the zonal modes (i.e. $m = 0$) sample the polar regions as well. Since each tesseral mode (i.e. $m \neq 0$ and $m \neq \pm\ell$) samples differently the solar acoustic cavity with latitude, latitudinal information will be carried by these modes.

Since the first confirmation of the global resonant nature of the 5-minute oscillations numerous techniques have been developed to observe the solar oscillations and high accuracy measurements of the acoustic spectrum for low- and intermediate-degree modes have been made.

Using non-imaging techniques, low-degree modes (i.e. $\ell = 0, \dots, 3$) have been observed in Doppler velocity measurements (Pallé *et al.*, 1986), total irradiance (Woodard, 1984) or narrow spectral band luminosity (Jiménez *et al.*, 1987). Intermediate-resolution, full-disk velocity or intensity measurements (i.e. imaging of the whole disk with some 8–10 arc sec of resolution) have probed the solar acoustic spectrum for low- and intermediate-degrees (i.e. $5 \leq \ell \leq 120$, see Tomczyk, 1988; Rhodes *et al.*, 1990; Duvall *et al.*, 1988; and Brown and Morrow 1987). Finally, high-resolution, full-disk intensity measurements, and disk-center, high-resolution measurements have extended the observation of the solar acoustics spectrum up to $\ell \sim 1400$ from the ground (Libbrecht *et al.*, 1990) and up to $\ell \sim 2500$ from space (Tarbell *et al.*, 1980).

While a wide range of observations of the solar acoustic spectrum for low- to high-degree modes (i.e. $0 \leq \ell \leq 2500$) exist, the accuracy of these measurements greatly varies with degree. In fact, while long time baseline measurements (from a few weeks to a few months) at low- and intermediate-degrees have led to relative uncertainties on modal frequencies around 2 to 5 10^{-5} , the limited set and the short temporal baseline (some 10 hours) of the high-degree measurements have provided modal frequencies with relative uncertainties

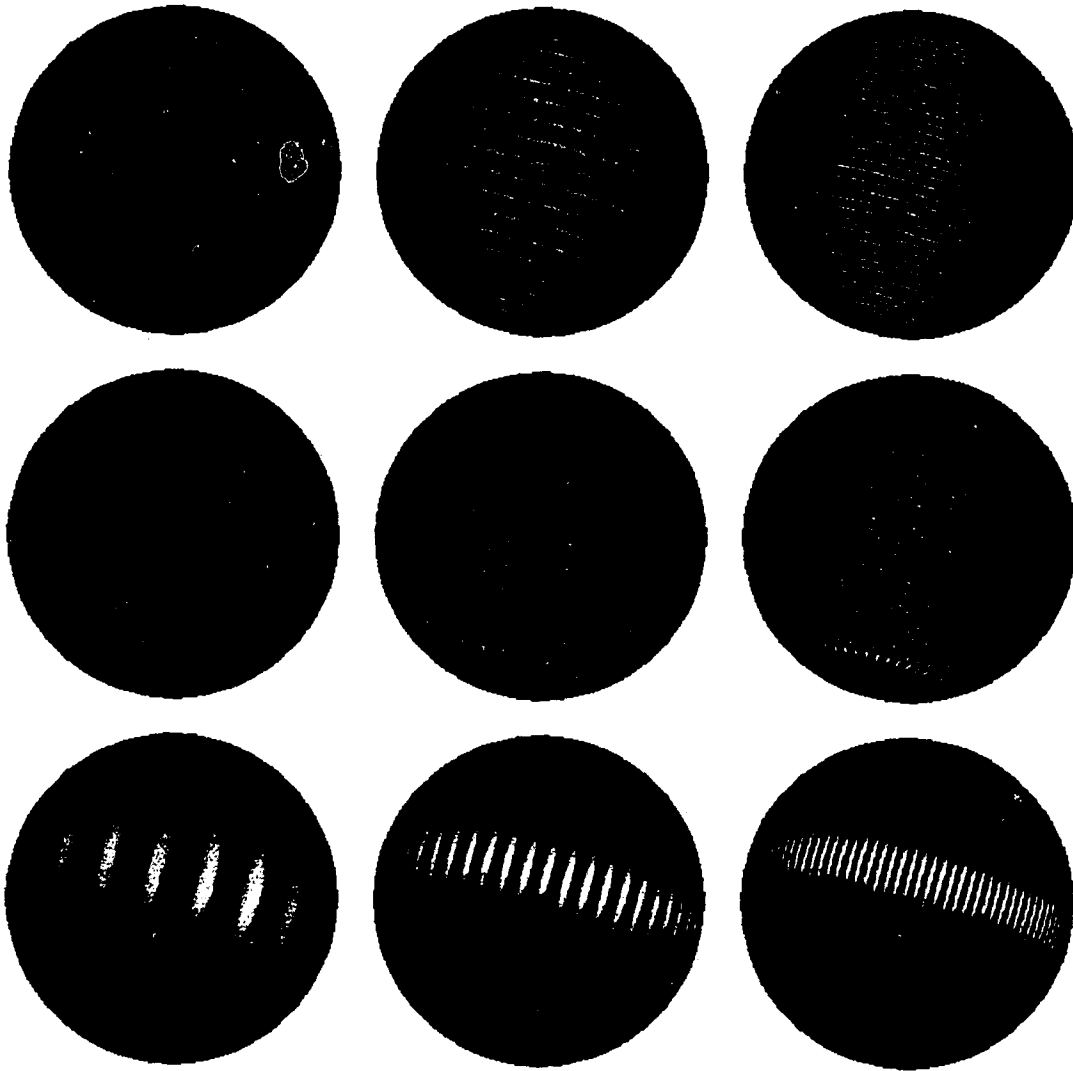


Figure 1.3: Selection of spherical harmonic functions for $\ell = 20, 50, 100$, and $m = 0, \ell/2, \ell$ respectively.

some two order of magnitude larger than for the low- and intermediate-degree modes. Moreover systematic effects present in the measurement of high-degree modes have plagued the initial determination of these modal frequencies (see discussion in Libbrecht *et al.*, 1990).

On the other hand the determination of the solar oscillation frequency splittings, namely the variation with azimuthal degree, m , of the modal frequency, has been restricted to low- and intermediate-degrees ($5 \leq \ell \leq 120$, Rhodes *et al.*, 1990; Libbrecht, 1989; Tomczyk, 1988; Duvall *et al.*, 1987; Brown and Morrow 1987). While dynamical information on the solar interior, i.e. the internal angular velocity, is carried by the frequency splittings, the short temporal baseline of the high-resolution measurements, and systematic effects associated with the observational instrumentation as well as the inherent limitation associated with the observation of high-degree modes, have prevented these initial measurements from providing information on the subsurface layers (see Woodard and Libbrecht 1988).

1.2 Present Study

The present study is based on full-disk, high-resolution Doppler velocity measurements of the solar surface, obtained between July 1st and July 20th 1988 at the Mt Wilson 60 foot Solar Tower, using a 1024×1024 pixel CCD camera, and a magneto-optical filter configuration. The high instrumental spatial resolution combined with the average seeing quality allowed us to observe the solar acoustic spectrum up to $\ell = 600$.

The purpose of this work is to provide a more accurate and more reliable set of measurements at high-degree modes ($\ell > 120$) of the modal frequency and the frequency splitting. The major motivations behind our attempt to achieve accurate measurements at high-degree modes are: first, since the high-degree modes sample the subsurface layers of the solar interior, a better understanding of the dynamics that prevails just below the solar

surface is only be accessible through the measurement of high-degree splittings. Second, a more accurate knowledge of the high-degree modal frequencies will allow a better study of some of the structural aspects that governs the solar envelope, for instance convection. Finally, from the nature of the acoustic cavity, all the modes are reflected at the surface and will be sensitive to the conditions that prevail just below the surface. While it has been argued that through differential analysis of low- and intermediate-degree modes, localized information independent of the subsurface conditions can be extracted, the residual sensitivity of such an analysis scheme to the subsurface regions may introduces ambiguities, or systematic errors, to such inferences associated to the absence of high-degree mode data.

We describe in Chapter 2 the instrumental configuration and the observational procedure we used to acquire the raw data set while in Chapter 3 we describe the data reduction procedures that lead from raw images to solar p-mode properties, that are the frequency splittings and the modal frequencies, widths and amplitudes. The frequency splitting measurements are presented in Chapter 4 while the modal frequency, width and amplitude measurements are presented in Chapter 5. Finally, we present in Chapter 6 the solar equatorial rotation rate as a function of depth, inferred from the frequency splittings measured in the present study.

Chapter 2

Instrument

The high-resolution, full-disk, line-of-sight velocity measurements used for the purpose of this investigation were acquired at the Mount Wilson 60-Foot Solar Telescope, during the summer of 1988, with a doppler analyzer based on a magneto-optical filter (MOF) configuration combined with a 1024 by 1024 pixel CCD camera. While earlier incarnations of the observing system have been extensively presented elsewhere (Rhodes *et al.*, 1983; Tomczyk, 1988, and references therein), we describe in the next sections the main components of the instrument with an emphasis on the aspects specific to the high-resolution configuration.

The main components of the instrument are outlined in Figure 2.1 and can be grouped as: the solar telescope with its auto-guider, the doppler analyzer and the image acquisition system.

In summary, the instrument consists of the following elements: at the top of a 60-foot high tower, a pair of flat mirrors (M1 and M2) direct a beam of unfocused sunlight down a light shaft to the observing room located at ground level. Some four meters above ground level, near the base of the light shaft, a 3000 mm focal length doublet objective lens (OL), stopped down to a 60 mm dia. aperture (OA), focuses a 28 mm dia. image of the sun just

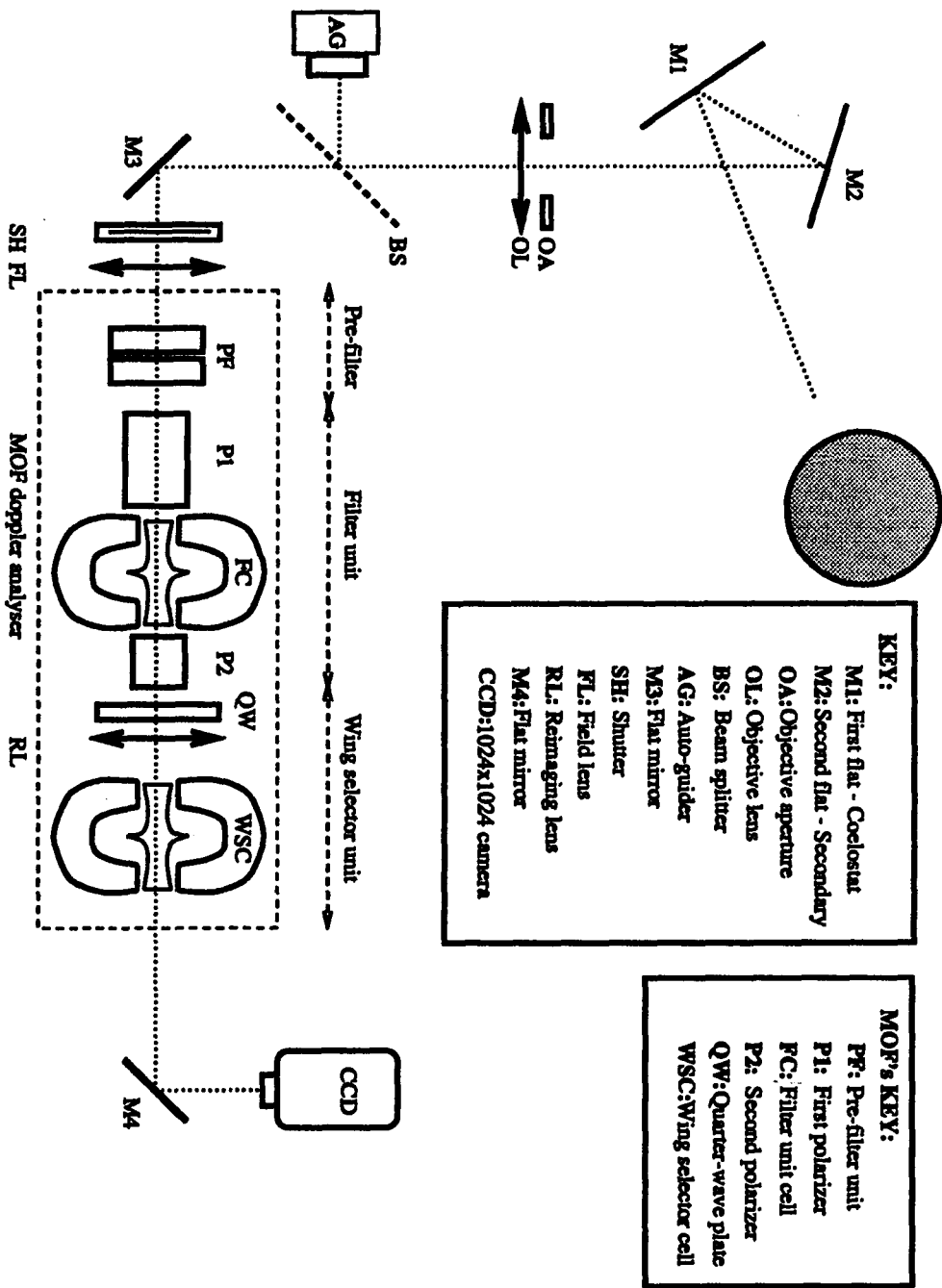


Figure 2.1: Schematic diagram of the instrument.

above an horizontal optical bench. A small fraction of the focused beam is at this point diverted by a 45 degree tilted beam splitter (BS) to the auto-guider (AG). The main part of the beam is reflected horizontally by a 45 degree tilted flat mirror (M3) and passes successively through the shutter (SH), the field lens (FL), the MOF doppler analyzer, and the reimaging lens (RL) to be refocused, after a last reflection by a 45 degree tilted flat mirror (M4) on the 1024×1024 pixels CCD camera. Three interconnected computers and their peripherals control the data acquisition and storage procedure, and record a pair of 12 bit deep narrow band solar images each minute on the mass storage subsystem.

2.1 Solar Telescope

The Mount Wilson 60-Foot Solar Telescope was the first vertical solar telescope erected on the Mount Wilson Observatory site. It was built July 1907 (Hale, 1908) and has since undergone various modifications. Nevertheless its basic double tower configuration has remained unchanged.

Two concentric four-legged towers were designed to provide, some 19 m above ground level, a stable platform supported only by the inner tower. The dome that covers the platform, the access stairway and the light baffling shaft that connects the platform to the observing room, located at the ground level, are in turn supported by the outer tower. Unfortunately some residual coupling between the towers prevents the platform that supports some of the telescope optics from being completely isolated from the second tower. Therefore vibrations induced in the outer tower (i.e. dome rotation) are partially transmitted to the optical platform and cause some image motion. Fortunately, the dome itself consists of two half-shells of slightly different radii that can be rotated a complete 360 degrees. This configuration allows, when the dome is opened wide, almost 180 degrees of clear azimuth, hence this reduces the need to rotate the dome to only once (or at most twice) per day.

The coelostat (M1) and the secondary (M2) are both located on the optical platform. The coelostat consists of a 560 mm dia. optically flat, fused quartz, aluminum coated mirror mounted on a rotating axis aligned with the earth's polar axis and tracks the sun at a constant rate of 180 degrees per 24 hours. A second optically flat, fused quartz, aluminum coated mirror of 450 mm dia. — the secondary —, located south of the coelostat, reflects the sunlight down the lightshaft to the observing room. The secondary is fitted with a pair of actuators in the north-south and east-west directions for fine guiding of the solar image.

An image of the solar disk is focused in the observing room by a 3000 mm focal length doublet objective lens (OL) stopped down to a 60 mm dia. aperture (OA). A 45 degree uncoated glass beam splitter follows the objective lens and diverts some 10 % of the beam horizontally southward to the auto-guider.

The telescope's auto-guider has been extensively described elsewhere (Rhodes *et al.*, 1983; Tomczyk, 1988), its main characteristics are a resonant frequency of 7.5 Hz and a long term drift of ≈ 2 arcsec/hour in the north-south direction and of ≈ 1 arc sec/hour in the east-west direction. In view of the limited size of the objective aperture and the short exposure time (i.e. of the order of 0.5 s) combined with the expected average seeing quality, the frequency response of the auto-guider was considered adequate. The long term drift component was corrected in the data reduction procedure, by an *a posteriori* image registration.

2.2 MOF Doppler Analyzer

Extensive description of the theory of operation and the characteristics of an MOF-based doppler analyzer can be found in Tomczyk, 1988 and references therein; therefore, we present here only a simplified description of it.

The magneto-optical filter (MOF) used as our imaging doppler analyzer, can be decomposed into three units, the pre-filter, the filter, and the wing selector, as shown schematically Figure 2.1. The pre-filter unit isolates a narrow part of the solar spectrum centered around the MOF atomic absorption line. The filter unit is designed to create two narrow-band transmission peaks in each wing of the absorption line, while the wing selector unit is set up as to absorb one or the other transmission peak of the filter unit. The combination of the three units allows us therefore to form a narrow-band imaging filter center around either wing of the selected absorption line. Thus, from a pair of images taken in each wing, a measure of the doppler displacement of the object's absorption line with respect to the instrument frame of reference can be made, which in turn allows a measurement of the line-of-sight velocity on the solar disk at a depth corresponding to the line formation region of the atomic line in the solar atmosphere.

More specifically, the pre-filter unit consists of a narrow band interference filter complemented by a trim filter. The trim filter absorbs the unwanted transmission orders of the interference filter which in turn presents a full width at half maximum of 30 \AA , centered around the sodium D lines. The filter unit consists of an atomic vapor (i.e. sodium), contained in an evacuated glass cell (FC), immersed in a longitudinal magnetic field, and inserted between a pair of crossed linear polarizers (P1 and P2). In the vicinity of the magnetically split absorption lines (i.e. the sodium D lines: 5896 and 5890 \AA), the atomic vapor modifies the induced linear polarization by circular dichroism (inverse Zeeman or Righi effect) and by circular birefringence (Faraday rotation or Macaluso-Corbino effect), allowing a fraction of light to be transmitted through the second polarizer. Hence, for a sufficiently large optical depth and magnetic field, two distinct transmission peaks, centered on each wing of each absorption line, can be formed. The wing selector unit consists of a rotatable quarter-wave plate (QW) followed by a second vapor cell (WSC) also immersed in a longitudinal magnetic field. The circular polarized light that enters the second vapor cell will be absorbed by the inverse Zeeman effect, in the vicinity of

one of the two components of the magnetically split absorption lines. Thus, whether the light entering the second vapor cell is right or left circularly polarized, the red or the blue component¹ will be absorbed. Therefore, a selection effect between each component of the filter transmission profile is obtained by a 90 degree rotation of the quarter-wave plate.

Theoretical and experimental transmission profiles for both units under various conditions are presented in Tomczyk's work. The overall transmission characteristics of the MOF (peak separation and degree of cancellation) depends on the strength of both magnetic fields and the vapor's optical depth (i.e. temperature) in each vapor cell.

During the 1988 summer observing campaign, the MOF was configured as to provide high transmission, good separation and nearly complete cancellation. Therefore a 1kG field was used in the filter unit in conjunction with initially a 4kG field in the wing selector unit (July 1st to July 5th). On July 6th the wing selector unit's vapor cell was damaged and replaced by a spare 1kG wing selector unit to ensure observation continuity. A new vapor cell was installed in the 4kG wing selector unit and replaced the 1kG unit from July 21st on.

The questions of linearity and temperature sensitivity as well as the effects of telluric contamination of the absorption lines, have been addressed in Tomczyk work. Under the selected operating conditions for 1988, the MOF instrumental non-linearity was expected to be of the order 10% (Tomczyk, 1988). To reduce the instrumental temperature sensitivity, the vapor temperature stability was improved. Using a temperature controlled circuit for the cell heating elements, a temperature stability better than 0.01 degree Celcius r.m.s. was achieved at the cell's pit. Moreover, instead of turning off the cell's heating overnight, the heating current for each cell was reduced to a lower value (≈ 70 °C) reducing significantly the time required for the cells to achieve temperature equilibrium under operating conditions. The ambient room temperature and the temperature of both heated pits of

¹for a magnetic field aligned in the direction of the light propagation

each cell were monitored by a digital thermometer and a second thermo-resistor probe embedded in the heating element at each cell's pit (the first one being used to servo the pit's heating). During the summer of 1987, the digital thermometer was connected, via a serial line, to one of the data acquisition processor and the temperature was readout each minute for a couple of days. Figure 2.2 presents the temperature curves for a typical day and demonstrates the thermal stability achieved. Note that the thermo-resistor probes were not calibrated, and therefore the temperature scale is only indicative of temperature changes and should not be considered in an absolute sense. Figure 2.2 shows that, despite the limited digital resolution of the thermometer, the cell's pit temperature drift remains within 0.2 °C for an ambient temperature drift of some 2 °C over some 10 hours of observations. Since the sensitivity of the MOF responsivity to the cell's temperature is on the order of 2-5%/°C, the long period residual drift of the cell's temperature may contribute at most a 1% variation of the sensitivity. As the heating circuit stability was demonstrated satisfactory, only an hourly monitoring of the temperature by the observer was retained during the summer of 1988²

2.3 Optical Layout

The optical layout consists of the objective lens, stopped down by the objective aperture, followed by the field lens and the reimaging lens.

The field lens (40 mm dia., 600 mm focal length) forms a virtual image of the solar disk and a real image of the objective inside the MOF doppler analyzer, near the filter unit vapor cell. The reimaging lens (30 mm dia., 300 mm focal length) is positioned between the quarter-wave plate and the vapor cell of the wing selector unit to form a real image of the solar disk on the camera focal plane. The purposes of this layout are: a)

²the temperature monitoring by the PDP-11 was also dangerously reducing the time tolerance of the whole acquisition procedure and was therefore only run on selected "engineering" days in 1987

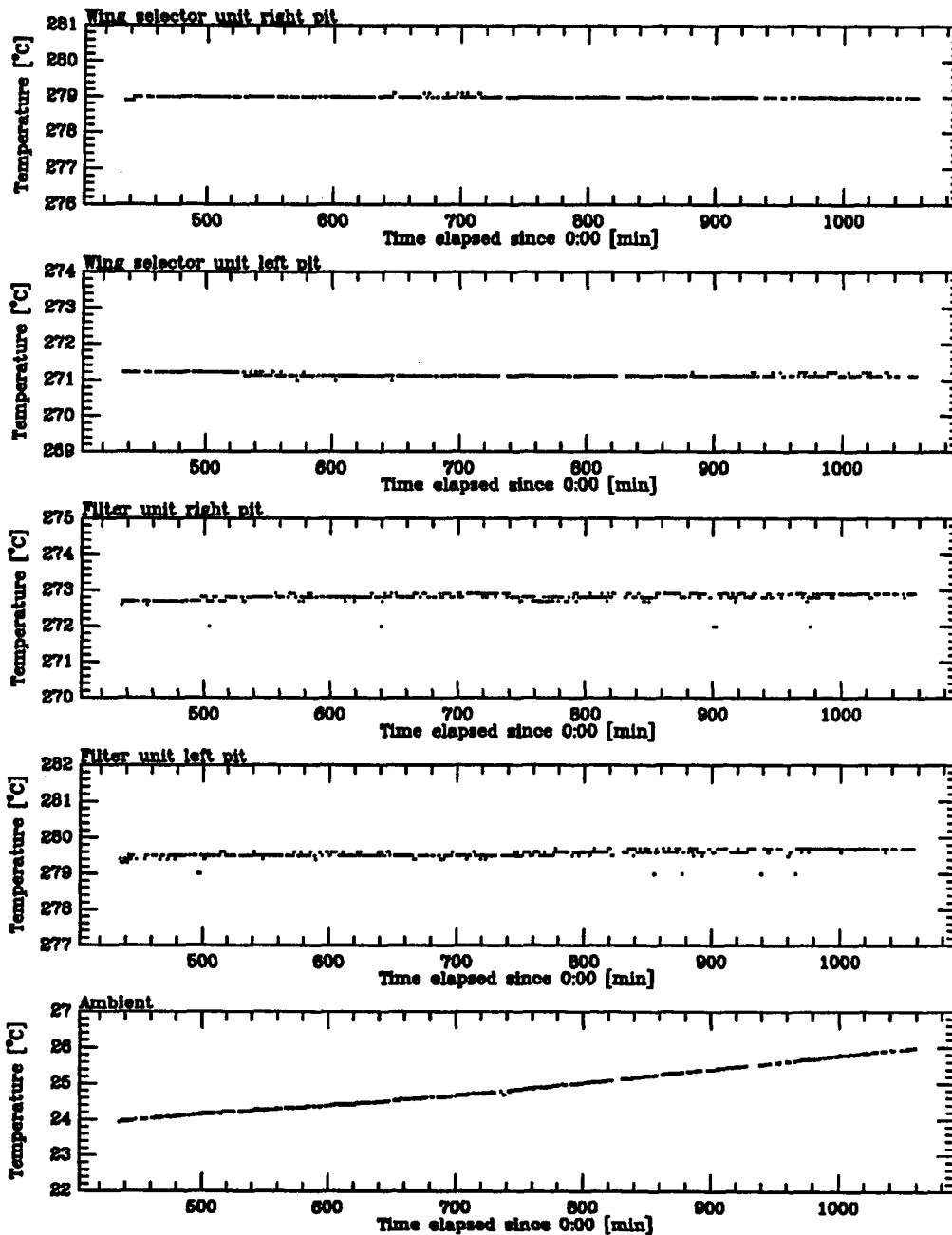


Figure 2.2: Typical variation as a function of time for the ambient temperature (bottom panel) and the cells pits (upper panels) during an “engineering” run on September 8th, 1987. Note that the thermo-resistor probes were not calibrated, and therefore the temperature scale is only indicative of temperature changes and should not be considered in an absolute sense.

to confine the beam within the physical constraints of the doppler analyzer, b) to reduce signal contamination by spatial inhomogeneities of the vapor clouds in the cells, and c) to focus an image of the solar disk that fills the camera detector's size.

The objective aperture is constrained, for a given field lens focal length and a fixed distance between the objective and the field lens, by the size of the smallest optical element in the set-up and the ability to fit the beam within the optical aperture of all of the required optical elements. Hence, allowing for some alignment tolerance, the diameter of the filter unit cell and the diameter of the second polarizer (both 20 mm) restricted the objective aperture to be no greater than 60 mm. At the wavelength of the sodium D lines a 60 mm aperture corresponds to a Raleigh diffraction limit of ≈ 2.5 arc sec.

Finally, the reimaging lens was positioned as to focus a 16.5 mm dia. image on the camera focal plane, corresponding to a 900 pixels dia. image or a 2.13 arc sec per pixel resolution. Since the actual point spread function of the optics is somewhat larger than the Raleigh diffraction limit, the instrumental spatial resolution was estimated to be of the order of or better than 3 arc sec, a values of the order of the average seeing level expected over a few-week-long period at Mount Wilson. Since a 3 arc sec resolution at disk center corresponds to a spherical harmonic degree of ≈ 1000 , the spatial resolution of the instrument was considered adequate for the purpose of this investigation.

2.4 1024×1024 CCD Camera and Data Acquisition System

A schematic diagram of the data acquisition system is presented Figure 2.3. Images were acquired with a custom made camera, build by JPL around Texas Instrument's 1024×1024 virtual-phase, front-side illuminated CCD array. Each pixel in the array is a 18.3 μm square element, providing a total square detection area of 18.7 mm on the side. Each pixel has a full-well depth of 200,000 electrons with a floor noise level of the order of

50 electrons. The camera electronic provides a 12 bit analog to digital conversion of the camera's signal and has been designed to provide a high readout rate (800,000 pixel per second), resulting in a total readout time of 1370 ms per frame (Rhodes *et al.*, 1986). For such low readout noise, a single exposure near saturation remains photon noise limited (no frame accumulation was performed contrary to the initial design). The exposure level was adjusted to reach at the detector levels around 70 % of the saturation level for a signal to noise ratio of some 370 to 1.

The instrument control and data acquisition system is build around three interconnected computers: a PDP-11/34A minicomputer, a CSPI Mini-MAP high-speed array processor and a LSI-11 control processor. A custom built interface connects the camera readout electronics to the array processor, which stores each frame in a 16 bit 1024×1024 array. The LSI-11 based system performs the real-time, interrupt driven, control operations (shutter, quarter-wave plate rotation, camera reset and readout, ...), while the PDP-11, after initializing the two other processors, takes care solely of the I/O operations. A 1.2 GB disk subsystem provides short term storage capabilities, while a 6250 bpi tape drive, provides the final mass storage capability. (The tape unit was later complemented by a 8mm helical scan tape drive). An accurate time base with long term stability was provided by a WWVB broadcast clock/receiver. Finally, a 1200 by 1024 8 bit color display monitor, a graphic terminal and a printer/plotter provided on site visualization capabilities.

2.5 Observation Procedure

Before starting the actual daily observing run the following steps were performed. First, the wing selector unit vapor cell was visually inspected for sodium deposition on the cell's windows. If judged necessary, the cell was removed from the optical bench, defogged³,

³defogging was performed by blowing hot air on the cell's window until the deposited sodium was completely vaporized

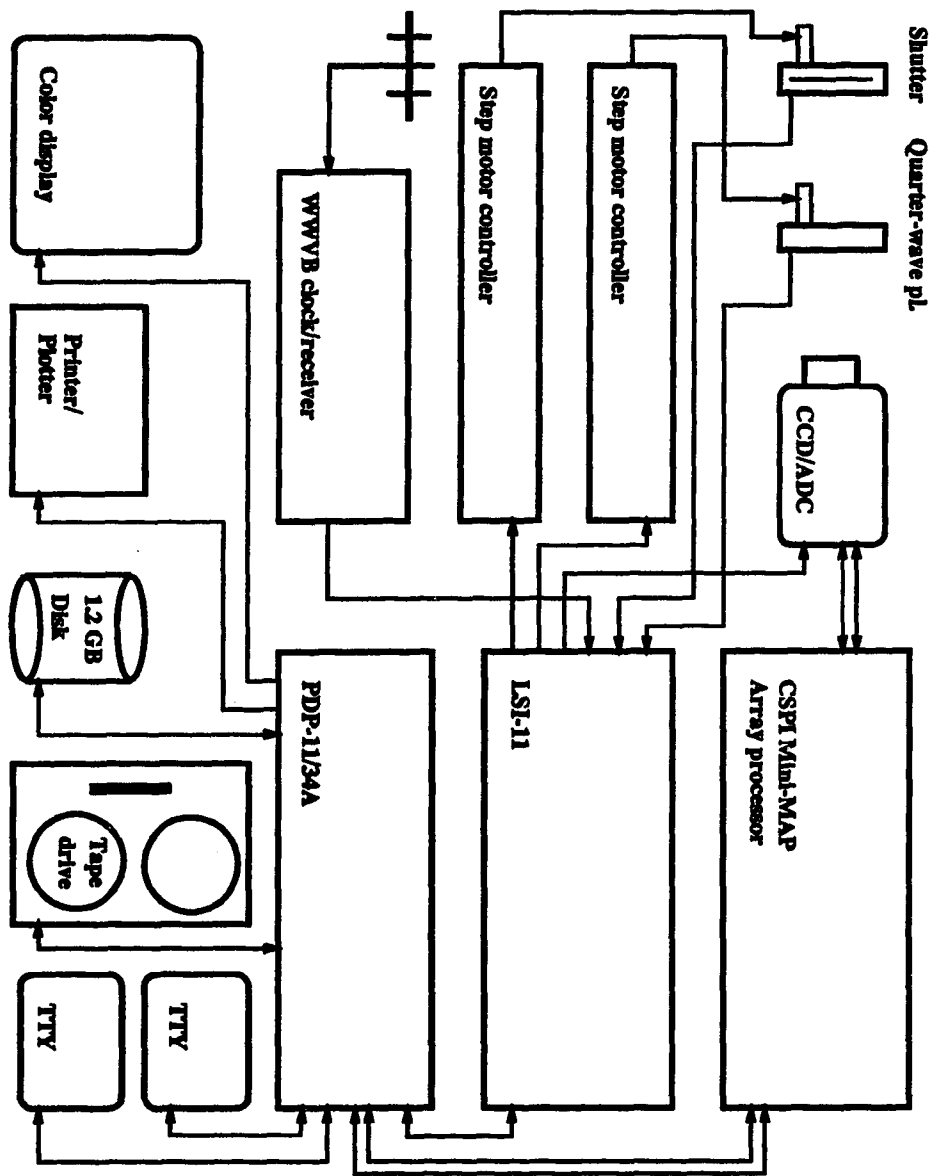


Figure 2.3: Schematic diagram of the data acquisition system.

and carefully repositioned on the optical bench. This operation was done every 3rd or 4th day of observation. The cell's heating current was then progressively brought up to the operating value. Rather than fixing the MOF operating point directly from the cell's temperatures, it was defined, for convenience reasons, by the intensity of the heating current dissipated in each the cell, through the accurate positioning of a high-resolution (i.e. 10 turns) potentiometer of the heating circuitry.

In the meantime, the dome was opened, and moved as far west as possible. The first flat was manually aligned in the east-west direction to project a centered beam on the second flat. Every few days, the altitude of the first flat was adjusted to compensate for the sun's declination variation. Then the second flat was manually aligned to reflect down the light shaft a beam centered on the objective aperture. At this point the first flat tracking mechanism and the second flat guiding actuators were engaged.

Before starting the velocity measurements, a white light direct picture of the sun was taken for synoptic purposes unrelated to this work. If required, the light beam was then centered on the shutter aperture by fine positioning of the auto-guider's detector assembly, and the image formed on the camera's detector was centered by fine positioning of the flat mirror located just in front of the camera (M4).

Then, a couple of images were acquired to check the instrumental configuration and the exposure time, so as to give an illumination level that would reach some 2500 counts at high noon. A dark frame, i.e. an exposure of the camera with the beam obscured in front of the shutter assembly was taken in order to check that the optics were properly baffled from indirect light.

As part of the daily observing procedure a second quarter-wave plate was inserted in the beam between the pre-filter and the filter unit, and a sequence of magnetogram measurements were taken for a couple of minutes (Rhodes *et al.*, 1984). The second quarter-wave

plate was then removed from the beam and a second test dopplergram sequence as well as a second dark frame sequence were taken to ensure that the optical alignment had remained undisturbed. From the test dopplergram sequence, a crude dopplergram was quickly computed and examined as part of the daily "quality control" procedure.

Before starting the observing run, a measurement of the location of the sky's north-south axis was performed with a Ronchi rule. A piece of glass with regularly spaced parallel black stripes (a Ronchi rule) was positioned in the beam at the focus plane of the objective lens (hence focused on the detector plane). The rule was fine positioned as to very precisely align the east-west drift direction of the sun with the engraved ruling. At this point, the doppler measurement sequence was initiated for that day's observing run. First a pair of images with the Ronchi rule in place was recorded⁴, from which the sky east-west axis position would be later computed. Then, the Ronchi rule was removed and a pair of dark frames, were recorded as well in order to provide a record of the dark current build-up during the camera exposure. Thereafter, for the duration of the day, weather permitting, a pair of images taken 5 seconds apart, in respectively the red and the blue wings of the sodium D lines were recorded at a sampling rate of one pair of images per minute for a raw data rate of some 4MB per minute. Around noon, just after a pair of images were exposed the dome was rotated as far west as possible. Since the dome rotation took some 20 seconds, only the following pair of images were partially degraded by any residual vibrations.

At the end of the observing run, a second sequence of magnetogram images was taken, weather permitting. The dome was then closed, the mirrors stowed in their storage position and the cell's heating reduced to a nominal low value.

The precise doppler measurement sequence was as follows: synchronized on the minute by the WWVB clock/receiver, the LSI-11 initiates the opening of the shutter, by rotating by

⁴actually, two sets of Ronchi ruled images were recorded and stored separately

180 degree the shutter's blade at a selected rate that in turns determines the exposure time. Upon detection of the opening edge of the shutter blade by a LED/photodiode assembly in the shutter, the camera's CCD is reset. The CCD is then exposed during some 0.5 second while the shutter is open. Upon detection of the closing edge of the shutter blade by a second LED/photodiode assembly, the camera readout sequence is initiated and a first 1024 by 1024 frame is stored in the array processor. The LSI-11 then commands a 90 degree rotation of the quarter-wave plate, mounted on a Geneva mechanism. The 90 degree rotation requires some 1.5 seconds to be completed. Thus, 5 seconds past the minute mark, the LSI-11 reinitiates the opening of the shutter by rotating the shutter blade in the opposite direction. As for the odd frame, the CCD is reset upon opening detection and readout upon closure detection. A second frame is then stored in the array processor. The LSI-11 then commands the -90 degree rotation of the quarter-wave plate, and the same cycle is restarted on the next minute. For each shutter opening an accurate time stamp (hundred of seconds elapsed since January 1st at 0 AM) and an instrument status word is generated by the LSI-11. For each cycle, once the PDP-11 is notified that the even frame has been completely readout by the array processor, its status word and time stamp are retrieved from the LSI-11, inserted in a header and the header followed by the frame are store to disk. The PDP-11 then repeats the same sequence for the odd frame.

The I/O transfers turned out to be the experiment's bottleneck, since up to 14 seconds were required, using tailored I/O calls, to write to disk the some 2MB of data per frame (i.e. 146 KB/s). Thus some 35 seconds were needed to acquire and store to disk one pair of images. Since a complete day of observation, lets say 11 hours, would generate data in excess of 2.5GB, the data had to be archived on the magnetic subsystem while the observations were done. For this purpose, a second program, using the disk as the intermediate buffer storage and an inter-process semaphore mechanism to communicate with the observing program, was running asynchronously on the PDP-11 to archive the

data on the magnetic tape subsystem.

Let us point out that, while a similar setup had been developed for earlier intermediate-resolution CID observations (see Rhodes *et al.*, 1983 and Tomczyk, 1988), several aspects of the setup, specific to the CCD configuration, had to be redefined. Namely, the optical layout and alignment has been adapted to accommodate the CCD camera and optimized for high spatial resolution. A large fraction of the observing and diagnostic software was rewritten to accommodate for the high-resolution mode and a modified hardware configuration, and the observing procedure itself was redefined. Finally, let us add that while we have personally carried out some of the initial set of observations, daily routine observations for most of the summer have been passed on to trained observers, namely Victoria Alten and Martin Iedema.

Chapter 3

Data Reduction

As indicated in the previous chapter, a set of pairs of high-resolution, full-disk solar images, taken 5 seconds apart at a rate of a pair each minute, forms the basis of the raw data set. Since each pair consists of a “red” and a “blue” image (i.e. a narrow band image of the solar disk centered respectively in the red or the blue wings of the sodium D lines), each pair provides a measure of the line of sight velocity at the solar surface, through an estimate of the doppler shift of the sun’s atmospheric sodium D lines with respect to the instrument.

The following sections describe the successive steps of the reduction procedure leading from raw images to solar p-modes characteristics. Its main steps may be grouped, as: 1) the conversion of raw images to dopplergrams¹, 2) the calibration of dopplergrams to velocity maps, 3) the spatial decomposition of the velocity maps into spherical harmonic coefficients, 4) the spectral analysis of the spherical harmonic coefficient time series, and finally, 5) the analysis of the power spectra that leads to the solar p-modes characteristics.

All the observations which form the basis of this investigation were obtained during the

¹These dopplergrams should not be confused with velocity maps, see Section 3.1

summer of 1988. More precisely, 20 continuous days of observation, spanning July 1st to July 20th of 1988, were reduced for the purpose of this work. At a rate of two 1024 by 1024 pixel images per minute and for a typical 10 hours long daily observing run, the raw data base consisted of some 24,000 images, or ~ 46 GB of data. With such a large data base, computational efficiency had to be considered at each step of the data reduction.

3.1 Dopplergram computation

The first step of the data reduction consists of converting each pair of “red” and “blue” images into a registered dopplergram.

For each day of observation, from the average of the “red” and the “blue” dark exposures taken at the beginning of that particular observing run, a “dark frame” was computed and was first subtracted from each frame. Next, a “despiking” procedure was performed on each frame, where isolated anomalously valued pixels were replaced by the average of their neighbors. Namely, the pixel to pixel intensity difference in the column direction was compared to a weighted running mean of that quantity. A pixel was declared anomalously valued when the absolute value of the deviation of the instantaneous difference from the running mean difference was above a given threshold. The threshold was itself adaptive, i.e. adjusted according to a measure of the local variation of the pixel to pixel differences. Logic to handle “spikes” larger than one pixel was built into the procedure. No flat-field correction was performed (see discussion below).

Then the location of the center of the solar image was computed. The position of the solar limb was estimated from the location of the maximum of the radial first derivative of the intensity signal (point of highest slope). In some 2750 equispaced azimuthal directions (c.f. $2750 \simeq 2\pi R$, where R , the image radius is of the order of ≈ 440 pixels) the radial derivative ($\frac{dI}{dr} = \frac{\partial I}{\partial x} \frac{\partial x}{\partial r} + \frac{\partial I}{\partial y} \frac{\partial y}{\partial r}$) was computed over a 5 pixel wide annulus centered around an initial

good estimate of the solar disk size and location. For each azimuthal direction, the pixel with the largest first derivative value was used to define the location of the limb. A fully parametrized ellipse (i.e. center, size and orientation) was fitted through a standard non-linear least-squares technique to those points defining the limb, with a 2.5 sigma rejection threshold. This procedure was initiated using first a crude guess of the image size and location in conjunction with a smaller number of azimuthal directions, a wider annulus and a larger rejection threshold. It was then bootstrapped using progressively a larger number of azimuthal directions, a thinner annulus and a tighter rejection threshold until the values mentioned above were reached.

Each frame was then translated to center the image on the frame, using a bi-cubic interpolation (Keys, 1981) and the dopplergram computed according to:

$$I_d(i, j) = \frac{I_{\text{red}}(i, j) - I_{\text{blue}}(i, j)}{I_{\text{red}}(i, j) + I_{\text{blue}}(i, j)} \quad (3.1)$$

where $I_{\text{red}}(i, j)$ and $I_{\text{blue}}(i, j)$ are respectively the intensities of the dark subtracted, “de-spiked” and registered “red” and “blue” images at the pixel (i, j) and $I_d(i, j)$ the doppler ratio at that pixel. Since the dopplergrams were stored as 16 bit integers in order to limit disk space usage, the doppler ratio I_d was multiplied by 30,000 before being fixed to an integer value.

Figures 3.1 to 3.3 present respectively a “red” and a “blue” raw frame, and the corresponding dopplergram for a typical day. Figure 3.4 shows the actual 5-minute oscillation velocity pattern revealed by taking the difference between two dopplergrams obtained two minutes apart.

As by-products of the doppler computation, the total intensity over the solar disk of the “red” and the “blue” images, and the sum of the doppler ratio over the entire solar disk were computed. For the purpose of image quality assessment, the sum of the doppler signal in 5 rectangular subarrays covering most of the solar disk was also computed; a

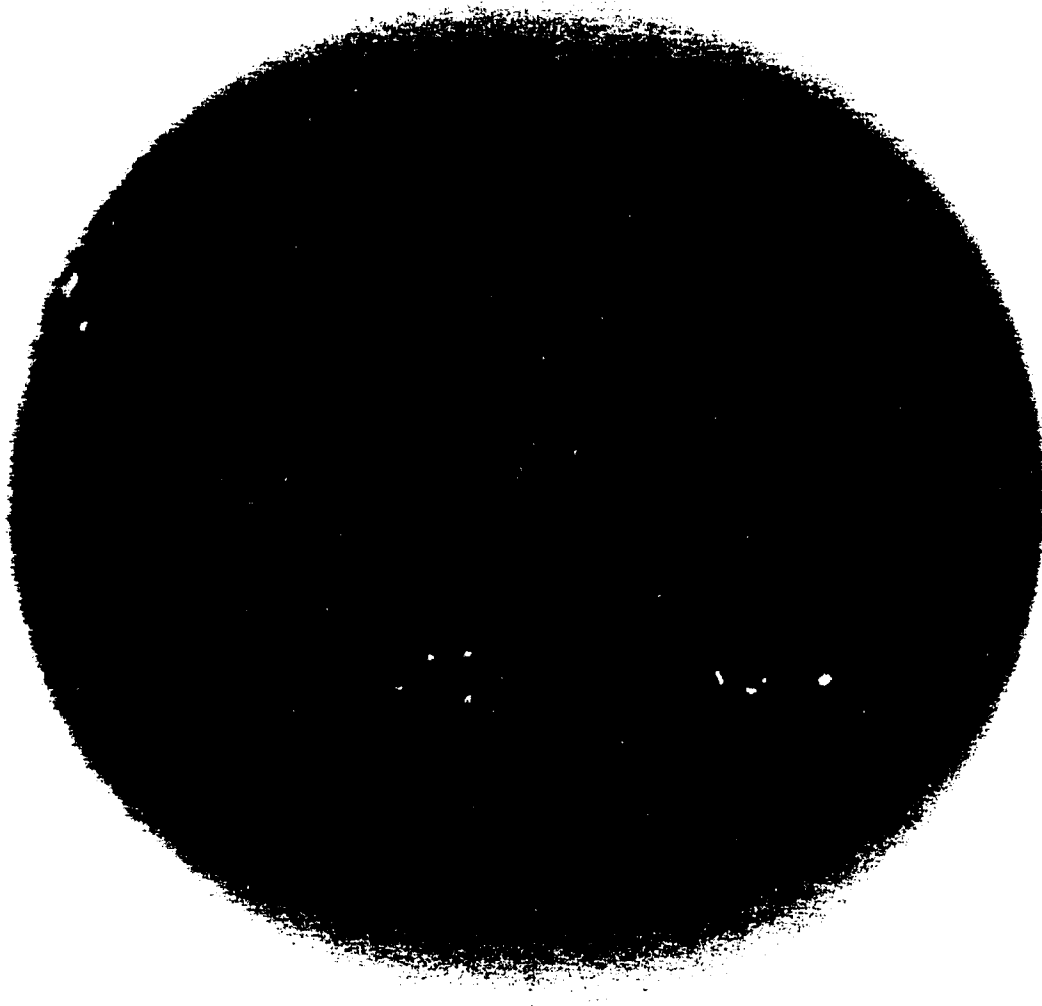


Figure 3.1: Typical "red" filtergram

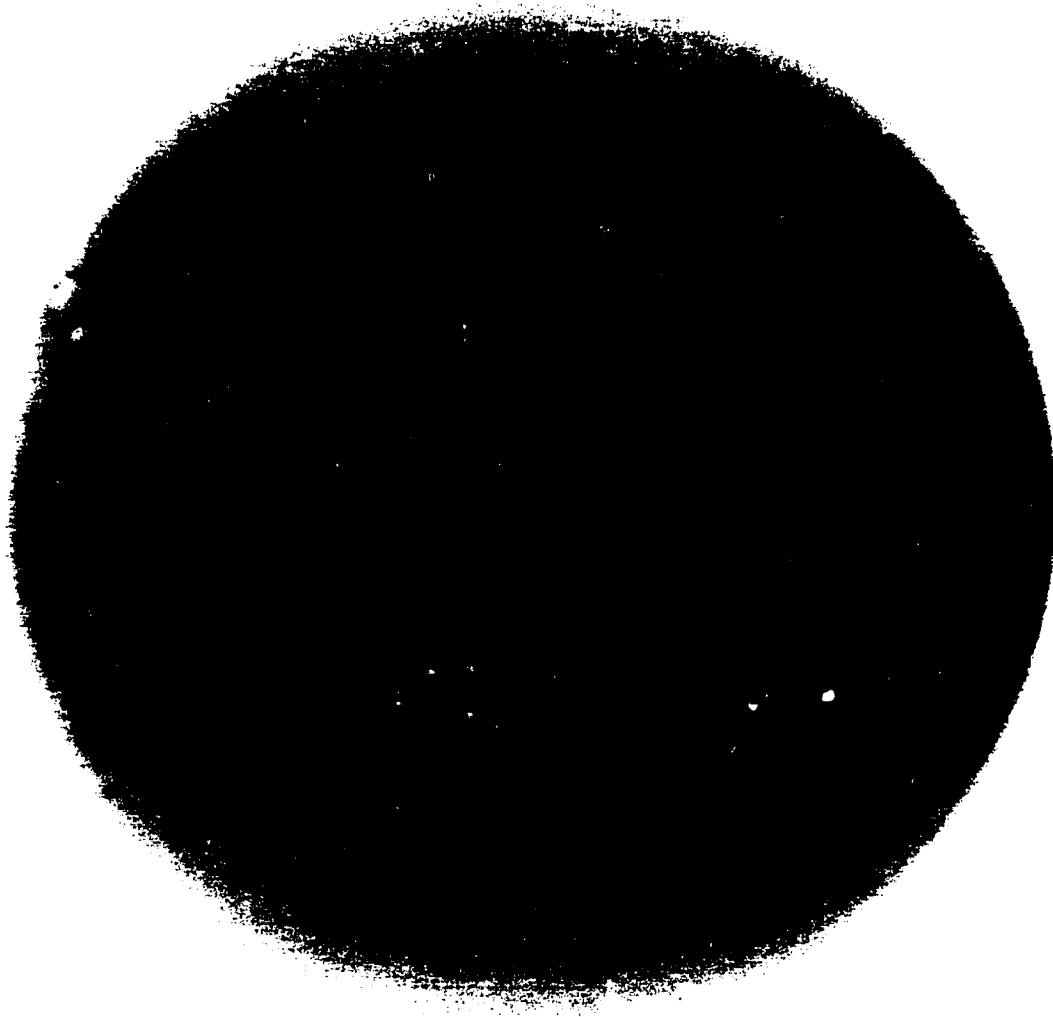


Figure 3.2: Typical "blue" filtergram

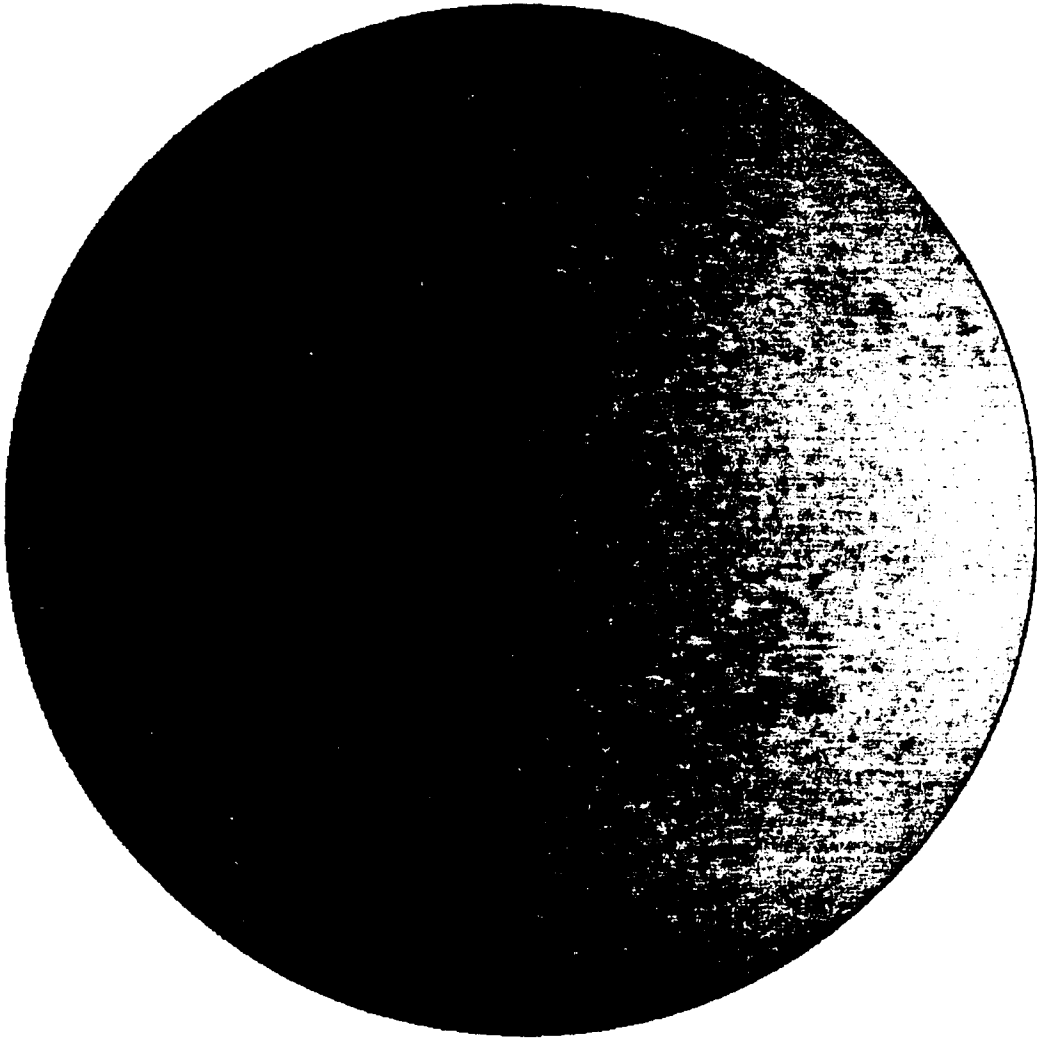


Figure 3.3: Typical dopplergram, corresponding to Figures 3.1 and 3.2



Figure 3.4: Difference of two dopplergrams obtained two minutes apart. The “salt and peper” signal represents the 5-minute oscillations. Notice that the modulation by the line-of-sight projection is clearly visible.

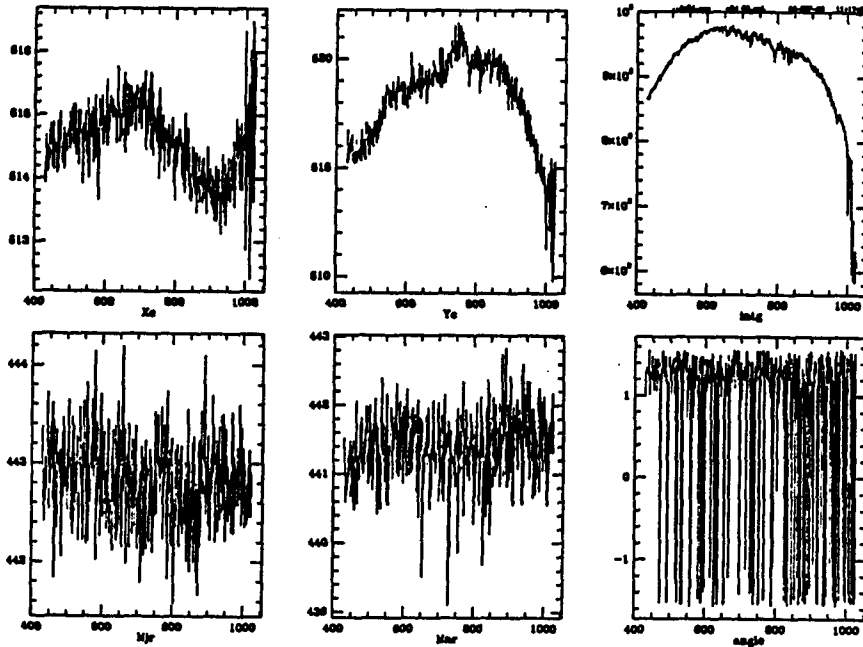


Figure 3.5: Typical “red” images statistics for July 13, 1988. Namely, for each minute, the location of the center, the major, minor axis and orientation of the principal axis the ellipse that defines the limb, and the total intensity as a function of time (in minutes elapsed since 0:00PST)

straight line was fitted to the doppler ratio in a 512 by 8 pixel region centered on the solar disk, and the differences in center location and size of the “red” and the “blue” image were computed. All of these different quantities were plotted versus time for each day. They were primarily used to spot bad images and to monitor the quality of the reduction procedure. Examples of some of these plots for a typical day are presented in Figures 3.5 to 3.7.

Finally, by averaging the doppler ratio over non overlapping 16 by 16 pixel regions, a 64 by 64 “super-pixel” dopplergram was also generated from each full resolution 1024 by 1024 pixel dopplergrams.

The flat-field correction was judged unnecessary from the following considerations: for a purely linear response of the detector, the normalization of the doppler ratio (see Equation (3.1)) makes it insensitive to the detector’s responsivity if the same detector ele-

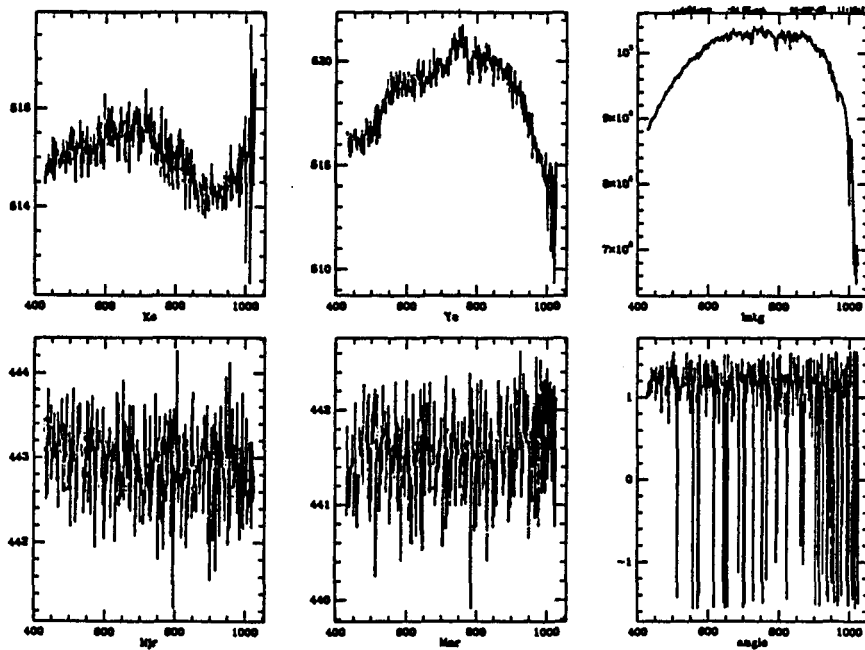


Figure 3.6: Typical "blue" images statistics for July 13, 1988. Namely, for each minute, the location of the center, the major, minor axis and orientation of the principal axis the ellipse that defines the limb, and the total intensity as a function of time (in minutes elapsed since 0:00PST)

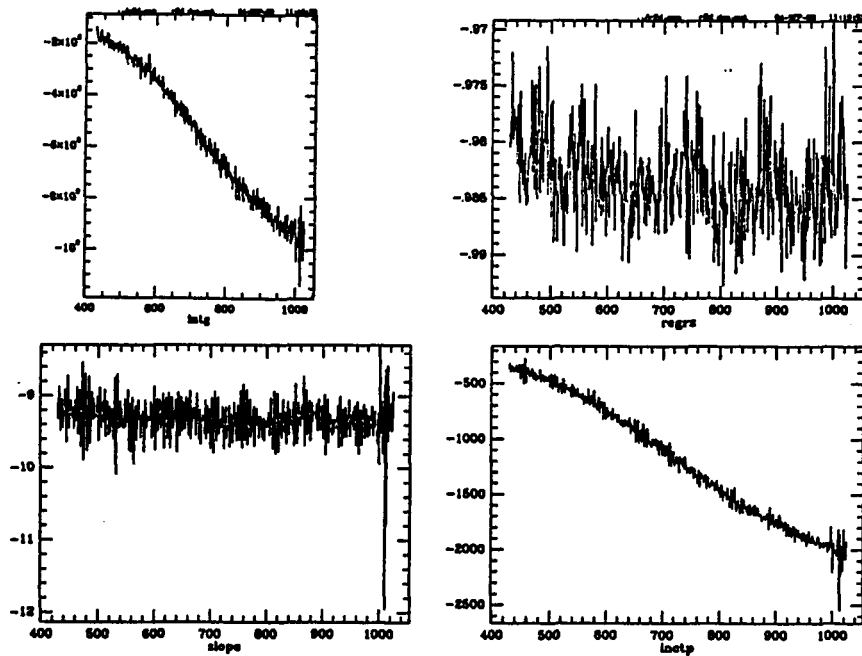


Figure 3.7: Typical dopplergram statistics for July 13, 1988. Namely, for each minute, the integrated doppler signal (uncalibrated, upper left), the slope at mid-frame (lower left), the intercept at mid-frame (lower right) and the regression coefficient for the mid-frame fit (upper right), as a function of time (in minutes elapsed since 0:00PST)

ment (i.e. pixel) is used for the “red” and “blue” measurements. Under that assumption, the contribution of a non-linear term can be easily estimated. Let us consider that the measured intensity, I , can be expressed as a function of the actual illumination, N , as $I = C_0 + C_1N + C_2N^2 + 0(N^3)$. Since a “dark frame” is subtracted from each image, we shall consider $C_0 = 0$. Let us define $\varepsilon = C_2/C_1N_{\text{red}}$ and $\alpha = N_{\text{blue}}/N_{\text{red}}$, and consider the region of the image where $N_{\text{red}} > N_{\text{blue}}$. It can be easily shown that the relative error of the doppler ratio, due to neglecting the non-linear term (C_2) is given by

$$\frac{\delta I_d}{I_d} = \frac{2\varepsilon\alpha}{1 + \alpha + \varepsilon(1 + \alpha^2)}. \quad (3.2)$$

Since typically $0 \leq \alpha \leq 0.3$ and $\varepsilon \approx 3 \sim 5\%$, the detector’s non-linearity contribution will be of the order of a few percent, a contribution substantially smaller than the intrinsic MOF non-linearity.

Since the images are interpolated when translated to the center of the frame, the spatial non-uniformity of the detector’s responsivity should also be considered. For each pair of frames, the centers of both the “red” and the “blue” images are located very close to each other (typically within 1/3 of a pixel), thus only the spatial non-uniformity over the range of the interpolation kernel (4 pixels in both directions) will affect the doppler ratio. Neglecting the spatial non-uniformity correction terms in computing the doppler ratio can be viewed as using a “wrong” interpolation kernel, and is therefore equivalent to introducing some degree of misregistration in each image. Such equivalent misregistration can be expected to be at most on the order of the interpolation itself (i.e. 1/2 of a pixel). Since the location of the center itself is not known to better than a third of a pixel (c.f. seeing limit), neglecting the spatial non-uniformity of the detector responsivity introduces an equivalent misregistration noise of similar amplitude and spatial scale as the seeing noise.

Thus, in view of the difficulty of measuring adequately the detector’s responsivity non-linearity and non-uniformity, in view of the computational cost of implementing such

corrections and considering the limited contribution to the noise from these effects, a flat field correction was not implemented.

Before we implemented the procedure described above in a self-contained program, some dopplergrams were generated using a set of codes developed at JPL. In this earlier procedure, the limb definition was based on an “activity” algorithm², an ellipse was fitted to the limb using an annealing method and the image “despiked” using an preliminary incarnation of the algorithm. Also, the “red” and “blue” images were rotated as well as translated to bring the principal axis of the ellipse fitted to the limb in alignment with the frame’s directions.

After noticing systematic problems with this set of codes (mainly related to the “activity”-based limb definition), and, in order to make the whole process more efficient, the procedure based on JPL’s codes was abandoned and replaced by a unique code implementing the procedure described in detail above. Fortunately, from a computational point of view, some of the dopplergrams generated with the initial procedure were not affected by these systematics and have not been regenerated (i.e. the first 5 days of data acquired with the 1kG/4kG magnet combination).

Note that since both methods used a different definition of the limb, a different image size was derived for the same frame. The activity-based algorithm computed image sizes systematically ~ 2 pixels larger (i.e. $\sim 0.5\%$) than the first derivative-based algorithm. A third centering algorithm, using the zero crossing of the second derivative (inflection point) to define the limb’s position was also developed and tested on a small set of images. This later method gave an image size systematically ~ 2 pixels smaller than the one using the first derivative definition and a standard deviation around the mean twice as large as the other two methods (see Table 3.1).

²The activity of a pixel was defined as the sum of the absolute values of the intensity differences of the neighboring pixels in the two diagonal directions

	Limb position definition		
	2nd derivative	1st derivative	"activity"
semi-major axis	440.87 ± 0.77	442.64 ± 0.46	445.00 ± 0.45
semi-minor axis	438.96 ± 1.04	441.36 ± 0.54	444.15 ± 0.54
eccentricity	9.3%	7.6%	6.2%

Table 3.1: Image size comparison for 88-07-12

Seeing, scattered light, and doppler shift contamination can be identified as the main phenomena that deform the limb's shape. Seeing will blur the image and can be considered as a convolution between the actual solar limb profile and the total point spread function (i.e. atmospheric and instrumental). Scattered light, on the other hand, will add a slowly varying (in space and in time) background contribution, proportional to the light being scattered, hence the local intensity. Since the doppler shift causes the intensity to vary from one part of the image to another, the amount of scattered light will be correlated with the doppler ratio. Finally, the limb profile itself will be modified by the doppler shift, since a different part of the line is sampled at different doppler ratio. Figures 3.8 and 3.9 show respectively north-south and east-west midframe scans of the intensity near the limb for a typical "blue" frame.

3.2 Calibration Procedures

In order to convert the doppler ratio into a velocity measurement, a known velocity signal has to be compared to the observed doppler ratio. Two independently known velocity signals can be used for this purpose. First, the solar rotation which superimposes its signal on top of the oscillation signal, provides a potential reference value of some ± 2 km/s in amplitude at the equator. Alternatively, the sun-earth line of sight diurnal velocity variation, due mainly to the earth's rotation provides a second potential reference value of some ± 400 m/s. The calibration based on the solar rotation is referred to as the spatial calibration while the calibration based on the sun-earth diurnal velocity is referred to as

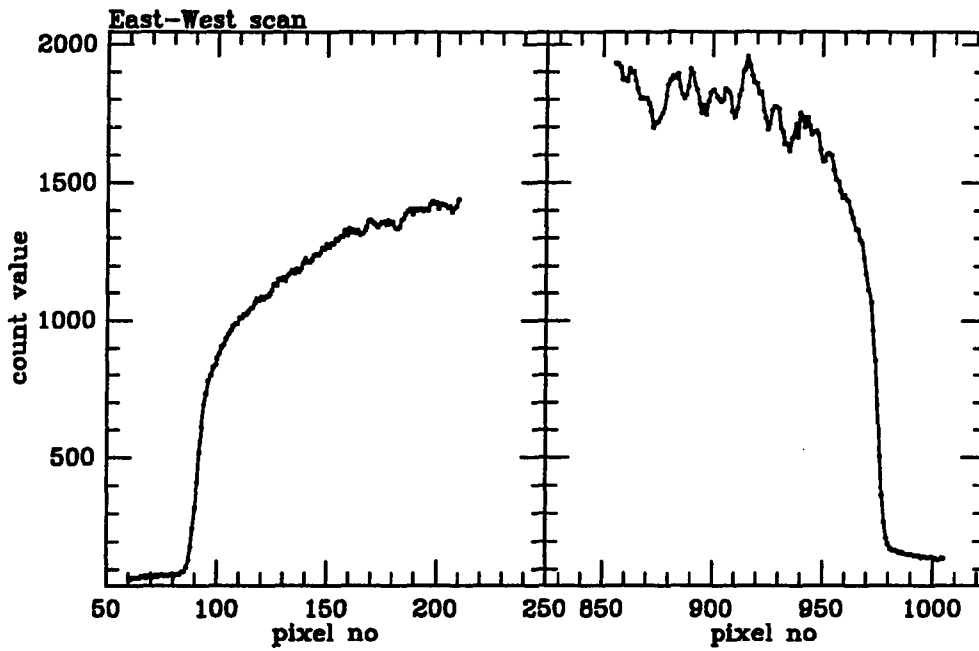


Figure 3.8: Typical North-South scan of a filtergram image

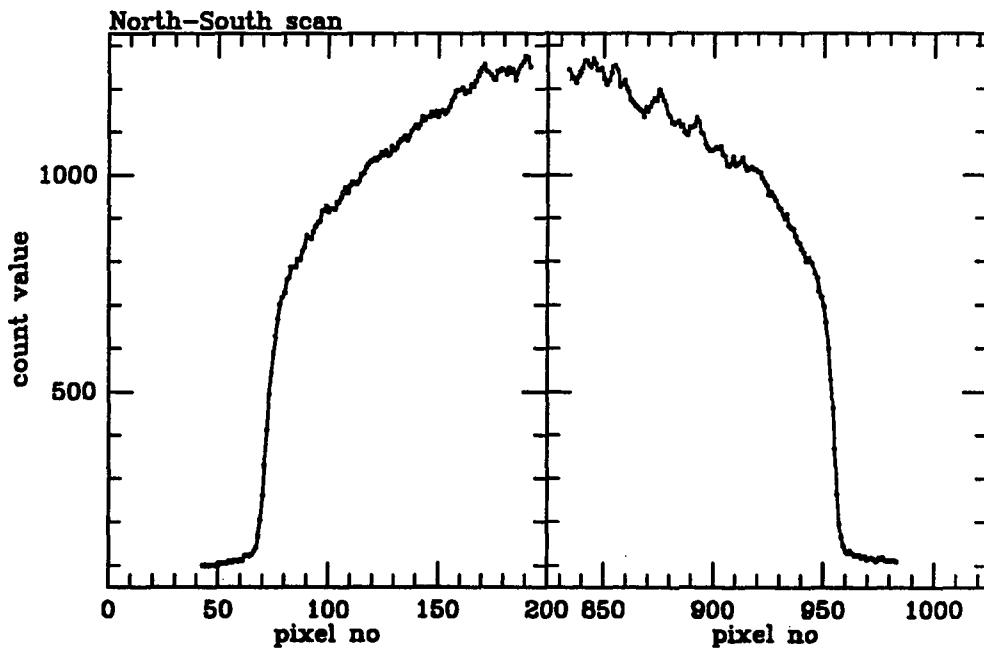


Figure 3.9: Typical East-West scan of a filtergram image

the temporal calibration. A complementary discussion of these calibration procedures can be found in Tomczyk (1988).

3.2.1 Spatial Calibration

The line-of-sight velocity, V_{los} due solely to the solar rotation, observed in the solar equatorial plane and along the sun's equator, is given by

$$V_{\text{los}} = \Omega_{\text{eq}} R_{\odot} \sin \phi \quad (3.3)$$

where Ω_{eq} is the equatorial rotation rate, R_{\odot} the sun's radius and ϕ the sun's longitude measured from disk center. Hence, the slope of the line-of-sight velocity versus $\sin \phi$ at disk center provides the spatial calibrator. Since we are not observing the sun from its equatorial plane, nor have we the sun's equator aligned with the camera's row direction, the slope at disk center is, for small angles, given by $\Omega_{\text{eq}} R_{\odot} \cos(P_{\text{eff}}) \cos(B_o)$, where P_{eff} is the angle between the sun's rotation axis and the camera's column direction and is the sum of the Ronchi angle, Θ_R and the position angle of the rotation axis P (hence the effective position angle), and where B_o is the inclination of the solar axis out of the plane of the sky. Since the oscillation signal perturbs the measured slope by some 5% (see Figure 3.7), the slope at disk center cannot be used as an instantaneous calibrator, hence averaging over periods larger than 5 minutes is therefore required. A potential perturbation of the disk center slope resides in the contamination of the doppler ratio by magnetic features, as can be observed Figure 3.3. The presence of such potential perturbations was not checked when the slope at mid-frame was initially computed, requiring an *a posteriori* verification. Hence, using only the portion of the day clear of potential magnetic contamination, the overall average of the mid-frame slope per pixel was computed. With a value of 2.83 $\mu\text{rad/s}$ for Ω_{eq} (Ulrich *et al.*, 1988) and 696 Mm for R_{\odot} (Wittmann, 1977), the averaged mid-frame slope per pixel was used, in conjunction with the image size and the solar orientation, to determine a "spatial" calibration factor, K_s , that relates the doppler ratio

to a velocity signal through a simple linear law: $V = K_s I_d$.

3.2.2 Temporal Calibration

The sun-earth line-of-sight velocity is the sum of the earth's rotation radial component and the earth's orbit radial component. Since both vary with time with known amplitudes, the temporal variation of the spatially averaged doppler ratio can be calibrated against the ephemeris velocity.

The orbital component of the earth's velocity was computed using the JPL planetary ephemeris, which takes into account the perturbation of the moon and the planets on the earth's orbit, and which contributes some 10 m/s. The rotational component is given by $V_r = V_{\oplus} \cos \delta \sin h$ where δ is the solar declination, h the solar hour angle, and V_{\oplus} the earth's rotation amplitude (385.1 m/s at Mt. Wilson). A regression analysis of the spatially averaged doppler ratio versus the ephemeris velocity provides a "temporal" calibration coefficient, K_t , when assuming again a simple linear law of the form: $V = K_t I_d$.

The temporal calibration method assumes implicitly that the calibration coefficient is independent of time. Since the instrumental temperature stability was improved upon since Tomczyk's observation, this assumption was expected to be valid. Figures 3.10 and 3.11 show a typical temporal calibration curve and regression analysis for July 13. The remarkably high linearity of the regression plot confirms that this assumption was indeed satisfied. Departure from linearity can be noticed in the early and late parts of the observing run and are attributed to telluric contamination and differential extinction at large air masses. Hence only the portion from 7:25 to 16:25 PST was used for the purpose of temporal calibration (this range correspond to an air mass ≤ 2 as of July 8th).

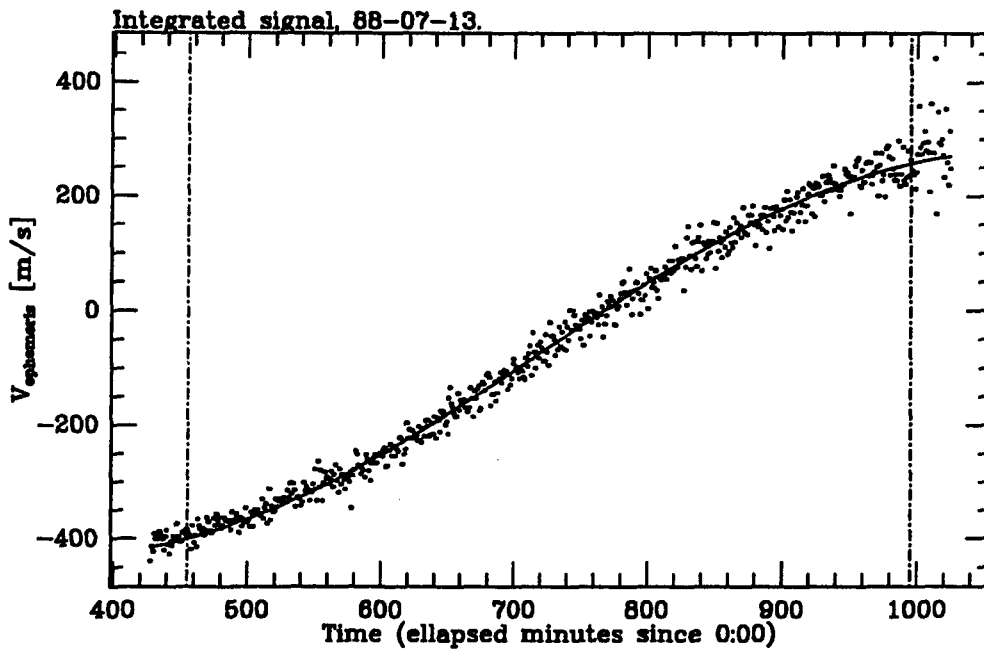


Figure 3.10: Temporal calibration curve. The dots represent the calibrated integrated Doppler signal, while the solid line represent the ephemeris computation.

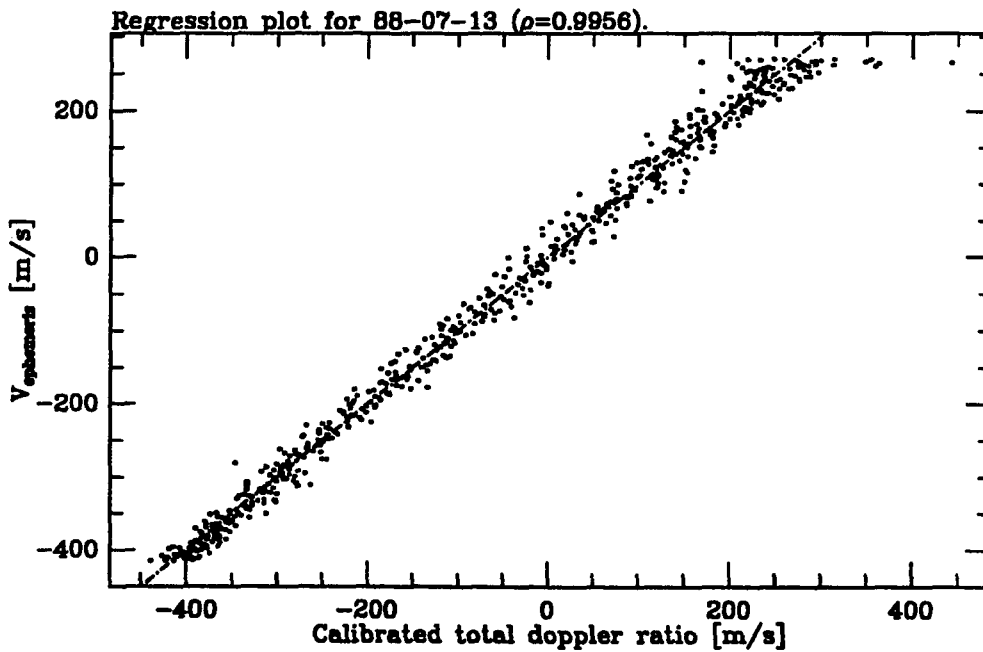


Figure 3.11: Temporal calibration regression curve. Calibrated integrated Doppler signal as a function of the ephemeris velocity, with a straight line drawn at $y = x$.

3.2.3 Non-linear calibration

Both calibration methods described so far assume a simple linear relation between the doppler ratio and the velocity, i.e. $V = KI_d$. As we know from Tomczyk's work the MOF response presents non-linearities on the order of 10% to 15%, therefore a non-linear temporal calibration method was also attempted. While the primary motivation for carrying out such a non-linear calibration was for non-seismic studies of the solar velocity field (see Hathaway *et al.*, 1991 in preparation, and Ulrich *et al.*, 1991 in preparation), the effect of including or not a non-linear correction of the doppler ratio has been estimated.

Since the dependence of the calibration coefficient, K , when performing a pixel-per-pixel temporal calibration, on (r/R) and I_d , for the 1kG/4kG configuration was dominated by a quadratic term, the following relation between velocity and doppler ratio was considered:

$$V = K_0(1 + K_r(r/R)^2)(1 + K_d(I_d)^2)I_d \quad (3.4)$$

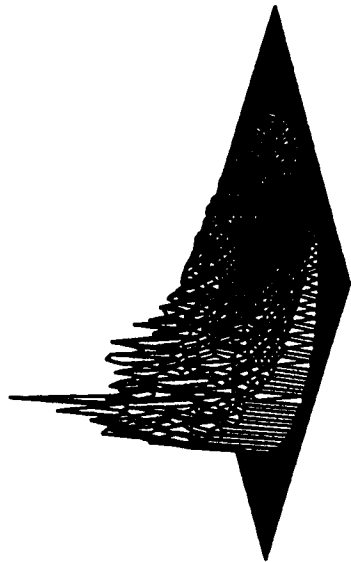
where r is the radius at the current pixel, R the image size, and K_0 , K_r and K_d are three independent calibration coefficients. A standard non-linear least-squares procedure was used to fit the ephemeris velocity V_{eph} to Equation (3.4).

This non-linear temporal calibration was performed on the 64 by 64 "super-pixel" dopplergrams and was carried out as follows: first at each "super-pixel" (hereafter referred to simply as pixel) $V_{\text{eph}}(t)$ was fitted to $V(i, j) + K(i, j)I_d(t, i, j)$ using a linear least-squares method. Along with the linear fit coefficients $V(i, j)$ and $K(i, j)$, the correlation coefficient at each pixel was computed. Only the pixels within 0.95 of the solar disk and whose linear fit correlations were larger than 0.95 were taken into account by the non-linear fitting procedure in order to reject magnetically contaminated pixels. Next, the total velocity, $V_{\text{tot}}(t, i, j)$ was fitted to

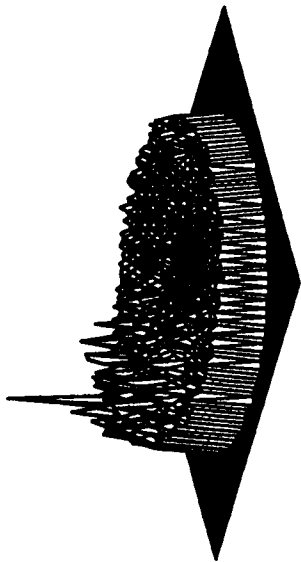
$$V_0 + K_0(1 + K_r(r/R)^2)(1 + K_d I_d^2(t, i, j))I_d(t, i, j) \quad (3.5)$$

where the total velocity, function of time and position, is the sum of a temporal component, i.e. the ephemeris velocity, and a spatial component, i.e. the steady line-of-sight velocity field (solar rotation, limb shift, ...). After fitting K_0 , K_r and K_d , a second linear fit was performed, fitting this time $V_{\text{eph}}(t)$ to $V'(i, j) + K'(i, j)I'_d(t, i, j)$, where $I'_d(t, i, j) = (1 + K_r(\tau/R)^2)(1 + K_d I_d^2(t, i, j))I_d(t, i, j)$. Rather than computing the spatial term of the total velocity field from an analytic expression, the matrix $V'(i, j)$ itself was used for the spatial term, since it represents precisely the actual observed steady field. Note that since the matrix V' is not known *a priori*, the procedure has to be iterated, over the last two steps, using V as first guess for V' .

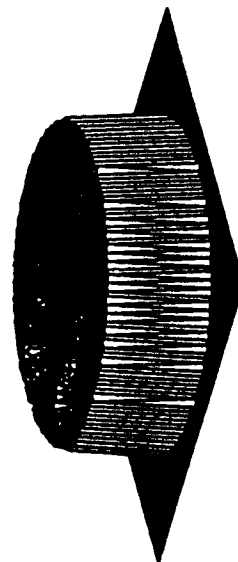
If the MOF response were linear, the matrix $K(i, j)$ would be “flat” (i.e. constant over the solar disk) and the coefficients K_r and K_d null. Similarly, if the non-linearity of the instrument were fully represented by the two coefficients K_r and K_d , the matrix $K'(i, j)$ in turn would be flat and the coefficient V_0 null. Figures 3.12 and 3.13 show, for a typical day, the matrices $K(i, j)$ and $K'(i, j)$ resulting from the non-linear calibration procedure, where a significant improvement in the uniformity of $K'(i, j)$ over $K(i, j)$ can be observed (i.e. from a factor 4 to a factor 1.5). Nevertheless, the residual 1.5 variation of K' indicates that the quadratic formulation used in Equation (3.4) was not totally adequate to fully represent the instrumental non-linearities. Moreover, this procedure failed to converged when applied to data acquired with the latter 1kG/1kG configuration. Indeed, the nature of the non-linearity was no longer dominated by a quadratic term, and the actual amplitude of the non-uniformity was smaller.



$V(i,j)$



$K(i,j)$



$\rho(i,j)$

Figure 3.12: Matrices $K(i,j)$ and $V(i,j)$ and the regression coefficient.

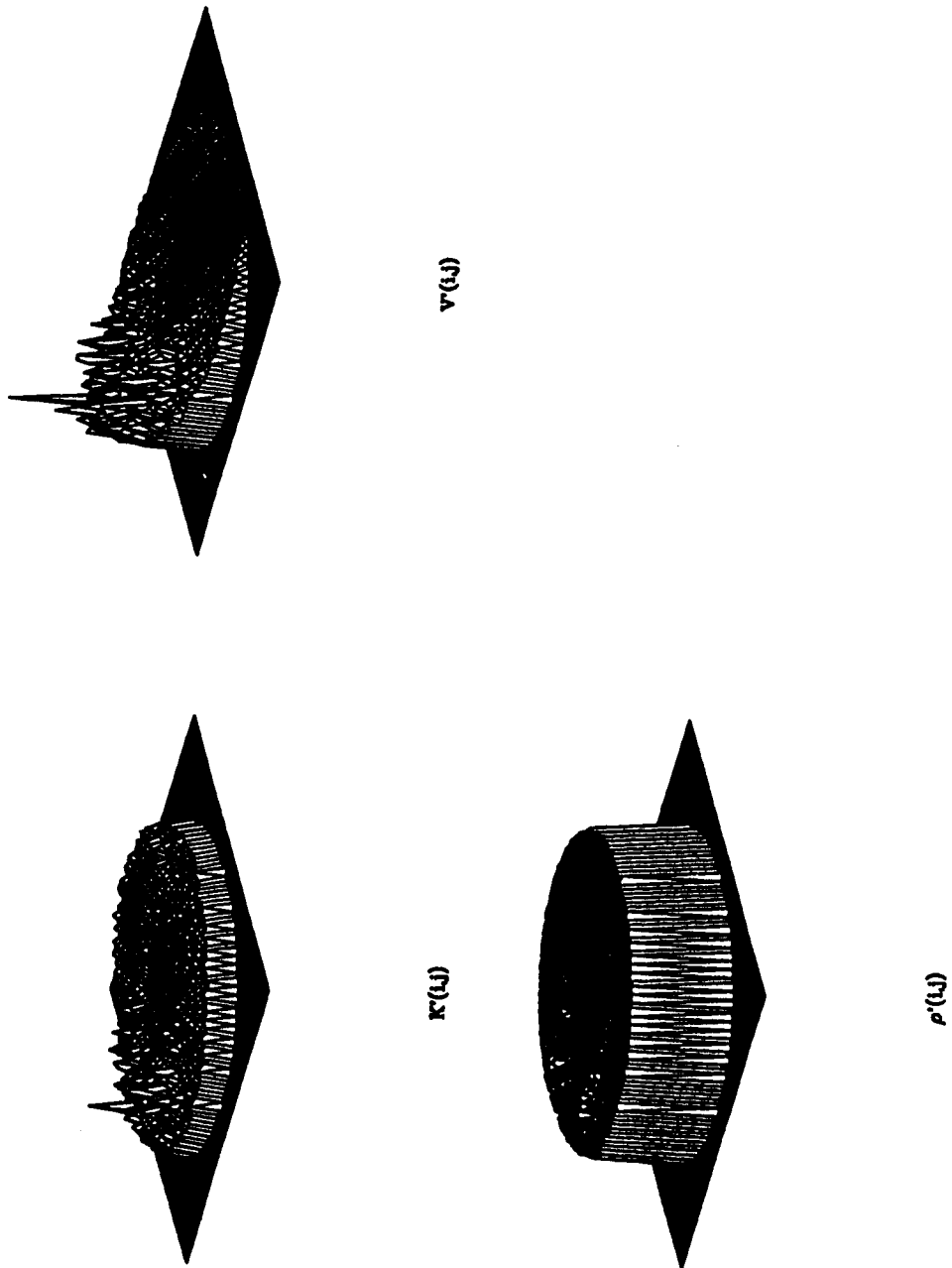


Figure 3.13: Matrices $K'(i,j)$ and $V'(i,j)$ and the regression coefficient.

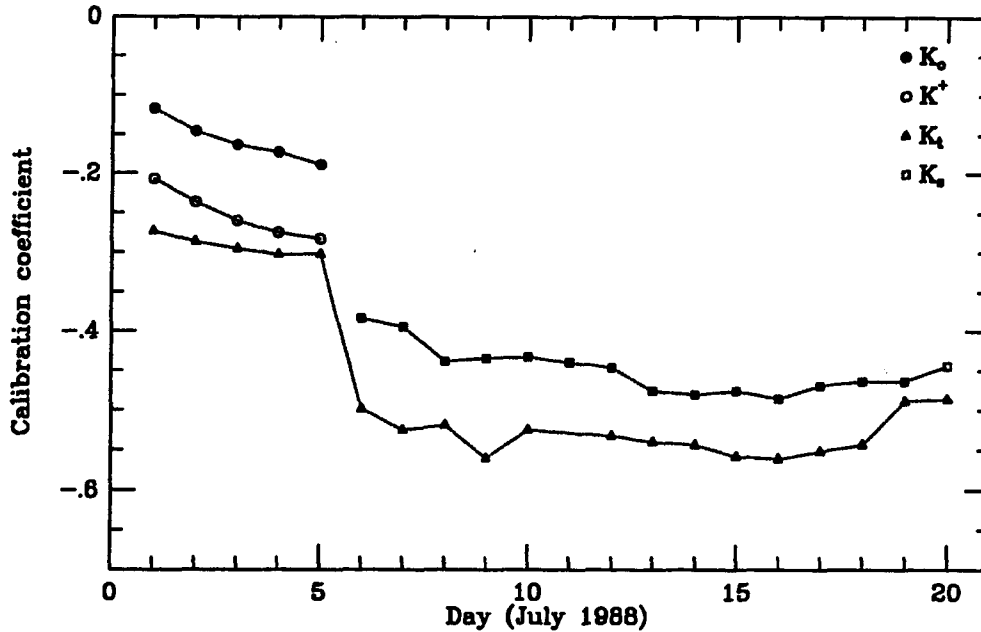


Figure 3.14: Comparison of calibration coefficients.

3.2.4 Comparison

While the temporal calibration was carried out for all 20 days, the spatial calibration was only performed for the 15 days acquired with the 1kG/1kG configuration³ and the non-linear calibration was only successfully carried out for the five days acquired with the 1kG/4kG configuration. Figure 3.14 and Table 3.2 present and compare the calibration coefficients obtained with each method.

Note that in order to compare the non-linear calibration coefficients to the spatial and temporal coefficients we have reduced the three coefficients K_o , K_r and K_d to a unique one, K^\dagger estimated at some intermediate value of r/R and I_d . This value was selected as to be representative of some overall average over the entire disk, namely $K^\dagger = K_o(1 + 0.6K_r)(1 + 0.6K_dI_{d,max}^2)$ where $I_{d,max}$ represent the largest value reached by the doppler ratio.

³The computation of the mid-frame slope was not implemented in the initial procedure used to generate the dopplergrams from the data acquired with the initial 1kG/4kG configuration

date	temporal	spatial	non-linear calibration				
	K_t	K_s	V_o	K_o	K_r	K_d	K^\dagger
07-01	0.2728	-	5.7	0.117	0.750	7.170	0.2067
07-02	0.2859	-	7.6	0.146	0.534	7.456	0.2363
07-03	0.2953	-	5.4	0.163	0.514	7.163	0.2595
07-04	0.3027	-	4.6	0.173	0.511	7.209	0.2749
07-05	0.3025	-	3.9	0.189	0.453	5.898	0.2828
07-06	0.4985	0.3839	-	-	-	-	-
07-07	0.5248	0.3944	-	-	-	-	-
07-08	0.5188	0.4389	-	-	-	-	-
07-09	0.5603	0.4345	-	-	-	-	-
07-10	0.5253	0.4333	-	-	-	-	-
07-11	0.5288	0.4399	-	-	-	-	-
07-12	0.5322	0.4465	-	-	-	-	-
07-13	0.5400	0.4757	-	-	-	-	-
07-14	0.5436	0.4801	-	-	-	-	-
07-15	0.5578	0.4753	-	-	-	-	-
07-16	0.5608	0.4858	-	-	-	-	-
07-17	0.5522	0.4692	-	-	-	-	-
07-18	0.5437	0.4640	-	-	-	-	-
07-19	0.4887	0.4639	-	-	-	-	-
07-20	0.4861	0.4447	-	-	-	-	-

Table 3.2: Comparison of calibration coefficients

The spatial calibration coefficients K_s , and the non-linear calibration coefficients K_o are systematically some 15% smaller than the temporal calibration coefficients K_t . Indeed, since the response of the MOF decreases with the velocity magnitude as well as the center-to-limb distance, (i.e. $K_d > 0$ and $K_r > 0$, see also figures 3.18 and 3.21 in Tomczyk, 1988), the integrated doppler ratio will underestimate the integrated velocity, while the slope at disk center is measured precisely where the MOF's response is the largest. Let us add that the value we used for Ω_{eq} was an August 1987 measurement and was not corrected to represent the actual rotation rate at the Na-D line formation altitude.

Since the temporal calibration was carried out successfully for all the 20 days of observation and its implementation straightforward, we have used the temporal calibration coefficients K_t in the reduction of the high resolution images. We have also investigated the effects of neglecting the instrumental non-linearities by decomposing some of the low-resolution

images (64 by 64 pixels) using the non-linear calibration results as well as the temporal ones. While using the non-linear calibration lead to a different set of time series, hence to small differences in the power spectra, the power spectra of the time series differences where an order of magnitude smaller than the time series spectra themselves.

3.3 Spatial Decomposition

3.3.1 Theory

The next step in the data reduction consists of decomposing the velocity maps into spherical harmonic coefficients. Since solar oscillations are a small perturbation of the solar structure, and the sun oblateness is itself small, an unperturbed solar model can be considered as spherically symmetric. The natural basis for parametrizing the angular dependence of small perturbations on a sphere is the complete set of orthonormal functions on the sphere formed by the spherical harmonic functions $Y_\ell^m(\theta, \phi)$. From a small perturbation modal analysis of an unperturbed spherically symmetric solar model, the radial displacement, δr , associated with the acoustic waves is given by

$$\delta r = \Re\left\{ \sum_{n,\ell,m} \xi_{r,n,\ell}(r) Y_\ell^m(\theta, \phi) \exp(i2\pi\nu_{n,\ell,m}t) \right\} \quad (3.6)$$

where $\xi_{r,n,\ell}$ is the radial eigenfunction associated to the mode vibrating at a frequency $\nu_{n,\ell,m}$, n is the mode's radial order, ℓ its spherical harmonic degree, and m its azimuthal order ($-\ell \leq m \leq \ell$). Hence, if the radial velocity field, V_r , associated with oscillations at the surface is a superposition of normal modes, it can be written as

$$V_r(t, \theta, \phi) = \Re\left\{ \sum_{\ell,m} C_{\ell,m}(t) Y_\ell^m(\theta, \phi) \right\} \quad (3.7)$$

where $C_{\ell,m}(t)$ is given by

$$C_{\ell,m}(t) = \sum_n A_{n,\ell,m} \exp(i2\pi\nu_{n,\ell,m}t + \varphi_{n,\ell,m}) \quad (3.8)$$

where A is the mode amplitude, φ its phase, and $\Re\{z\}$ stands for the real part of z .

From the orthonormal properties of spherical harmonic functions, since $\Re\{z\} = \frac{1}{2}(z + z^*)$, and using the property that $Y_\ell^{m*} = (-)^m Y_\ell^{-m}$, it can be easily derived from Equation (3.7) that

$$C_{\ell,m}(t) + (-)^m C_{\ell,-m}^*(t) = 2 \int V_r(t, \theta, \phi) Y_\ell^{m*}(\theta, \phi) d \cos \theta d \phi \quad (3.9)$$

where the integration is over the whole sphere. The spectral analysis of $C_{\ell,m}(t) + (-)^m C_{\ell,-m}^*(t)$ will separate in the frequency domain the prograde ($m > 0$) from the retrograde ($m < 0$) modes, hence, the right hand side part of Equation (3.9) needs to be only computed for the prograde (or retrograde) modes.

In all practical cases, the observed velocity, V_{obs} , is the line of sight component rather than the radial component, and can only be measured on the visible hemisphere. Since the spherical harmonic function are not orthogonal on a fraction of the sphere, Equation (3.9) has to be rewritten as

$$\tilde{C}_{\ell,m}(t) = \sum_{\ell',m'} \langle \ell', m' | \ell, m \rangle \left(C_{\ell',m'}(t) + (-)^{m'} C_{\ell',-m'}^*(t) \right) \quad (3.10)$$

$$= 2 \int W_s(\theta, \phi) V_r(t, \theta, \phi) Y_\ell^{m*}(\theta, \phi) d \cos \theta d \phi \quad (3.11)$$

where W_s , defined by $V_{\text{obs}}(t, \theta, \phi) = W_s(\theta, \phi) V_r(t, \theta, \phi)$, contains the line-of-sight projection factor $\cos \rho$ over the observed part of the sphere and is zero elsewhere; and where

$$\langle \ell', m' | \ell, m \rangle = \int Y_{\ell'}^{m'}(\theta, \phi) W_s(\theta, \phi) Y_\ell^{m*}(\theta, \phi) d \cos \theta d \phi \quad (3.12)$$

The net effect of the spatial window function, $W_s(\theta, \phi)$, is referred to as spatial leakage. Indeed, some of the non-target mode coefficients $C_{\ell',m'}$ will "leak" into the target coefficient $C_{\ell,m}$ time series, hence, the target spectrum.

3.3.2 Practical Considerations

The observed line-of-sight velocity signal can be viewed as the sum of a steady field associated with the solar rotation, a slowly varying field associated with large scale flows, and the oscillatory field. Therefore, in order to isolate the oscillatory velocity field, a centered 21-minute-long running mean of the velocity maps was computed and subtracted from each frame before performing the spatial decomposition. Incidentally, this running mean subtraction also removed any slowly varying spurious instrumental signals from the data (i.e. scattered light).

Since no radial components can be measured near the limb, where a small misregistration introduces large spurious signals, the image was spatially apodized. Only 95 % of the solar disk, tapered by a 5% wide cosine bell, was used for the spatial decomposition.

From a practical standpoint, the estimate of the right-hand side of Equation (3.9) by a direct numerical integration is highly inefficient. Brown (1985) first pointed out that the spherical harmonic decomposition can be greatly speeded up by performing a fast Fourier transform (FFT) in the longitudinal direction, followed by a Legendre transform in the latitudinal direction. Indeed, the spherical harmonic functions Y_l^m are defined as

$$Y_l^m(\theta, \phi) = \sqrt{\frac{2l+1}{4\pi} \frac{(l-m)!}{(l+m)!}} P_l^m(\cos \theta) e^{im\phi} \quad (3.13)$$

where P_l^m are associated Legendre polynomials. Thus, the integration over ϕ in Equation (3.9) is equivalent to a Fourier transform in the longitudinal direction. While the use of an FFT accelerates greatly the numerical computation, it requires the image to be sampled on an equispaced grid, hence a rebinning of the frame.

Therefore, after subtraction of the running mean and apodization, the velocity images were interpolated, using also a bi-cubic algorithm, onto a grid equispaced in longitude and latitude. A 1024-point-long FFT was performed in the longitudinal direction, while the

associated Legendre polynomials needed for the transform in the latitudinal direction were generated from a recurrence relation at each decomposition. Even though the amount of memory or even disk space required to store the complete set of required polynomials remained prohibitive, the recurrence coefficients themselves were stored in memory.

The routines used to perform the spatial decomposition were provided to us by T. Duvall, from the GONG project. The routines were adapted to accommodate our particular image size and geometry, and modified to handle a fully parametrized elliptical image geometry. The routines were extensively checked, and in particular, the accuracy of the recurrence procedure at high-degree. Hence, on 16-bit-long word machines (i.e. 32-bit-long floating-point arithmetic) the associated Legendre recursive generation was performed in double precision (i.e. 64-bit-long floating-point arithmetic). The option of computing only the zonal ($m = 0$) and sectoral ($m = \ell$) coefficients up to a higher degree than the tesseral was added as well.

All the 90,601 even- m coefficients for $0 \leq \ell \leq 600$ were computed for each velocity frame. For a subset of the data set, the zonal and sectoral decomposition alone was carried out up to $\ell = 900$, but was later abandoned since no significant solar oscillation signal was initially found above $\ell = 600$. Note that since that time, some of the dopplergrams have been analyzed using only a portion of the image near disk center and a plane wave approximation for the spatial decomposition (i.e. replacing the spherical harmonic decomposition by a two dimensional Fourier transform). When reduced this way, the solar oscillation signal for degrees up to $\ell = 900$ can be seen at a significant level in the resulting power spectra (Brown 1990, private communication).

Note that to perform correctly the image rebinning, the image geometry as well as the solar geometry must be taken into account. This includes, for the image, the location of the image center, the image size and orientation (major and minor axis as well as principal axis orientation), and the orientation of the celestial north on the frame (the Ronchi angle,

Θ_R). For the sun's geometry, it includes the rotation axis orientation, P , the inclination of the rotation axis out of the plane, B_o , as well as the finite sun-earth distance projection effect.

The Ronchi angle was computed from the Ronchi ruled pair of frames taken at the start of each observing run (see Section 2.5). Edges of the pattern imprinted by the rule on the image were detected by the peaks of the first derivative in the column direction⁴ lying above a given threshold. Peaks were grouped into lines and for lines longer than a given minimal length the slope computed with a standard least-squares method. Finally, the mean and standard deviation around the mean of the slopes was computed. The Ronchi angle was typically measured with a 0.1 degree of uncertainty. The uncertainty in the actual positioning of the rule by the observer was estimated to be on the order of 0.1 degree⁵. The P and B_o angles were taken from the Astronomical Almanac tables and linearly interpolated for 12:00 PST. The noon values were used to decompose the entire day, introducing at most an error, early in the morning and late in the evening, of ± 0.1 degree for the P angle and ± 0.02 degree for the B_o angle. The finite sun-earth distance projection geometry was included (a 0.5% effect), using the average sun-earth distance (a quantity that varies less than 0.003% per day).

The image center was fixed by translating the "red" and "blue" image centers to the frame center, but misregistration on the order of a fraction of a pixel is more likely to have been present (see discussion Section 3.1). More important, the image size (but not its orientation) had been found to differ by up to some 0.5% when using different algorithms to define the limb's position (see Section 3.1). For purely practical reasons the "activity" based image size was adopted early on in the reduction phase (since the first dopplergrams were generated using the procedure based upon the JPL codes, and were already spatially

⁴The Ronchi rule was always oriented within 5 degrees of the detector's row direction

⁵The Ronchi rule had some 60 lines covering the solar disk. A deviation from alignment of half a line, over a displacement of the solar image by 5 solar diameters can be easily detected by a casual observer

decomposed) and was used throughout the 20 days to preserve consistency. For the days where the dopplergrams were not computed by the JPL code based procedure, the image size alone was computed for 1 hour of data around noon, with the JPL centering code.

3.4 Spectral Analysis

After decomposing each image in spherical harmonic coefficients, a time series for each coefficient was formed and a spectral analysis carried out through a forward Fourier transform.

The “trivial” task of reordering the 90,601 \tilde{C}_ℓ^m coefficients computed for each image in 90,601 distinct time series requires the transposition of a matrix of 90,601 by 600 complex coefficients for a typical 10-hours-long run. Since transposing in memory a 415 MB array remains, even by today’s standards, an unrealistic approach, the size of the data set made it, in practical terms, a significant task. Hence, the transposition has been performed in successive steps using a disk-to-disk approach, limited in turn by the available disk space. Figure 3.15 presents plots of the resulting time series for some selected tesseral coefficients for a typical day.

In order to assess the quality of data after the spatial decomposition without having to perform the complete transposition, the zonal and sectoral coefficients alone were also saved separately from all the tesseral coefficients. Hence, the zonal and sectoral time series could be formed by a trivial transposition of 2 by some 600 coefficient matrix, and plotted versus time for selected values of ℓ . Since including one “bad” image in the running mean subtraction would affect the decomposition of the 20 neighboring images, the inspection of the zonal and sectoral time series allowed a *post-facto* detection of unspotted “bad” frames. When required, these “bad” frames were discarded and the affected 20 minutes of good data re-decomposed.

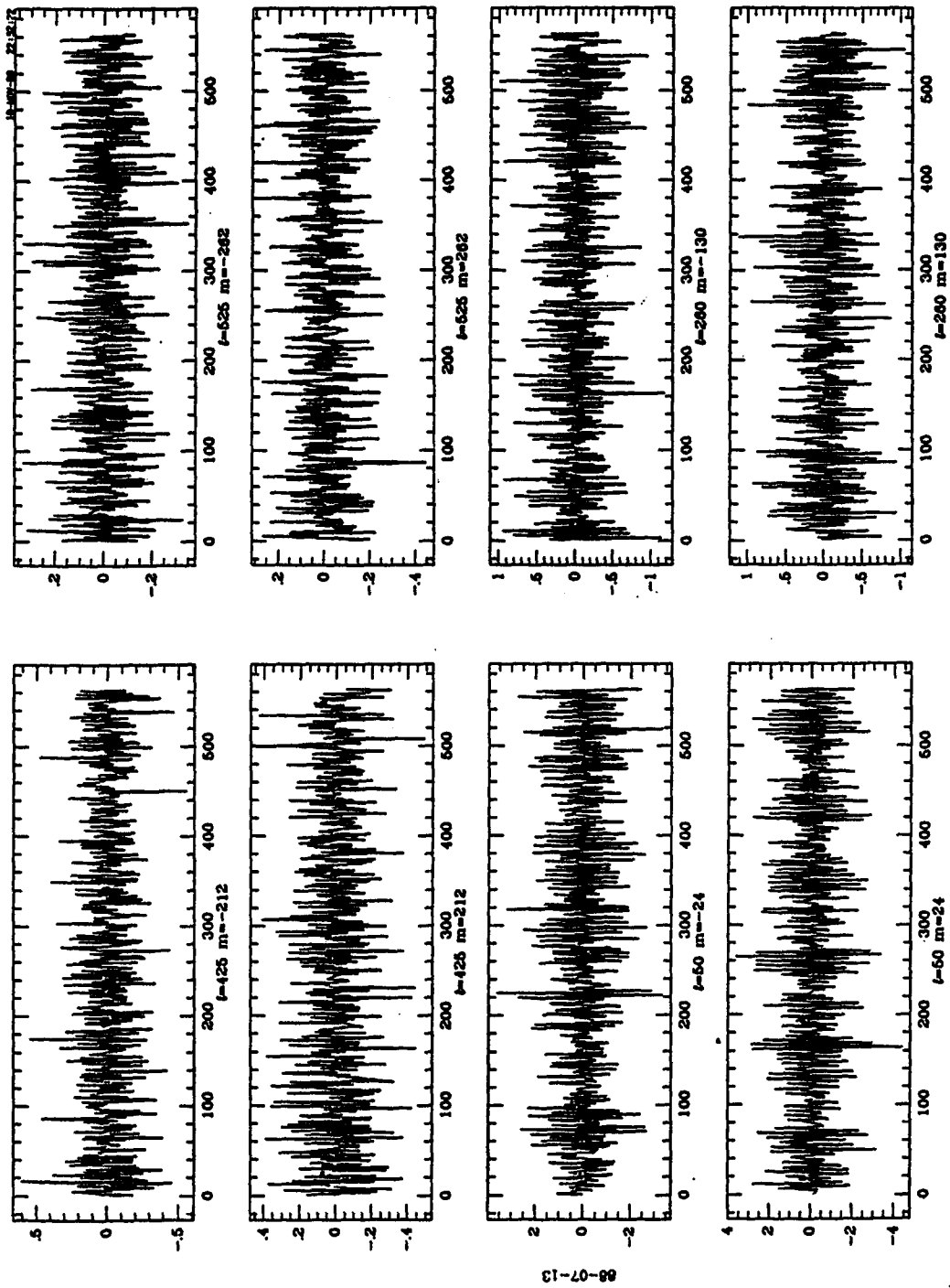


Figure 3.15: Time series for a selection of spherical harmonic coefficients

Once transposed, each time series was ready to be Fourier analyzed. Before computing the FFT of the time series, each time series was zero-averaged and coefficients above a 5 sigma threshold weeded out.

High-resolution spectra were computed by combining the consecutive 20 days of data into a 27,970-minute-long time series. Only data acquired between 06:55 and 17:05 PST were considered (corresponding to an air mass ≤ 2.5), and tapered with a 20-minute-long cosine bell at the beginning and the end of each day. Gaps were filled with zeros and each time series padded with zeros to 65,536 points. A 65,536-point-long FFT was then computed and the modulus of each spectrum computed and saved.

Figures 3.16 and 3.17 show the window function in the time domain and the frequency domain of the high-resolution spectra. The intrinsic frequency resolution, given by $1/N_{\text{FFT}}/T_s$, where N_{FFT} is the length of the FFT and T_s the sampling time, is $0.252 \mu\text{Hz}$. The actual window function frequency resolution, given by $1/T_t$, where T_t is the total time spanned with data, is $0.596 \mu\text{Hz}$, hence using a 65,536 point-long FFT provided an oversampling factor in the frequency domain of ~ 2 . Since we do not have uninterrupted observation over the 20-day-long period, the presence of regularly spaced gaps introduces temporal sidelobes situated $1/24\text{h}$, or $11.57 \mu\text{Hz}$ away from the main lobe.

Low-resolution power spectra (square of the modulus) were also computed from one-day-long time series with a 1,024-point-long FFT. For each tesseral coefficient the respective 20 power spectra computed for each day were then averaged together. The window function in the frequency domain for the averaged low-resolution spectra (hereafter referred to as the low-resolution spectra) is also shown in Figure 3.17. For the low resolution spectra the intrinsic frequency resolution is $16.3 \mu\text{Hz}$ and the actual window function frequency resolution is $27.8 \mu\text{Hz}$.

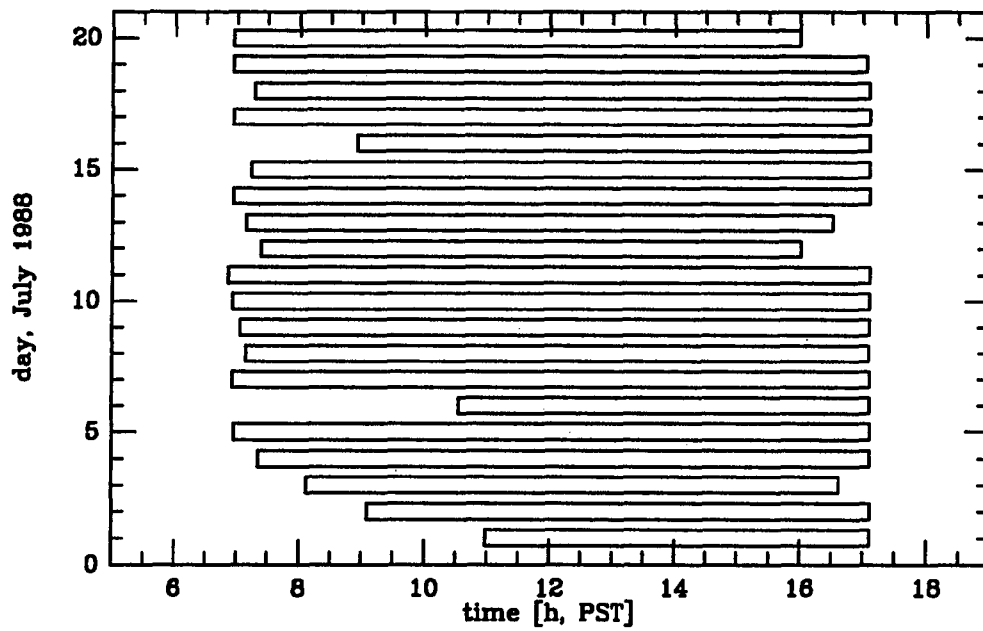


Figure 3.16: Window function, in the time domain.

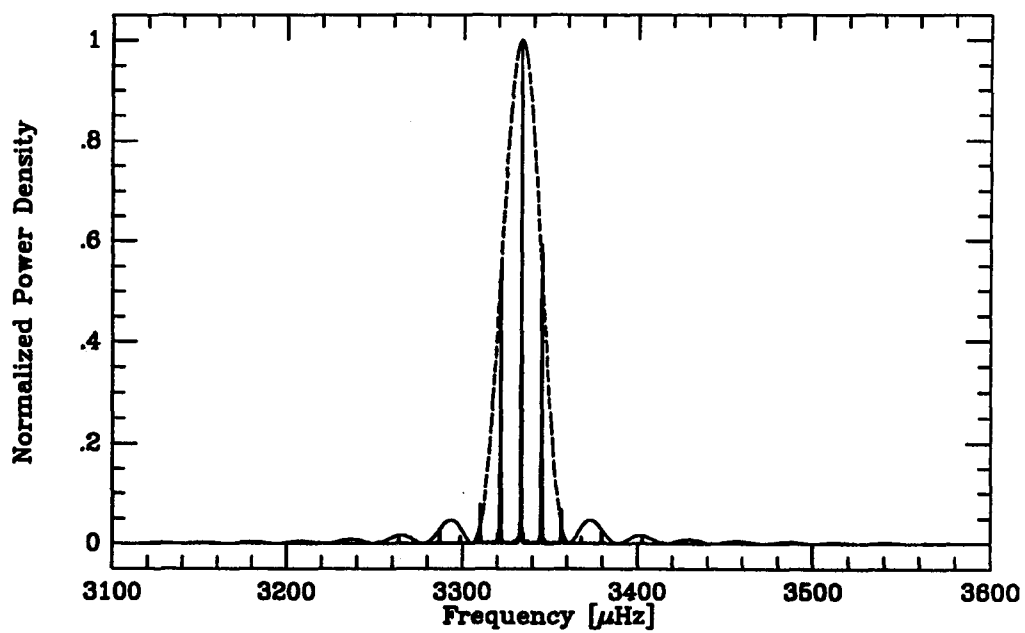


Figure 3.17: Window functions, in the frequency domain for the high-resolution (solid) and low-resolution (dashes) spectra.

3.5 Power Spectra Analysis

The p-mode oscillation characteristics that will, in turn, give us an insight into solar internal properties, are the modal frequencies, amplitudes, and widths. While conceptually it would be desirable to measure these three parameters for each observed mode, the sheer number of modes (i.e. on the order of one million tesseral modes for $0 \leq \ell \leq 600$) makes it an impractical approach. Moreover, the presence of spatial and temporal sidelobes, the finite resolution of the power spectra and the finite lifetime of the modes themselves complicate the interpretation of the observed spectra in these simple terms.

In a spherically symmetric model of the sun, the absence of a preferred axis for the spatial parametrization of the eigenfunctions causes the eigenfrequencies to be degenerate in m . This degeneracy is actually lifted by all of the non-spherical perturbations of the solar structure and dynamics, such as solar rotation, magnetic field, temperature asphericity, and oblateness. Since these are small perturbations of the spherical model, they will introduce small perturbations of the eigenfrequencies, or frequency splittings. Therefore, we can write

$$\nu_{n,\ell,m} = \bar{\nu}_{n,\ell} + \Delta\nu_{n,\ell,m} \quad (3.14)$$

where $\bar{\nu}_{n,\ell}$ represents the unperturbed eigenfrequency, and $\Delta\nu_{n,\ell,m}$ the frequency splitting. Hence, the measurement of the frequency splittings can be formally dissociated from the estimate of the unperturbed eigenfrequencies.

Note that the signal to noise ratio (SNR) can be significantly increased by collapsing all of the tesseral spectra into a unique spectrum for a given degree. Such a collapsing is performed by averaging all of the $\ell + 1$ even- m spectra, each shifted in frequency by the respective frequency splitting estimated for that degree and azimuthal order. Unperturbed modal frequencies, widths and amplitudes are then estimated from these collapsed spectra.

3.5.1 Frequency Splittings

It is customary to parametrize the frequency splittings dependence in m by a Legendre polynomials expansion

$$\Delta\nu_{n,\ell,m} = L \sum_{i=1}^N a_{i,n,\ell} P_i\left(-\frac{m}{L}\right) \quad (3.15)$$

where $L^2 = \ell(\ell + 1)$, $P_i(x)$ are Legendre polynomials, and $N = 5$. Indeed, the solar rotation is the dominant factor in the frequency splitting, and the rotational frequency splittings is related to the rotation rate Ω by

$$\Delta\nu_{n,\ell,m} = -\frac{m}{2\pi} \frac{1}{C_{\ell,m}} \int P_{\ell}^{m2}(x) K_{n,\ell}(r) \Omega(r, x) dr dx \quad (3.16)$$

where $C_{\ell,m} = \int P_{\ell}^{m2}(x) dx$, $K_{n,\ell}$ is the unimodular rotation kernel (see Section 6.1.1), $x = \cos(\theta)$ and θ the colatitude. While a solid body rotation leads to a simple linear relation in m (i.e. $\Delta\nu = -m\bar{\Omega}/2\pi$), differential rotation introduces a non-linear m dependence of the splitting that can be parametrized by an odd-indexed polynomial expansion, since the equatorial symmetry implies that the even-indexed coefficients to be null. Selecting orthogonal polynomials on the $[-1,1]$ segment renders the expansion coefficients mutually independent.

The Legendre expansion coefficients a_i were estimated using the “traditional” cross-correlation method (Brown, 1985; Tomczyk, 1988). In this iterative method, for a given spherical harmonic degree, ℓ , the frequency shift between a template of the unperturbed spectrum and each tesseral spectrum is computed from a cross-correlation analysis, and the Legendre expansion coefficients, a_i , fitted in the least-squares sense to the set of frequency shifts. The template spectrum is itself computed by averaging all but one tesseral spectra, each shifted and linearly interpolated in frequency by the respective frequency splitting estimated from the polynomial expansion at the previous iteration. At each iteration the template spectra are recomputed and the analysis carried out until no significant changes of the expansion coefficients are observed. To avoid an auto-correlation contribu-

tion in the cross-correlation function, the respective tesseral spectrum is not included in the computation of the template spectrum with which it is correlated.

The main advantages of the cross-correlation approach over a method based on some individual mode fitting (see Libbrecht, 1989) are its high computational efficiency and the improvement of the SNR of the frequency shift measurement obtained by using a frequency range that covers more than one radial overtone. The use of several overtones performs an implicit n -averaging of Equation (3.15) hence only provides the measure of some weighted average of the frequency splitting expansion coefficients, i.e. $a_{i,\ell} = \langle a_{i,n,\ell} \rangle_n$. A second drawback of the method resides in the inclusion of the sidelobes in the cross-correlation analysis. While including the temporal sidelobes actually increases the SNR of the cross-correlation function, the presence of spatial sidelobes makes the method susceptible to systematic errors (see discussion in Tomczyk, 1988).

3.5.2 Mode Frequency, Amplitude and Width

An estimate of the unperturbed spectrum at each spherical harmonic degree ℓ was obtained by averaging all the tesseral spectra, each shifted in frequency by the respective frequency splitting estimated from the polynomial expansion measured for that degree. Averaging over the $\ell + 1$ even- m spectra greatly increased the SNR of the collapsed spectra. Hence, the frequencies, amplitudes and widths of the unperturbed modes were estimated from the collapsed spectra.

A standard non-linear least-squares method was used to fit a Lorentzian profile plus a background term to the collapsed spectrum, i.e.

$$\bar{\mathcal{S}}_{\ell}(\nu) = \frac{A_{n,\ell}}{1 + 4\left(\frac{\nu - \nu_{n,\ell}}{w_{n,\ell}}\right)^2} + B \quad (3.17)$$

where $\bar{\mathcal{S}}_{\ell}$ is the collapsed spectrum, B the background term, $A_{n,\ell}$, $\nu_{n,\ell}$ and $w_{n,\ell}$ respectively the mode's amplitude, frequency and full width at half-maximum (FWHM).

The complete non-linear fitting was performed in several steps. First, using a broad section of the spectrum and starting from an initial reasonable estimate of the mode frequency, the location and the amplitude of the closest maximum to the initial guess was used as initial estimate of the mode frequency and amplitude. Using a fixed value of the mode width, the amplitude and position were first solely fitted. In the second phase, the background term was fitted as well and the frequency range used for the fit reduced. Only then was the width fitted. Finally, only the frequency range spanning twice the fitted FWHM was used to perform the fit.

Chapter 4

Frequency Splittings

We have described in Chapter 3 the successive steps of the reduction procedure that lead from the raw set of filtergrams to solar oscillation characteristics, namely the frequency splittings, and the unperturbed modal frequencies, amplitudes, and, widths. In the following sections, we present the frequency splitting measurements obtained from both our low- and high-resolution spectra at low, intermediate and high degree.

More precisely, we present first results obtained using all of the $\ell + 1$ even- m tesseral spectra for low and intermediate degrees, computed from the high-resolution spectra. We next present results obtained using also all the tesseral spectra for intermediate- and high-degree modes, but computed from the low-resolution spectra. Finally, we present results based solely on the pairs of sectoral spectra ($m = \pm\ell$), for intermediate- and high-degree modes, computed from both the high- and low-resolution spectra. In each case, we discuss the potential sources of systematic errors and describe the procedure we used to correct for them when required and possible.

4.1 Tesseral Measurements

4.1.1 Results from the High-Resolution Spectra

The results of the iterative cross-correlation analysis using the high resolution spectra are shown in Figures 4.1 and 4.2, where each expansion coefficient and its 1σ uncertainty, estimated from the scatter to the fit, is plotted as a function of the spherical harmonic degree, ℓ , for $20 < \ell < 120$. Note that the uncertainties computed from the scatter to the fit underestimate the actual uncertainties on the expansion coefficients since no provision for systematic errors (namely systematics associated with sidelobe contamination) has been included. Conversion from synodic to sidereal values was done by adding $31.7\mu\text{Hz}$ to the first order coefficients ($a_{1,\ell}$). For each plot, the expected “surface” coefficients, estimated from seismic independent measurements, are indicated: namely, the “gas” surface rate ($a_1 = 435, a_3 = 21, a_5 = -4$, Snodgrass 1985) estimated from spectroscopic measurements, and the “magnetic” surface rate ($a_1 = 442.8, a_3 = 21.7, a_5 = -2.5$, Snodgrass 1983), estimated from magnetic feature motion.

Only the portion from 1.8 to 4.8 mHz of the amplitude spectra were used for the cross-correlation analysis and the frequency shifts were computed from a 3 point parabolic fit centered on the highest peak of the cross-correlation functions. The cross-correlation functions were themselves computed over ± 64 lags ($\pm 16.3\mu\text{Hz}$) around the predicted shift estimated at the previous iteration for 3 initial iterative steps, where only a third order Legendre expansion was fitted. The cross-correlation functions were then computed over ± 21 lags ($\pm 5.34\mu\text{Hz}$) to prevent temporal sidelobe misidentification, and a fifth order expansion was fitted. A 3σ rejection threshold was applied to the Legendre expansion coefficients least-squares fit. The procedure was iterated until the σ -weighted average of the absolute values of the relative differences of the fitting coefficients between successive iterations was smaller than 1%.

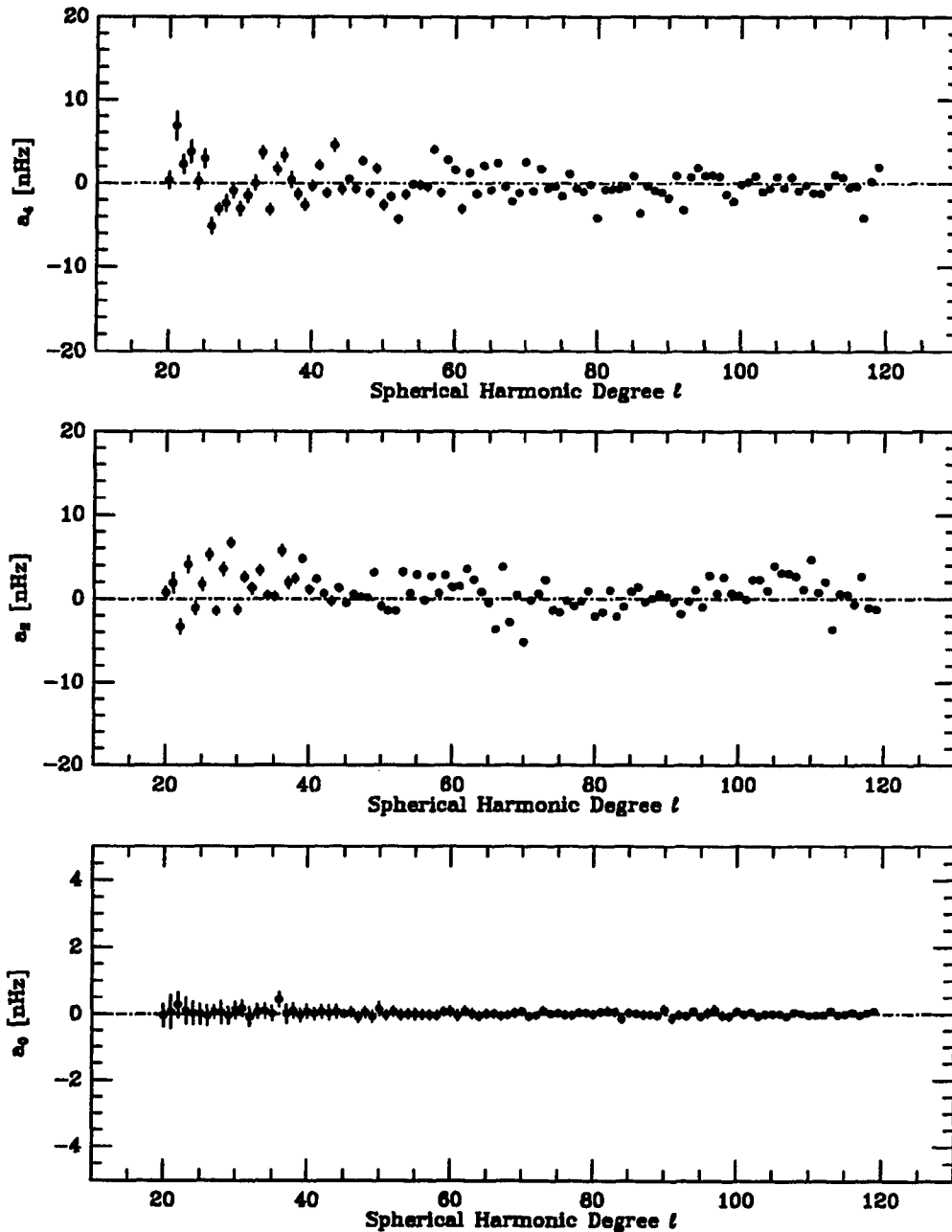


Figure 4.1: Even-indexed Legendre polynomials expansion coefficients, estimated from the high-resolution spectra, for $20 \leq l < 120$. The error bars represent the 1σ uncertainty, estimated from the scatter to the fit, and underestimate the actual uncertainty on the expansion coefficients. If the frequency splitting were solely due to rotation, symmetry about the equator would imply that the even-indexed should be zero (as indicated by the dash-dotted line).

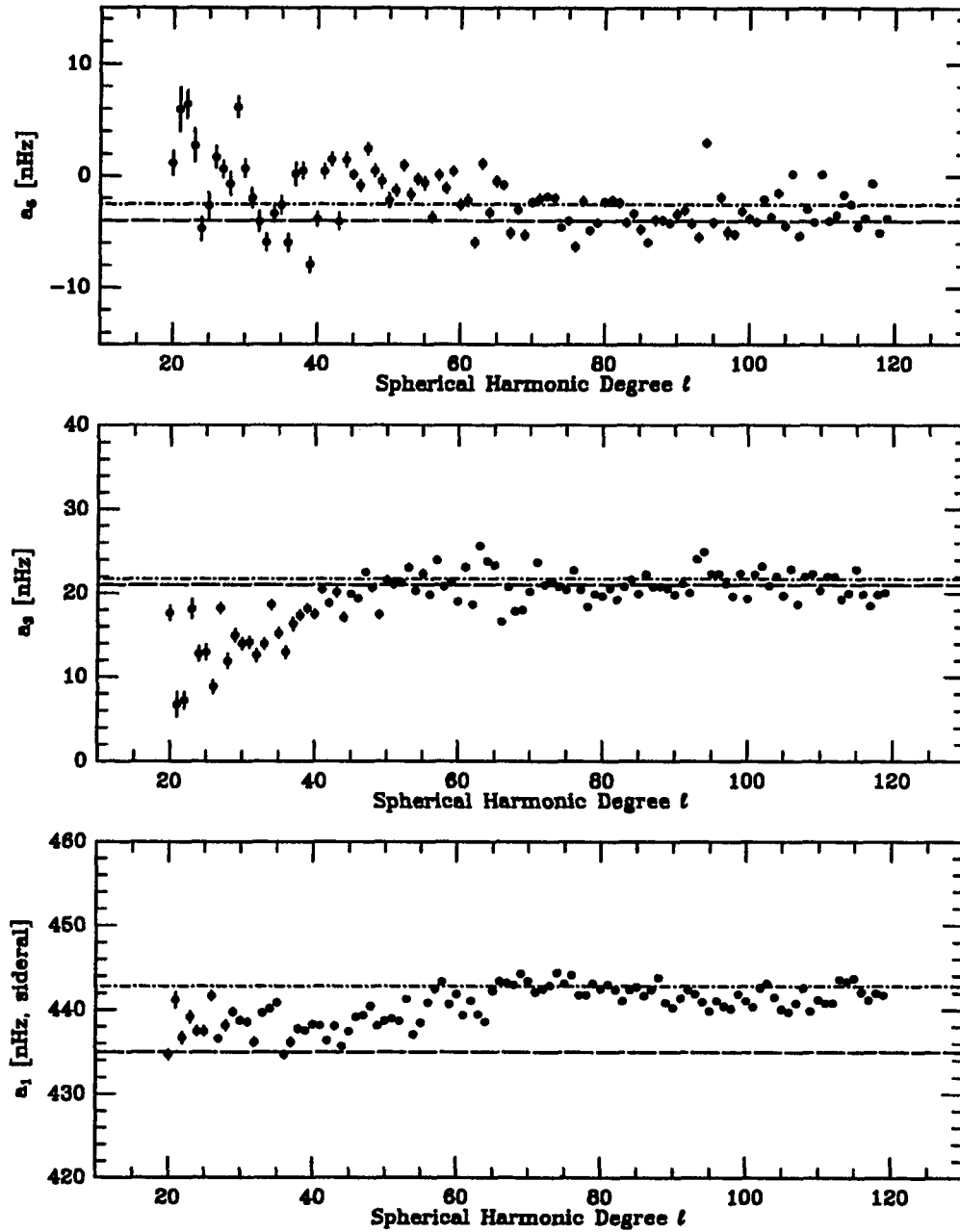


Figure 4.2: Odd-indexed Legendre polynomials expansion coefficients, estimated from the high-resolution spectra, for $20 \leq \ell < 120$. The error bars represent the 1σ uncertainty, estimated from the scatter to the fit, and underestimate the actual uncertainty on the expansion coefficients. Expected “surface” values corresponding to the spectroscopic rotation rate (long dashes) and the magnetic feature rotation rate (dot-dashes) are also indicated (see text for references).

Above $\ell = 120$, the decreasing modal lifetimes (see Chapter 5) and the decreasing slopes of the ridges (i.e. $\delta\nu/\delta\ell$) that determine the location of the spatial sidelobes, cause the peaks and their sidelobes to overlap. Peaks and sidelobes cannot be resolved any more in the collapsed spectrum and blend into ridges. This effect is illustrated Figures 4.3 to 4.8 where the $m = 0$ spectrum, the collapsed spectrum, and their cross-correlation functions are plotted for $\ell = 50$ and $\ell = 140$. Indeed, while in both cases the $m = 0$ spectra present similar features, namely sharp peaks with their temporal and spatial sidelobes, in the collapsed spectrum for $\ell = 50$ individual modes and sidelobes can easily be identified while in the collapsed spectrum for $\ell = 140$ individual modes overlap enough to blend into a ridge. Once peaks and sidelobes start to overlap, the contrast of the cross-correlation function is dramatically reduced, as clearly illustrated when comparing Figure 4.5 to Figure 4.8, and the highest peak of the cross-correlation can no longer be identified as a measure of the modal frequency shift. Moreover, small scale features present in the collapsed spectrum cause the cross-correlation of the individual tesseral spectra to “latch on” to these features and render the results of the iterative procedure dependent on the initial guess.

To remove this “latch on” behavior, we have smoothed the high-resolution spectra, replacing each spectral bin by a 17-bin-wide ($4.23 \mu\text{Hz}$) centered average, and carried out the cross-correlation analysis for $100 \leq \ell < 230$. The only other differences with the unsmoothed case were to restrict the fit to an odd term expansion for the initial 3 iterative steps and to relax the convergence criteria to 5%. Results from this analysis are shown in Figures 4.9 and 4.10, where the results of the unsmoothed analysis for $\ell < 120$ are also plotted for comparison.

While, for the overlapping range in ℓ , (i.e. for $100 \leq \ell \leq 120$), the results of both methods agree within the internal scatter, suspicious results above $\ell = 120$ are obtained. Indeed, after a short transitional region in ℓ , the odd-indexed coefficients deviate largely from

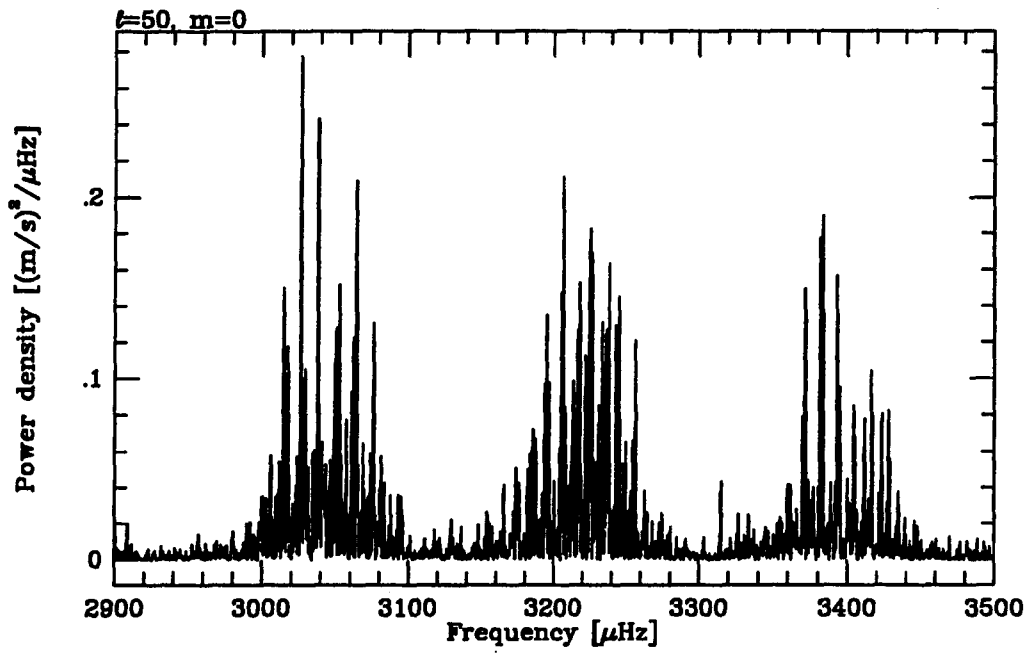


Figure 4.3: Portion of the $\ell = 50$ and $m = 0$ high-resolution spectrum.

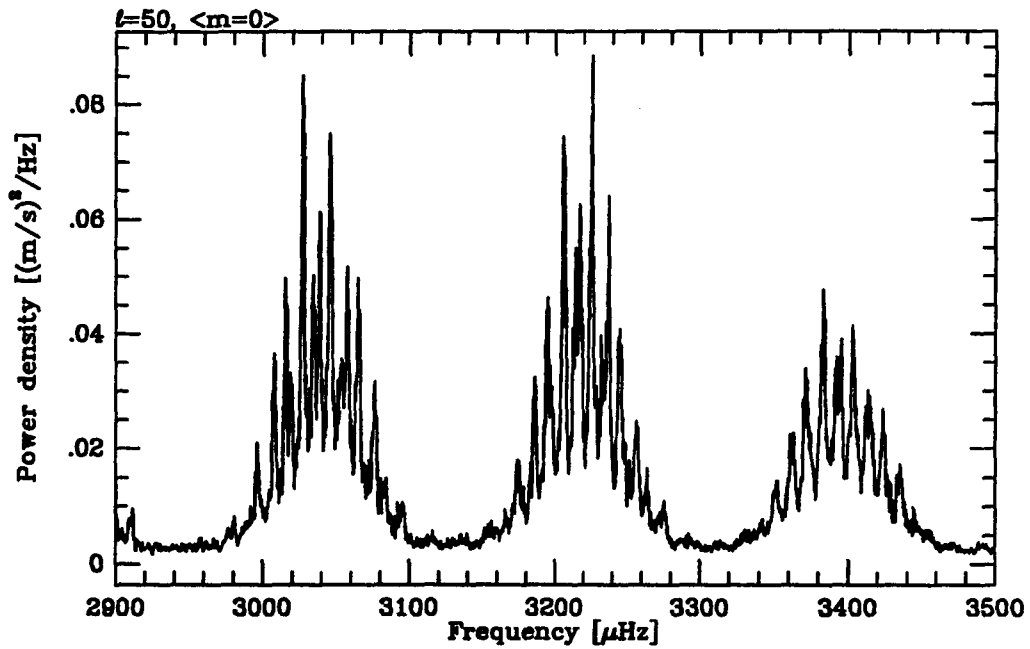


Figure 4.4: Portion of the collapsed, $\ell = 50$ and $\langle m = 0 \rangle$ high-resolution spectrum.

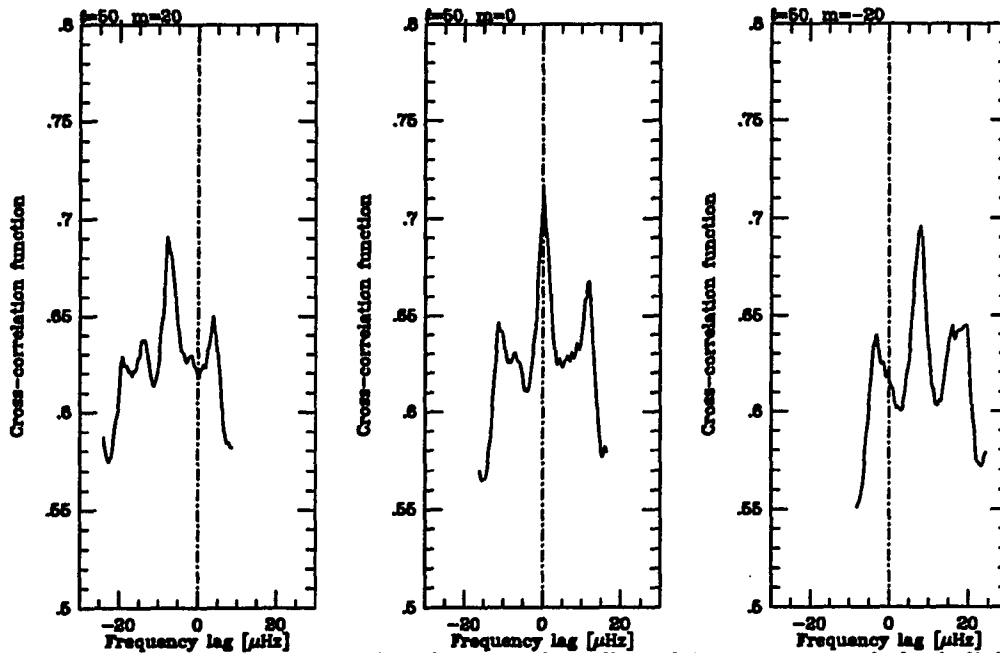


Figure 4.5: Cross-correlation functions between the collapsed $\langle m = 0 \rangle$ and the individual $m = 20$, $m = 0$ and $m = -20$ high-resolution spectra, for $\ell = 50$. Note the clear signature of the temporal sidelobes as secondary cross-correlation peaks $11.57 \mu\text{Hz}$ away from the main peak. The asymmetry in the cross-correlation function is an indication of contamination by the spatial sidelobes.

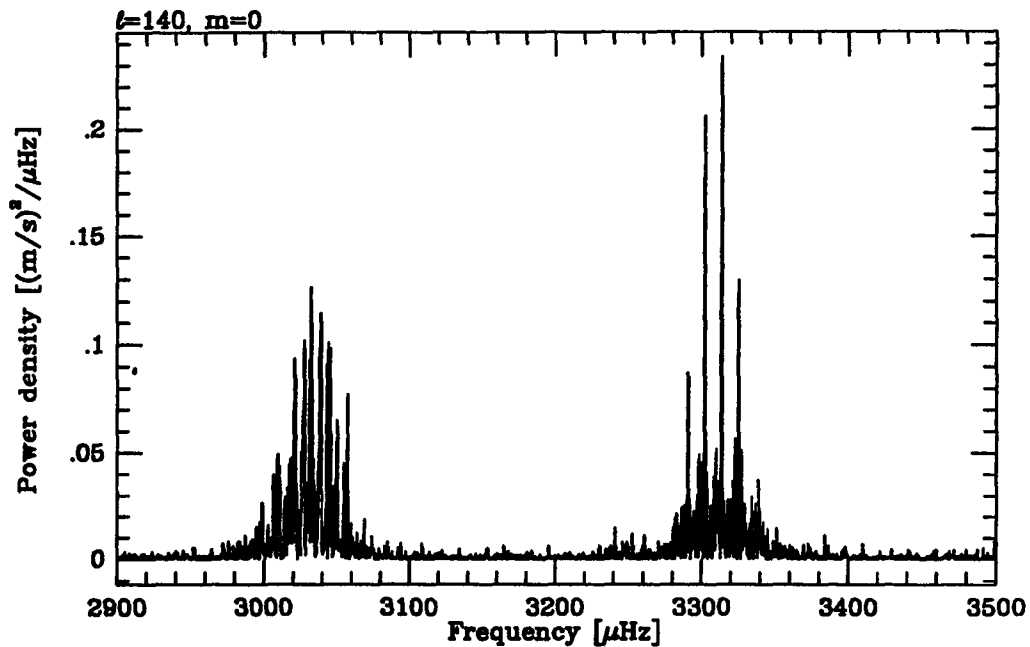


Figure 4.6: Portion of the $\ell = 140$ and $m = 0$ high-resolution spectrum.

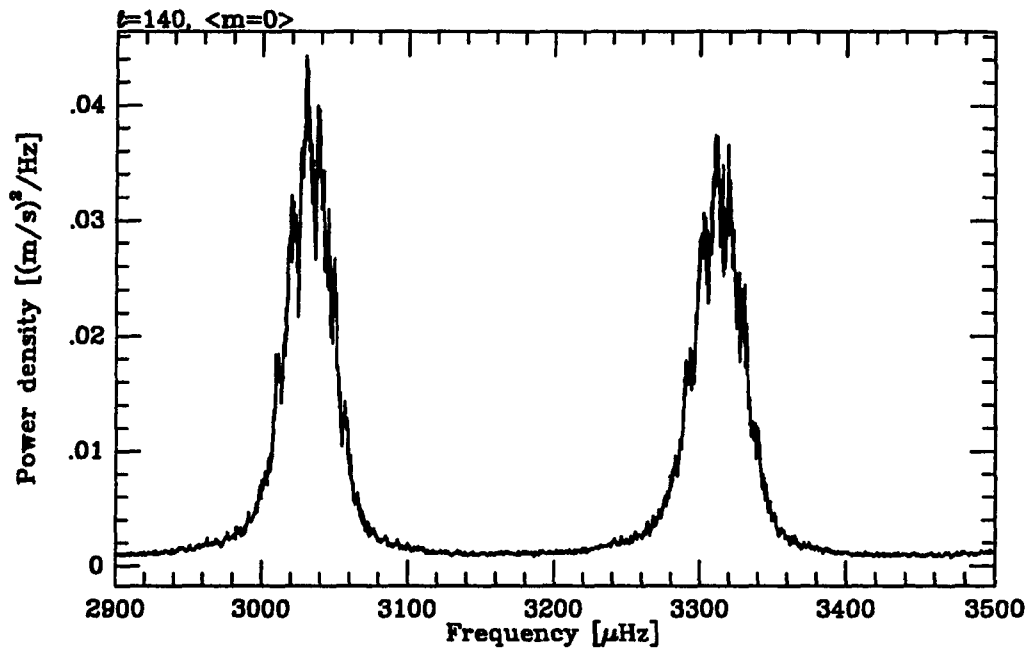


Figure 4.7: Portion of the collapsed, $\ell = 140$ and $\langle m = 0 \rangle$ high-resolution spectrum.

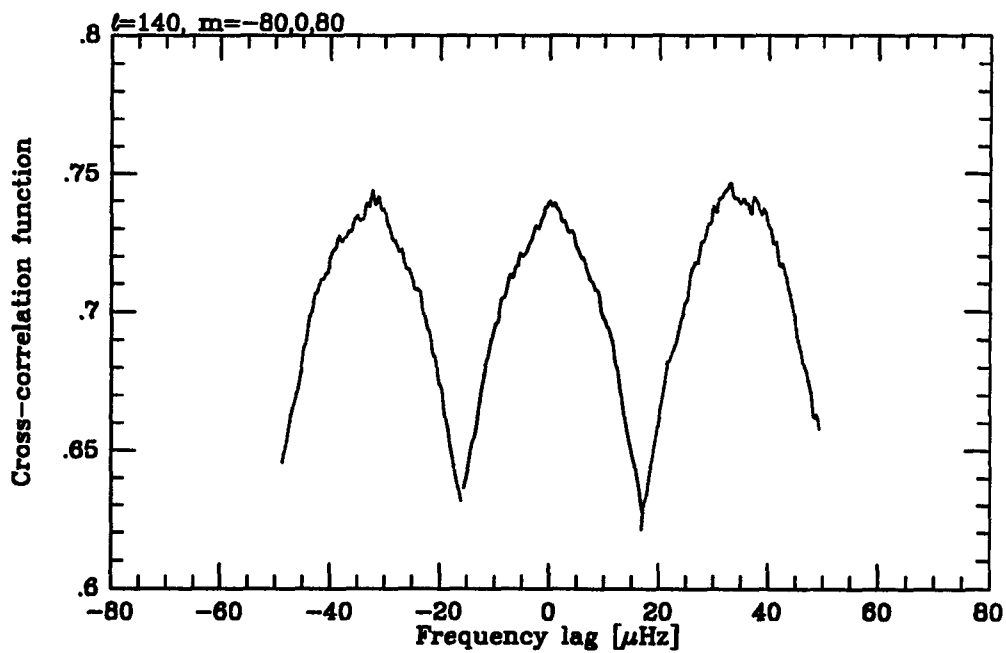


Figure 4.8: Cross-correlation functions between the collapsed $\langle m = 0 \rangle$ and the individual $m = 80$, $m = 0$ and $m = -80$ high-resolution spectra, for $\ell = 140$. Note that the temporal sidelobes $11.57 \mu\text{Hz}$ away from the main peak cannot be identified by contrast to Figure 4.5

the expected “surface” values and the even-indexed coefficients deviate significantly from zero. While deviation from expected values does not necessarily render the results as being suspicious, the suddenness in the transition, if of solar origin, would imply an abrupt major change in the solar structure located at a depth of around $0.1 R_{\odot}$. Moreover, the significant deviation from zero of the a_2 coefficient can not be explained in its magnitude by any of the potential solar perturbations (i.e. magnetic field, temperature asymmetry, ...). But, since this deviation occurs very precisely at the transition between resolved and unresolved collapsed spectra, the source of these systematic errors is most probably associated with the fact that the modes become unresolved.

In order to establish that the peculiar results obtained above $\ell = 120$ were not due to the iterative nature of the cross-correlation procedure, nor to the fact that a collapsed spectrum with unresolved modes was correlated with individual spectra where resolved modes may have seemed to be present, we also used the following two alternative methods on a restricted set of high resolution spectra.

For both alternative methods, all of the cross-correlation functions of each possible pair of tesseral spectra (m, m') for $m \neq m'$ were first computed. In the first alternative method, for each m , an average over m' , with $|m - m'| \geq 4$, of the cross-correlation functions was then computed, shifting each correlation function in frequency lag by the frequency splitting estimated from the polynomial expansion at the previous iteration. Frequency shifts were then computed from the m' -averaged correlation functions, and the polynomial expansion coefficients fitted in the least-squares sense to the frequency shifts. The method was iterated on the m' -averaged correlation functions rather than on the template spectrum.

In the second alternative method, to avoid any form of iteration entirely, all the frequency shift differences, $\delta(\Delta\nu)_{m,m'}$, were estimated from the (m, m') cross-correlation functions, and the Legendre polynomial expansion fitted to frequency shift differences. Since differ-

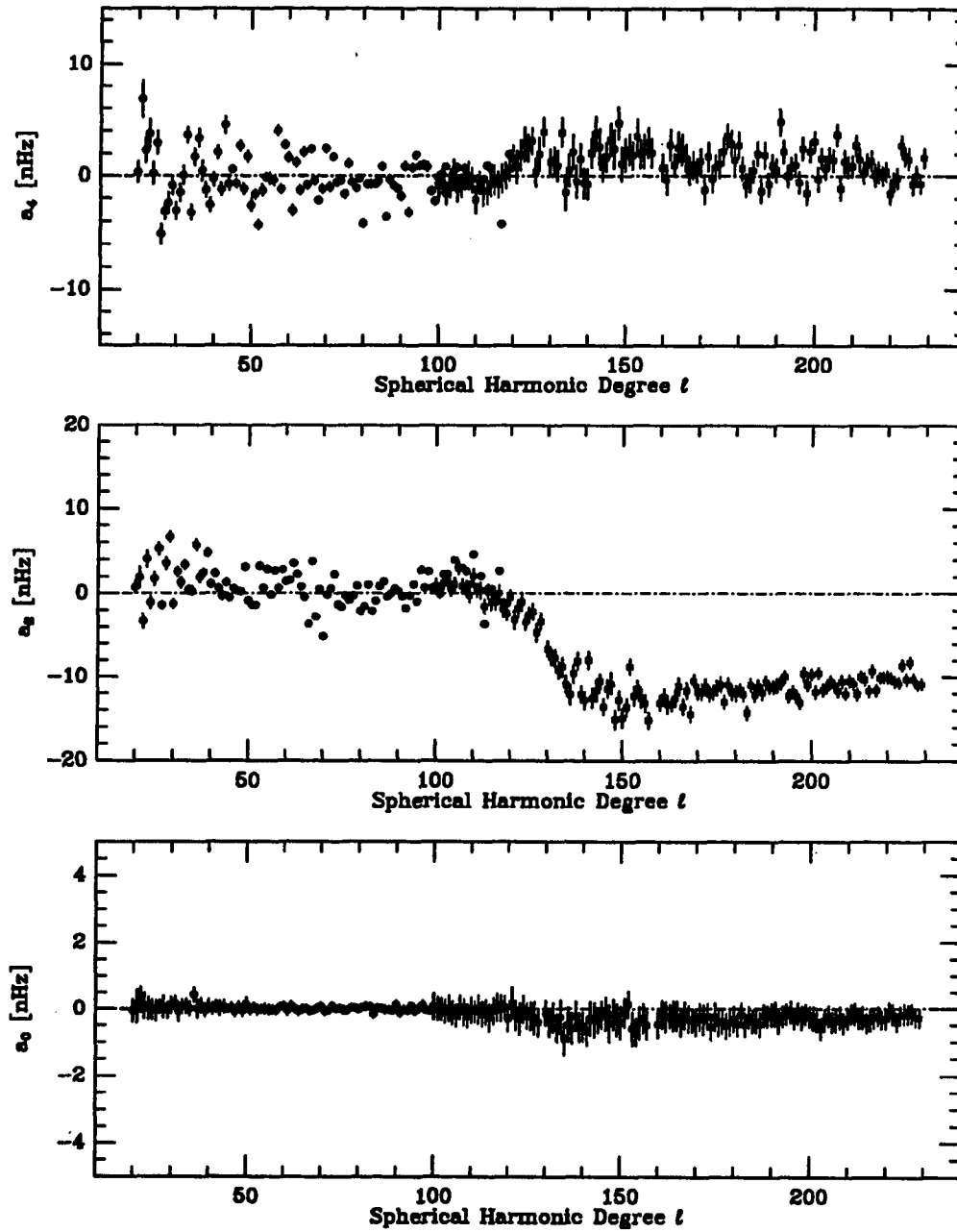


Figure 4.9: Even-indexed Legendre polynomial expansion coefficients, estimated from the high-resolution spectra, for $20 \leq \ell < 120$, and from the smoothed high-resolution spectra for $100 \leq \ell < 230$. Uncertainties and “surface” values as in Figure 4.1.

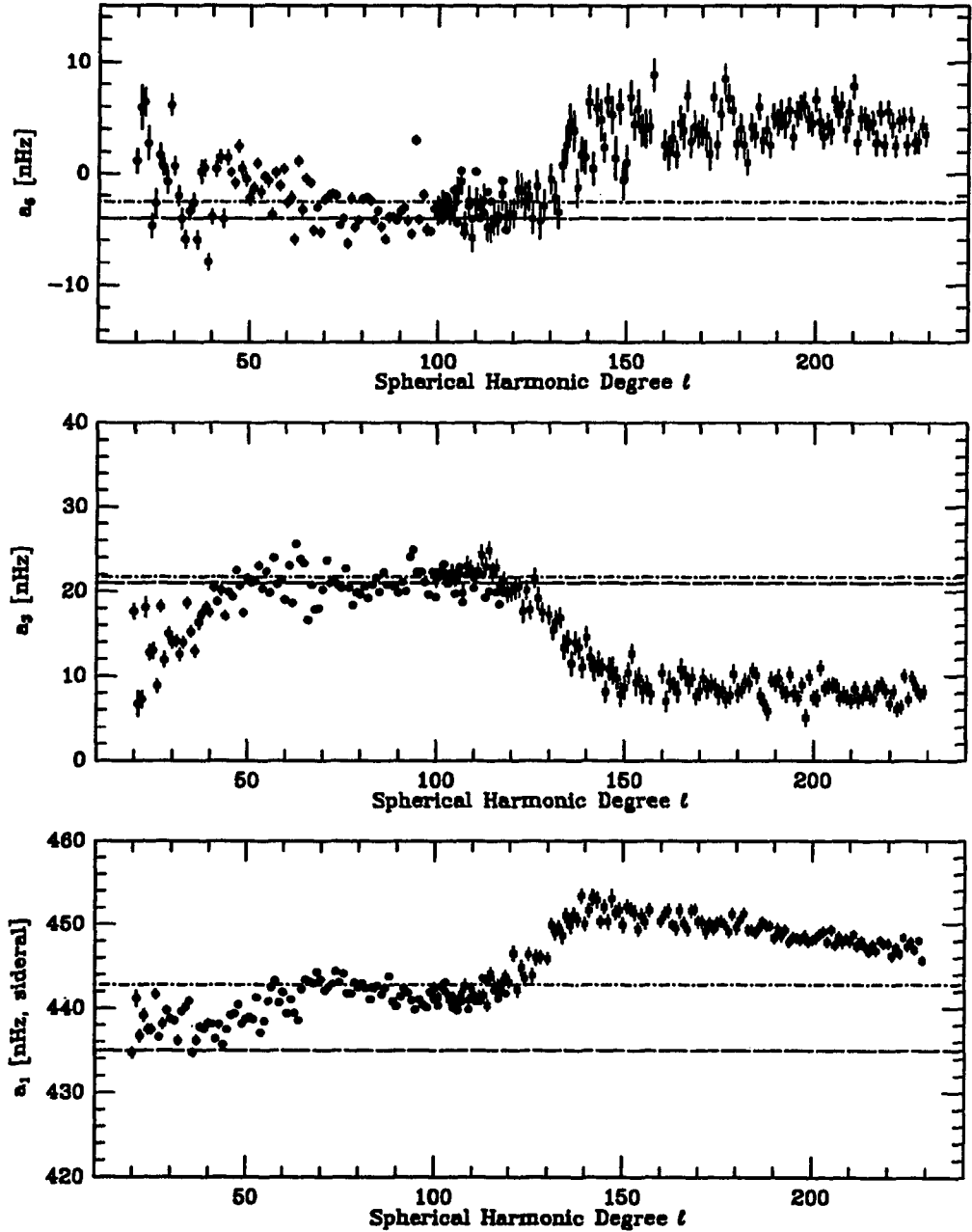


Figure 4.10: Odd-indexed Legendre polynomial expansion coefficients, estimated from the high-resolution spectra, for $20 \leq \ell < 120$, and from the the smoothed high resolution spectra for $100 \leq \ell < 230$. Uncertainties and "surface" values as in Figure 4.2.

†	a_0	a_1	a_2	a_3	a_4	a_5
(1)	0.16 ± 0.19	407.01 ± 0.33	-0.89 ± 0.42	21.56 ± 0.49	-2.59 ± 0.55	-2.14 ± 0.61
(2)	-0.22 ± 1.09	406.93 ± 1.88	1.59 ± 2.40	23.85 ± 2.82	-1.41 ± 3.17	-0.86 ± 3.49
(3)	-	407.82 ± 0.50	0.06 ± 0.64	22.98 ± 0.75	-0.65 ± 0.84	-2.46 ± 0.92

† methods: (1)=traditional iterative method (2)=alternative iterative method (3)=alternative non-iterative method

Table 4.1: Comparison of Legendre polynomial fitting coefficients, computed for $\ell = 50$ with different methods

†	a_0	a_1	a_2	a_3	a_4	a_5
(1)	-0.47 ± 0.39	418.70 ± 0.68	-13.14 ± 0.87	10.34 ± 1.03	0.74 ± 1.17	2.57 ± 1.28
(2)	0.01 ± 0.62	417.93 ± 1.08	-14.33 ± 1.39	7.66 ± 1.63	0.07 ± 1.84	6.48 ± 2.02
(3)	-	419.87 ± 0.22	-13.63 ± 0.28	9.92 ± 0.33	0.43 ± 0.37	2.45 ± 0.41

† methods: (1)=traditional iterative method (2)=alternative iterative method (3)=alternative non-iterative method

Table 4.2: Comparison of Legendre polynomial fitting coefficients, computed for $\ell = 160$ with different methods

ences of frequency shifts rather than the shifts themselves were estimated, a zero order term could not be fitted, and the procedure was modified to fit

$$\delta(\Delta\nu)_{m,m'} = L \sum_{i=1}^5 a_i \left(P_i\left(-\frac{m}{L}\right) - P_i\left(-\frac{m'}{L}\right) \right) \quad (4.1)$$

from all the (m, m') pairs with $|m - m'| \geq 4$. The rejection of the cross-correlation functions for $|m - m'| < 4$ was performed in order to reduce any peak/sidelobe correlation that would introduce a contribution equivalent to an auto-correlation into the cross-correlation functions.

Tables 4.1 and 4.2 compare results obtained with each method for two representative ℓ values. Since, for both values of ℓ , all three methods agree at the 1σ level, we can rule out as source of the systematic effects the potential different nature of the collapsed spectrum from the individual spectra and the iterative character of the “traditional” cross-correlation method.

4.1.2 Results from the Low-Resolution Spectra

Results of the cross-correlation frequency splitting analysis on the low-resolution spectra are presented in Figures 4.11 and 4.12. As for the high-resolution case, only the portion from 1.8 to 4.8 mHz of the power spectra were used in the cross-correlation analysis. The frequency shifts were computed here from a 5 point parabolic fit centered on the highest peak of each cross-correlation function. The cross-correlation functions were themselves computed over ± 16 lags (260 μHz) around the predicted shift estimated at the previous iteration for 3 initial iterative steps where only a third order Legendre expansion was fitted. The cross-correlation functions were then computed over ± 11 lags (179 μHz) and a fifth order expansion fitted. As for the high-resolution spectra analysis, a 3σ rejection threshold was applied to the Legendre expansion least-squares fit and the procedure was iterated until the σ -weighted average of the absolute values of the relative differences of the fitting coefficients between successive iteration was smaller than 1%.

4.1.3 Comparison of High- and Low-Resolution Results

Figures 4.13 and 4.14 compare the results obtained in the three different cases, shown by the three different sets of symbols, namely: 1) the low-degree, unsmoothed, high-resolution case, 2) the intermediate-degree, smoothed, high-resolution case, and 3) the low-resolution case. For purposes of clarity the low-resolution results are shown binned in $10\text{-}\ell$ wide bins. Notice that: a) below $\ell \sim 120$ the smoothed high resolution results agree with the unsmoothed high-resolution results, and b) above $\ell \sim 140$ the smoothed high-resolution results agree with the low resolution results, while c) the low-resolution results disagree with the unsmoothed high-resolution results (for the overlapping range in ℓ).

These comparisons clearly indicate that, when the individual modes are not resolved (i.e.

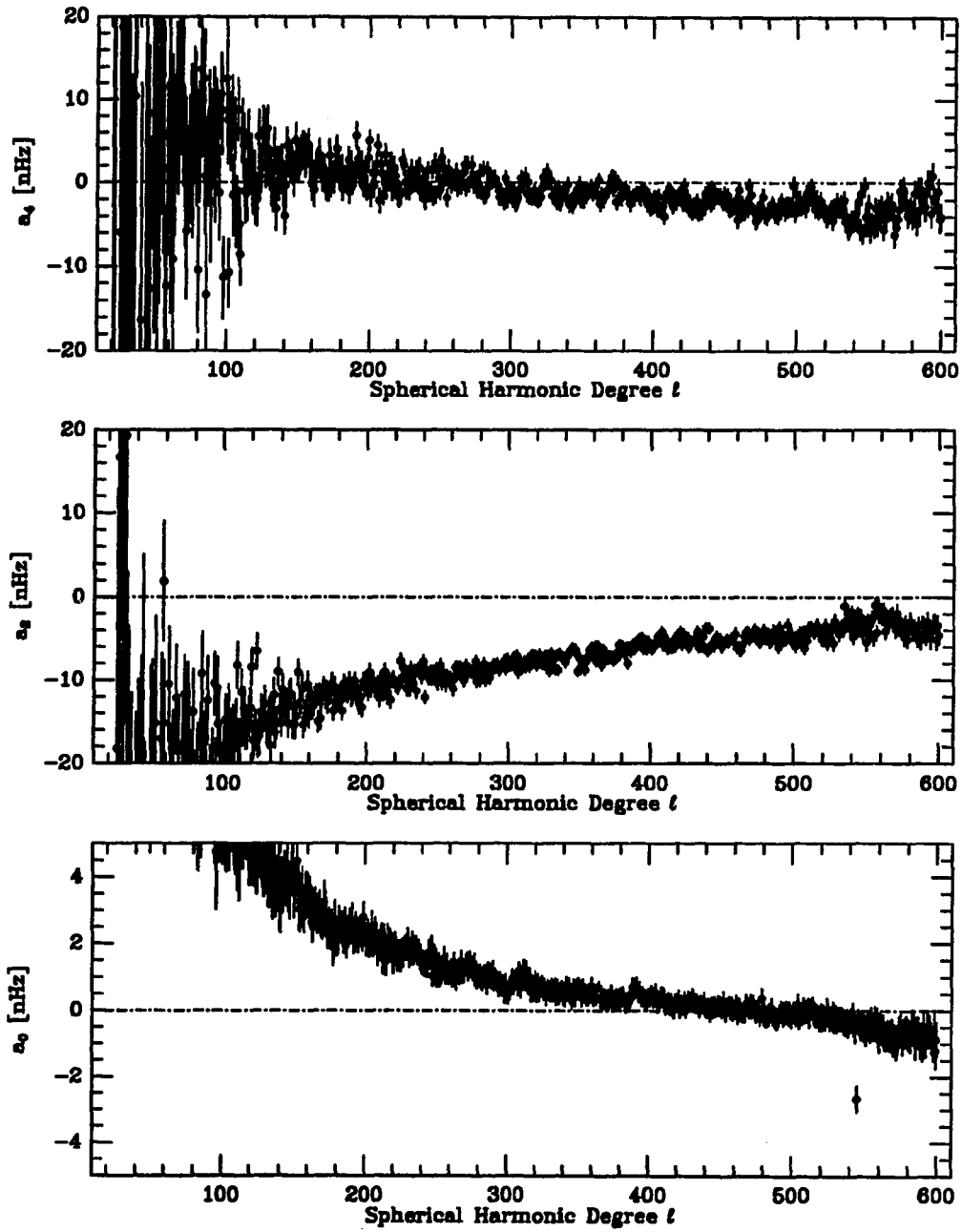


Figure 4.11: Even-indexed Legendre polynomials expansion coefficients, estimated from the low-resolution spectra, for $20 \leq l \leq 600$. Uncertainties and “surface” values as in Figure 4.1.

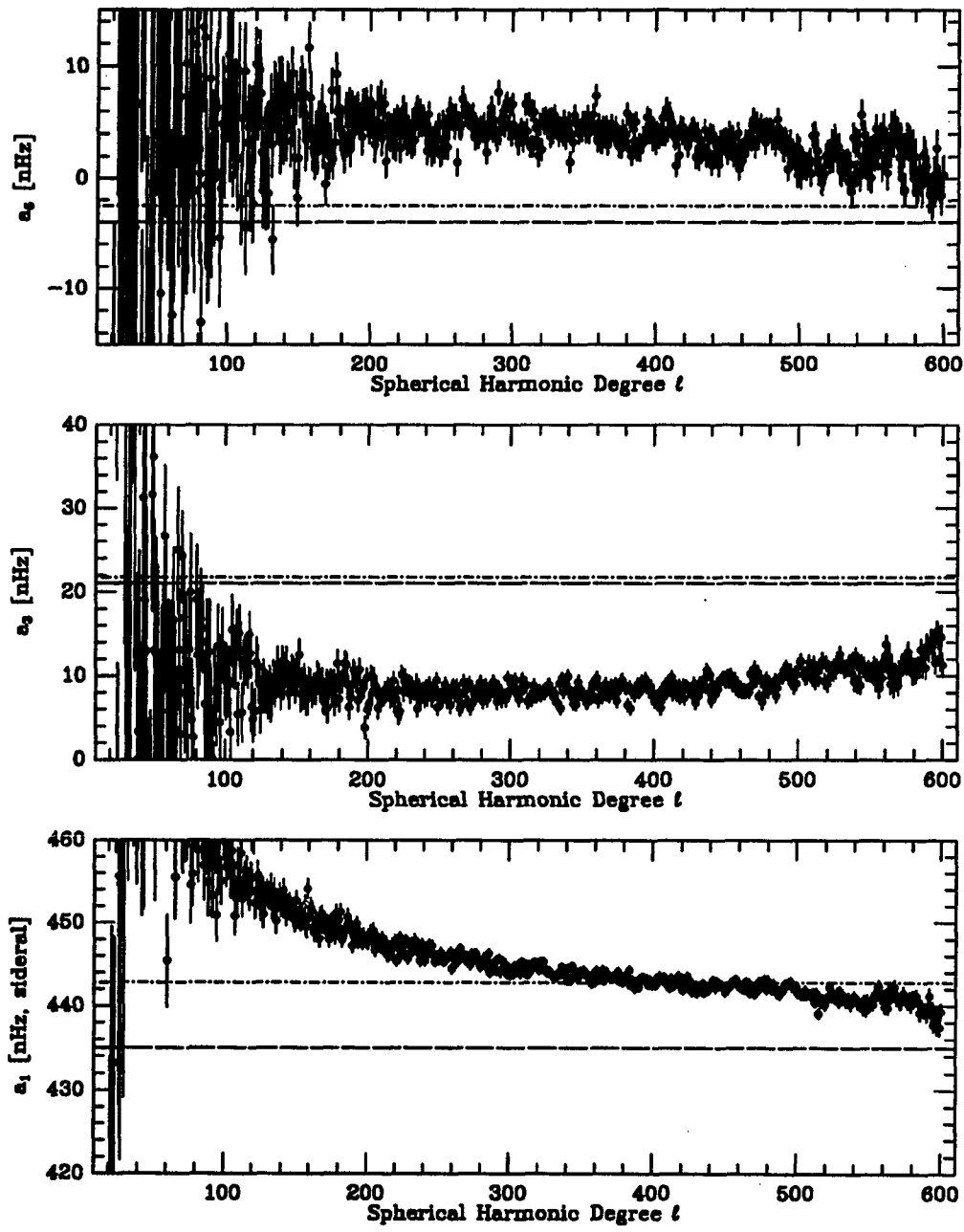


Figure 4.12: Odd-indexed Legendre polynomial expansion coefficients, estimated from the low-resolution spectra, for $20 \leq l \leq 600$. Uncertainties and "surface" values as in Figure 4.2.

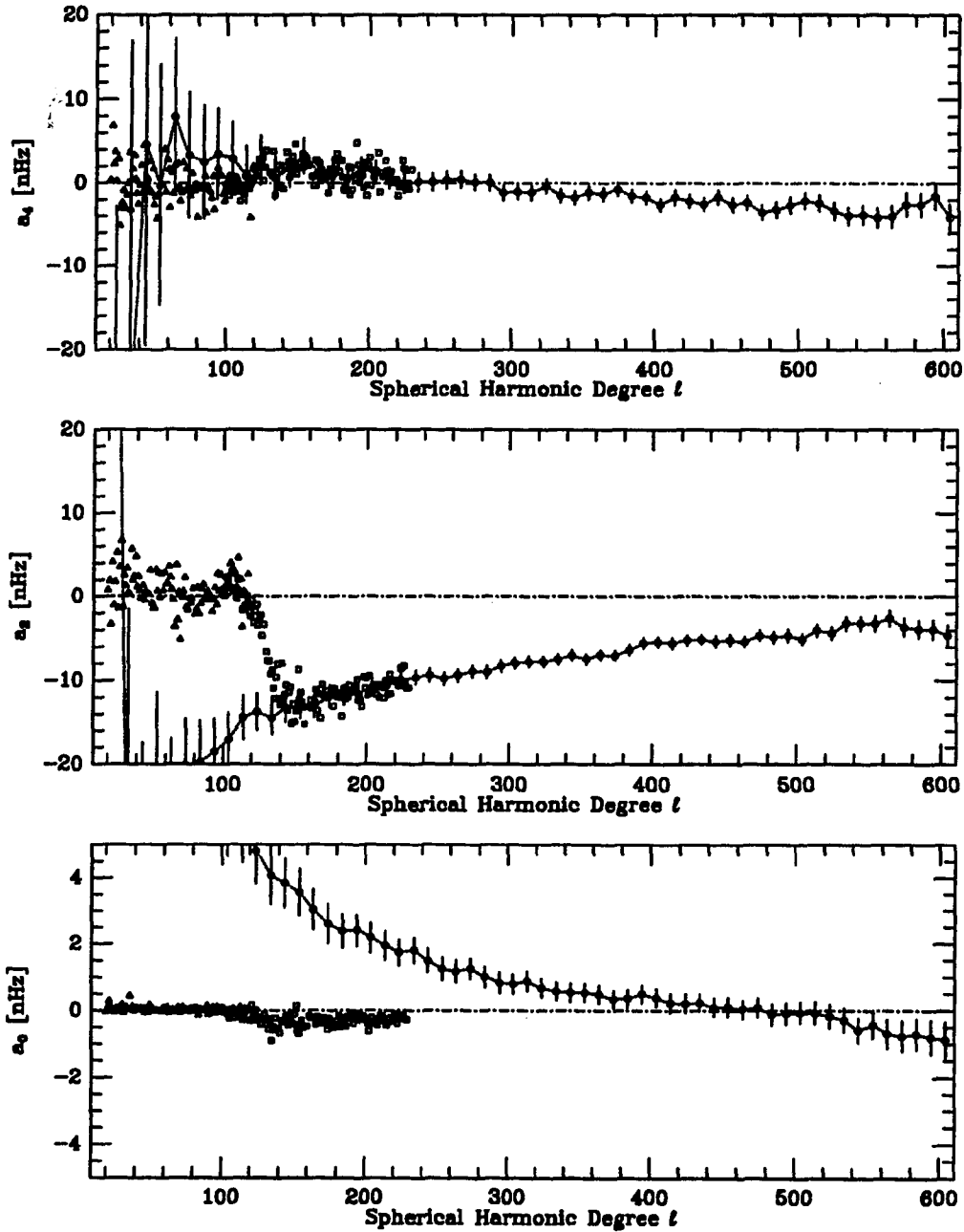


Figure 4.13: Comparison of the even-indexed Legendre polynomial expansion coefficients, estimated from the high-resolution spectra for $20 \leq \ell < 120$ (triangles), from the smoothed high-resolution spectra for $100 \leq \ell < 230$ (squares), and binned in $10\text{-}\ell$ wide bins, from the low-resolution spectra for $20 \leq \ell \leq 600$ (circles with error bars)

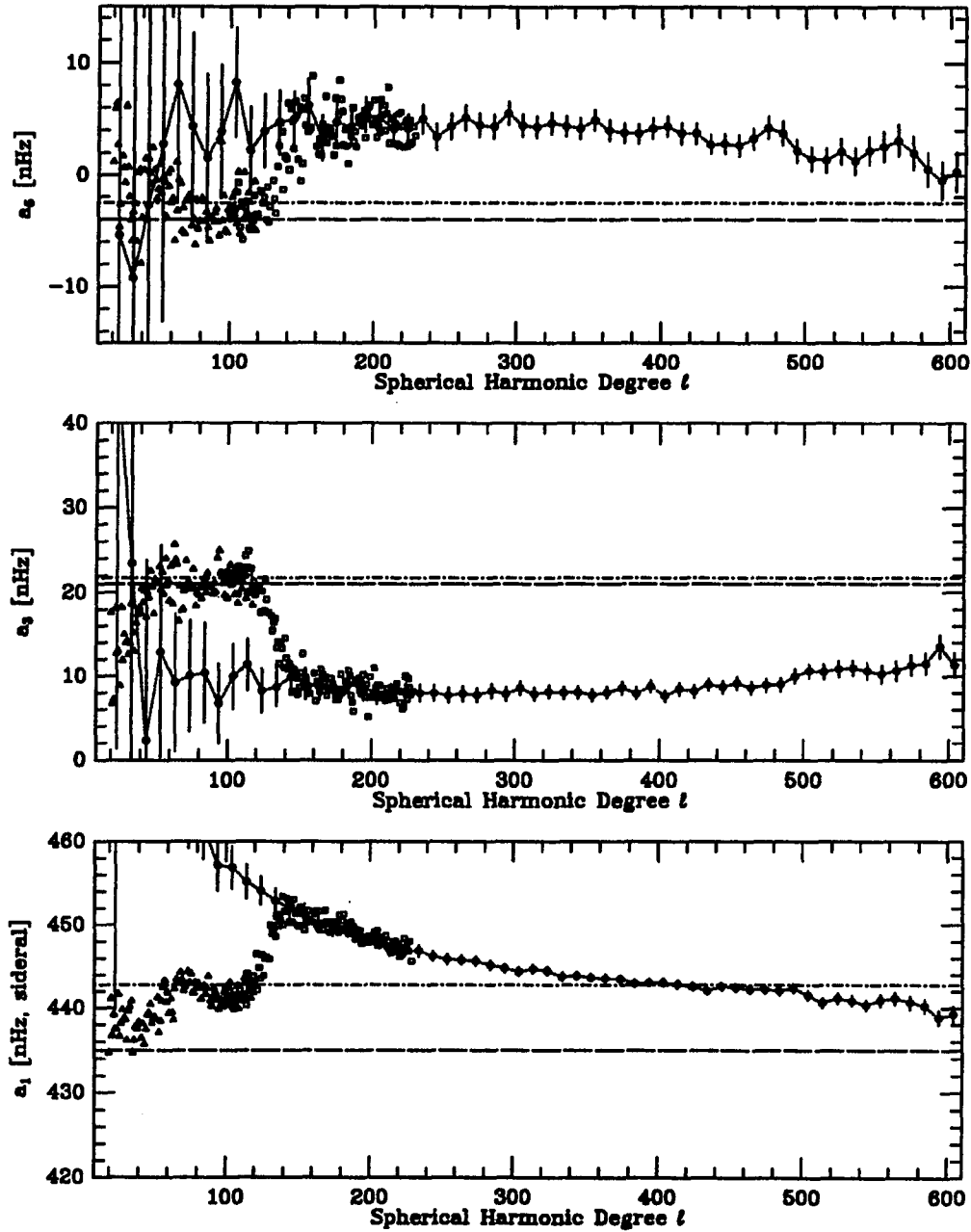


Figure 4.14: Comparison of the odd-indexed Legendre polynomials expansion coefficients, estimated from the high-resolution spectra for $20 \leq l < 120$ (triangles), from the smoothed high-resolution spectra for $100 \leq l < 230$ (squares), and binned in $10l$ wide bins, from the low-resolution spectra for $20 \leq l \leq 600$ (circle with error bars)

$\ell > 120$ for the high-resolution spectra and at all ℓ for the low-resolution spectra), the measured splittings are systematically erroneous. Moreover, the agreement of the low-resolution results with the intermediate-degree, smoothed high-resolution results indicates that the source of the systematic errors is the same in both cases. In addition, it indicates that no improvement in measuring frequency splittings is gained at high degrees by computing high-resolution spectra, rather than low-resolution ones, when high-degree individual modes cannot be resolved any more¹.

We must conclude from these comparisons that above $\ell = 120$ systematic effects associated to the non-resolved nature of the spectra introduce systematic errors in the computation of the frequency splittings, and that these systematics are the same whether low-resolution or high-resolution spectra are used. In order to understand the nature of these systematics we present in the next section a discussion of their sources, and our attempt to model them. Unfortunately, our modeling was unable to reproduce in the details the observed systematics, and therefore, we shall present in the following section the *ad hoc* procedure we have developed to correct for these systematics.

4.1.4 Sources of Systematic Errors

Once modes and sidelobes blend into ridges, or when the frequency resolution prevents us from resolving individual modes, the measured frequency splittings will represent ridge centroid frequency shifts rather than modal frequency shifts. Therefore, if the centroid of the ridge does not correspond to the target mode frequency, the ridge frequency shifts will not represent the target frequency splittings. Hence, any asymmetry with respect to the target mode central frequency in the power density distribution of a ridge will introduce systematic deviations in the frequency splitting measurements based on unresolved modes.

¹Note that from a computational point of view, the computation of low-resolution spectra requires significantly less resources (disk and memory) than the computation of high-resolution ones

Indeed, recall that each individual spectrum is the Fourier transform of the $\tilde{C}_{\ell,m}(t)$ time series, where the spherical harmonic coefficients, $\tilde{C}_{\ell,m}(t)$, are defined by Equation (3.10). Hence, if $\mathcal{L}_{n,\ell,m}(\nu)$ represents the limit spectrum for an individual mode (n, ℓ, m) , each tesseral spectrum, $\tilde{\mathcal{S}}_{\ell,m}(\nu)$, can be written as

$$\tilde{\mathcal{S}}_{\ell,m}(\nu) = \sum_{\ell',m'} |\langle \ell', m' | \ell, m \rangle| \sum_n \mathcal{L}_{n,\ell,m}(\nu) \otimes \mathcal{W}_t(\nu) + \text{noise} \quad (4.2)$$

where $\langle \ell', m' | \ell, m \rangle$, the leakage matrix, is defined by Equation (3.12), $\mathcal{W}_t(\nu)$ is the temporal window function in the frequency domain and \otimes represents the convolution operator. Since spherical harmonic functions are orthogonal on the sphere, leakage matrix elements are only significantly different from zero for $\ell' \approx \ell$ and $m' \approx m$.

In order to resolve individual modes, the width of the convolved spectrum of each individual mode, $\mathcal{L}_{n,\ell,m} \otimes \mathcal{W}_t$, must be significantly smaller than the mode separations, $\delta\nu/\delta n$, $\delta\nu/\delta\ell$, and $\delta\nu/\delta m$. Since $\delta\nu/\delta n \approx 134\text{--}300 \mu\text{Hz}$, mode resolution in n will always be realized for observing runs longer than a few hours, while, since $\delta\nu/\delta m \simeq \Omega/2\pi \approx 0.42 \mu\text{Hz}$, mode resolution in m would only be possible if the modal lifetimes were significantly longer than a month. Since, except for some low-frequency and low-degree modes, modal lifetimes range from a few weeks for low-degree modes, to a few days for intermediate degree modes, to a few hours for high-degree and high-order modes (see Chapter 5), resolution in m cannot be achieved. While “ m -blending” will introduce systematic errors, the small value of $\delta\nu/\delta m$ causes this effect to remain negligible at the present level of accuracy.

Thus, while at $\ell = 50$, with $\delta\nu/\delta\ell \approx 20 \mu\text{Hz}$, individual peaks can easily be resolved in ℓ from high-resolution spectra, around $\ell = 140$, where $\delta\nu/\delta\ell \approx 8 \mu\text{Hz}$ and where the convolved FWHM $\approx 4 \mu\text{Hz}$, modes and sidelobes overlap enough to blend individual modes into ridges².

²Note also that the presence of temporal sidelobes in the high-resolution spectra contributes to further blending of the overlapping modes

Since the temporal window function in the frequency domain, \mathcal{W}_t , and the limit spectrum, \mathcal{L} , are symmetric functions, while the leakage matrix is itself symmetric by definition ($\langle \ell', m' | \ell, m \rangle = \langle \ell, m | \ell', m' \rangle^*$), since the curvature of the ridges is small (i.e. $\delta\nu/\delta\ell$ is a slowly varying function of ν) and the mode power density distribution is expected to be a slow function of degree (i.e. $\delta \log P_{n,\ell,m}/\delta\ell \ll 1$), the asymmetry of the ridges should be small and ridge frequency shifts should have provided a good estimate of the modal frequency splittings. Unfortunately, in all practical cases (see discussion below), the actual leakage matrix is not symmetric and the measured modal power density distribution is a steep function of degree. Therefore, these observationally dependent systematic effects deform the power density distribution in the ridges, and hence, systematically affect the frequency splitting measurements.

The leakage matrix, as defined by Equation (3.12), can be estimated numerically once the spatial window, $W_s(\theta, \phi)$, is known. The main contributors to the spatial window function are the line-of-sight projection factor, $\cos \rho$, the spatial apodization, the image rebinning, and the solar geometry (i.e. P_{eff} , B_o , and the finite earth-sun distance projection) that defines the visible part of the solar sphere. From a practical standpoint, the same numerical efficiency related remarks apply to the computation of the leakage matrix elements, as was the case for the spatial decomposition (see Section 3.3). Hence, we have estimated leakage matrix elements by decomposing simulated images of the real part of spherical harmonic functions. These simulated images included the line-of-sight projection factor and the solar geometry parametrization (including the finite earth-sun distance projection effect); they were then decomposed using similar apodization and rebinning parameters as those used for the decomposition of the dopplergrams. Examples of some selected leakage matrix elements are shown in Figures 4.15 to 4.17.

Since the geometry of the simulated images is perfectly known, the computed leakage matrix is indeed symmetric. But, in practice, the image geometry is not perfectly known

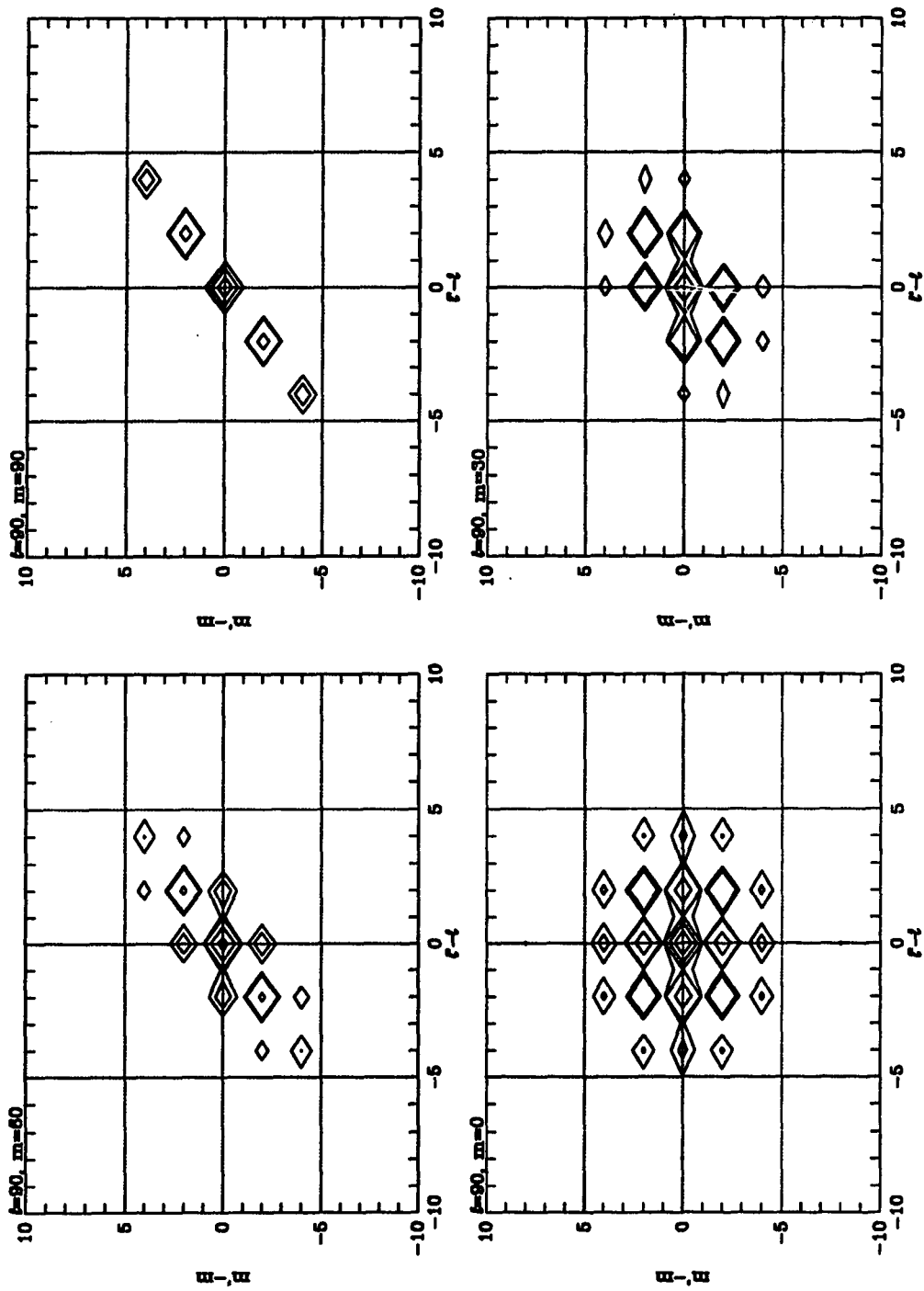


Figure 4.15: Leakage matrix for $\ell = 90$, namely $|\langle \ell, m | \ell', m' \rangle|$ for $|\ell - \ell'| \leq 10$ and $|m - m'| \leq 10$ for selected values of m .

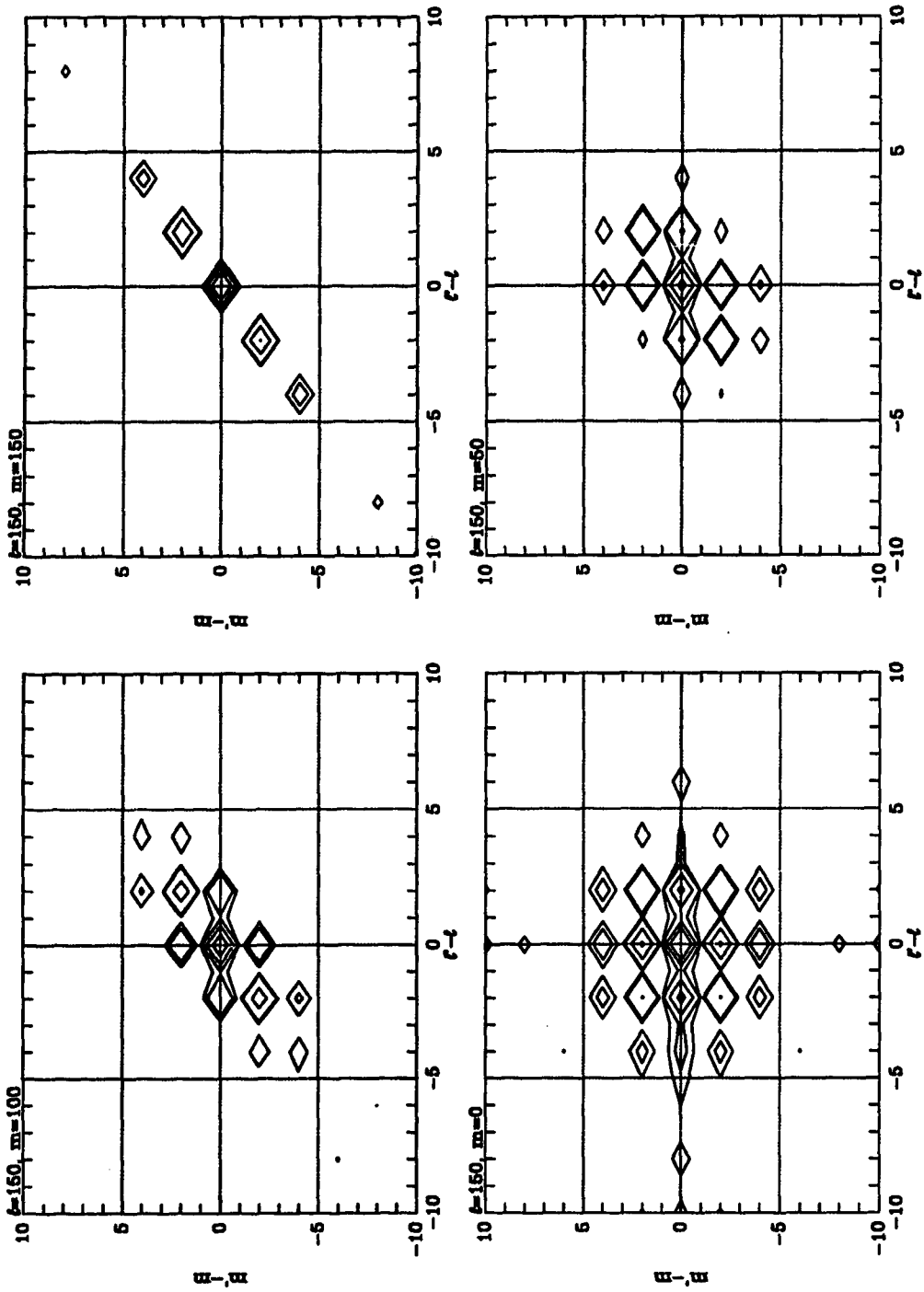


Figure 4.16: Leakage matrix for $\ell = 150$, namely $|\langle \ell, m | \ell', m' \rangle|$ for $|\ell - \ell'| \leq 10$ and $|m - m'| \leq 10$ for selected values of m .

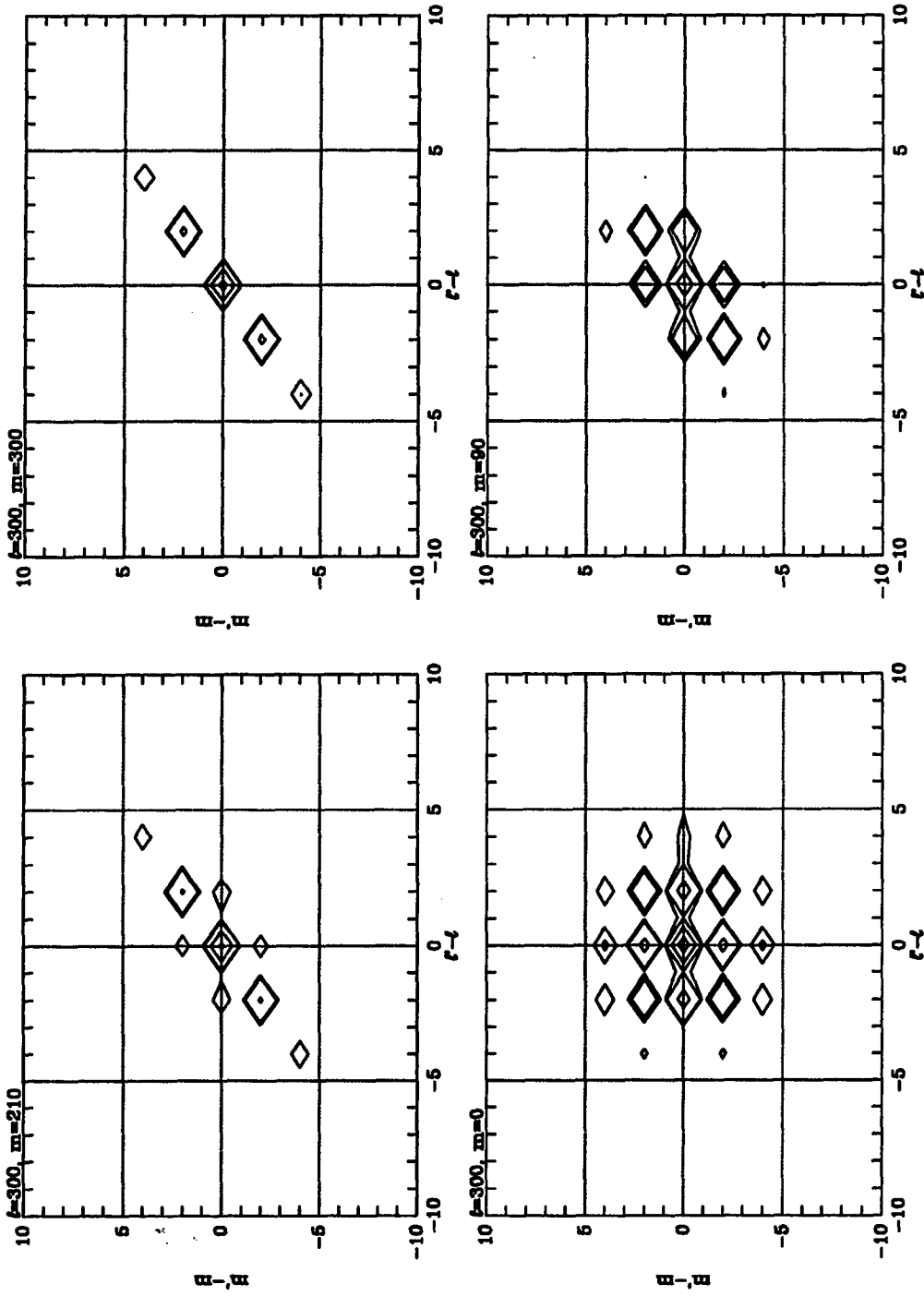


Figure 4.17: Leakage matrix for $\ell = 300$, namely $|\langle \ell, m | \ell', m' \rangle|$ for $|\ell - \ell'| \leq 10$ and $|m - m'| \leq 10$ for selected values of m .

and some error in the measured image geometry that is used in the spatial decomposition will always be present, hence will cause a perturbation of the leakage matrix. Indeed, an error in the image geometry corresponds to actually using spatial masks with an erroneous geometry. Hence, in terms of leakage (c.f. Equation (3.10)), the computed $\tilde{C}_{\ell,m}$ will be related to the $C_{\ell,m}$ through what we shall refer to as the “actual” leakage matrix, a matrix that is slightly different from the leakage matrix that would have been obtained if the “correct” image geometry had been used. Once the geometry of the image and the geometry of the spatial masks are different, the symmetry relation is broken and the leakage matrix cannot be expected to be symmetric any more. More specifically, a minor error in the image size introduces a significant asymmetry in the leakage matrix, as illustrated in Figures 4.18 to 4.20, where perturbed leakage matrix elements are presented. These perturbed leakage matrix elements were computed by decomposing simulated images and using for the decomposition an image size 0.5% larger than the actual simulated image size.

Note that the leakage matrix asymmetry remains small at low- ℓ while it becomes significant at high- ℓ . This ℓ dependency can be easily understood, by noticing that the spherical harmonic decomposition can be approximated by a two dimensional spatial FFT. Thus, an image size error is equivalent to an error in the spatial sampling interval, which in turn translates to an error in the spatial frequency interval. Hence, for a given relative image size error, the absolute error remains small at low spatial frequencies (i.e. low- ℓ) but becomes significant at larger spatial frequencies (i.e. high- ℓ).

A second factor that introduces an asymmetry in the leakage matrix, and hence in the ridge power density distribution, is the observed modal power distribution as a function of degree, ℓ , and azimuthal order, m . Indeed, the observed modal power density distribution is modulated by the total point spread function (PSF) (i.e. seeing and instrumental), hence, the observed distribution corresponds to the convolution of the actual modal power

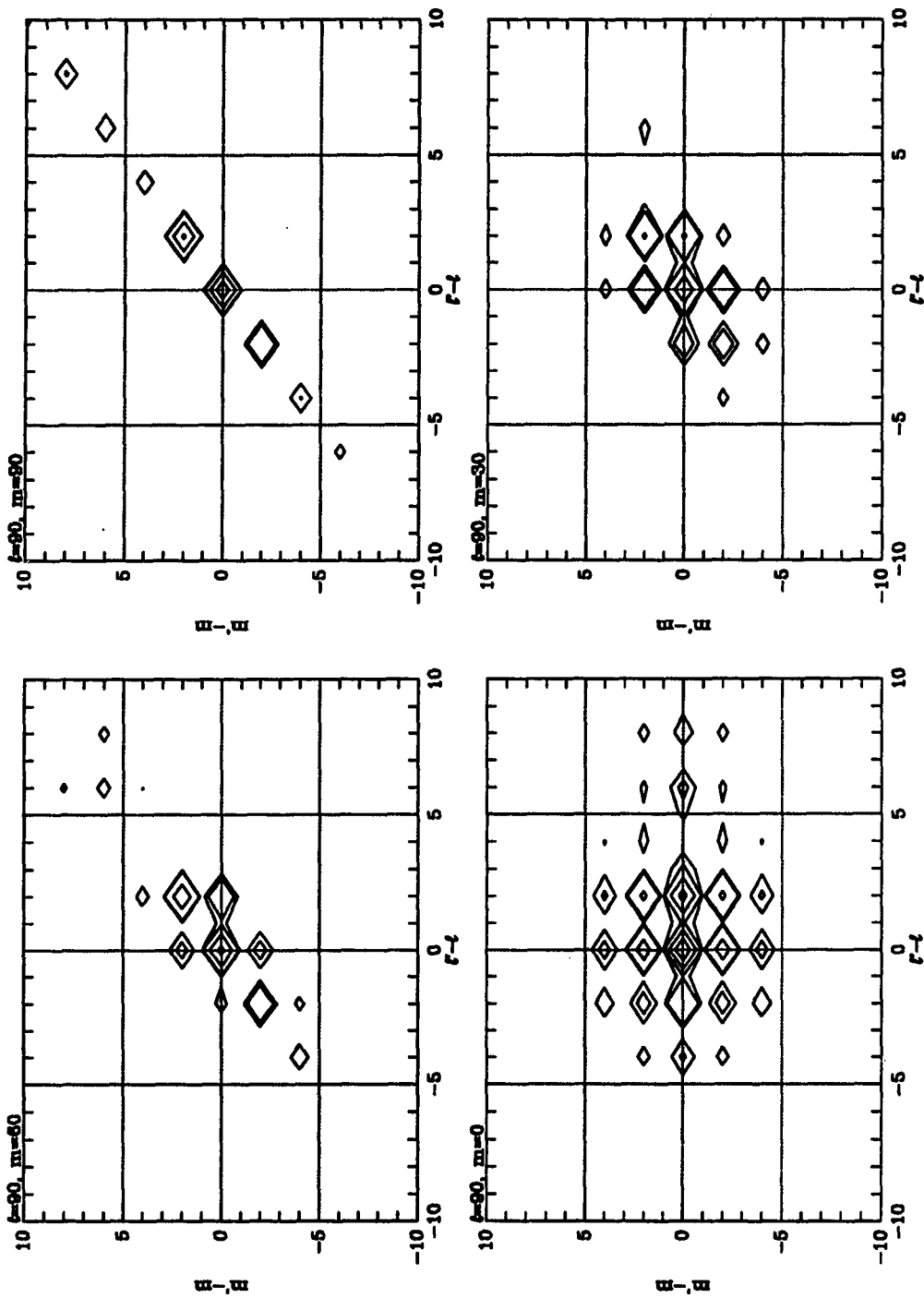


Figure 4.18: Perturbed leakage matrix for $\ell = 90$. By contrast to Figure 4.15 the simulated image was decomposed with a radius 0.5% larger than the simulated image radius.

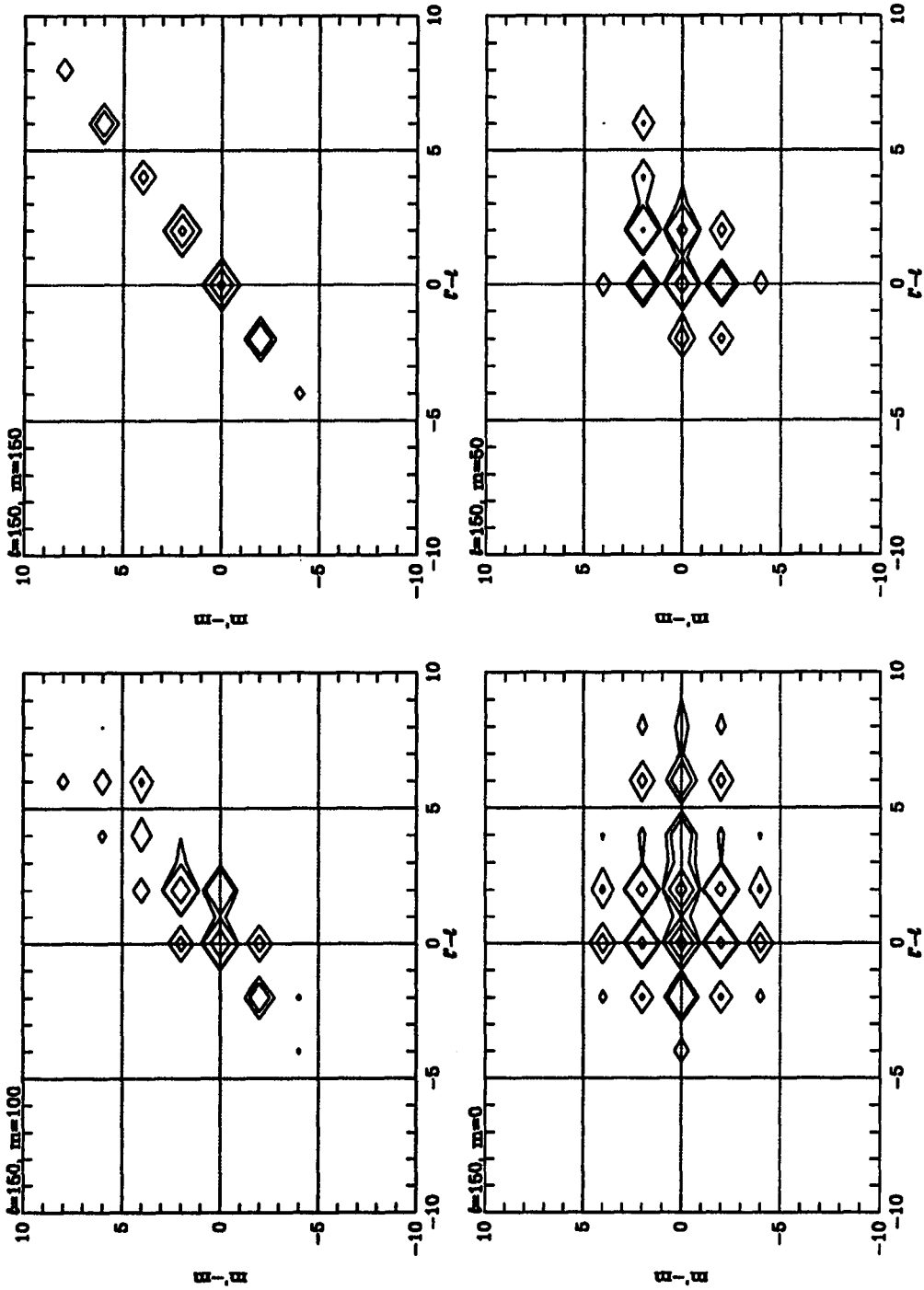


Figure 4.19: Perturbed leakage matrix for $l = 150$. By contrast to Figure 4.16 the simulated image was decomposed with a radius 0.5% larger than the simulated image radius.

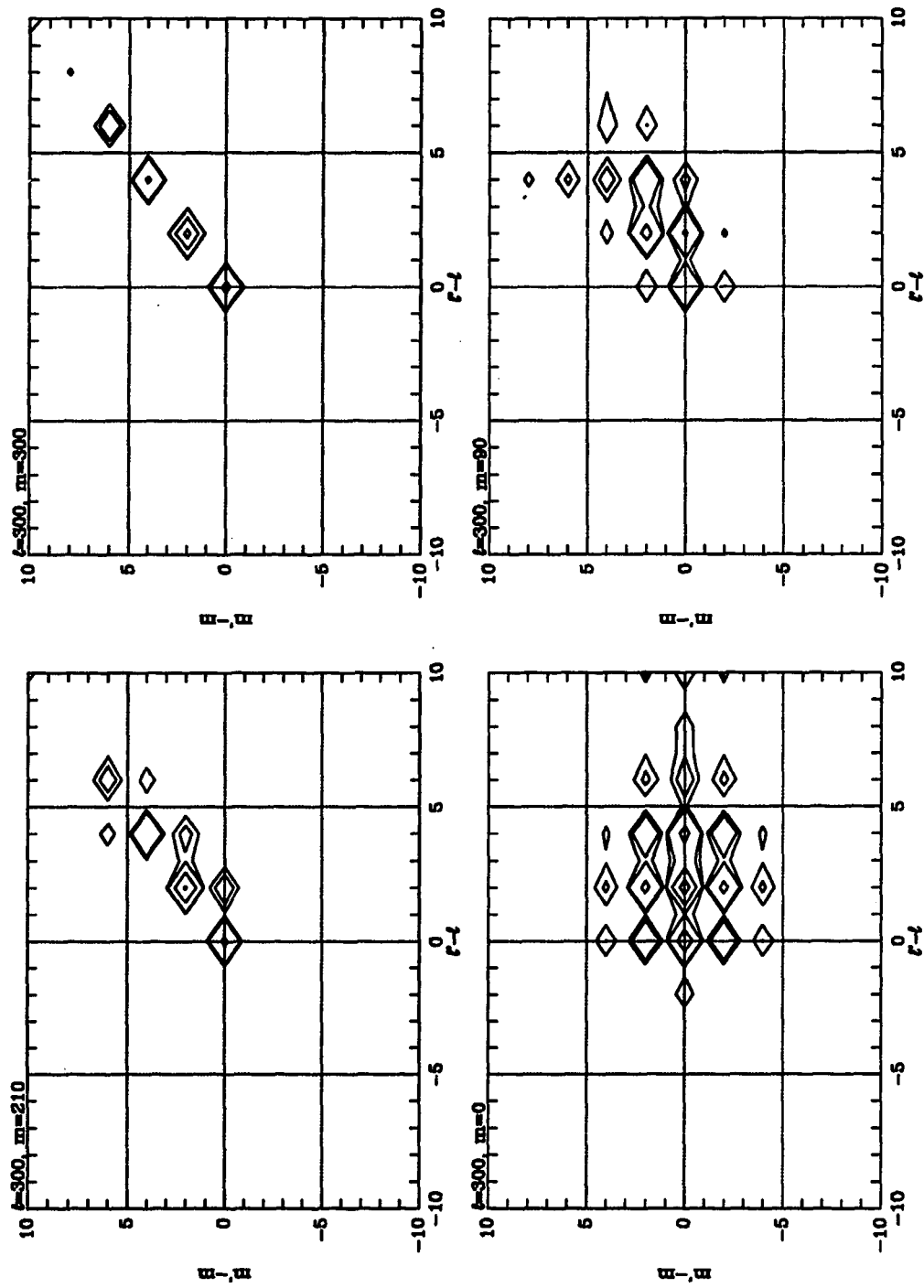


Figure 4.20: Perturbed leakage matrix for $\ell = 300$. By contrast to Figure 4.17 the simulated image was decomposed with a radius 0.5% larger than the simulated image radius.

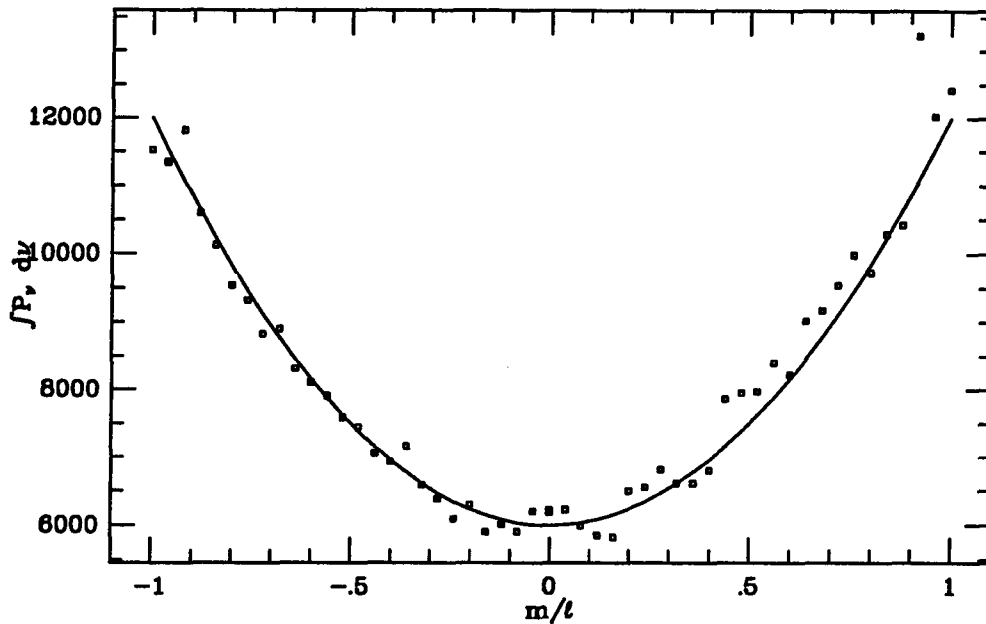


Figure 4.21: Total power in the 5-minute band as a function of m/ℓ for $\ell = 50$. The function $C^{ste}(1 + (m/\ell)^2)$ is plotted as the solid line.

distribution by the total PSF. In terms of spatial frequencies, since the total modulation transfer function (MTF) (i.e. the Fourier transform of the PSF) decreases with increasing spatial frequency (c.f. seeing and finite objective aperture, see also further discussion in Section 5.2.3), the measured power distribution will be a steeper function of spatial frequency than the “actual” one. Moreover, the rebinning over an equispaced grid in longitude and co-latitude of an apodized, line-of-sight velocity measurement³ will introduce an instrumental contribution to the distribution of the observed power density with azimuthal order, m , as illustrated in Figure 4.21 where the total power between 1.5 and 4.5 mHz is plotted as a function of m for $\ell = 50$ and can be reasonably fitted to a parabolic function of the ratio m/ℓ .

In order to confirm and assess the magnitude of such systematic effects, we have attempted to model the frequency shift perturbations associated with the ridge power density distri-

³Recall the the line-of-sight projection factor can be view as a *de-facto* apodization

bution asymmetries.

Analytical Simulation of Systematics

Firstly, we have estimated the systematic effects introduced by mode blending from an approximate analytic expression. Let us consider that the ridge frequency is the weighted mean of the individual modes that have leaked into the target mode, weighted by the leakage matrix and by the modal amplitudes. Namely, that the ridge centroid, $\tilde{\nu}$, is given by

$$\tilde{\nu}_{n,\ell,m} = \frac{\sum_{\ell',m'} \langle \ell', m' | \ell, m \rangle |A_{n,\ell',m'} \nu_{n,\ell',m'}|}{\sum_{\ell',m'} \langle \ell', m' | \ell, m \rangle |A_{n,\ell',m'}|} \quad (4.3)$$

where $\langle \ell', m' | \ell, m \rangle$ is the leakage matrix as defined by Equation (3.10), and $A_{n,\ell',m'}$ the modal amplitude.

The systematic error on the frequency splitting measurement due to the displacement of the ridge centroid frequency with respect to the target mode frequency is then simply given by

$$\delta(\Delta\nu) = \tilde{\nu}_{n,\ell,m} - \nu_{n,\ell,m} \quad (4.4)$$

In order to estimate Equation (4.4) from Equation (4.3), let us introduce the following approximations

$$\nu_{n,\ell',m'} \approx \nu_{n,\ell,m} + \frac{\partial\nu}{\partial\ell} \Delta\ell + \frac{\partial\nu}{\partial m} \Delta m \quad (4.5)$$

$$A_{n,\ell',m'} \approx A_{n,\ell,m} \left(1 + \frac{\partial \log A}{\partial \ell} \Delta\ell + \frac{\partial \log A}{\partial m} \Delta m \right) \quad (4.6)$$

where $\Delta\ell = \ell' - \ell$ and $\Delta m = m' - m$. For the leakage matrix, we have used a simple Gaussian representation, namely

$$\langle \ell', m' | \ell, m \rangle = \exp\left(-\frac{(x - \epsilon \ell \sec\alpha)^2}{2s_x^2} - \frac{y^2}{2s_y^2}\right) \quad (4.7)$$

where

$$x = +\Delta\ell \cos \alpha + \Delta m \sin \alpha \quad (4.8)$$

$$y = -\Delta\ell \sin \alpha + \Delta m \cos \alpha \quad (4.9)$$

$$\alpha = \alpha(m, \ell) \approx \frac{\pi}{4} \left(\frac{m}{\ell} \right) \quad (4.10)$$

$$s_x = s_x(m, \ell) \approx s_{x,0} \quad (4.11)$$

$$s_y = s_y(m, \ell) \approx s_{y,0} \left(1 - s_{y,1} \left(\frac{m}{\ell} \right)^2 \right) \quad (4.12)$$

The term $\epsilon \ell \sec \alpha$ has been introduced to model the leakage matrix asymmetry due to a minor image scale error on the order of ϵR_\odot , while the functions $\alpha(m, \ell)$, $s_x(m, \ell)$ and $s_y(m, \ell)$ have been approximated by simple analytic expressions and adjusted to represent the *overall* behavior of the leakage matrix.

Hence, after replacing the summations over $\Delta\ell$ and Δm by integrations, Equation (4.4) can be rewritten, after some algebra, as

$$\begin{aligned} \delta(\Delta\nu) = -\frac{1}{\mathcal{D}} [& \epsilon\ell \left(\frac{\partial\nu}{\partial\ell} + \frac{\partial\nu}{\partial m} \tan \alpha \right) \\ & + Q_\ell \frac{\partial\nu}{\partial\ell} \sigma_1 + Q_m \frac{\partial\nu}{\partial m} \sigma_2 + \left(Q_\ell \frac{\partial\nu}{\partial m} + Q_m \frac{\partial\nu}{\partial\ell} \right) \sigma_0 \\ & + \epsilon^2 \ell^2 \left(Q_\ell \frac{\partial\nu}{\partial\ell} + Q_m \frac{\partial\nu}{\partial m} \tan^2 \alpha + \left(Q_\ell \frac{\partial\nu}{\partial m} + Q_m \frac{\partial\nu}{\partial\ell} \right) \tan \alpha \right)] \end{aligned} \quad (4.13)$$

where

$$\mathcal{D} = 1 + \epsilon\ell(Q_\ell + Q_m \tan \alpha) \quad (4.14)$$

and where $Q_\ell = \partial \log A / \partial \ell$, $Q_m = \partial \log A / \partial m$, $\partial\nu/\partial\ell$ and $\partial\nu/\partial m$ are directly measurable quantities, and

$$\sigma_0 = \sqrt{2} s_x \frac{1 - \beta^3}{\beta} \sin \alpha \cos \alpha \quad (4.15)$$

$$\sigma_1 = \sqrt{2} s_x \left(\frac{1}{\beta} \cos^2 \alpha + \beta^2 \sin^2 \alpha \right) \quad (4.16)$$

$$\sigma_2 = \sqrt{2} s_x \left(\frac{1}{\beta} \sin^2 \alpha + \beta^2 \cos^2 \alpha \right) \quad (4.17)$$

where $\beta = s_y/s_x$.

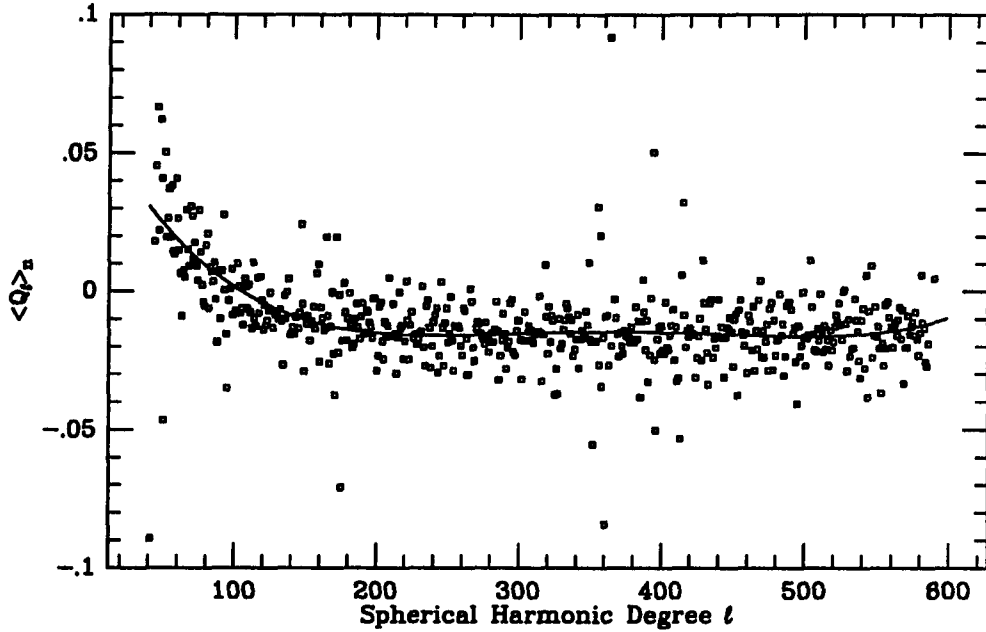


Figure 4.22: $\langle Q_l \rangle_n$ as a function of spherical harmonic degree l . The solid line represents the fourth order polynomial fitted to the raw values.

Since the cross-correlation method computes n -averaged splittings, a weighted n -average of Equation (4.13) must be performed, using the respective values of Q_l , $\partial\nu/\partial l$, and $\partial\nu/\partial m$ for each ridge. In order to assess the dominant terms in Equation (4.13) we have initially n -averaged the quantities Q_l , and $\partial\nu/\partial l$ themselves rather than $\delta(\Delta\nu)$. In each case, the n -averaging was performed using a frequency dependent weighting, estimated from a Lorentzian centered at 3.0 mHz with a FWHM of 3.0 mHz, in order to represent the power distribution in the 5-min band. Figures 4.22 and 4.23 present these n -averaged quantities, namely $\langle Q_l \rangle_n$ and $\langle \partial\nu/\partial l \rangle_n$, estimated from the low resolution spectral frequency and amplitude measurements (see Section 5.2), as well as the fourth order polynomials fitted to these quantities, and used in the simulations.

If we also introduce the Legendre polynomial parametrization of the frequency splittings, namely $\nu_{n,\ell,m} = \bar{\nu}_{n,\ell} + L \sum a_i P_i(-\frac{m}{L})$ we can simply write

$$\frac{\partial\nu}{\partial m} = - \sum a_i P_i'(-\frac{m}{L}) \quad (4.18)$$

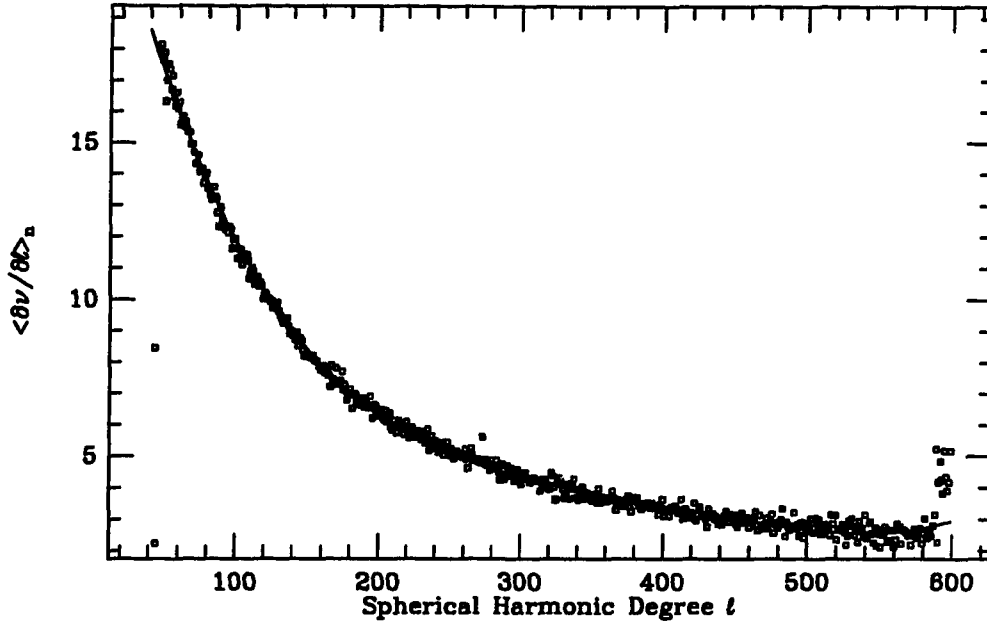


Figure 4.23: $\langle \partial \nu / \partial \ell \rangle_n$ as a function of spherical harmonic degree ℓ . The solid line represents the fourth order polynomial fitted to the raw values.

where

$$P'_i(x) = \frac{dP_i}{dx} \quad (4.19)$$

Hence, we used for these simulations an even-indexed Legendre expansion to evaluate $\partial \nu / \partial m$ from Equation (4.18).

Finally, the dependency with m of the amplitude distribution was simply parametrized as $A^2(m) = A^2(0)(1 + \gamma(m/\ell)^2)$, and γ estimated empirically to be ~ 1 (see Figure 4.21), leading to a straightforward expression for Q_m , namely

$$Q_m = \frac{1}{\ell} \left(\frac{\gamma m/\ell}{1 + \gamma(m/\ell)^2} \right) \quad (4.20)$$

First note that $\mathcal{D} \approx 1$, since $\epsilon \simeq 10^{-3}$, $\ell \simeq 10^3$ and $Q_\ell \simeq 10^{-3}$, while $Q_m \simeq 1/\ell$, second, since $|\alpha| \leq \pi/4$, we have $\sqrt{2}/2 \leq \cos \alpha$, $|\sin \alpha| \leq \sqrt{2}/2$ and $|\tan \alpha| \leq +1$.

In order to estimate the magnitude of the dominant terms in Equation (4.13), recall that the frequency splitting itself can be parametrized as $\Delta \nu = L \sum a_i P_i(-\frac{m}{\ell})$, with coefficients

a_i fairly constant with ℓ , while $L \simeq \ell$ at large ℓ ; hence, it is the quantity $\delta(\Delta\nu)/L$ that should be compared to the a_i

Since $\epsilon\ell \simeq 1$ at ℓ large enough, we shall rewrite Equation (4.13) as

$$\begin{aligned}
\frac{\delta(\Delta\nu)}{L} \approx & \epsilon \frac{\partial\nu}{\partial\ell} (1 + \epsilon\ell Q_\ell) \\
& + \epsilon \frac{\partial\nu}{\partial m} \tan\alpha (1 + \epsilon\ell(Q_\ell + Q_m \tan\alpha)) \\
& + \frac{1}{\ell} \left(Q_\ell \frac{\partial\nu}{\partial\ell} \sigma_1 + Q_m \frac{\partial\nu}{\partial m} \sigma_2 + (Q_\ell \frac{\partial\nu}{\partial m} + Q_m \frac{\partial\nu}{\partial\ell}) \sigma_0 \right) \\
& + \epsilon \frac{\partial\nu}{\partial\ell} \tan\alpha \epsilon\ell Q_m
\end{aligned} \tag{4.21}$$

Figures 4.24 and 4.25 present separately each term on the right-hand-side of Equation (4.21) as grouped above, and as a function of m/ℓ , for selected values of ℓ and for respectively $\beta = 1 - 0.75(m/\ell)^2$ and $\beta = 1 - 0.5(m/\ell)^2$. These curves have been computed with $s_x = 2$, $\gamma = 1$, $a_1 = 403$, $a_3 = 21$, $a_5 = -4$ and the n -averaged values of Q_i and $\partial\nu/\partial\ell$ presented Figures 4.22 and 4.23.

Firstly, notice that the first term on the right-hand-side (RHS) of Equation (4.21) contributes to a constant offset with m , for a given value of ℓ , and could have been ignored in the frequency splitting context. But its constancy results directly from the $\epsilon\ell \sec\alpha$ nature of our parametrization of the asymmetry of the perturbed leakage matrix (c.f. Equation (4.7)). Since in all likelihood, the actual perturbed leakage matrix will not display such regular behavior in its asymmetry, the departure from this regularity will introduce an m dependency, modulated by $\epsilon\partial\nu/\partial\ell$. Since the quantity $\epsilon\partial\nu/\partial\ell$ is significant when compared to the a_i , mostly at low- and intermediate- ℓ , an m -modulated contribution of this term, absent in Equation (4.13), is most likely to be present and significant.

The second term on the RHS of Equation (4.21) is, at first order, an ℓ independent term. Indeed, only Q_i and Q_m are the ℓ -dependent terms, and their contribution, scaled by ℓ remains small compared to 1. Hence the m -modulation of the second term is dominated

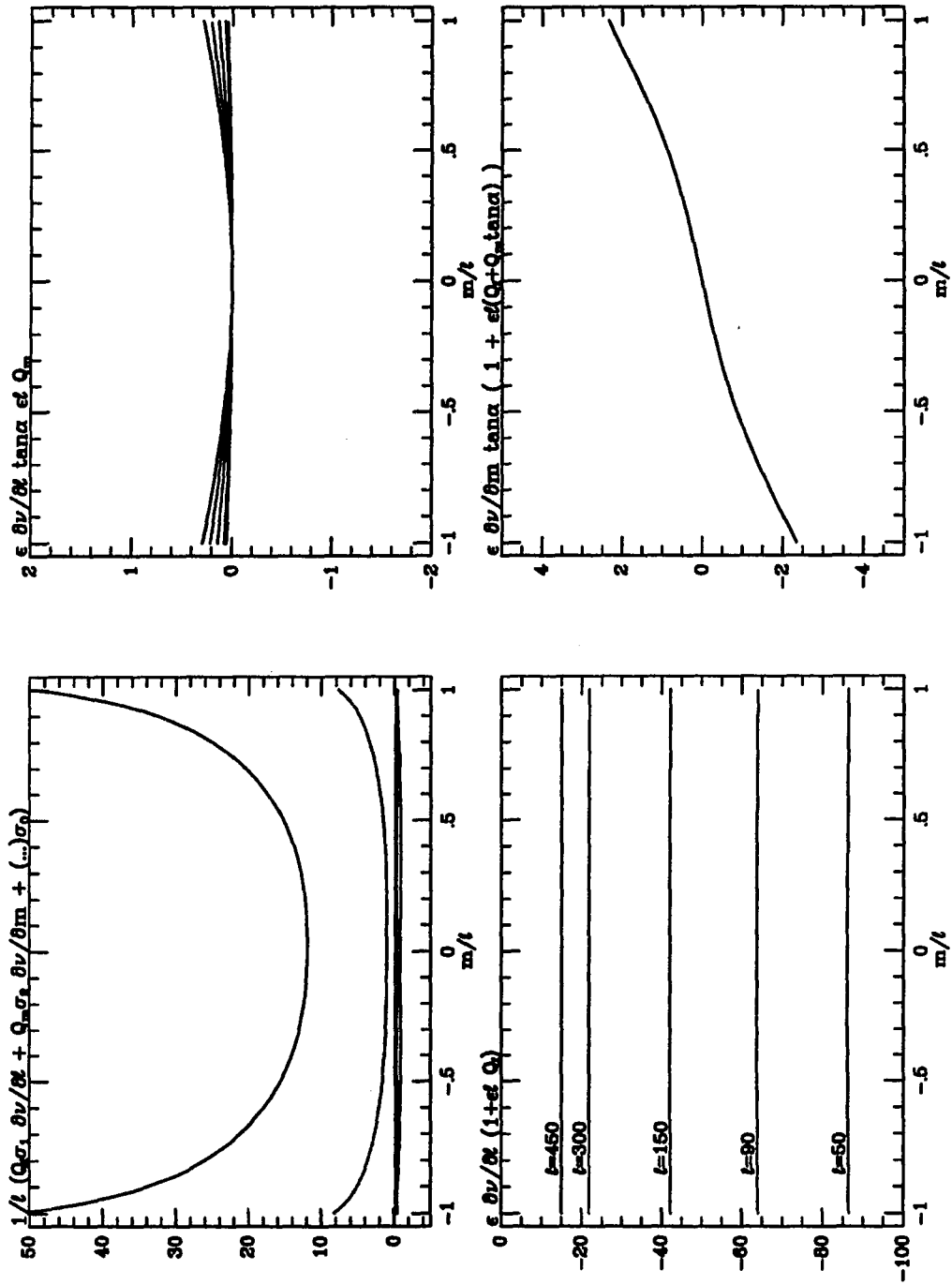


Figure 4.24: Individual terms on the right-hand-side of Equation (4.21) as a function of m/l , for $\beta = 1 - 0.75(m/l)^2$ (see text for further details).

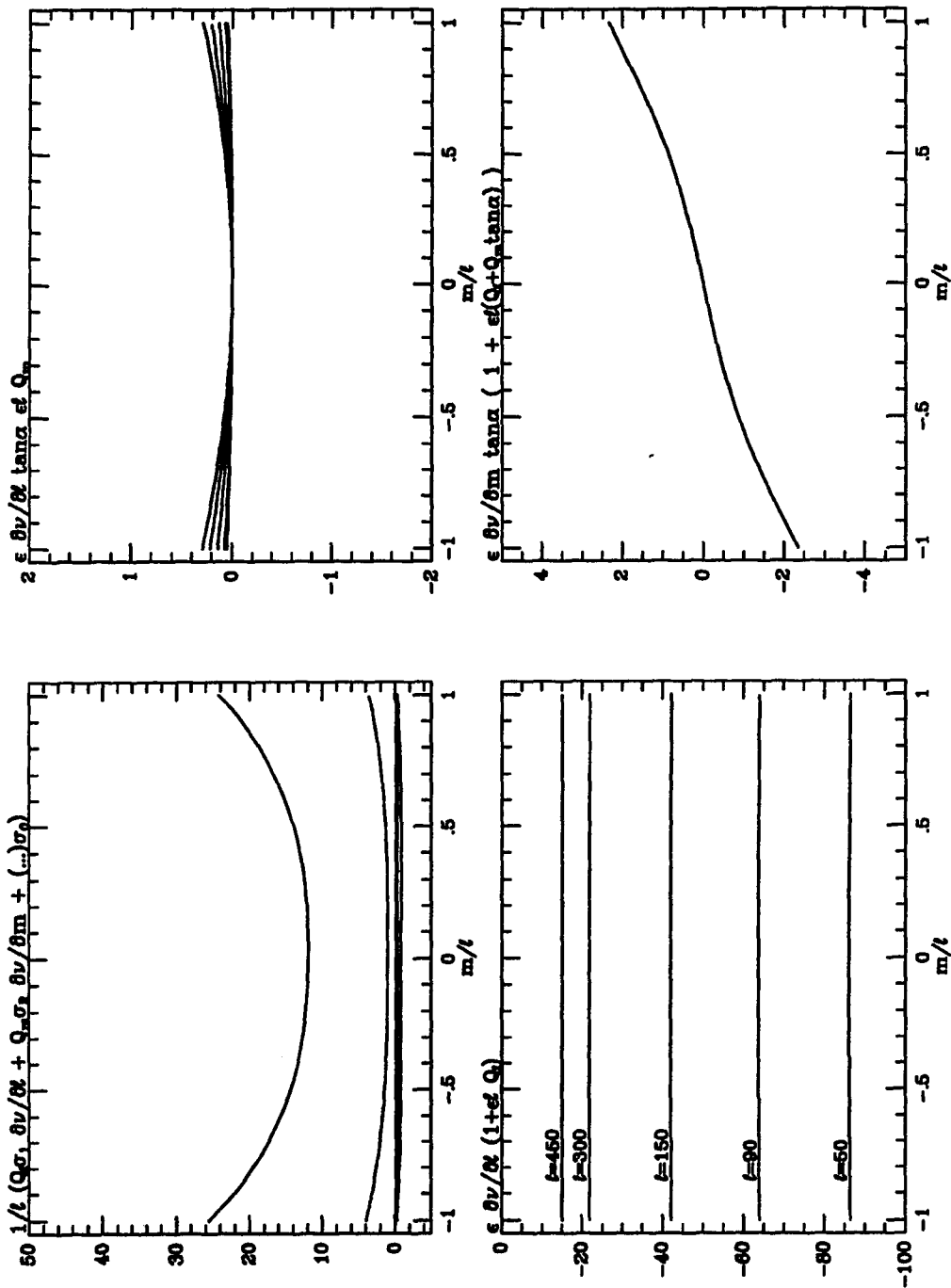


Figure 4.25: Individual terms on the right-hand-side of Equation (4.21) as a function of m/l , for $\beta = 1 - 0.5(m/l)^2$ (see text for further details).

by the m -dependency of $\partial\nu/\partial m$ and α , while its amplitude is dominated by ϵ , the image scale error.

The third term on the RHS of Equation (4.21) results only from amplitude distribution asymmetries with ℓ and m , and would still be present even for a perfectly symmetric leakage matrix. Its m -modulation is directly related to the m dependency used for the functions α , s_x and s_y , while its amplitude variation with ℓ is dominated by $\partial\nu/\partial\ell$. Since the slope of the ridge is an order of magnitude larger than the frequency splitting slope, this term will be dominant for low- and intermediate-degrees. Its actual m -modulation should be expected to be different from the simple curves shown here, since the actual m -dependency of the width and principal axis orientation of the actual leakage matrix is expected to be more complex than our simple-minded modelization.

Finally, the last term on the RHS of Equation (4.21), included for completeness, is a second order term in ϵ^2 , since $lQ_m \approx 1$. Nonetheless, since the slope of the ridge is large, as mentioned above, this second order contribution remains non-trivial at low and intermediate degrees.

In conclusion, while we have used an oversimplified approach to model the leakage matrix⁴, its asymmetries (by considering only a well behaved minor image scale error), as well as the asymmetries in the amplitude distribution, we have derived an analytic expression to estimate the frequency splitting perturbation associated with mode blending. This expression indicates that asymmetries in the leakage matrix combined to the slope of the ridges, with respect to ℓ as well as to m , contribute significantly to this perturbation, but it also indicates that the uneven distribution of modal amplitude with ℓ and m contributes to this perturbation as well.

⁴For instance we have completely ignored the parity rules that determine which are the significant elements in the leakage matrix

Numerical Simulation of Systematics

Our second approach to estimate the systematics introduced by mode blending on the frequency splitting measurements, has been based on a direct numerical estimation of Equation (4.3). In order to demonstrate that indeed, the weighted average is a good representation of the actual measured splitting by the traditional iterative cross-correlation procedure, we have also generated artificial low-resolution tesseral spectra, $\tilde{S}_{\ell,m}(\nu)$, computed from a weighted superposition of overlapping individual modes and analyzed them for frequency splittings with the iterative cross-correlation method.

Each simulated spectrum was computed from a superposition of sinc functions, centered around $\nu_{n,\ell',m'} = \bar{\nu}_{n,\ell'} + \Delta\nu_{\ell',m'}$, weighted by a numerically computed leakage matrix element and by an empirical modal amplitude distribution, function of n , ℓ and m , according to

$$\tilde{S}_{\ell,m}(\nu) = \sum_{\ell',m'} |\langle \ell', m' | \ell, m \rangle| \sum_n A_{n,\ell',m'} \left(\frac{\sin \xi}{\xi} \right) \quad (4.22)$$

where

$$\xi = 2\pi \frac{\nu - \nu_{n,\ell',m'}}{w_{n,\ell'}} \quad (4.23)$$

and $A_{n,\ell',m'}$ given by Equation (4.6)

For both methods, namely the direct weighted average and the artificial tesseral spectra generation, leakage matrix elements were computed by decomposing simulated images of the real part of spherical harmonic functions, multiplied by a line-of-sight factor. The simulated images were generated using a realistic solar geometry (i.e. $P = 12$ and $B_o = 3$, and a finite sun-earth distance), apodized, rebinned and decomposed with parameters similar to those used in the decomposition of the actual solar dopplergrams. The modulus of the decomposition coefficients for $\Delta\ell = \pm 10$ and $\Delta m = \pm 10$ around the simulated image (ℓ, m) value were computed and used as leakage matrix elements. Since the forward computation of a high-degree spherical harmonic function is a computationally expensive

task, only a subset of tesseral simulated images were generated and decomposed (i.e. typically some 10–15 m values, equispaced in m , at a given ℓ), and a linear interpolation in m/ℓ was performed to estimate the missing elements. A set of perturbed leakage matrix elements were computed using for the decomposition an image size 0.5% larger than the actual size of the simulated images.

The unperturbed frequency splittings, $\Delta\nu_{\ell,m'}$, were themselves simulated using an even-indexed Legendre polynomial expansion, with $a_1 = 403$, $a_3 = 21$ and $a_5 = -4$ (nHz, synodic), and 5 n values were included in the simulation, selected as to represent the 5 ridges in the 5-minute band with the largest amplitude.

Figure 4.26 presents scaled frequency shifts, $\delta(\Delta\nu)/L - \omega(-m/L)$, with $\omega = 420$ nHz, obtained from perturbed and unperturbed leakage matrices, for $\ell = 90, 150$ and 300 , based on both numerical methods. The solid line represents the results of the weighted average procedure, while the symbols represent the frequency shifts obtained at the last iteration step of the cross-correlation based analysis of the simulated spectra. The dashed line represents the frequency splittings that should have been measured in absence of systematics. Since a constant offset is irrelevant in the frequency splitting context, the curves were shifted to present a null splitting at $m = 0$, allowing a better comparison of the ridge shape deformation.

Figure 4.26 clearly indicates that in most cases the weighted average procedure agrees with the simulated spectrum procedure and that indeed the cross-correlation analysis measures the ridge centroid frequency shift. It also indicates that a small error in the image size introduces through the leakage matrix asymmetry a significant deformation of the measured frequency shifts.

The numerical simulations also present a “fine structure”, that can be traced to secondary asymmetries in the leakage matrix at large $\Delta\ell$. Indeed, since the slope of the ridge,

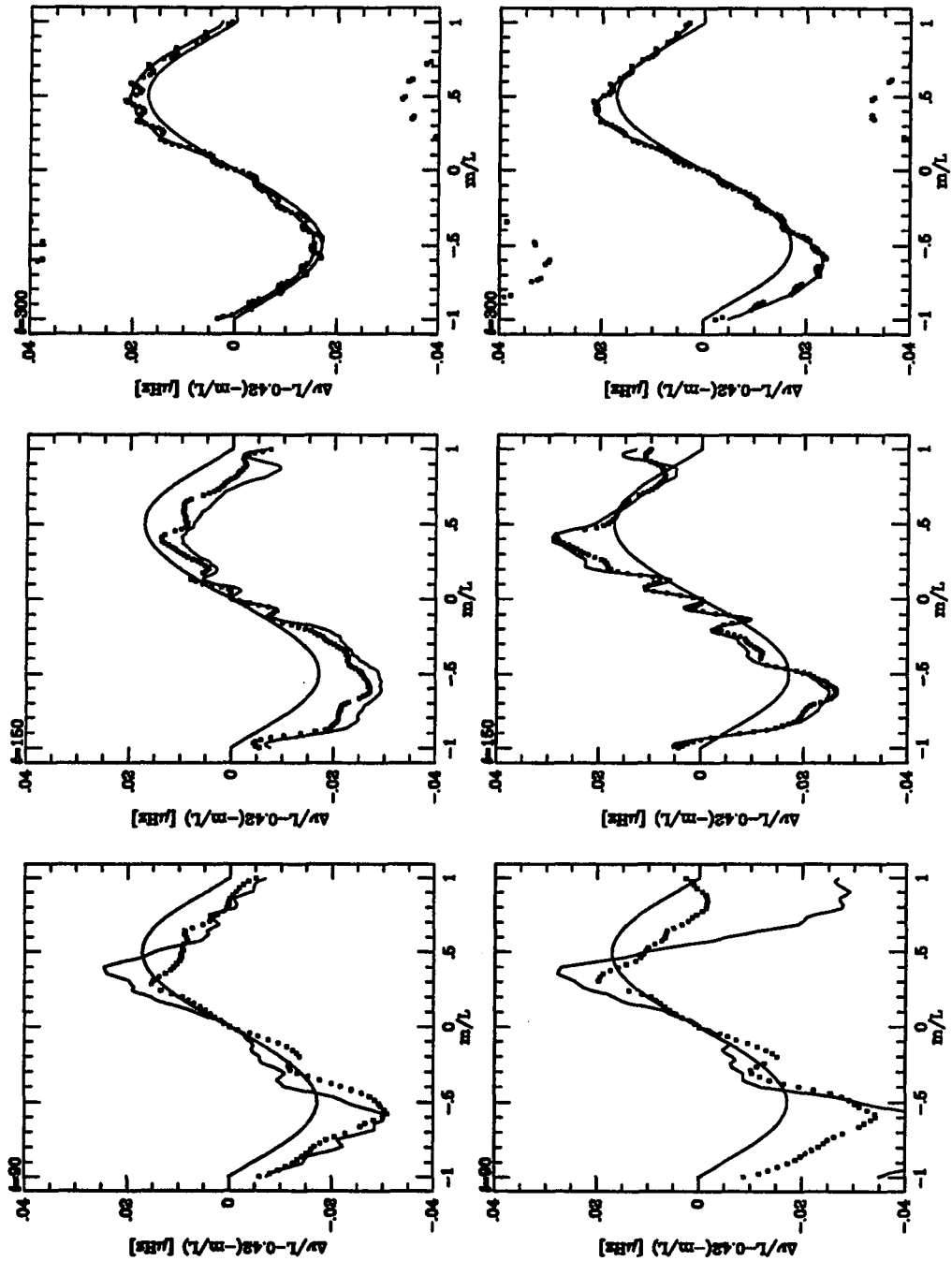


Figure 4.26: Numerical simulations for $\ell = 90, 150$ and 300 . Top panels: results using the correct image size to estimate the leakage matrix elements; bottom panels: results using an overestimated image size by 0.5% . The solid line represents the results from the weighted average procedure, while the symbols represent the frequency shifts obtained at the last iteration step of the cross-correlation based analysis of the simulated spectra. The dashed line represents the frequency splittings that should have been measured in absence of systematics.

$\partial\nu/\partial\ell$, is large compared to the frequency splitting, $\Delta\nu$, a significant asymmetry of a small leakage matrix element at large $\Delta\ell$ will introduce a non-negligible effect. This effect is especially significant at low and intermediate ℓ , where the slope of the ridge is large. The asymmetries in these small leakage matrix elements are most probably associated to some second order numerical noise associated to the simulated images or their decomposition.

Furthermore, Figure 4.26 also indicates than even in the absence of a image size error, the decomposition procedure introduces asymmetries in the leakage matrix due to the non-zero value of the B_o angle, the finite sun-earth distance projection effect, the line-of-sight attenuation and the apodization combined to the image rebinning. Hence even for a uniform amplitude distribution with ℓ and m , and in the absence of image scale error, such asymmetries introduce, through the procedural details of the spatial decomposition, systematic shifts in the ridge centroid, as illustrated in Figure 4.27, where resulting deformations for uniform and non-uniform amplitude distribution, and for $P = B_o = 0$ as well as $P = 12, B_o = 3$ are presented.

As for the analytical simulations, the numerical simulations of frequency splitting perturbation resulting from mode blending confirm that besides a contribution associated with a minor image scale error, observational and procedural related asymmetries in the leakage matrix and the amplitude distribution do contribute significantly to the perturbation. Since for all practical cases there will be an amplitude attenuation associated to the instrumental MTF, and a residual asymmetry of the leakage matrix associated to the solar geometry, a non negligible perturbation of the frequency splitting will always be present when frequency splitting measurements are based on ridge centroid frequency shifts.

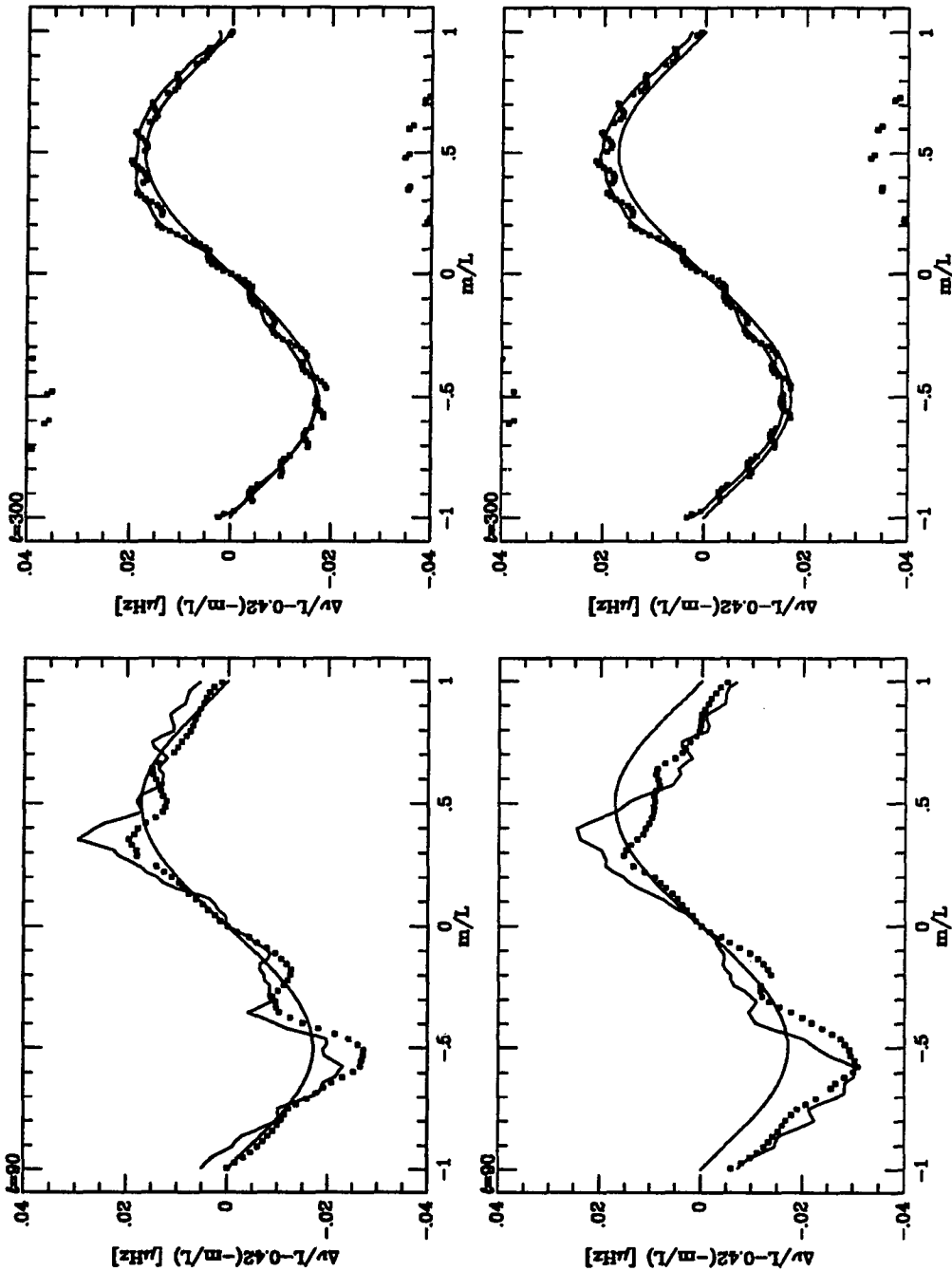


Figure 4.27: Numerical simulations for $\ell = 90$ and 300 . Top panels: results using the correct image size and $P = B_0 = 0$ to estimate the leakage matrix elements; bottom panel: results using correct image size but $P = 12$, and $B_0 = 3$. The solid line represents the results from weighted average procedure, while the symbols represent the frequency shifts obtained at the last iteration step of the cross-correlation based analysis of the simulated spectra. The dashed line represents the frequency splittings that should have been measured in absence of systematics.

Comparison of the Simulations

For a direct comparison with Figures 4.26 and 4.27, Figure 4.28 presents scaled frequency shifts estimated from the analytical simulations, while Figure 4.29 shows the corresponding actual values measured from the high-resolution, the smoothed high-resolution, and the low resolution spectra.

These simulations indicate that indeed asymmetries in the leakage matrix and in the modal amplitude distribution, (which in turn translates into an asymmetry in the ridge amplitude density distribution) introduce, when individual modes cannot be not resolved, systematic errors in the measurements of the frequency splittings on the same order of magnitude as the observed systematics. On the other hand, the comparison with actual measured values indicates that none of these simulations were able to represent in detail the observed systematics, assuming that at high degrees, the measured splittings should remain in close agreement with the surface differential rotation.

Since the detailed profile of the simulated perturbations varies significantly with the nature and with some of the numerical details of the simulations, those simulations have been unable to provide a definite estimate of the systematics introduced by mode blending as a function of degree, ℓ , or azimuthal order m . We can most probably attribute the discrepancies between the simulated and the observed perturbations to the simple-minded nature of some of the aspects of our simulations, namely our inability to simulate in detail the actual asymmetries of the "real" leakage matrix, and to model the asymmetries of the amplitude distribution as a function of ℓ and m .

Nevertheless, these simulations indicates that besides systematics introduced by the asymmetries associated to a minor image scale error, systematics related to the asymmetries associated to the solar geometry and to the amplitude density distribution should also be considered. Since the amplitude of the curvature of the frequency splittings as a function

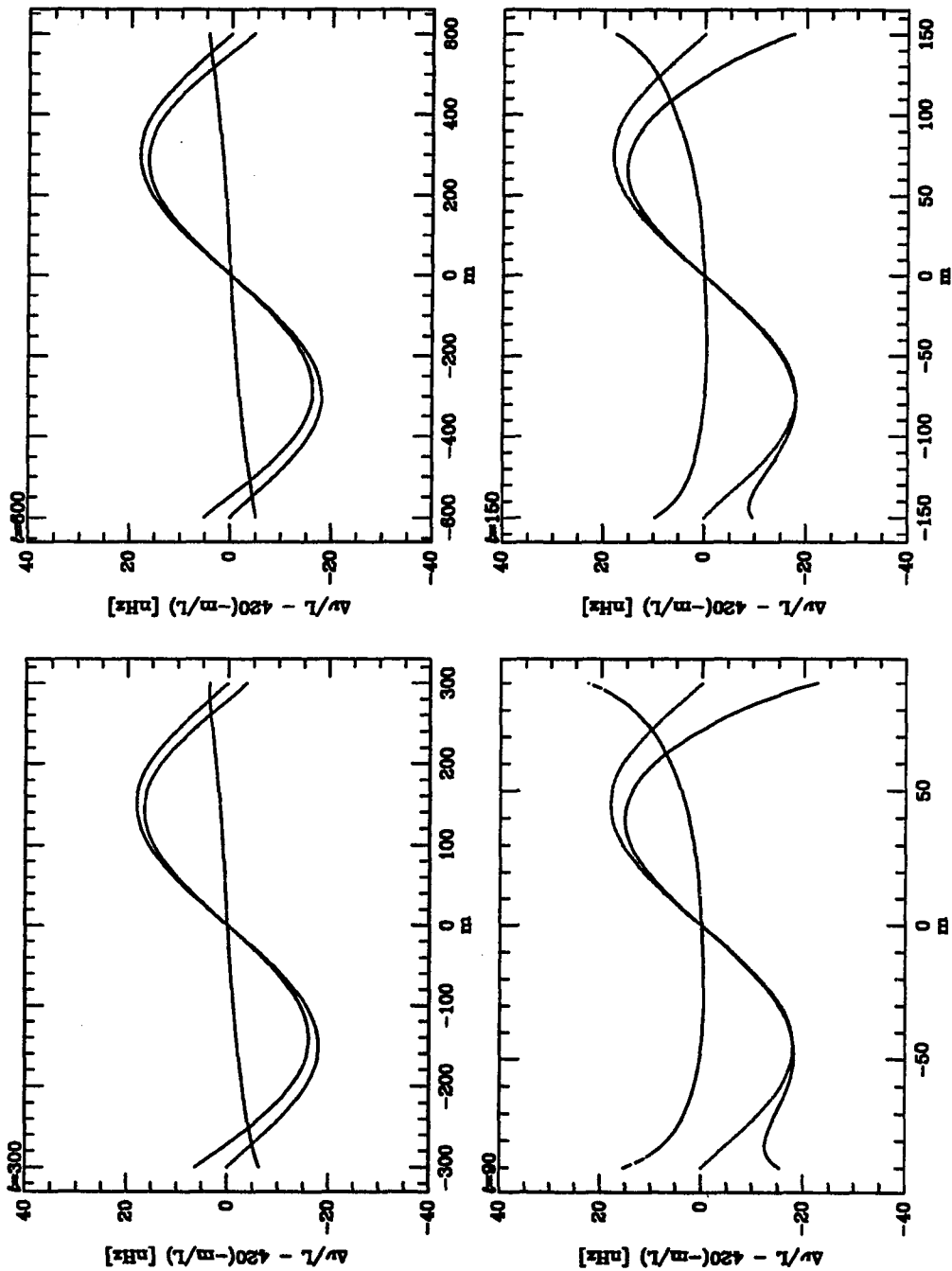


Figure 4.28: Analytical simulations for $\ell = 90, 150, 300,$ and 600 , estimated for an image scale error of 0.5%. The solid line represents the result from the simulation, the dashed line the represents the frequency splittings that should have been measured in absence of systematics, while the long dash line the amplitude of these systematics $\delta(\Delta\nu)/L$.

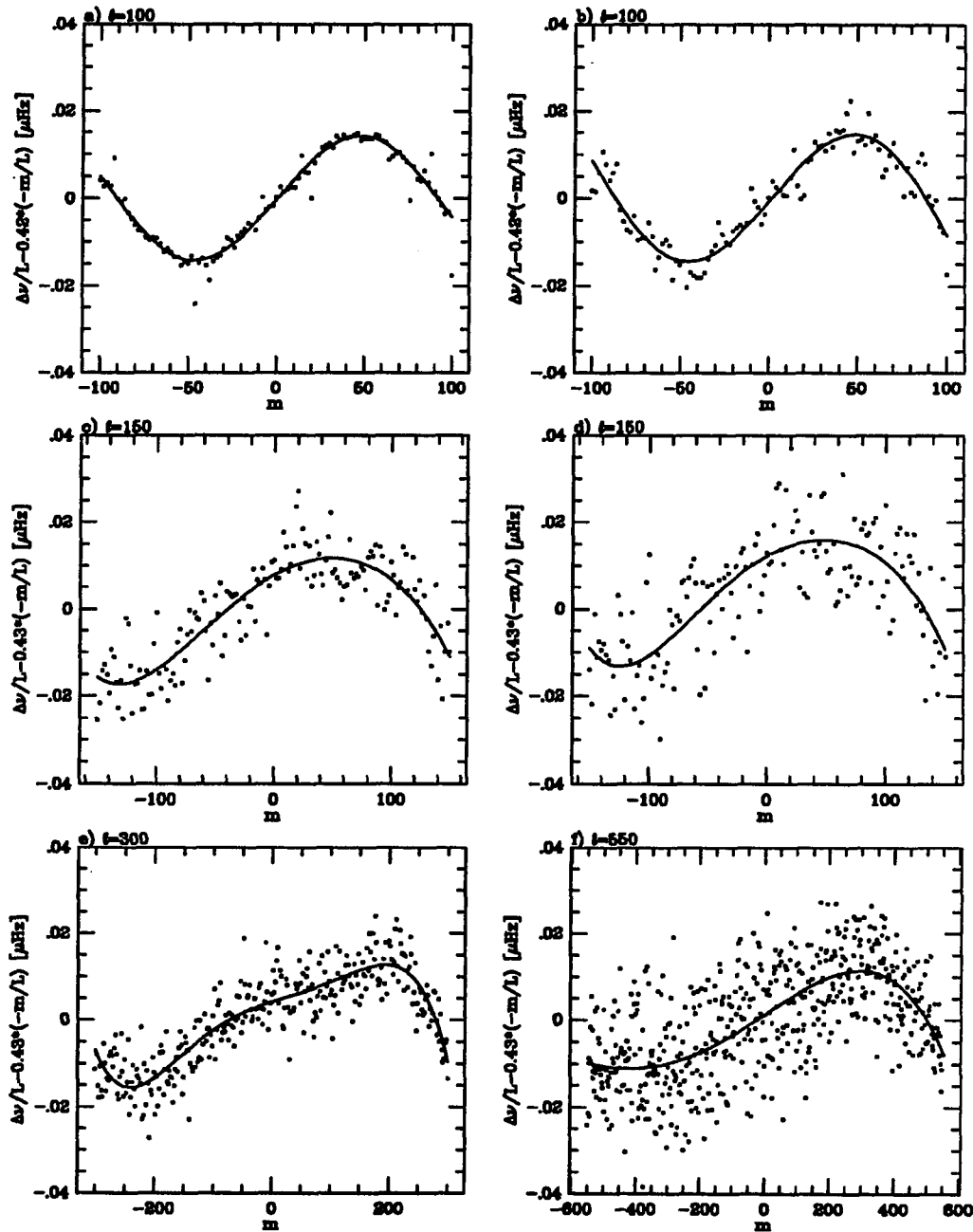


Figure 4.29: Observed frequency shifts, scaled as in Figures 4.26 and 4.28. The symbols represent the frequency shifts at the last iterative step and the solid line the Legendre polynomial expansion fit. a) for $l = 100$ using high-resolution spectra; b) for $l = 100$ but using smoothed high-resolution spectra; c) for $l = 150$ using smoothed high-resolution spectra; d) for $l = 150$ using low-resolution spectra; e) for $l = 300$ using low-resolution spectra and f) for $l = 550$ using low-resolution spectra.

of m/L is only some 5% of the slope's amplitude, it should come as no surprise that small perturbations in the ridge amplitude distribution perturb significantly the measured curvature.

4.1.5 Correction for Systematic Errors

In order to correct for the systematic errors introduced when individual modes are not resolved, we are left to rely on an *ad hoc* correction scheme rather than a model dependent one, since our modelization of the systematics was unable to satisfactorily represent in all details the effect of mode blending on frequency splitting measurements.

Such an *ad hoc* correction scheme is based on the overlapping region in ℓ between the high spectral resolution “resolved” results and the low spectral resolution “unresolved” results. Indeed, for $40 < \ell < 120$, the systematic errors introduced by not resolving individual modes can be directly estimated by comparing “resolved” results to “unresolved” ones⁵.

Thus, for each degree, ℓ , we have computed differences of frequency shifts, as measured at the last steps of the iterative cross-correlation analysis, between the high-resolution “resolved” results and the low resolution “unresolved” results, to directly estimate $\delta(\Delta\nu_{\ell,m})$, from

$$\begin{aligned} \delta(\Delta\nu_{\ell,m}) &= (\Delta\nu_{\ell,m})_{\text{unresolved}} - (\Delta\nu_{\ell,m})_{\text{resolved}} \\ &\stackrel{\text{def}}{=} L \varepsilon_{\ell}\left(-\frac{m}{L}\right) \end{aligned} \quad (4.24)$$

The scaled “error” function $\varepsilon_{\ell}(-m/L)$ as defined by Equation (4.24) has then been estimated by averaging over several ranges of ℓ , the respective sets of $\delta(\Delta\nu)/L$, using a fixed number of bins for the ratio m/L . This ℓ averaging was performed to reduce the scatter

⁵Note that below $\ell = 40$ the low spectral resolution results become too noisy to perform a reliable comparison, indeed, recall that around $\ell = 40$ the frequency splitting between prograde and retrograde sectoral modes is around $2\Omega\ell \approx 34 \mu\text{Hz}$, i.e. of the order of the spectral resolution

ℓ	q_0	q_1	q_2	q_3	q_4	q_5
50	13.1 ± 1.3	34.3 ± 2.2	-25.7 ± 2.8	-9.2 ± 3.3	2.6 ± 3.5	1.4 ± 3.7
70	10.3 ± 0.6	22.4 ± 1.2	-21.7 ± 1.5	-11.3 ± 1.7	5.1 ± 1.8	9.2 ± 2.0
90	7.6 ± 0.5	18.1 ± 0.8	-18.9 ± 1.0	-12.7 ± 1.3	3.3 ± 1.4	5.9 ± 1.4
110	5.9 ± 0.5	14.3 ± 0.9	-16.1 ± 1.1	-11.5 ± 1.3	2.7 ± 1.4	7.7 ± 1.5
in nHz, with an ℓ range of $\bar{\ell} \pm 10$, and a 21 equispaced points for the m/L binning.						
80	-8.4 ± 0.4	-20.0 ± 0.8	19.5 ± 1.0	11.4 ± 1.2	-3.5 ± 1.2	-6.6 ± 1.3
80	-8.5 ± 0.3	-20.1 ± 0.6	19.6 ± 0.8	11.4 ± 0.9	-3.4 ± 1.0	-6.9 ± 1.1
in nHz, with $40 \leq \ell \leq 119$, and respectively a 21 or 41 equispaced points for the m/L binning.						

Table 4.3: Correction coefficients q_i

present in the individual “error” functions. Once ℓ -averaged, the average error functions, $\bar{\varepsilon}$, have been parametrized with a Legendre polynomial expansion

$$\bar{\varepsilon}_{\bar{\ell}}\left(-\frac{m}{L}\right) = \sum_i q_{i,\bar{\ell}} P_i\left(-\frac{m}{L}\right) \quad (4.25)$$

through a least-squares fit procedure, where $\bar{\ell}$ is the average value of ℓ corresponding to the ℓ range used to compute each average error function.

It directly follows from the definition of ε_{ℓ} that the “resolved” results can be recovered from the “unresolved” results through the correction coefficients, $q_{i,\ell}$, namely that

$$(a_{i,\ell})_{\text{resolved}} = (a_{i,\ell})_{\text{unresolved}} - q_{i,\ell} \quad (4.26)$$

Figure 4.30 presents several $\bar{\varepsilon}$ functions, computed using 21 equispaced bins for the m/L ratio, and averaged over different ranges in ℓ , as well as the least-squares fitted Legendre polynomial expansion, while Table 4.3 and Figure 4.32 present the correction coefficients themselves obtained for each ℓ range. The overall averaged $\bar{\varepsilon}$ function (i.e. using $40 \leq \ell \leq 119$) and corresponding correction coefficients, based on 21 and 41 equispaced bins for the m/L ratio are presented in Figure 4.31 and listed in Table 4.3.

In order to correct the “unresolved” frequency splittings above $\ell = 120$, the $q_{i,\ell}$ coefficients need to be extrapolated. A good modelization of the function ε_{ℓ} would have provided a strict framework for this extrapolation, hence reliable corrected frequency splittings

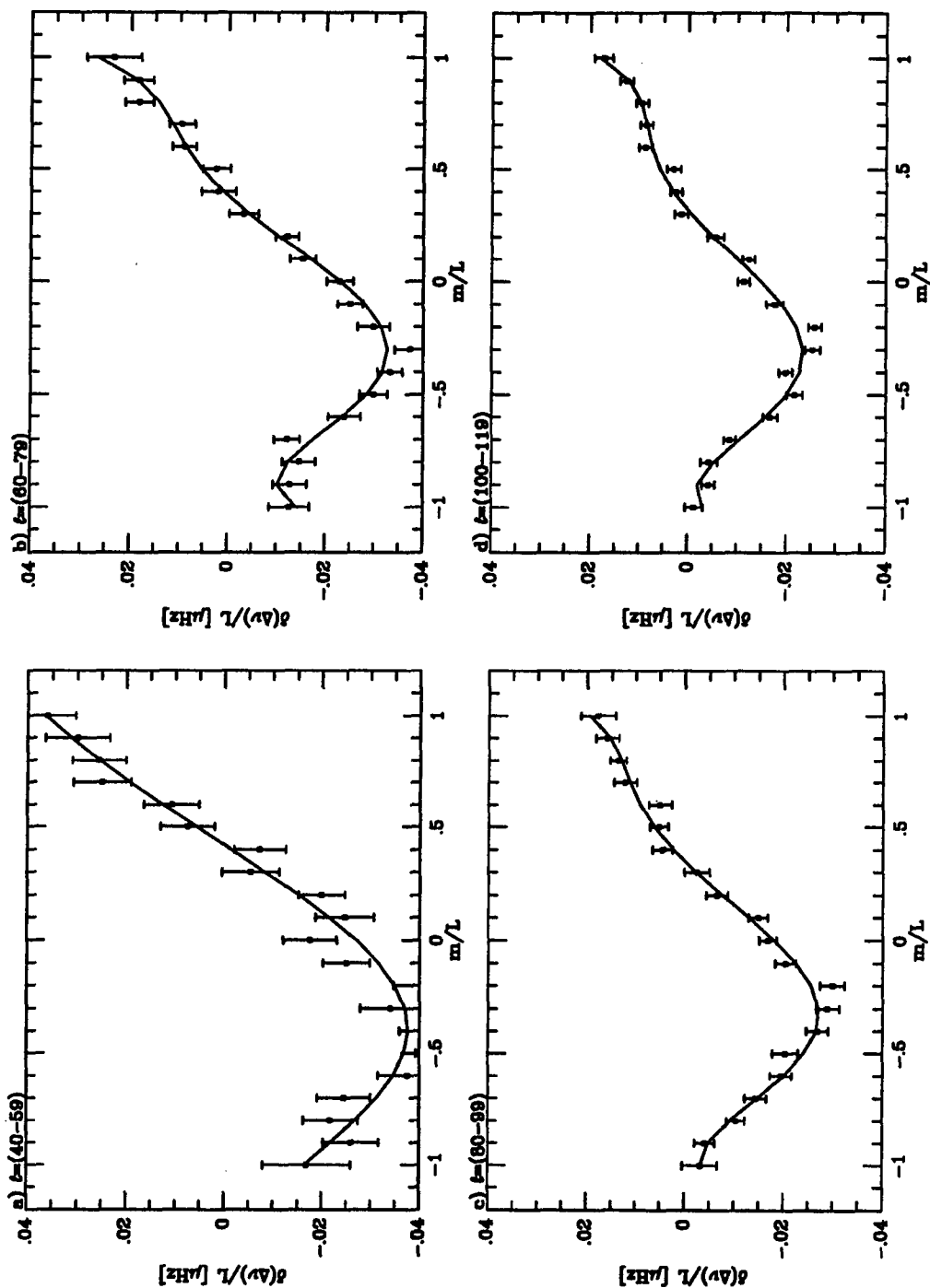


Figure 4.30: Functions $\epsilon = \delta(\Delta\nu)/L$ as a function of m/L , computed using 21 equispaced bins for m/L , a) estimated from $\ell = 40-59$, b) estimated from $\ell = 60-79$, c) estimated from $\ell = 80-99$, and d) estimated from $\ell = 100-119$.

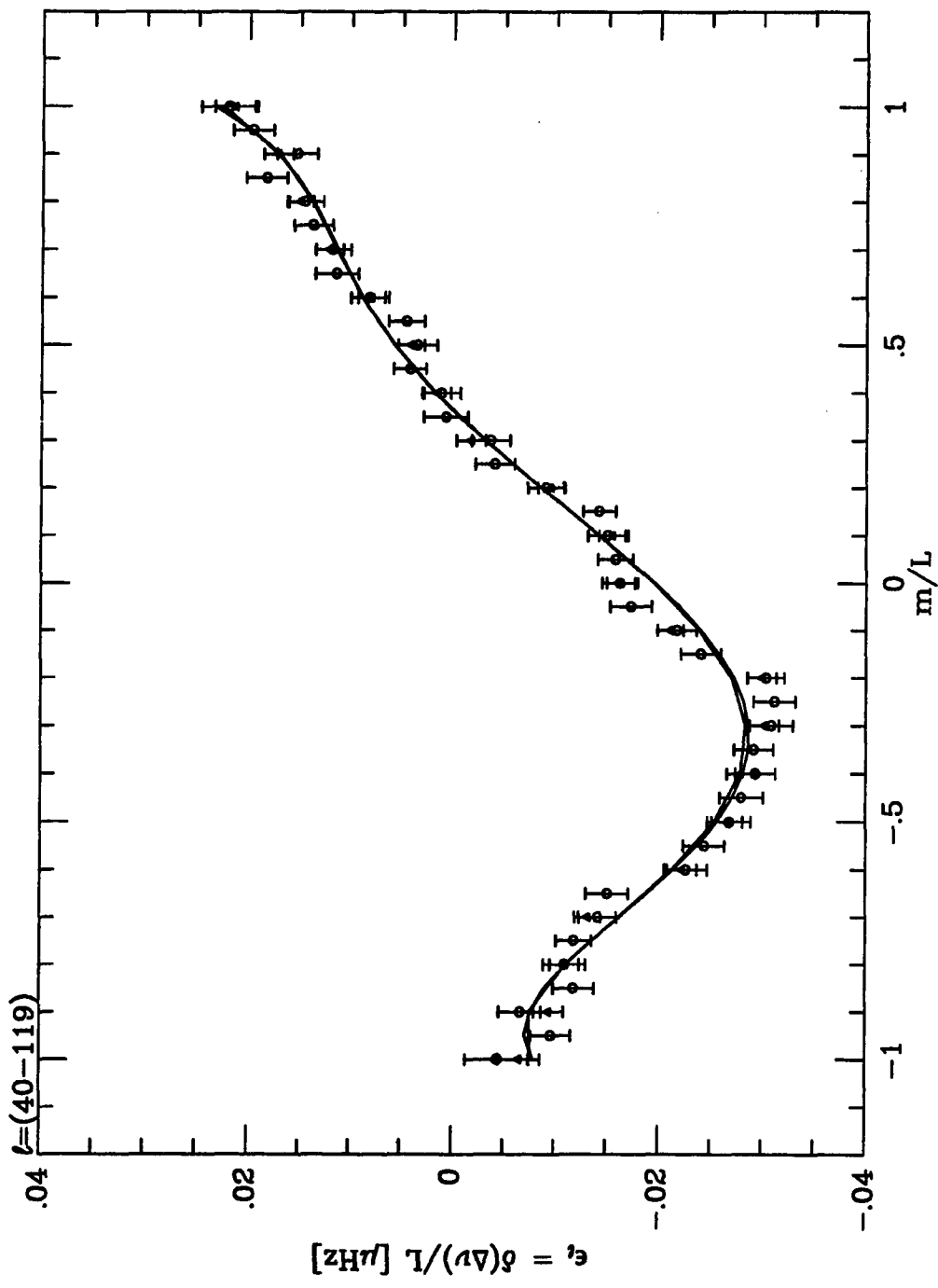


Figure 4.31: Overall averaged function ϵ , computed using 21 (triangles) and 41 (circles) equispaced bins for m/L , estimated from $\ell = 40-119$.

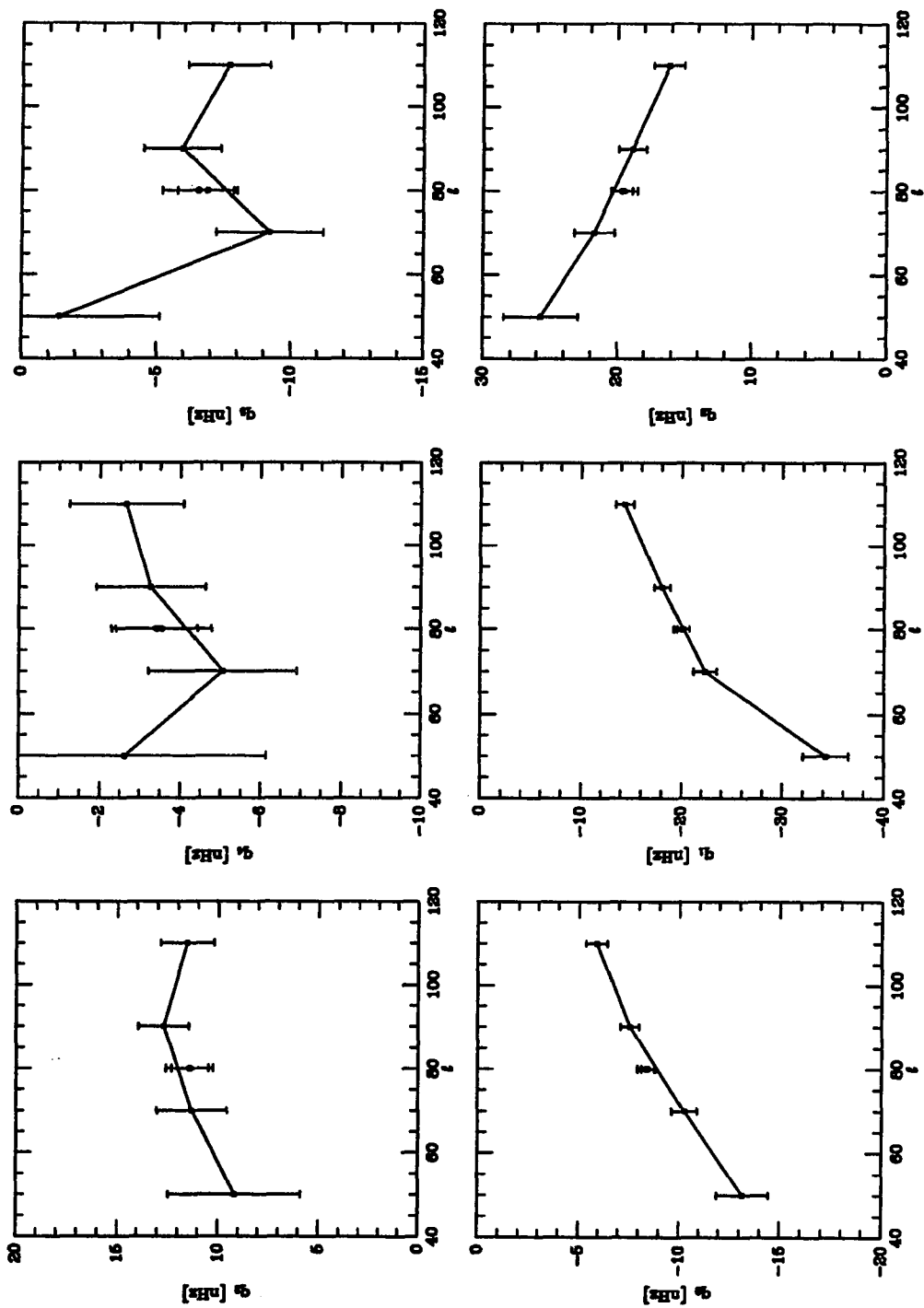


Figure 4.32: Correction coefficients, q_i , plotted as a function of the spherical harmonic degree l . The overall value, based on a 21 and 41 point binning respectively are also indicated.

at high-degrees. Unfortunately, our simulations were unable to reproduce in detail the observed error functions; therefore such an extrapolation must be carried out with extreme caution and the extrapolated results treated with a reasonable degree of scepticism.

Note that, on one hand, the ℓ dependence of the low order $q_{i,\ell}$ coefficients (namely for $i = 0, 1, 2$) follows the general ℓ -dependent trend indicated in our simulations. Namely that the systematic error introduced by mode blending decreases (in absolute terms) with increasing degree. But on the other hand, the high-degree $q_{i,\ell}$ coefficients (i.e. for $i = 3, 4, 5$) display no significant trend with degree, ℓ , compared to their uncertainties.

Therefore, we have arbitrarily considered in our attempt to extrapolate the corrective terms, $q_{i,\ell}$, a simple $1/\ell$ variation for the low-degree coefficients (i.e. $q_{i,\ell}$ constant with ℓ for $i = 0, 1, 2$) and constant values with degree for the high-degree coefficients (i.e. $q_{i,\ell}$ constant with ℓ for $i = 3, 4, 5$). Corrected Legendre polynomial expansion coefficients, based on these extrapolated correction coefficients are plotted in Figures 4.33 and 4.34.

While these corrected results should be considered with a reasonable degree of scepticism, the corrected odd-indexed coefficients do not indicate the presence of any significant variation of the differential rotation with degree, for $100 \leq \ell \leq 400$. A marginally significant variation seen at high-degree (i.e. $\ell > 400$) indicates that a more pronounced differential rotation may be present closer to the surface as the discrepancy between the “gas” and “magnetic” surface rotation rate themselves would suggest. This result relies heavily on the assumption that the above-mentioned ℓ dependence of the correction coefficients remains valid at such high-degrees.

The residual departure from zero of the corrected even-indexed coefficients is also delicate to interpret. A conservative approach would consider these values as an indication of the residual systematic errors present in the corrected set, while a speculative interpretation would infer a potential presence near the surface of non-symmetric perturbations (i.e.

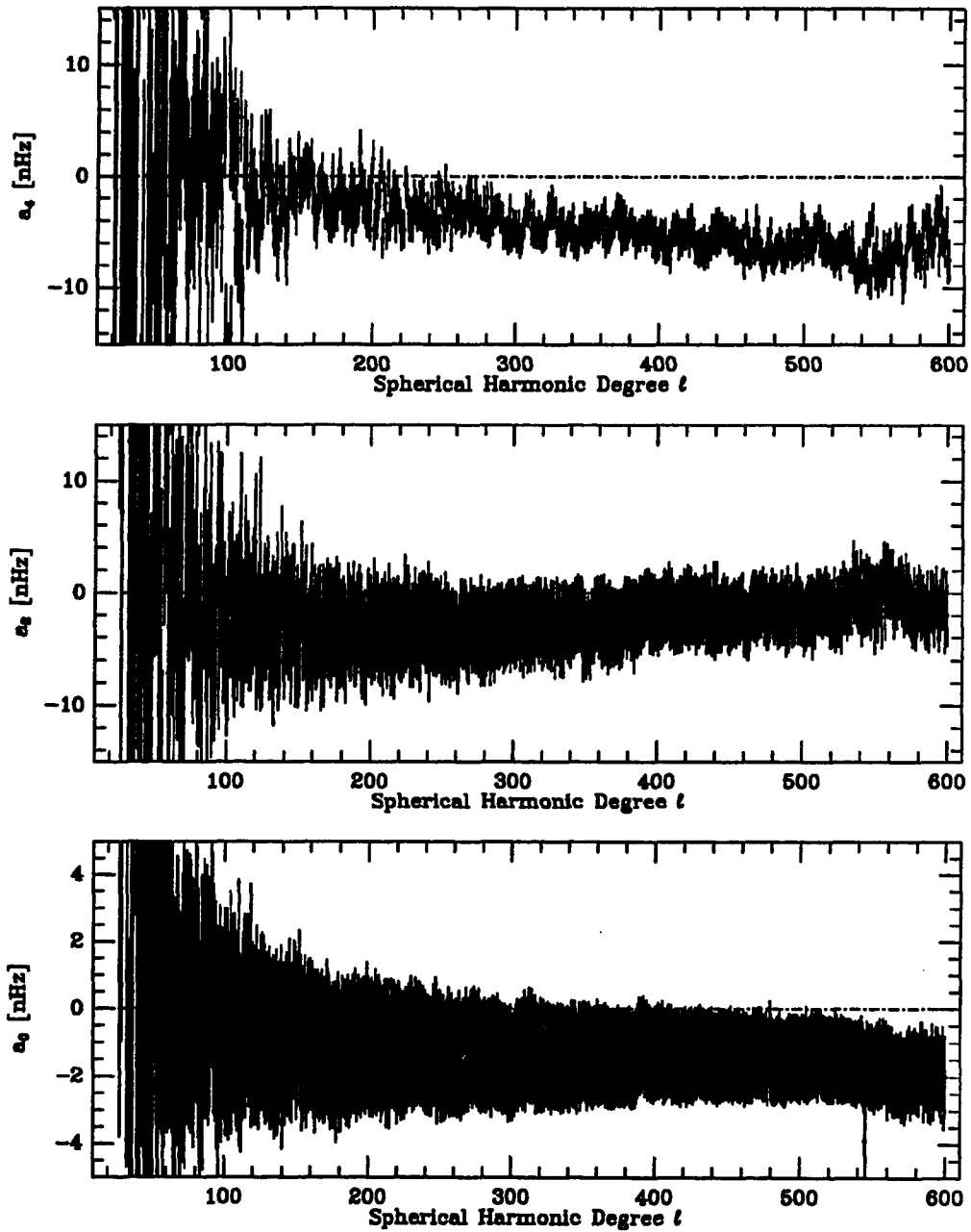


Figure 4.33: Even-indexed Legendre polynomial expansion coefficients, estimated from the low-resolution spectra, after being corrected for systematics introduced by mode blending.

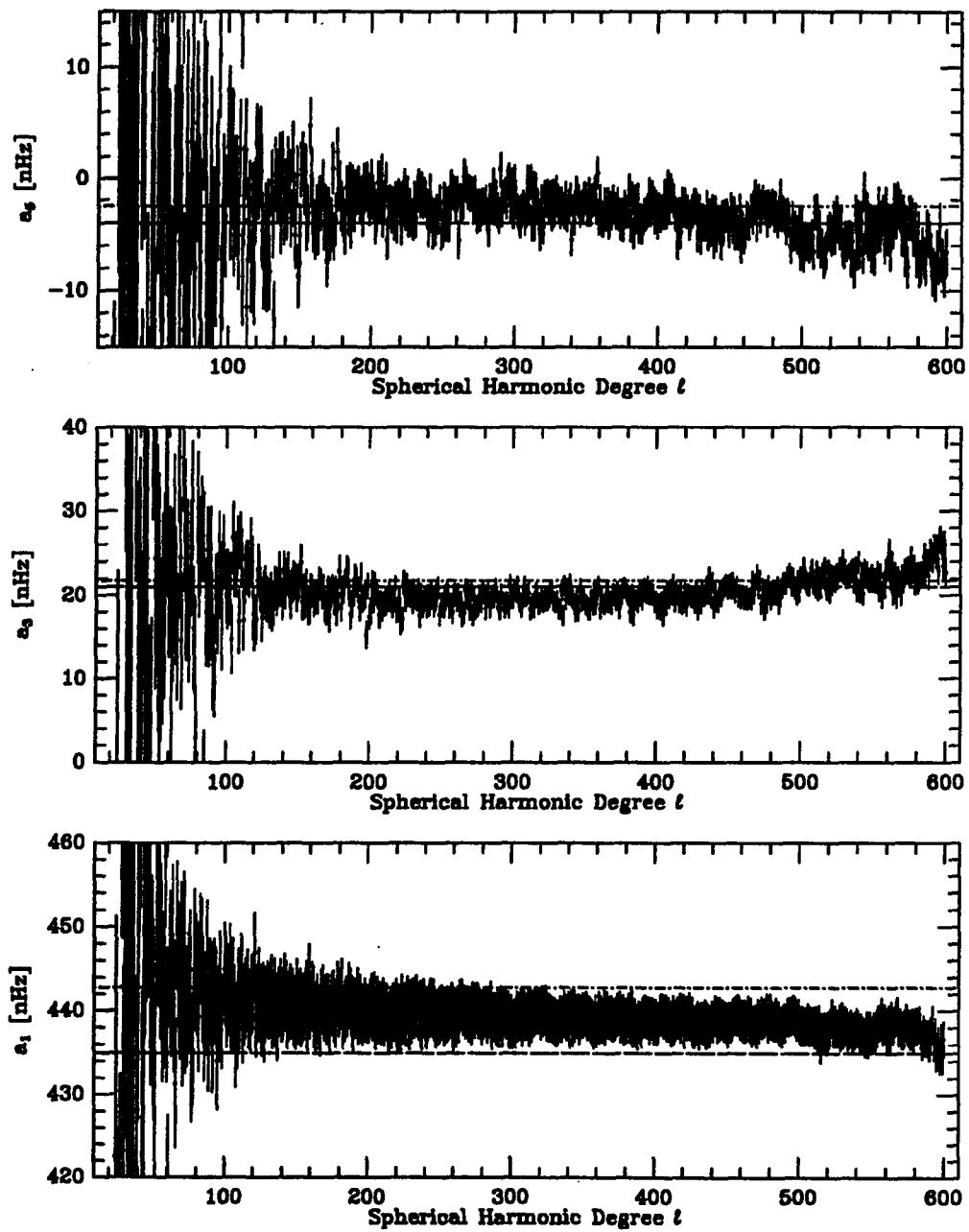


Figure 4.34: Odd-indexed Legendre polynomial expansion coefficients, estimated from the low-resolution spectra, after being corrected for systematics introduced by mode blending.

asphericity, magnetic field, ...). Until a more realistic theoretical characterization of the error function is available to provide a strict framework for the correction coefficients extrapolation, we shall take a conservative approach and will not infer any speculative interpretation from the odd-indexed frequency splitting coefficients.

4.2 Sectoral Measurements

An alternative approach to deriving an estimate of the equatorial solar rotation rate is to measure frequency splittings between prograde and retrograde sectoral modes directly (i.e. $m = \pm\ell$). Indeed, since sectoral modes are localized around the equator, sectoral splittings provide a direct measure of some weighted average of the rotation rate localized around the equator, hence to first order the equatorial rotation rate (see further discussion in Section 6.1.1).

While the sum of the even-indexed Legendre polynomial coefficients represents very precisely the sectoral frequency splittings (to a factor $2L$), the direct determination of sectoral frequency differences provides an alternative measurement of the sectoral splittings, and therefore a check for self-consistency. Note also that since only information localized near the equator is used in determining sectoral splittings, since only nearly-sectoral modes (i.e. including leakage effects) are considered, the direct determination of sectoral splittings from sectoral spectra alone is potentially less susceptible to systematic effects.

While the transposition of the sectoral spherical harmonic coefficients into time series is a fairly trivial task, and since the total volume of data represented by the sectoral time series alone is a small fraction of all the tesseral time series we were able, at small extra cost, to compute high resolution spectra for all of the even- ℓ sectoral spectra, up to $\ell = 600$. From these high-resolution sectoral spectra, we have estimated the sectoral frequency splittings by performing a straightforward cross-correlation between the prograde and the retrograde

spectra.

A second approach which we used to obtain a measure of the sectoral frequency splitting was based on the low-resolution sectoral spectra. Here, we directly measured ridge centroid frequency differences between prograde and retrograde spectra by fitting a Lorentzian profile to each ridge for each sectoral spectrum.

4.2.1 Results from the High-Resolution Spectra

Figure 4.35 presents the scaled sectoral frequency splittings (i.e. $\Delta\nu/2\ell$) obtained by directly cross-correlating the prograde and retrograde high-resolution sectoral spectra for each even degree, ℓ . After editing out a small set of spurious measurements⁶, the raw scaled splittings have been averaged over $10\text{-}\ell$ wide bins, and the r.m.s. of the scatter around the average computed to estimate the uncertainty.

4.2.2 Results from the Low-Resolution Spectra

Figure 4.36 presents the scaled sectoral frequency splittings computed from direct differences between prograde and retrograde ridge frequency centroids. Ridge centroids were estimated from a non-linear least-squares fit using a Lorentzian profile plus a background term. Only frequency centroids resulting from fits satisfying some predetermined quality criteria were considered. For both low degrees ($\ell < 50$) and high degrees ($\ell > 500$) the direct difference method breaks down. Indeed, at low degrees the frequency shifts remain comparable to the spectral resolution⁷, hence the frequency uncertainty contributes to a large uncertainty on the differences, while at high degree, the severe degradation of the

⁶The uneven modal excitation in a given observation run may lead in some cases to more power associated to a spatial sidelobe than to the target mode, hence a spurious measurement of the frequency splitting at that particular degree

⁷At $\ell = 50$ the frequency shift between prograde and retrograde frequency is of the order $42 \mu\text{Hz}$, while the low resolution spectra have a resolution of $27.8 \mu\text{Hz}$

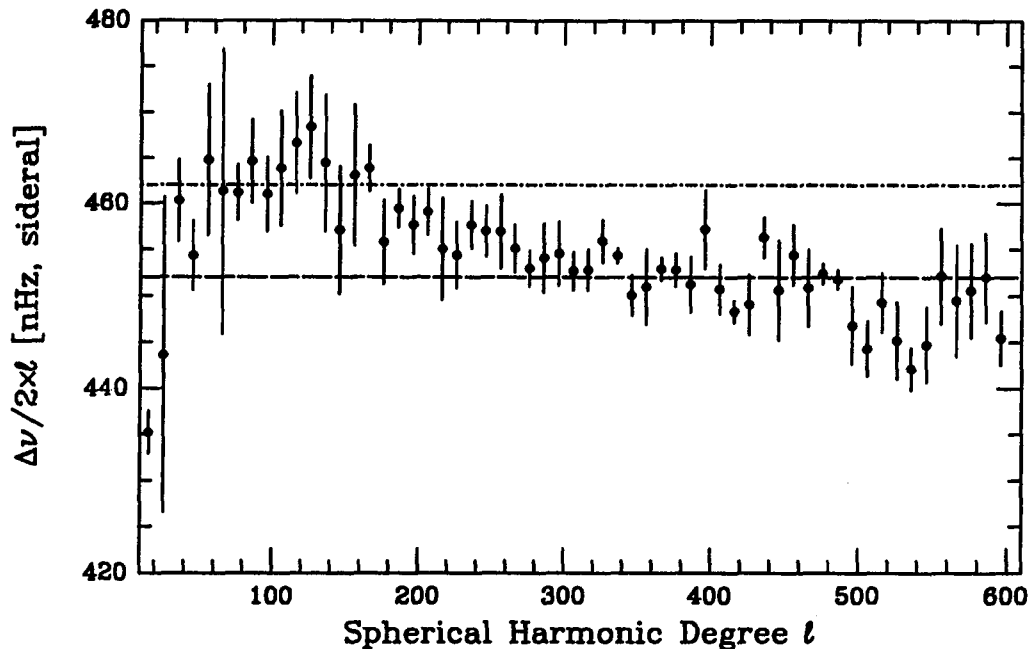


Figure 4.35: Scaled frequency splittings, $\Delta\nu/2\ell$, estimated from cross-correlation of high-resolution sectoral spectra. Splitting equivalent to the surface rotation rate, estimated from non-seismic measurement, are indicated by the dashed (spectroscopic) and dot-dashed (magnetic feature) lines.

SNR of a single sectoral spectrum brings the quality of the fits systematically below the predefined quality criteria.

The raw scaled differences were averaged over radial order, n , and over degree, ℓ , by $10\text{-}\ell$ wide bins while uncertainties were estimated from the standard deviation of the mean.

4.2.3 Comparison of High- and Low-Resolution Sectoral Splittings

The remarkable agreement between the low-resolution ridge fitting and the high-resolution cross-correlation, as shown in Figure 4.37, confirms, if still needed, that indeed at high-degree individual modes are not resolved any more, and that at such degrees, “raw” frequency splitting measurements correspond to ridge frequency centroid shifts.

While low- and high-resolution sectoral measurements display such remarkable agreement,

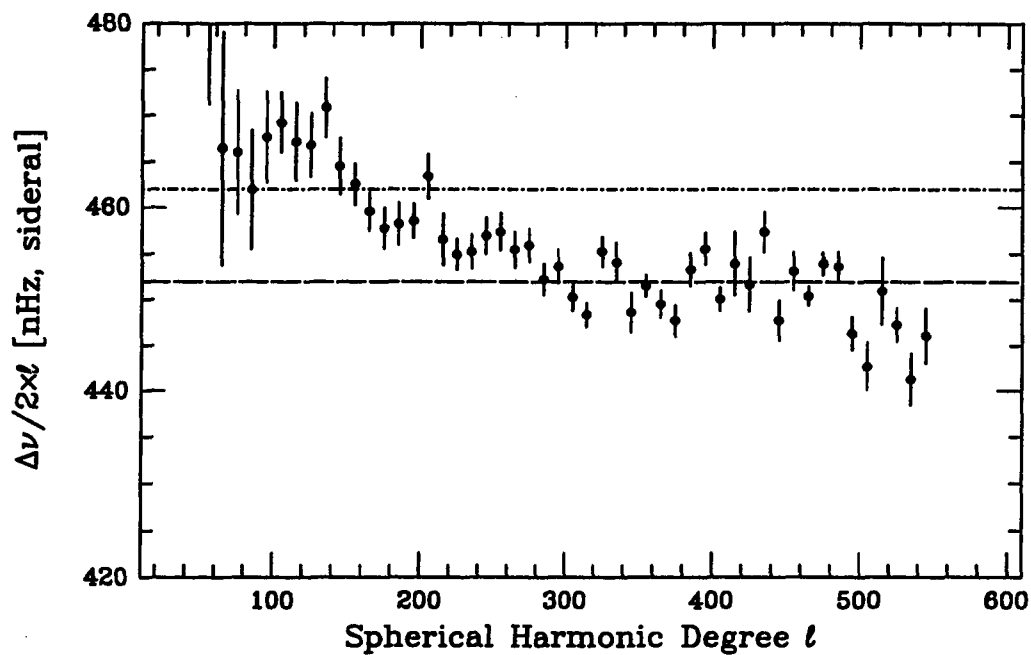


Figure 4.36: Scaled frequency splittings, $\Delta\nu/2\ell$, estimated from ridge fitting to the low-resolution sectoral spectra

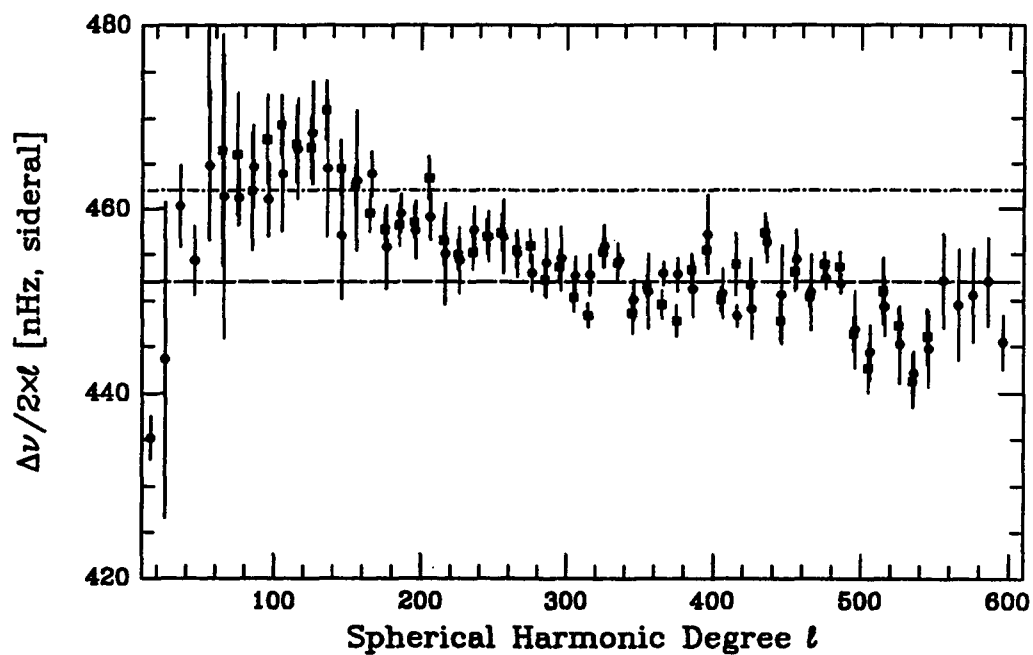


Figure 4.37: Comparison of the scaled frequency shifts estimated from the high resolution cross-correlation (filled circles) with the low-resolution ridge fitting results (open squares)

the sectoral equivalent of the tesseral measurements estimated from the low-resolution spectra (namely $a_1 + a_3 + a_5$) presents a systematic difference of some 4 nHz with the strictly sectoral measurements. This difference can be easily traced to the large scatter of the frequency shifts in the tesseral measurements. Indeed, if we compute the scaled frequency differences directly between prograde and retrograde spectra, as measured at the last iterative step of the tesseral analysis, the same systematic difference is present, namely that the sum of the odd-indexed coefficients systematically overestimates the direct scaled difference.

Since the scatter of the frequency shifts with respect to the template spectrum is large, the 5th order polynomial fit cannot be tight, allowing the fitted polynomials to overestimate the sectoral frequency splitting by $\approx 1\%$. Such discrepancy between direct differences and sum of odd-indexed coefficients is not present in the high-resolution resolved tesseral measurements since the fit in that case is much tighter than for the unresolved cases (see for instance Figure 4.29).

This discrepancy disappears once the order of the fitted polynomial is increased, allowing the fitted curve to better reproduce the fine details of the splittings curvature hence to better match the end points. As a direct consequence of the intrinsic large scatter of the frequency shifts, increasing the order of the fit adds only marginally significant terms, therefore it increases the scatter and the uncertainty of the sectoral equivalent frequency splittings (i.e. the sum of the odd-indexed coefficients) and renders it comparable to the sectoral measurements scatter and uncertainty. Nevertheless, when extending the Legendre polynomial expansion to the 11th order, the sum of the odd-indexed coefficients, for $\ell > 100$, agrees to within the internal scatter with the the sectoral measurements, and presents very similar scatter. This is illustrated Figure 4.38 were the strictly sectoral splitting measurements (from the high-resolution spectra) and sectoral equivalent tesseral measurements (from the low-resolution spectra) computed from an 11th order polynomial

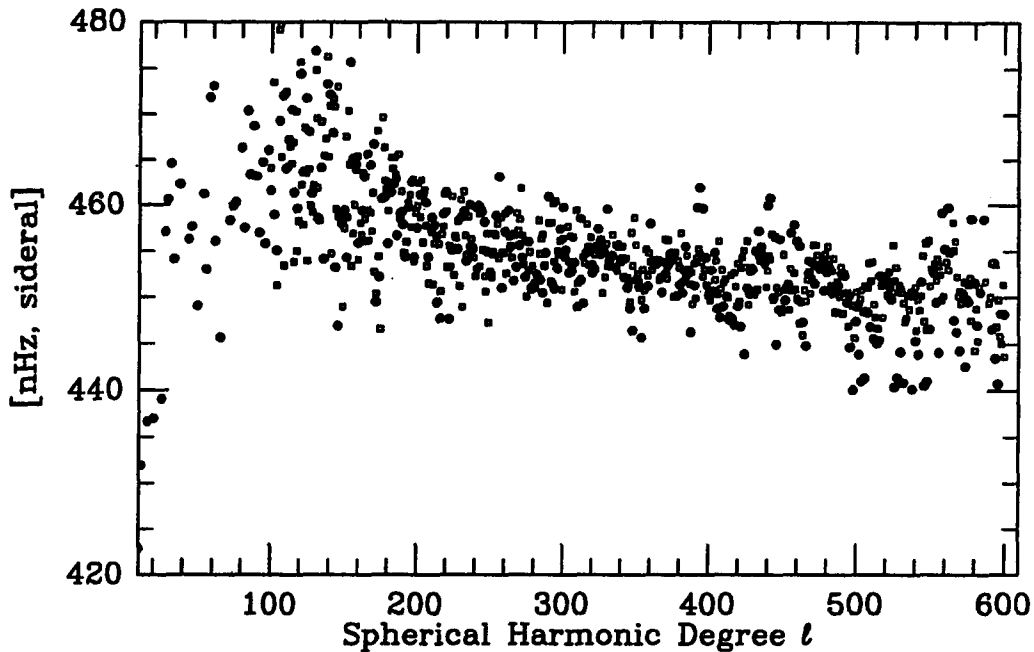


Figure 4.38: Comparison of sectoral and tesseral equivalent (11th order) splittings. Namely, unbinned sectoral scaled frequency shifts ($\Delta\nu/2\ell$) estimated from the cross-correlation of the high-resolution sectoral spectra (filled circles) and sum of the odd-indexed coefficients using an 11th order Legendre polynomial expansion and the low-resolution tesseral spectra for $\ell > 100$ (open squares).

fits are compared⁸ and establishes the self-consistency of our splitting results.

4.2.4 Source of systematic errors

Despite the fact that all three measurements of sectoral frequency splittings agree remarkably well, they all represent frequency shifts between ridge frequency centroid and will also be affected by systematic errors associated to the displacement of that centroid with respect to the target mode frequency. Fortunately, as we shall demonstrate in the present section, the relative amplitude of these systematics in the sectoral case remains small, hence the sectoral splittings can be considered as more robust estimates.

⁸Note that the 11th order Legendre polynomial fit was carried out on the frequency shifts measured at the last step of the iterative cross-correlation analysis, which itself was performed using only a 5th order fit to compute the template spectrum

As for the tesseral case, we can estimate the systematic error on the measurement of the sectoral splitting due to mode blending from the displacement of the centroid of the ridge with respect to the target frequency. Such systematic error can be written as

$$\delta(\Delta\nu)_{\text{sectoral}} = \frac{\sum_{\ell', m'} |\langle \ell', m' | \ell, -\ell \rangle| A_{n, \ell', m'} (\nu_{n, \ell', m'} - \nu_{n, \ell, -\ell})}{\sum_{\ell', m'} |\langle \ell', m' | \ell, -\ell \rangle| A_{n, \ell', m'}} - \frac{\sum_{\ell', m'} |\langle \ell', m' | \ell, +\ell \rangle| A_{n, \ell', m'} (\nu_{n, \ell', m'} - \nu_{n, \ell, +\ell})}{\sum_{\ell', m'} |\langle \ell', m' | \ell, +\ell \rangle| A_{n, \ell', m'}} \quad (4.27)$$

or simply

$$\delta(\Delta\nu)_{\text{sectoral}} = \delta(\Delta\nu)|_{m=-\ell} - \delta(\Delta\nu)|_{m=+\ell} \quad (4.28)$$

Using the same approximations and notations as for the tesseral case, after considering the parity properties of the different terms in Equation (4.21), and neglecting the denominator, \mathcal{D} , Equation (4.27) can be rewritten as

$$\frac{\delta(\Delta\nu)_{\text{sectoral}}}{2\ell} \approx \frac{\partial\nu}{\partial m} \left[\epsilon (1 + \epsilon\ell(Q_l + Q_m)) + \frac{1}{\ell} (\sigma_0 Q_l + \sigma_2 Q_m) \right] \quad (4.29)$$

where the derivatives are estimated at $m = +\ell$, and where

$$\sigma_0 = \frac{\sqrt{2}}{2} \left(\frac{s_x^3 - s_y^3}{s_x s_y} \right) \quad (4.30)$$

and

$$\sigma_2 = \frac{\sqrt{2}}{2} \left(\frac{s_x^3 + s_y^3}{s_x s_y} \right) \quad (4.31)$$

While the parity properties that lead to the cancellation of several terms of Equation (4.13) may not be rigorously satisfied in any actual situation, the incomplete cancellation of some of these terms would only introduce second order correction to the above result and may be safely ignored here.

Figure 4.39 presents the sectoral splitting correction factor estimated for $\epsilon = 0$ and $\epsilon = 0.5\%$ based on n -averaged values of Q_l and $\partial\nu/\partial\ell$, $\gamma = 1$ and $\partial\nu/\partial m|_{m=+\ell} = 469$

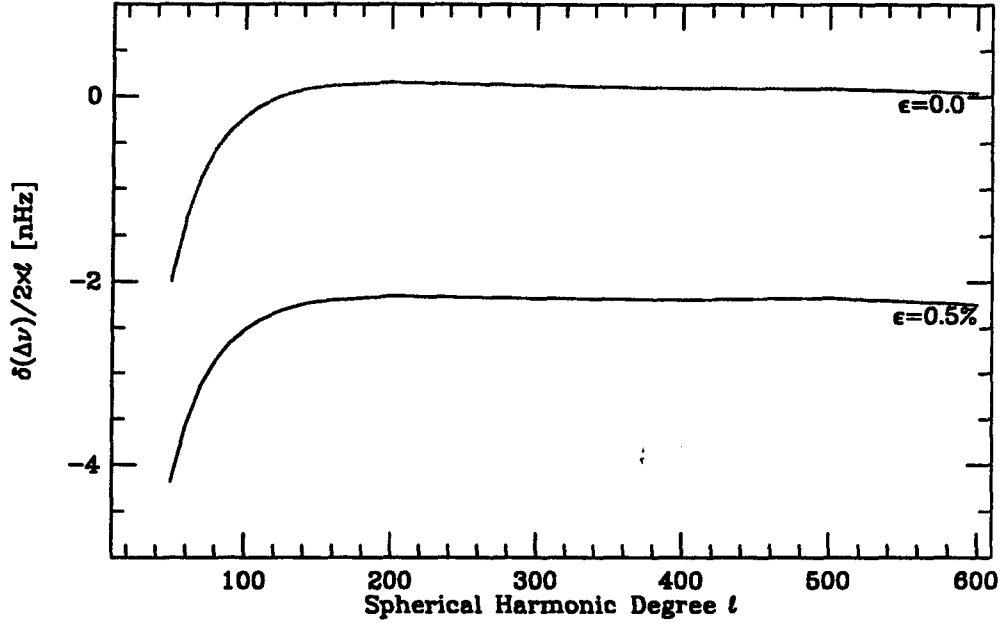


Figure 4.39: Simulated sectoral splitting systematic error, for no image size error (dashes) and for a 0.5% image size error (solid) as a function of degree ℓ .

nHz (i.e. $a_1 = 403$, $a_3 = 21$ and $a_5 = -4$, nHz synodic). It clearly indicates, as does Equation (4.29), that at low degrees, the systematics will be dominated by the amplitude density distribution asymmetries, while at high-degree, they will be dominated by any image size error, and will be, in relative terms, on the order of that image size error.

4.2.5 Correction for systematic errors

Figure 4.39 clearly indicates that above $\ell = 150$ an almost constant correction of some $\epsilon \partial \nu / \partial m$ is required to account for a minor image scale error (i.e. ≈ 2.5 nHz for $\epsilon = 0.5\%$). More rigorously, if we assume that the frequency splitting is given by a strict odd-indexed expansion, we can write

$$\begin{aligned} \frac{\Delta \nu}{2\ell} &= \frac{L}{\ell} (a_1 + a_3 + a_5) \\ &= \frac{\Delta \nu}{2\ell} \Big|_{\text{ridge}} - \frac{\delta(\Delta \nu)}{2\ell} \end{aligned}$$

$$= \frac{\Delta\nu}{2\ell}|_{\text{ridge}} + \zeta(a_1 + 6a_3 + 15a_5) \quad (4.32)$$

where

$$\zeta = \epsilon(1 + \ell(Q_l + Q_m)) + \frac{1}{\ell}(\sigma_0 Q_l + \sigma_2 Q_m) \quad (4.33)$$

is a measurable quantity if ϵ can be independently estimated and $\frac{\Delta\nu}{2\ell}|_{\text{ridge}}$ is the scaled sectoral ridge centroid frequency shift. Equation (4.32) can be solved for $\frac{\Delta\nu}{2\ell}$ once the ratios a_3/a_1 and a_5/a_1 are known. Since a small error on those ratios translates into a small error on the correction, i.e. a second order effect, we have used the corrected low resolution tesseral results, binned in $10\text{-}\ell$ wide bins, to estimate these ratios, and the n -averaged values of $\partial\nu/\partial\ell$ and Q_l to estimate ζ .

Since the image scale error has been calibrated to be $\epsilon = -0.607\%$ by direct comparison of resolved mode frequency to ridge centroid frequencies computed from the high- and low-resolution collapsed spectra respectively (see Chapter 5), we have corrected the measured sectoral splittings according to Equation (4.32). While a residual systematic error on the order of 1 nHz is more likely to be still present, the general trend of the sectoral splittings, namely a decrease from some 461 nHz at $\ell = 150$ to some 448 nHz at $\ell = 600$ can be regarded as significant. This indicates that based on high-degree p-mode oscillation frequency splittings we are able to confirm a rotation rate near the surface, compatible with the spectroscopic “surface” rotation rate, and that just below the surface, the equatorial rotation rate increases with depth to reach a rotation rate compatible with the observed magnetic feature rate. These results will be further discussed in Chapter 6 where the results of formal inversions of the equatorial rotation rate as a function of depth will be presented.

4.3 Comparison with Previous Measurements

4.3.1 Low- and Intermediate-Degree Modes

Numerous observations of low-degree frequency splittings have been made in the past decade, based on low-resolution velocity and intensity measurements, ranging from short quasi-uninterrupted observing runs to 3-month-long data sets (see for instance Duvall *et al.*, 1988).

Rather than presenting a complete review of frequency splittings and introducing some confusion due to potential time variations and different analysis techniques, we have limited ourselves to comparing our high-resolution low-degree splitting measurements with the most contemporary set available of comparable measurements.

We have compared our measurements with frequency splittings estimated from a 3-month-long data set acquired during the summer of 1988 as well, at the Big Bear Solar Observatory (BBSO) by Libbrecht. While these are preliminary results, the 1988 BBSO data set and its analysis are in all points similar to the 1986 data set and analysis that are described in Libbrecht (1989). These studies are based on low-resolution velocity images obtained with a birefringent narrow band filter centered on the 6439 Å Ca line, and analyzed for frequency splittings for $10 \leq \ell \leq 60$, using a singlet fitting procedure. The high SNR and high frequency resolution resulting from such long observing runs allowed the Caltech group to perform a 6th order Legendre polynomial expansion fit for each individual radial order, n .

In order to compare Libbrecht's results to those of the present study, we have performed a weighted average over n of each expansion coefficient $a_i(n, \ell)$. The weighting was adjusted to represent the overall power distribution in the 5-minute band, namely using a Lorentzian profile centered around 3.3 mHz, with a FWHM of 3.0 mHz. To avoid pulling of the average

by possible outliers, a 3σ rejection threshold was included in the averaging process.

Figures 4.40 to 4.42 present comparisons of the frequency splittings obtained from the present study with the BBSO results. Despite the larger internal scatter present in our measurements, resulting from the lower SNR due to a shorter run (by a factor 5), the even-indexed coefficients are in good agreement. Indeed, while there is no splitting a_0 coefficients in the singlet fitting method⁹ to compare to, Figure 4.40 shows that for both sets a_2 is marginally positive and a_4 may be marginally negative. On the other hand, the agreement for the odd-indexed coefficients is less satisfactory. For a_1 , while at low- and high-degrees both sets agree at the 1σ level, our measurements are some 3 nHz smaller than the BBSO results for $36 \leq \ell \leq 54$. A less significant difference for the a_3 coefficient is present, but nevertheless our measurements are again systematically smaller (by some 1.5 nHz) than the BBSO results, for the same limited range in ℓ . Finally, for a_5 , our measurements are this time marginally but systematically larger than the BBSO results, again for the same limited range in ℓ . If we now compare the sum of the odd-indexed coefficients the remaining discrepancy is very marginally significant, if significant at all, and mainly for $36 \leq \ell \leq 54$.

While no contemporaneous measurements above $\ell = 60$ are presently available, we have nevertheless extended our comparison to $\ell = 120$ using the frequency splittings estimated from the Mt Wilson 1984 observing run (Tomczyk, 1988). These splittings are based on full-disk intermediate-resolution doppler measurements, covering five weeks of observations, in two contiguous 19-day-long and 16-day-long sets, respectively. Figure 4.43 compares the sum of the odd-indexed and the sum of the even-indexed coefficients. As for the comparison with the BBSO set, the sum of the even-indexed coefficients presents no significant differences, while marginally significant differences at the 1–2 nHz level may be present in the the sum of the odd-indexed coefficients.

⁹The singlet method fits at each radial order $\nu_{n,\ell,m} = \bar{\nu}_{n,\ell} + L \sum a_{i,n,\ell} P_i(-m/L)$, where the polynomial expansion is carried out for $i = 1, 6$

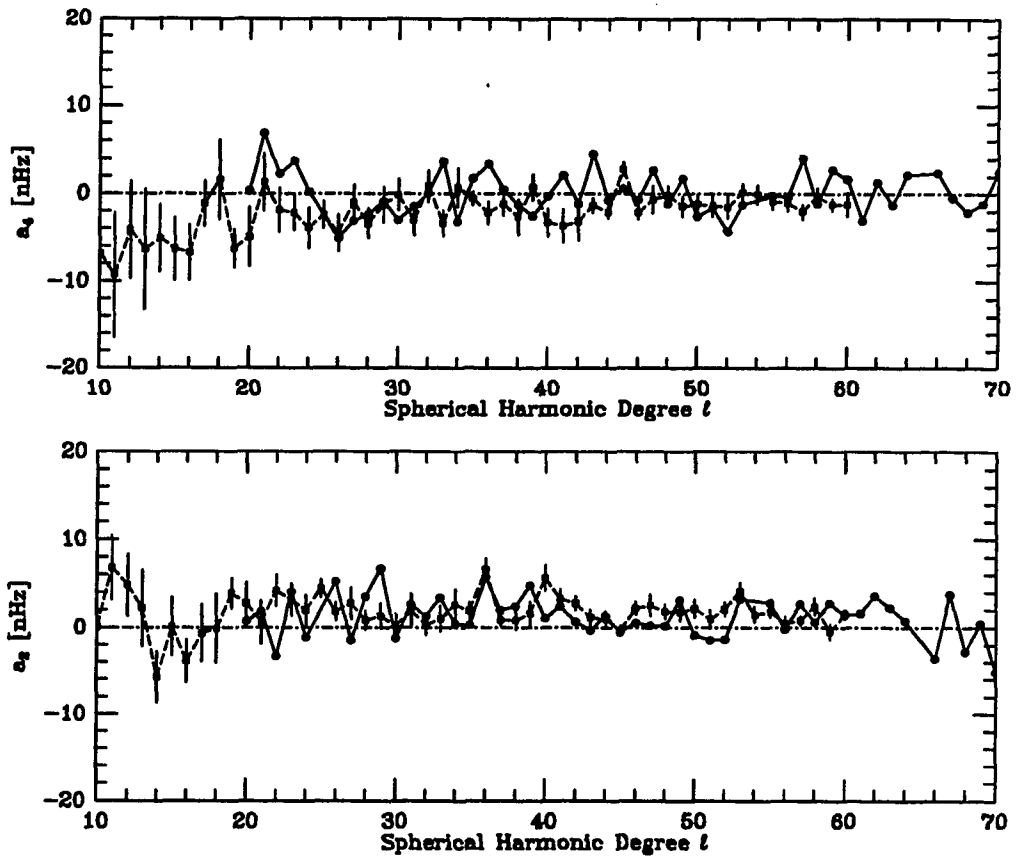


Figure 4.40: Even-indexed coefficients compared with contemporaneous BBSO measurements, reduced to n -averaged values.

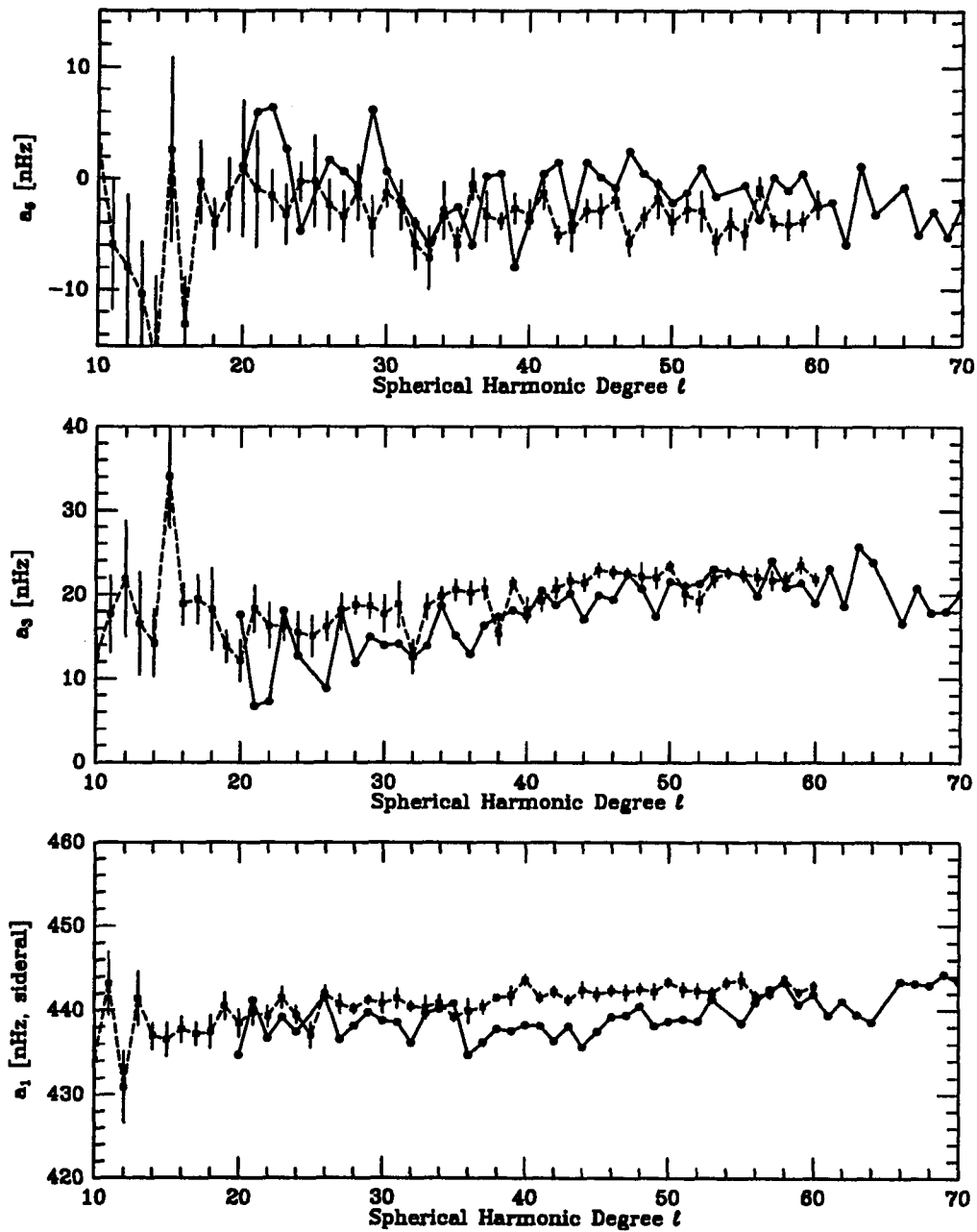


Figure 4.41: Odd-indexed coefficients compared with contemporaneous BBSO measurements, reduced to n -averaged values.

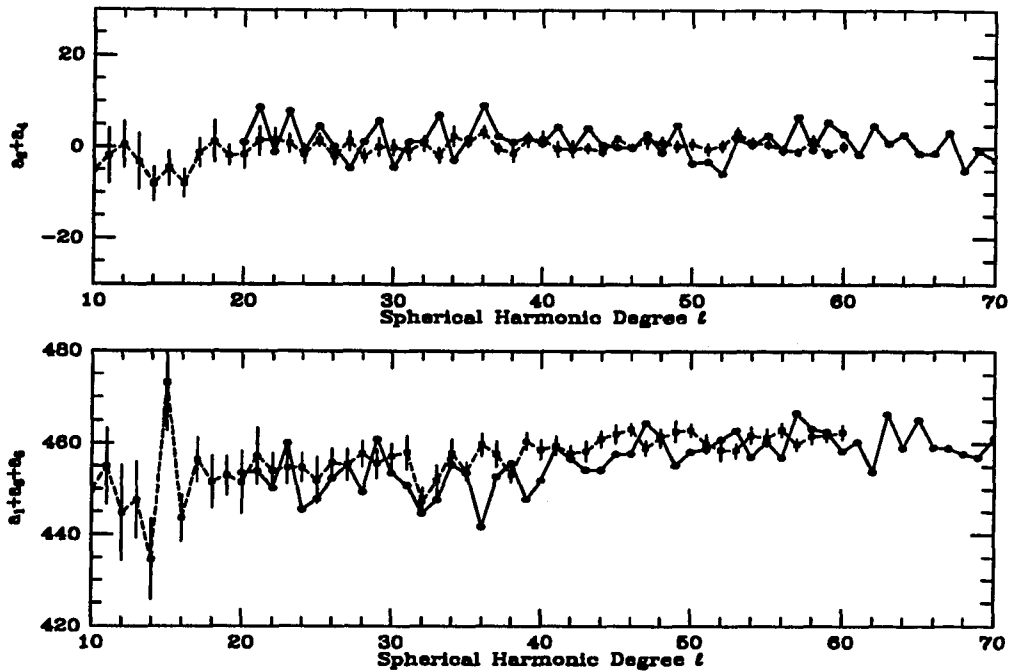


Figure 4.42: Sum of the odd-indexed coefficients compared with contemporaneous BBSO measurements, reduced to n -averaged values.

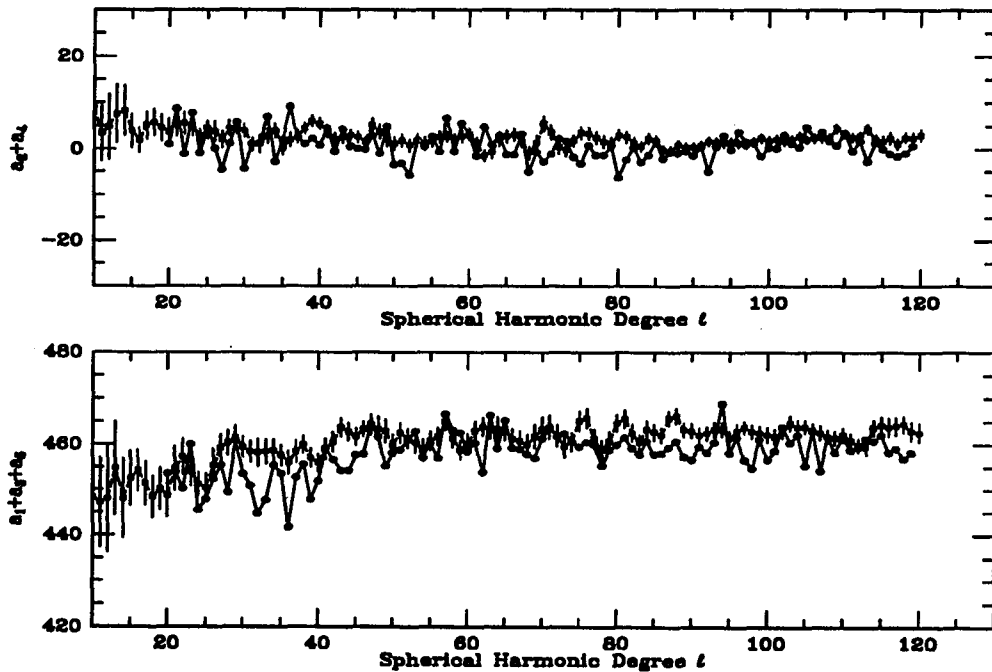


Figure 4.43: Sum of the odd-indexed coefficients compared with 1984 Mt Wilson measurements at low- and intermediate-degrees.

We can conclude from these comparisons that the sectoral equivalent measurements, as well as the individual even-indexed measurements agree quite well, with the exception of a marginally significant systematic difference at the 1–2 nHz level with previous determinations.

4.3.2 High-Degree Modes

While there have been several observations of high-resolution solar oscillations over the past decades, no conclusive frequency splitting measurements above $\ell = 120$ have been available prior to this work.

Since the pioneer work of the late seventies (see Deubner *et al.*, 1979), only a few studies have concentrated on measuring high-degree splittings to infer the subsurface solar rotation. While several high-resolution observations have been carried out and reduced by the Caltech group (Woodard and Libbrecht 1988; Kaufman, 1988; Libbrecht and Kaufman, 1988), the shortness of these runs (~ 8 – 10 hours) combined to instrumental limitations (see for instance Woodard and Libbrecht 1988) have greatly limited the potential of these data.

Longer runs (i.e. ~ 3 – 5 days) have been acquired and analyzed for the dedicated purpose of splitting measurements (Hill *et al.*, 1988a; Hill *et al.*, 1988b). In these observations only a small portion of the solar surface was observed, and no intermediate-degree resolved modes were observed. Therefore, as acknowledged in these studies, systematic errors associated with the nature of the observation (i.e. image drift, scanning procedure, ...) have not been assessed nor corrected for. Since the splittings themselves have not been presented in these studies, we are unable to make any direct comparison with the results of the present study.

Chapter 5

Mode Frequency, Width and Amplitude

We have described in Chapter 3 the reduction procedure we used to convert raw filtergrams to power spectra as well as the procedures we used to estimate from these spectra solar oscillation properties, namely frequency splittings and unperturbed mode frequencies. While the frequency splittings resulting from the analysis of the low- and high-resolution spectra have been presented in Chapter 4, we present in the following sections the estimates of modal frequency, width and amplitude, based on the low- and high-resolution collapsed spectra which resulted from the frequency splitting analysis.

More precisely, we present for low- and intermediate-degree modes (i.e. $20 \leq \ell < 120$) frequency, width and amplitude measurements of individually identified modes computed from the collapsed, high-resolution spectra. We also present estimates of modal frequencies, widths and amplitudes, for intermediate- and high-degree modes (i.e. $\ell \leq 600$), based on ridge centroid frequencies, widths and amplitudes computed from the collapsed, low-resolution spectra. We present and discuss the procedures we used to convert these ridge

characteristics to modal properties. Finally we compare these results to independent measurements and discuss some of the implications of these new estimates.

5.1 Results of the High-Resolution Spectra

Figure 5.1, 5.2 and 5.3 present the individual mode frequency, FWHM, and modal total power¹ respectively, estimated from the high-resolution collapsed power spectra. Only modes for which the non-linear least-squares fitting procedure converged, and for which the r.m.s. of the residuals to the fit is below a given fraction of the mode amplitude, and for which the uncertainty of the frequency is below a given threshold, have been kept.

In Figure 5.1 the size of the symbols used to plot each individual mode has been drawn proportionally to the measured FWHM. From that figure, two features can be noted. First, no modes above $\nu \approx 3.7$ mHz have been identified, and second, a bimodal distribution of the FWHM is present, where, for modes above $\ell \approx 45$ at low frequency and above $\ell \approx 75$ at high frequency, the measured FWHM is systematically larger than for lower degree modes at similar frequencies. The absence of modes above 3.6 mHz is easily explained by the fact that, since the mode FWHM increases with frequency, modes blend into ridges due to spatial and temporal sidelobes, hence individual modes cannot be identified any longer. On the other hand, the apparent bimodal distribution of the FWHM can be explained by sidelobe contamination. Indeed, if the temporal sidelobe of a spatial sidelobe falls too close to a mode, both peaks will blend and a corrupted measurement of the frequency, FWHM, and amplitude will result. Since modal FWHM are on the order of 1–2 μ Hz, corrupted measurements will occur when the spatio-temporal sidelobes fall within 1–2 μ Hz of a mode, hence, both frequency and FWHM will be corrupted by some 1–2 μ Hz

¹Modal total power refers to the total power associated with the mode, hence the area under the main lobe, namely $2\pi Pw$, where P is the amplitude — i.e. power density — and w the FWHM of the fitted Lorentzian profile

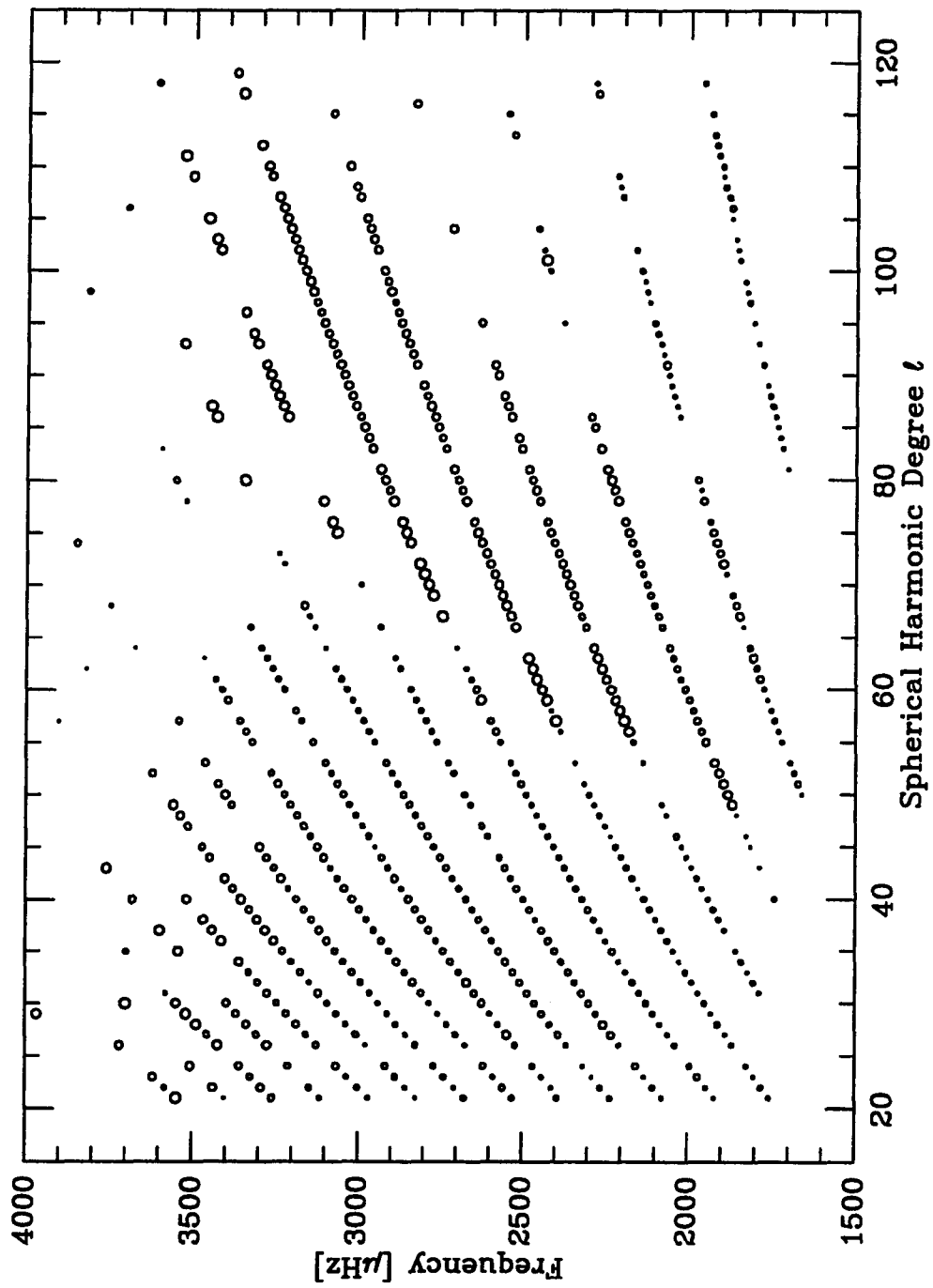


Figure 5.1: ℓ - ν diagram for the modes obtained from the high-resolution spectra. The size of the symbols is drawn proportionally to the measured FWHM. Note the bimodal distribution of the FWHM.

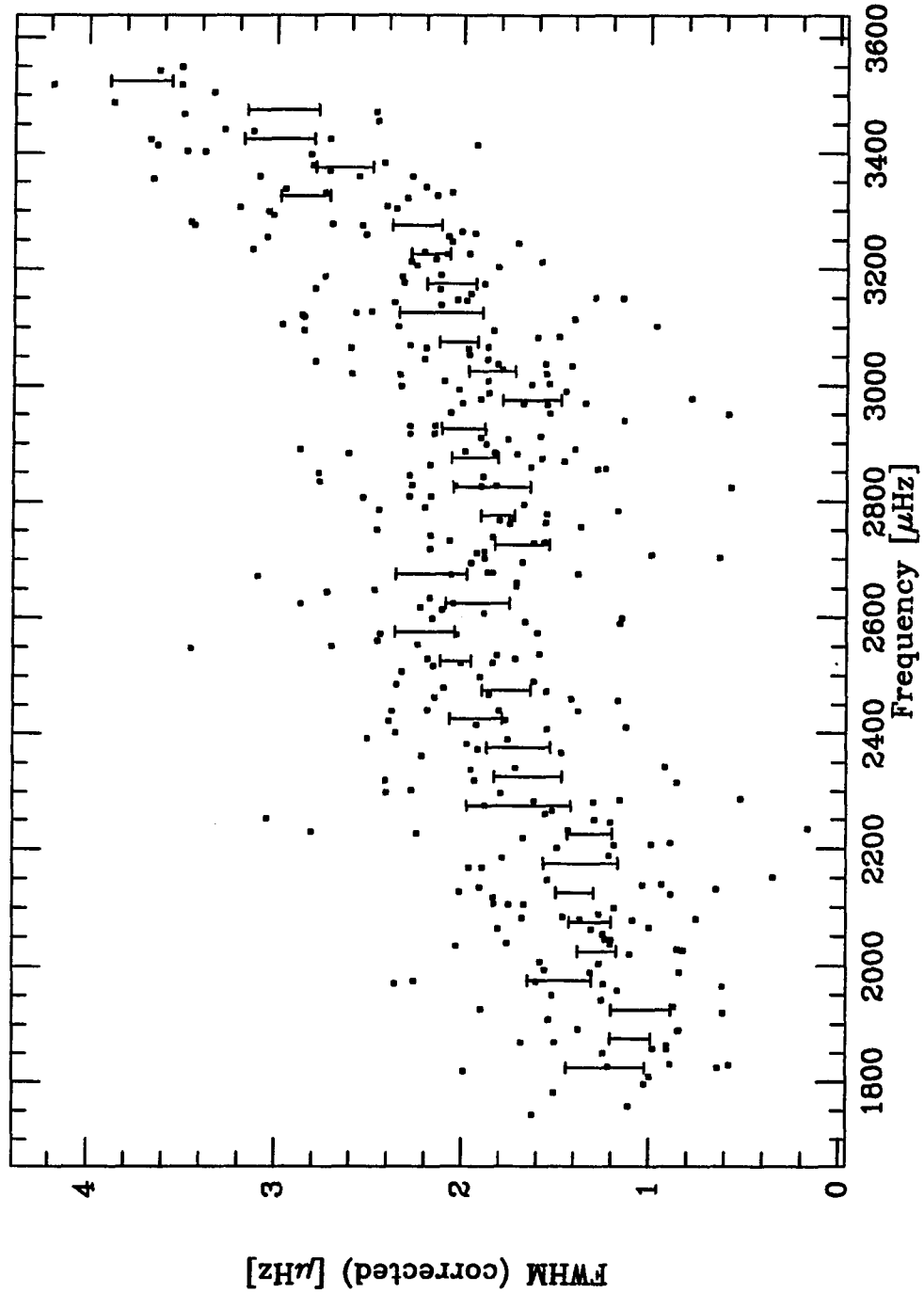


Figure 5.2: FWHM for the modes obtained from the high-resolution spectra. Only FWHM outside the spatio-temporal sidelobes contamination region have been plotted. The error bars correspond to \pm one standard deviation about the mean of $50 \mu\text{Hz}$ wide bins.

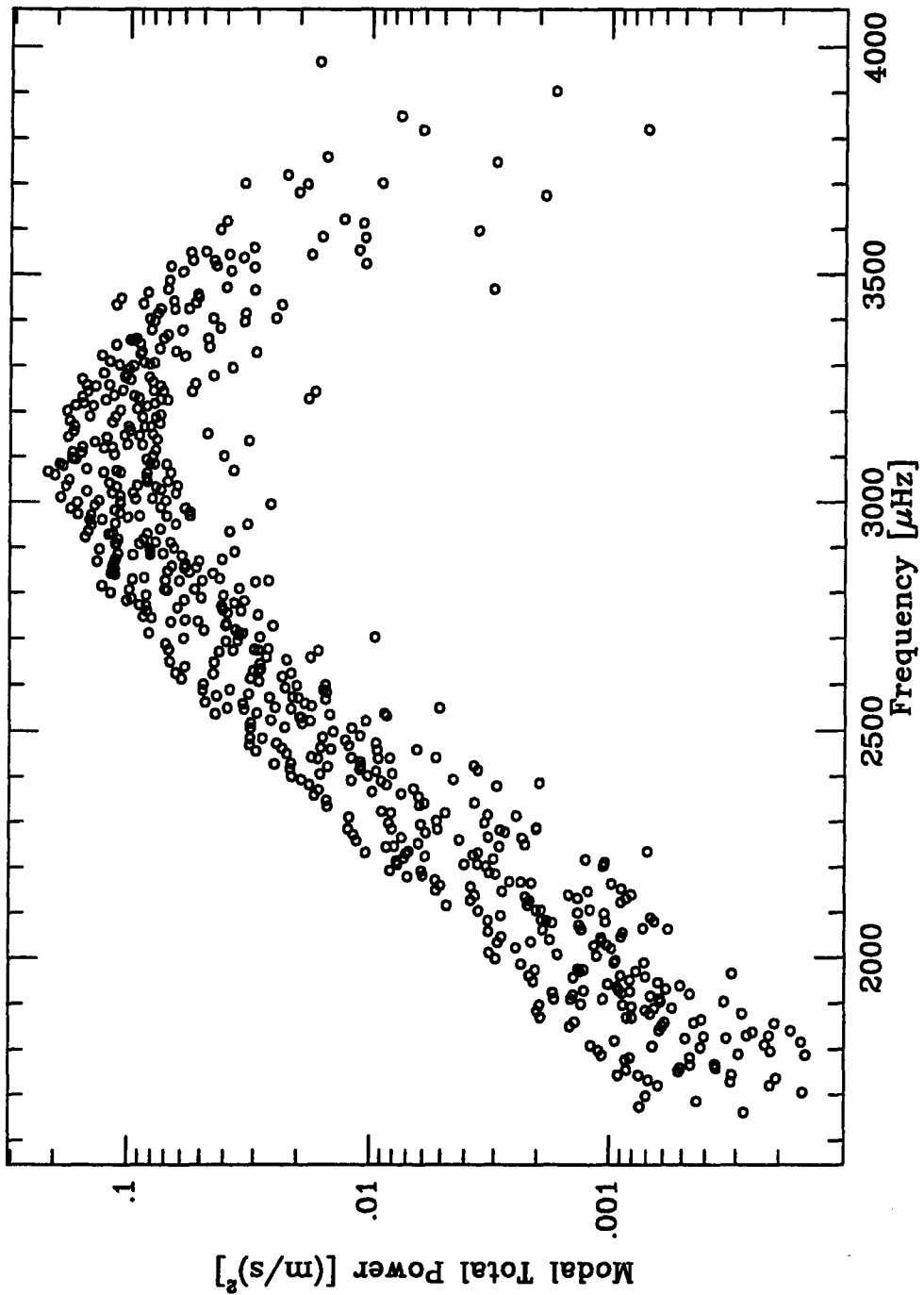


Figure 5.3: Total modal power, corrected for PSF attenuation, for the modes obtained from the high-resolution spectra.

(i.e. $\sim 0.05\%$ for the frequency and $\sim 50\%$ for the FWHM). The analysis of the ℓ - ν plane for mode/sidelobe overlap indicates several regions susceptible to spatio-temporal sidelobe contamination, namely when $\bar{\nu}_{n,\ell} - \bar{\nu}_{n,\ell'} \approx 11.57 \mu\text{Hz}$. These regions are illustrated in Figure 5.4, where cases for which a spatio-temporal sidelobe falls within 2 and 1 μHz respectively of a mode have been plotted.

Therefore, the FWHM plotted in Figure 5.2 were restricted to modes located outside the spatio-temporal sidelobe contamination region. Binned values, with \pm one standard deviation of the mean over the bin (50 μHz wide bins), have been superimposed on top of the individual FWHM. To correct for the convolution by the window function, the FWHM have been corrected by subtracting in quadrature the window function FWHM. Namely, in the Gaussian convolution approximation, we have considered

$$w_{n,\ell}'^2 = w_{n,\ell}^2 + w_{\text{WF}}^2 \quad (5.1)$$

where w' is the measured FWHM and w_{WF} the window function width, namely 0.596 μHz .

Note also that the modal total power plotted in Figure 5.3 was not corrected for spatio-temporal leakage attenuation. Indeed, spatio-temporal leakage causes only a fraction of the mode power to be present in the main lobe of the target spectrum, but this fraction is independent of frequency or degree, and only depends on the normalization used for the spatial decomposition and the Fourier analysis. Since, as discussed at length in Section 5.2.3, the PSF attenuation reduces the observed power at large spatial frequencies, Figure 5.3 presents modal total power corrected for PSF attenuation using the procedure described in Section 5.2.3.

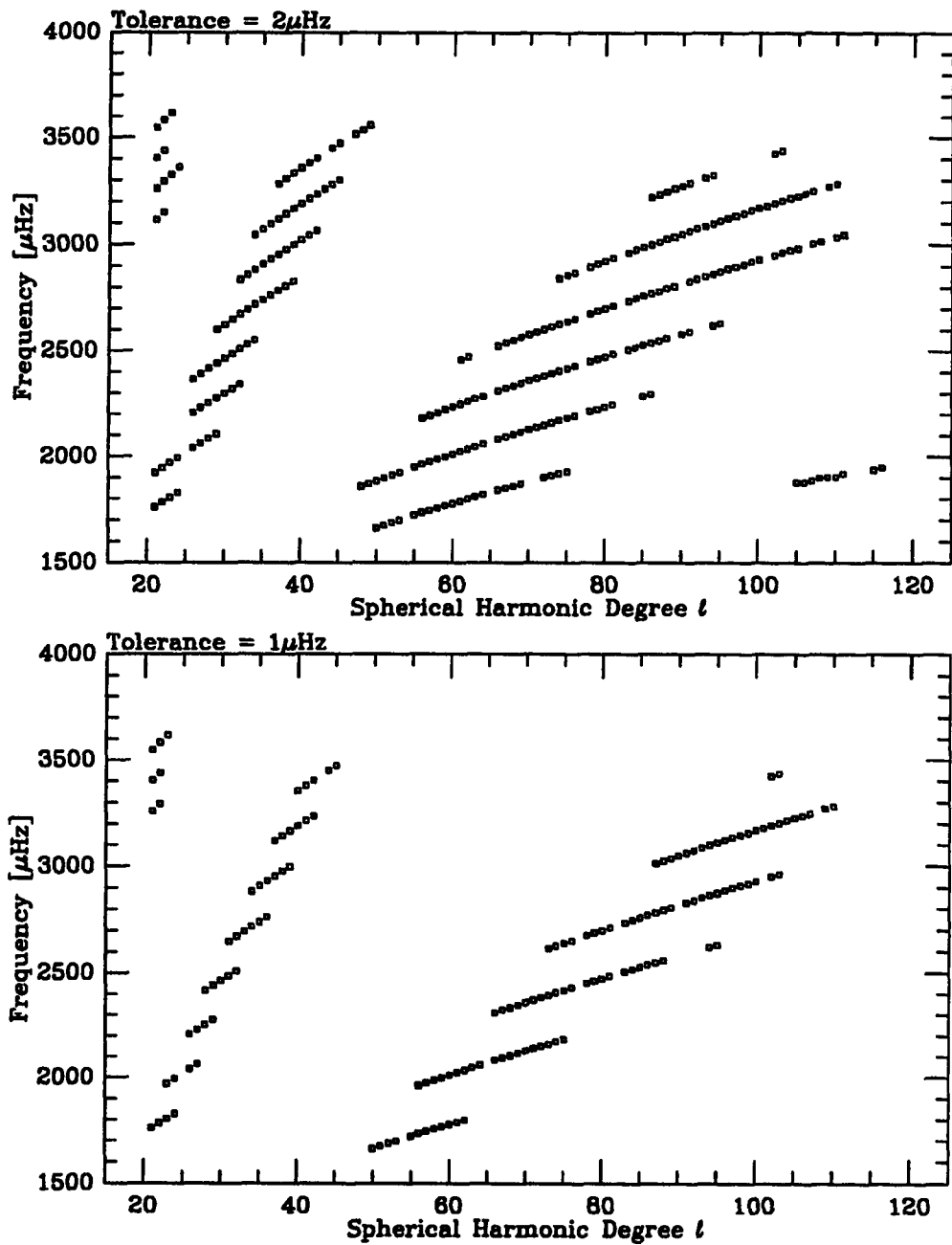


Figure 5.4: Sets of modes sensitive to spatio-temporal sidelobe contamination, namely modes with a spatio-temporal sidelobe that falls within $2\ \mu\text{Hz}$ (upper panel) and $1\ \mu\text{Hz}$ (lower panel) of that mode.

5.1.1 Systematic Effects

We have identified and investigated several potential sources for systematic errors, namely the collapsing procedure, the fitting procedure, and the sidelobe contamination.

Since we have estimated unperturbed mode properties by collapsing all of the even- m tesseral spectra, these measurements are susceptible to systematic effects introduced by the collapsing procedure itself. In order to estimate if any systematic effects were introduced by this procedure, we have performed the frequency splitting analysis and the collapsing using tesseral power spectra as well as tesseral amplitude spectra. While the difference in the frequency splittings ($a_1 + a_3 + a_3$) between the two methods is on the order of one sigma (i.e. -0.08 ± 0.56 nHz² or $0.95 \pm 1.3 \sigma$), the frequency difference is 2.6 ± 2.2 nHz (less than 1 ppm), the FWHM difference is -3.1 ± 8.6 nHz (or $-0.16 \pm 0.43\%$), and the relative difference in the total power is -25.5 ± 0.4 %. In all cases, the differences presented no correlation with frequency or degree. While the two different collapsing procedures lead to a systematic 26% difference in total power³, (depending on whether power spectra or amplitude spectra were used), no significant differences in the measured frequencies and FWHM were observed. Hence, we can conclude with confidence that no systematic errors in the mode width or frequency have been introduced by the collapsing procedure.

Since the fitting procedure used is a multiple steps non-linear procedure (see Section 3.5.2), final results may be dependent on procedural details. In order to estimate these effects we have carried out the fitting procedure using different procedural set-ups. While changing the initial or intermediary steps leads to marginal differences (i.e. due to numerical round-off effects), the portion of the spectrum used for the fit at the last steps of the fitting procedure does influence the final results. Indeed, reducing the portion of the spectrum used for the fit from ± 2 to ± 1.25 times the mode FWHM introduces noticeable differences,

²Mean of the differences and standard error of the mean, i.e. $r.m.s./\sqrt{N}$

³Recall that the sum of the squares is not equal to the square of the sum

namely -2.5 ± 0.5 nHz for the frequency, 114 ± 14 nHz for the FWHM (or $-5.7 \pm 0.7\%$ in relative terms), and -4.7 ± 0.8 % for the total power, in relative terms. Thus, reducing the portion of the spectrum used for the fit introduces a small (but systematic) effect in the frequency (1 ppm), but a non negligible 6% effect for the mode width, and hence, a 5% effect in the total power.

Sidelobe contamination introduces the largest systematic errors, but only in the mode/sidelobe overlapping regions. While it is not possible to directly estimate the amplitude of these systematics since, without uninterrupted observations, the temporal sidelobes cannot be eliminated, they can be nevertheless estimated to be a fraction of the FWHM.

Since, on one hand, the precise location in the ℓ - ν plane of the mode/sidelobe overlapping regions is known, and, on the other hand, the sudden increase of the measured FWHM provides a direct indication of the presence of such contamination, the subset of contaminated modes can be easily identified. Therefore, rather than attempting an *ad hoc* correction, we have simply flagged the contaminated modes.

Note also that, on average, the sidelobe contamination of the frequencies cancelled out. Namely, for the whole subset of contaminated modes, there are an equal number of modes whose frequencies are pulled towards higher values as pulled towards lower values. Hence, since we have used the high-resolution modal frequencies to correct for systematics in the low-resolution results (see Section 5.2.1), the correction itself will not be affected by the contamination.

5.1.2 Uncertainties

Appendix A lists the frequencies, corrected widths, and corrected power amplitudes with their 1σ uncertainties for all of the modes that were successfully fitted. This set has been restricted to modes for which $\sigma_\nu \leq 150$ nHz and $\sigma_P/P < 0.05$.

The uncertainties were estimated from the r.m.s. of the residuals to the fit, based on the following considerations. Let us consider that the r.m.s. of the residual, τ , is actually due to an error in the fitting parameter. We can write, if $f(\nu; c)$ represents the fitting function and c the fitted coefficient,

$$\tau^2 = \int (f(\nu; c) - f(\nu; c'))^2 d\nu \quad (5.2)$$

where $c - c'$ represents the error in the fitting coefficient that would account for the residuals. Approximating $f(\nu; c) \approx f(\nu; c') + (c - c')\partial f/\partial c$, and using $\sigma_c = c - c'$ as an estimate of the uncertainty, we can rewrite Equation (5.2) as

$$\tau^2 = \frac{\sigma_c^2}{2w_{\text{fit}}} \int_{-w_{\text{fit}}}^{w_{\text{fit}}} \left(\frac{\partial f}{\partial c}\right)^2 d\nu \quad (5.3)$$

where w_{fit} is the portion of the spectrum used for the fit. If we replace f by a Lorentzian, centered around ν_o , of amplitude⁴ P , and FWHM w , we obtain

$$\sigma_{\nu_o} = \alpha_{\nu} \frac{\tau w}{P} \quad (5.4)$$

$$\frac{\sigma_P}{P} = \alpha_P \frac{\tau}{P} \quad (5.5)$$

$$\sigma_w = \alpha_w \frac{\tau w}{P} \quad (5.6)$$

where the constants α_{ν} , α_P and α_w are given by some simple dimensionless integrals. For a fitting range twice the FWHM, and assuming ‘‘equipartition’’ of the residuals between the three fitting coefficients, we obtain $\alpha_{\nu} = 0.242$, $\alpha_P = 0.272$, and, $\alpha_w = 0.275$.

5.2 Results from the Low-Resolution Spectra

Frequency, width and power density amplitudes have been computed from the low-resolution m -averaged power spectra for $20 \leq \ell \leq 600$, by fitting a Lorentzian plus a background term, as for the high-resolution case. Since ridges rather than individual modes

⁴Recall that the amplitudes of the Lorentzian profiles fitted to the power spectra represent actually power densities

have been fitted in this case, the frequency, width, and total power needed to be corrected to truly reflect modal properties. Indeed, as discussed in Chapter 4, the ridge centroid, $\tilde{\bar{\nu}}_{n,\ell}$, will be displaced from the target mode frequency, $\bar{\nu}_{n,\ell}$, due to leakage matrix asymmetry and observed modal power distribution. On the other hand, the ridge width reflects not only the convolved mode width but also the ridge slope, while the ridge total power includes leaked power as well as target mode power.

5.2.1 Correction for Systematics: Frequencies

More quantitatively, we can estimate the ridge centroid frequency, $\tilde{\bar{\nu}}_{n,\ell}$ from a simple weighted average, namely

$$\tilde{\bar{\nu}}_{n,\ell} = \frac{\sum_{\ell'} \langle \ell|\ell' \rangle A_{n,\ell'} \bar{\nu}_{n,\ell'}}{\sum_{\ell'} \langle \ell|\ell' \rangle A_{n,\ell'}} \quad (5.7)$$

where $\langle \ell|\ell' \rangle$ represents the m -averaged leakage matrix and $A_{n,\ell'}$ the individual mode amplitude density. As for Section 4.1.4 let us approximate the m -averaged leakage matrix by a Gaussian profile, i.e.

$$\langle \ell|\ell' \rangle \approx \exp\left(-\frac{1}{2}\left(\frac{\Delta\ell - \epsilon\ell}{s}\right)^2\right) \quad (5.8)$$

where $\Delta\ell = \ell' - \ell$, and where the $\epsilon\ell$ term represents the asymmetry introduced by an image scale error of the order of ϵR_\odot . Using $A_{n,\ell'} \approx A_{n,\ell}(1 + d \log A / d\ell \Delta\ell)$, and $\bar{\nu}_{n,\ell'} \approx \bar{\nu}_{n,\ell} + d\bar{\nu} / d\ell \Delta\ell$, we can rewrite Equation (5.7) as

$$\delta\bar{\nu} \approx \frac{\sum_{\Delta\ell} \exp\left(-\frac{(\Delta\ell - \epsilon\ell)^2}{2s^2}\right) \left(1 + \frac{d \log A}{d\ell} \Delta\ell\right) \frac{d\bar{\nu}}{d\ell} \Delta\ell}{\sum_{\Delta\ell} \exp\left(-\frac{(\Delta\ell - \epsilon\ell)^2}{2s^2}\right) \left(1 + \frac{d \log A}{d\ell} \Delta\ell\right)} \quad (5.9)$$

where $\delta\bar{\nu} = \tilde{\bar{\nu}}_{n,\ell} - \bar{\nu}_{n,\ell}$. Replacing the summation by an integral, after some algebra, Equation (5.9) leads to

$$\delta\bar{\nu} = \left(\frac{1}{1 + \epsilon\ell \frac{d \log A}{d\ell}} s^2 \frac{d \log A}{d\ell} + \epsilon\ell \right) \frac{d\bar{\nu}}{d\ell} \quad (5.10)$$

Since $\epsilon\ell \approx 1$ and $d \log A/d\ell = \frac{1}{2}d \log P/d\ell \ll 1$ we can write

$$\delta\bar{\nu} = \left(\frac{1}{2}s^2 \frac{d \log P}{d\ell} + \epsilon\ell\right) \frac{d\bar{\nu}}{d\ell} \quad (5.11)$$

an expression identical to the expression derived by Libbrecht (Libbrecht and Kaufman, 1988).

Using the overlapping results from the high and low resolution cases to measure $\delta\bar{\nu}$ and, since $d\bar{\nu}/d\ell$ and $d \log P/d\ell$ can be directly estimated, s and ϵ can be calibrated and the correction extrapolated to high ℓ . While s could be estimated by computing m -averaged leakage matrices, we have chosen to consider it as a free parameter and to estimate it from the fit.

Note that the derivatives $d\bar{\nu}/d\ell$ and $d \log P/d\ell$, which are total derivatives with respect to degree ℓ at a fixed radial order n , were directly estimated from the set of frequencies obtained from the high resolution spectra and the set of uncorrected power density amplitudes obtained from the low-resolution spectra. For each mode, these derivatives were estimated from the slope of a least-squares straight line fit. The range of the fit, restricted to the modes of the same radial order, was $\pm 5\ell$ for $d\bar{\nu}/d\ell$ and $\pm 7\ell$ for $d \log P/d\ell$.

Using some 230 modes, for $35 \leq \ell \leq 119$ and $2 \leq n \leq 14$, we have fitted in the least-squares sense η and ϵ to

$$\delta\bar{\nu}/\frac{d\bar{\nu}}{d\ell} = \eta \frac{d \log P}{d\ell} + \epsilon\ell \quad (5.12)$$

resulting in $\eta = 2.12$ and $\epsilon = -0.00607$. Figures 5.5 and 5.6 show the partial and total regression plots for the fit and indicate that, indeed, the relation expressed by Equation (5.12) was well satisfied.

These results give a leakage matrix width s of 2.06, and imply that the image size was overestimated by some 0.61%, a value in close agreement with the image size difference observed between the "activity" results and the first derivative results (c.f. 0.58% from Table 3.1). In order to check the validity of the measured leakage matrix width s , and

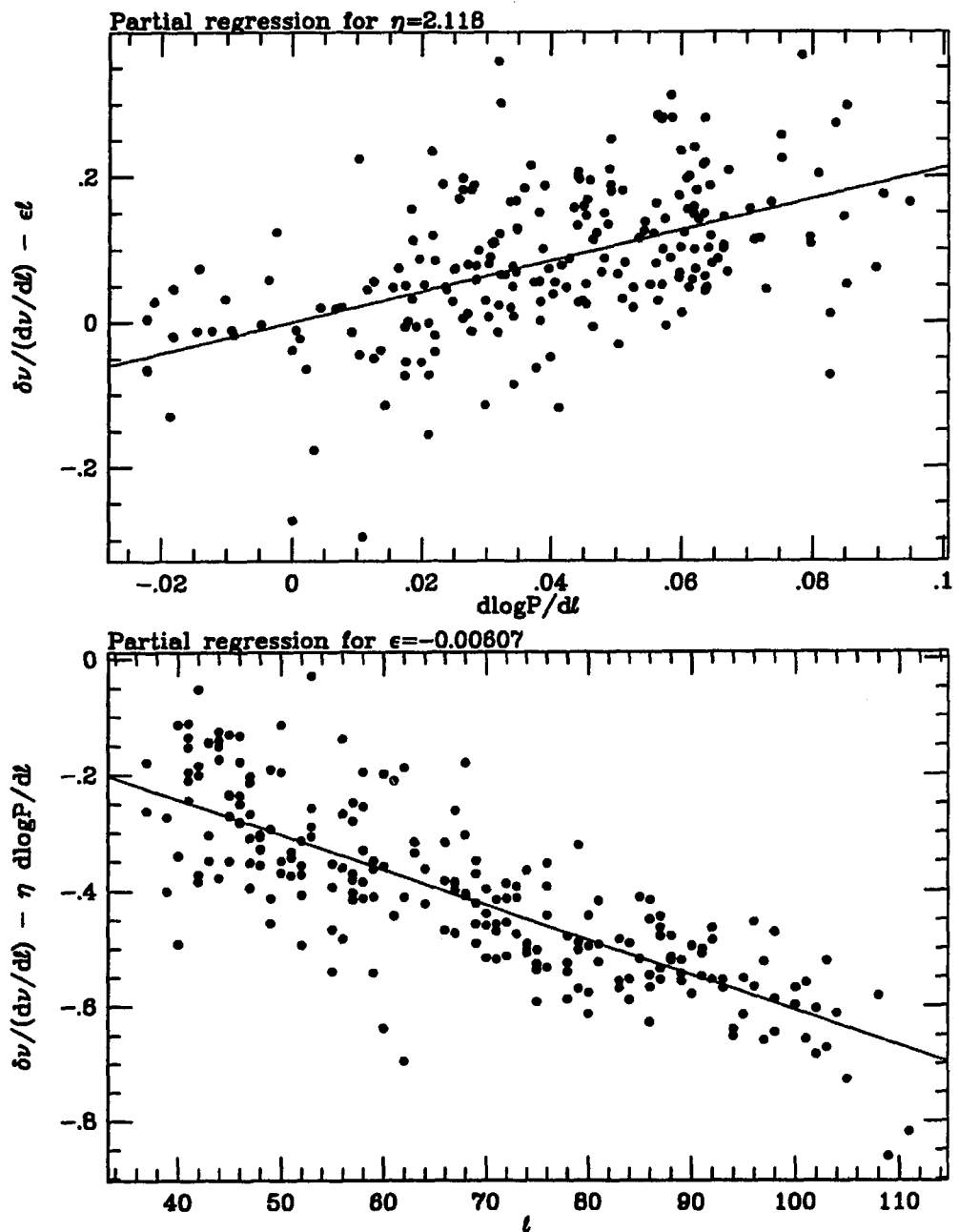


Figure 5.5: Partial regression plots corresponding to Equation (5.12).

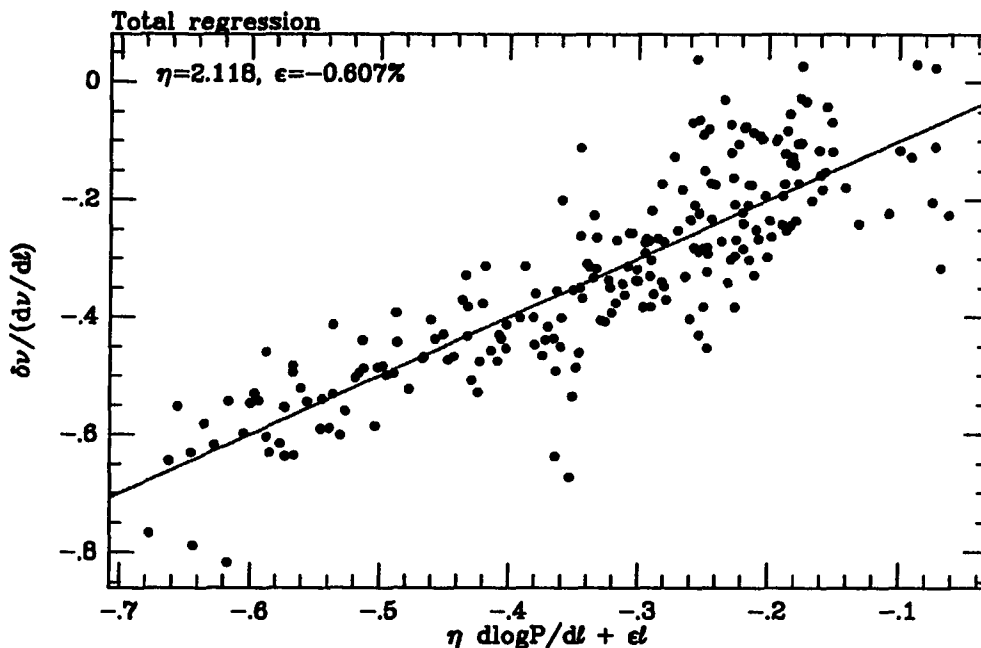


Figure 5.6: Total $\delta\nu/(d\nu/d\ell)$ regression plot corresponding to Equation (5.12).

to confirm that it does not vary with degree ℓ we have computed m -averaged leakage matrices from simulated $\langle \ell, m|\ell', m' \rangle$ leakage matrices (as described in Section 4.1.4). The resulting matrices for $\ell = 90, 150$ and 300 are presented in Figure 5.7, where a Gaussian profile computed with a width $s = 2$ has been superimposed. From this figure we can conclude with confidence that indeed, the leakage width does not vary with ℓ , and that it is indeed adequately represented by a Gaussian profile of width 2. Hence, Equation (5.12) holds for high-degree modes for fixed values of η and ϵ , and therefore can be used to estimate modal frequencies from ridge centroid frequencies.

Some 4370 modal frequencies were estimated from the low spectral resolution ridge centroid frequencies, for $20 \leq \ell \leq 600$, as shown Figure 5.8. The derivatives $d\nu/d\ell$ and $d \log P/d\ell$ were computed using first order centered differences, to which a 4th order polynomial was fitted in the least-squares sense. The fitted polynomials were then used to estimate the derivatives needed to apply the frequency correction as expressed by Equation (5.10) Note that the actual instrumental attenuation of the power density with degree

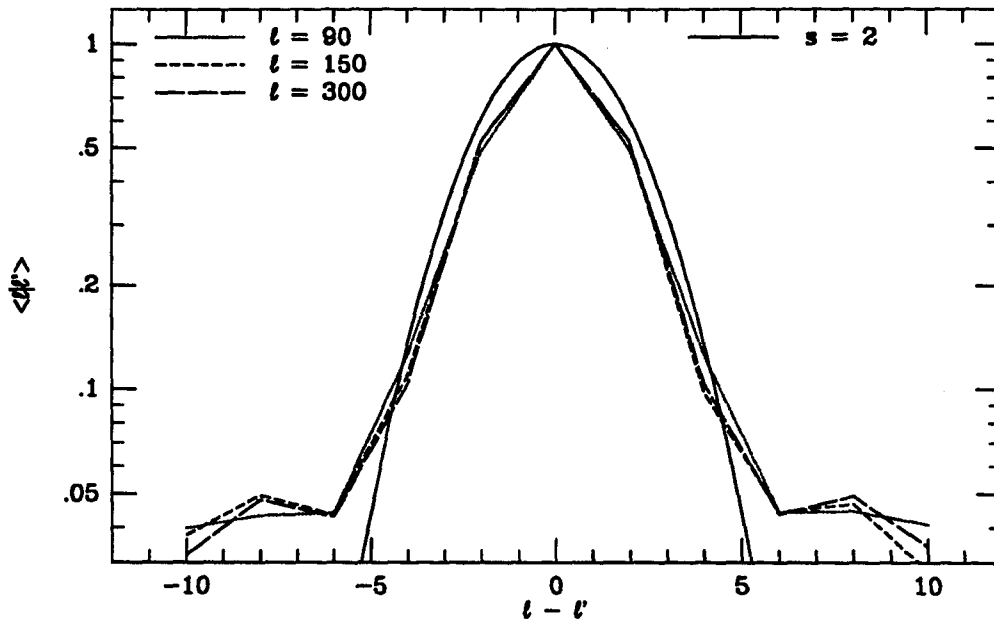


Figure 5.7: Comparison of m -averaged leakage matrices computed from simulated images for $l = 90, 150$ and 300 and a Gaussian profile with $s = 2$.

is properly taken into account by estimating the power density derivative from the uncorrected power density amplitude measurements.

For the overlapping region, the differences between the high-resolution frequencies and the corrected low-resolution frequencies average to 85.0 ± 67.7 nHz (standard deviation of the mean), with no remaining significant dependency on frequency nor degree.

5.2.2 Correction for Systematics: Widths

The ridge width results from a form of convolution between the convoluted mode width and the ridge slope, while the convoluted mode width is the strict result of the convolution of the mode width and the observing window function width. Therefore the ridge width cannot be used as a reliable measurement of the mode lifetime, unless it becomes significantly larger than the ridge slope and the window function width. When both of

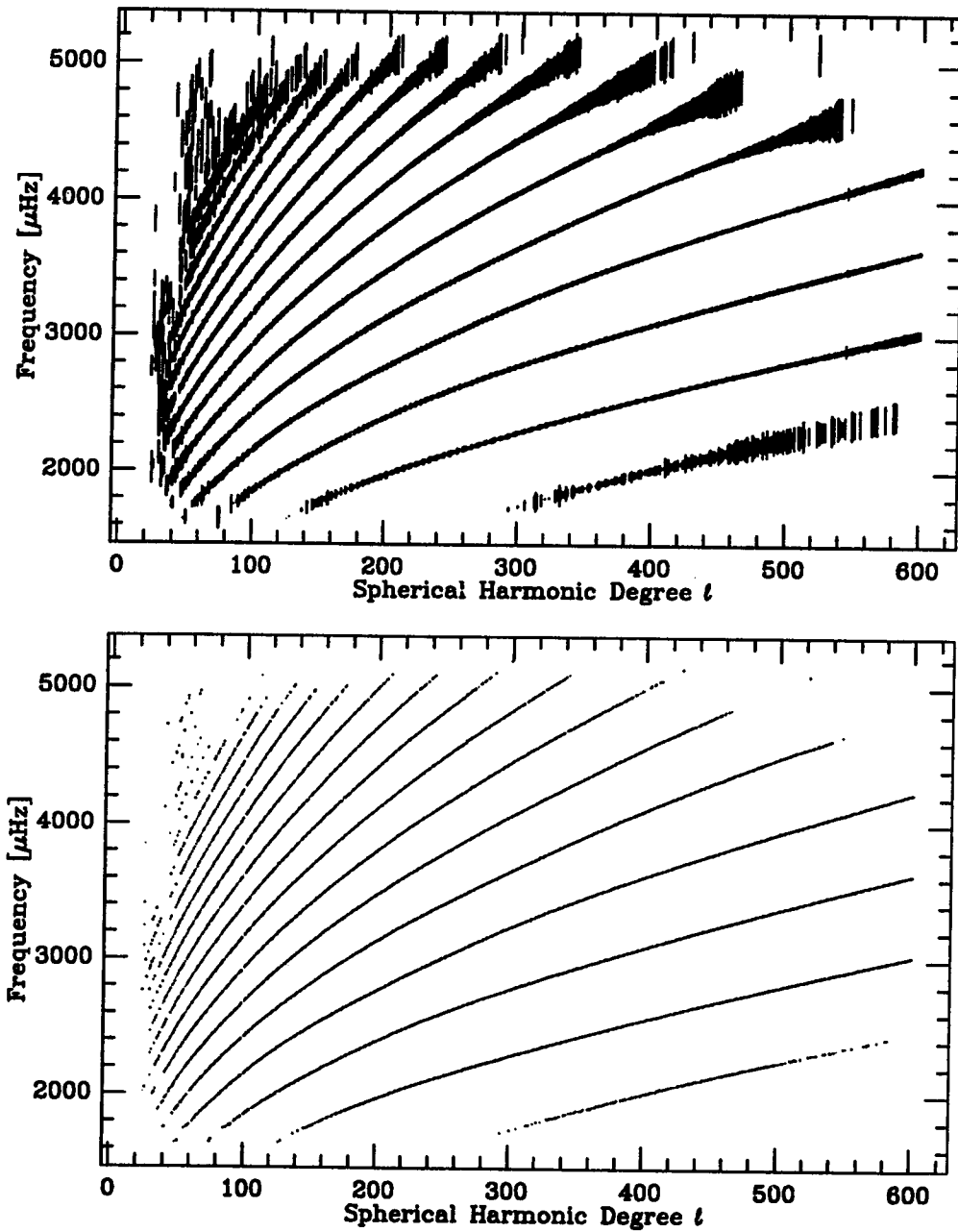


Figure 5.8: l - ν diagram for the modes obtained from the low-resolution spectra; the upper panel shows 100σ error bars.

these conditions are met, we can estimate the modal width through a simple-minded deconvolution. Let us approximate the mode limit spectrum and the window function by Gaussian profiles and assume that the leakage effect can be modelled by a convolution of a Gaussian leakage. Since the convolution of a Gaussian remains a Gaussian, we can write

$$w_{n,\ell,\text{ridge}}^2 = w_{n,\ell}^2 + w_{\text{WF}}^2 + 4 \log 2 \left(s \frac{d\nu}{d\ell} \right)^2 \quad (5.13)$$

where w_{WF} is the window function width, and $s d\nu/d\ell$ the leakage matrix width in frequency space⁵.

Ridge widths (i.e. uncorrected FWHM) are presented in Figure 5.9, while Figure 5.10 presents modal FWHM, corrected according to Equation (5.13), with $w_{\text{WF}} = 27.8 \mu\text{Hz}$ and $s = 2$. Only valid corrected widths (i.e. $w_{n,\ell}^2 > 0$ and with a relative uncertainty smaller than 1/3) have been kept (see also Section 5.2.4). Note that at low degree the vast majority of corrected widths turned out to be not valid. Indeed, since the intrinsic widths at low degree are only a few μHz we should not expect to be able to estimate them from the low-resolution spectra. Moreover, the small FWHM obtained from the low-resolution spectra are the most susceptible to systematic errors associated with the crude deconvolution. Therefore we cannot expect to see a smooth transition between the widths estimated from the low-degree, high-resolution spectra and the widths estimated from the intermediate-degree, low-resolution spectra.

5.2.3 Correction for systematics: Amplitudes

The total power in the ridge does not represent the total power of the target mode but the total power that leaked into the target mode from adjacent mode spatial sidelobes as well as the target mode total power. Hence we can write

$$P_{n,\ell,\text{tot}} = \sum_{\ell'} \langle \ell|\ell' \rangle^2 P_{n,\ell'} \quad (5.14)$$

⁵The factor $4 \log 2$ is introduced by converting e -folding width to FWHM

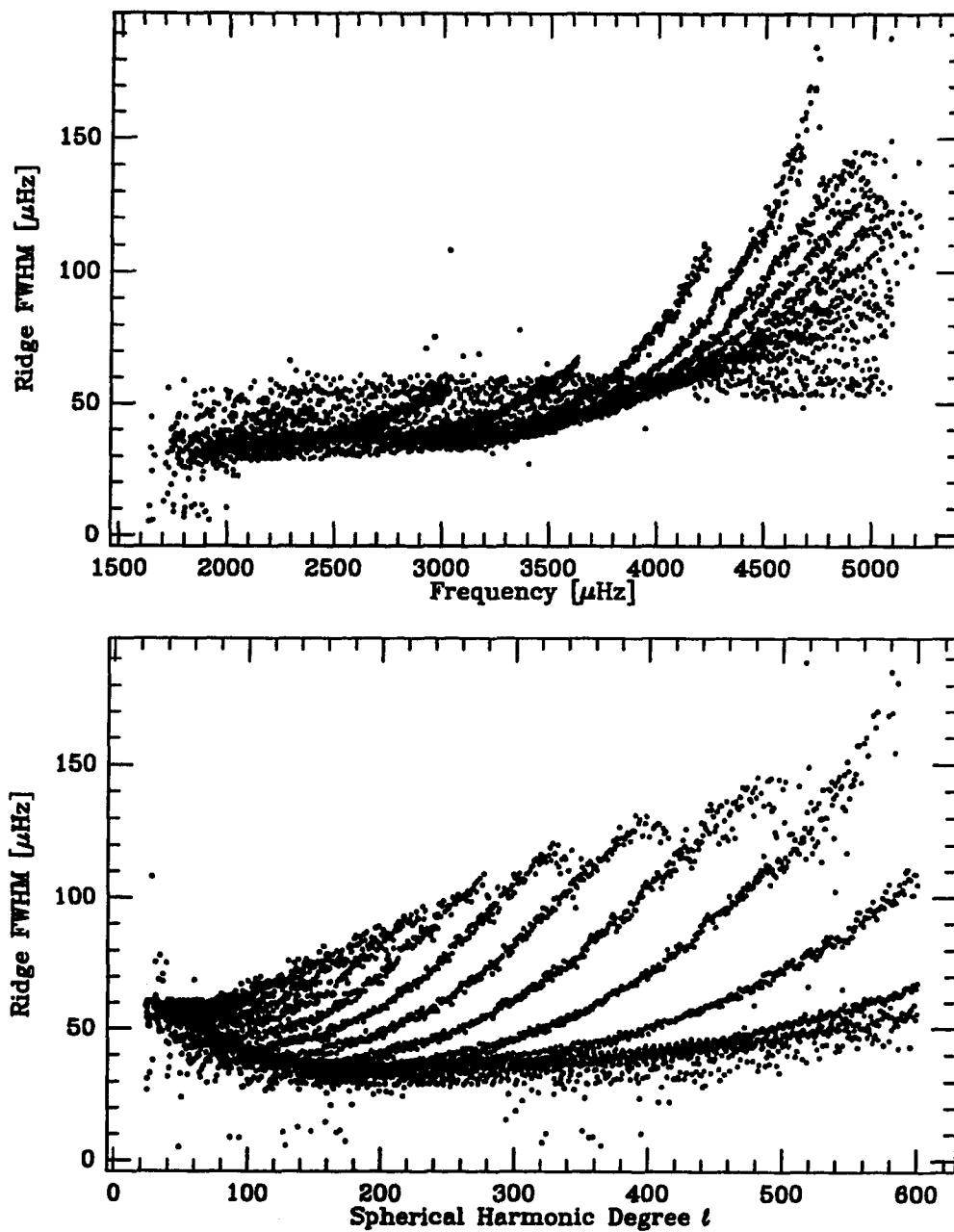


Figure 5.9: Ridge FWHM (i.e. uncorrected FWHM) computed from the low-resolution spectra, as a function of degree (lower panel) and as a function of frequency (upper panel).

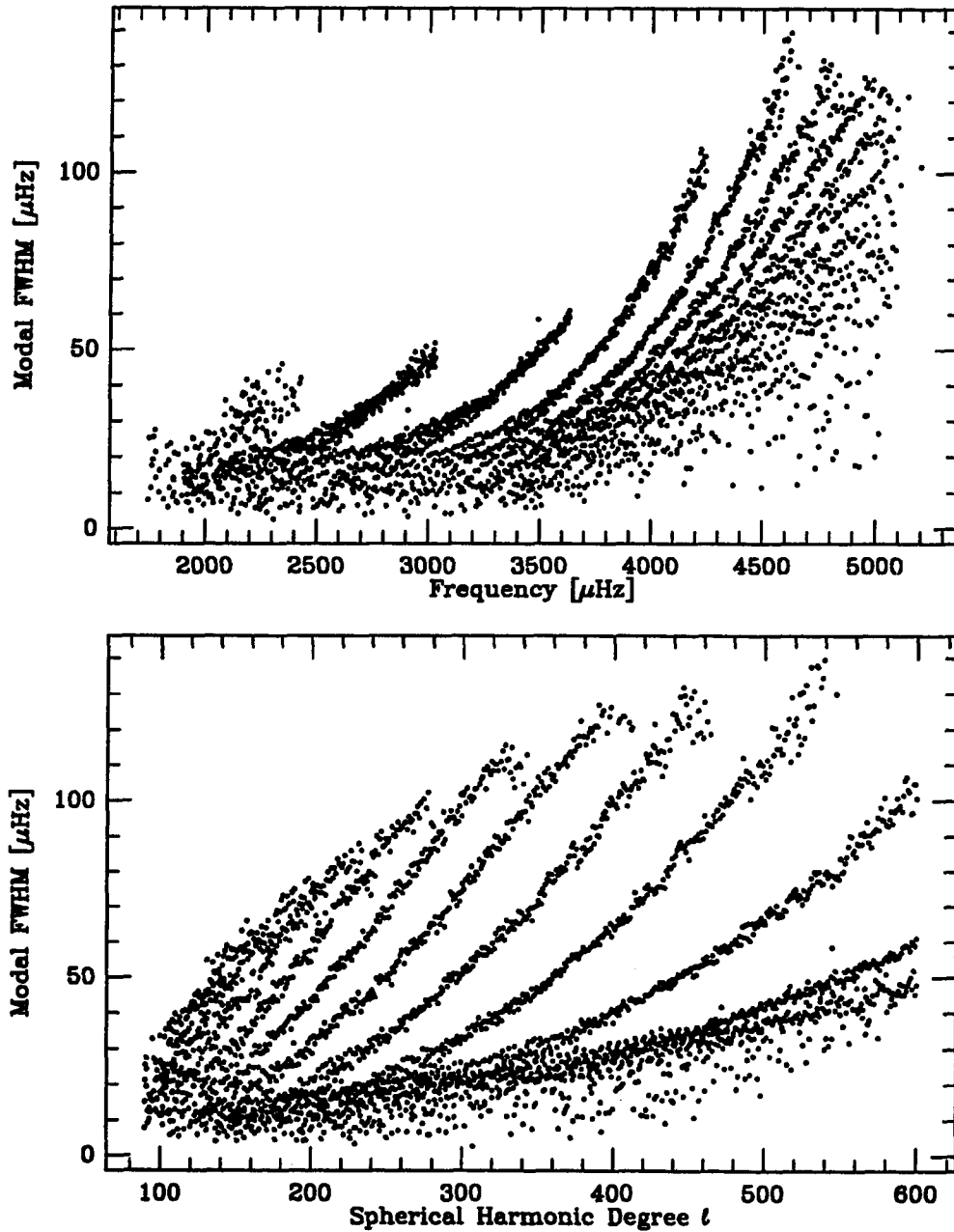


Figure 5.10: Modal FWHM (i.e. corrected FWHM) computed from the low-resolution spectra, as a function of degree (lower panel) and as a function of frequency (upper panel). Only valid corrected widths (i.e. $w_{n,\ell}^2 > 0$ and with a relative uncertainty smaller than $1/3$) have been kept.

and, after the same approximations as above, we can write

$$P_{n,\ell,tot} = P_{n,\ell} s \sqrt{\pi} \left(1 + \epsilon \ell \frac{d \log P}{d \ell} \right) \quad (5.15)$$

Note again that the factor $\epsilon \ell d \log P / d \ell$ remains on the order of 3% and can be neglected, hence only a correction by a constant factor $2\sqrt{\pi}$ is required to account for the leakage.

For high-degree modes, hence high spatial frequencies, the MTF attenuation becomes significant. In order to estimate the mode energy, the observed total power needs to be corrected to account for image smearing by the PSF. Therefore, we have attempted to estimate the total MTF by comparing actual limb profiles to a theoretical limb profile. Since the observed limb profile should be regarded as the convolution of the true limb profile by the PSF, the MTF can be estimated from the the ratio of the Fourier transforms of the observed limb profile and the theoretical “true” limb profile. Thus, the ridge total power was corrected for PSF attenuation by dividing the observed power by the square of the MTF, and for leakage by dividing by the leakage correction factor to obtain an estimate of the modal total power.

Using north-south limb profiles to minimize potential doppler contamination in the limb shape, we have estimated the MTF from the ratio of the average of the Fourier transforms of a small set of observed limb profiles with the Fourier transform of a theoretical limb profile. More precisely, we have used 10 limb profiles (i.e. 5 north and 5 south limbs), extracted from 5 minutes of observation taken on the morning of July 12th. The raw images were converted to “intensity-grams”, namely the registered sum of the red and the blue filtergrams, computed using the same steps as for the computation of a dopplergram, except that at the last step a sum was computed instead of the Doppler ratio. The theoretical limb profile was estimated using the Pierce-Waddell limb darkening parametrization at 5900 Å (Pierce and Waddell, 1961) and only the portion of the limb between -2% and +5% was considered. The resulting averaged and smoothed Fourier transforms and their ratio are shown in Figure 5.11. A two-Gaussian profile was then used to parametrize the

MTF and fitted in the least-squares sense to the ratio. Namely

$$\text{MTF}(\ell) = \frac{1}{1 + \alpha} \left(\exp\left(-\left(\frac{\ell}{\sigma_1}\right)^2\right) + \alpha \exp\left(-\left(\frac{\ell}{\sigma_2}\right)^2\right) \right) \quad (5.16)$$

was fitted to the observed ratio, as presented also in Figure 5.11, giving $\sigma_1 = 250.2$, $\sigma_2 = 1227.2$ and $\alpha = 0.1203$. The resulting estimate of the total modal power as a function of frequency and degree is presented in Figure 5.12.

Let us point out that this estimate of the MTF was based on small subset of limb profiles, extracted from early morning images obtained on an average seeing day. Most probably, the overall average MTF for the full 20 days of observations is worse than our 5 minute based estimate, since the seeing quality degrades later in the day. A better approach to estimate the correction for the PSF attenuation would have been to estimate the MTF for each day, if not for each hour of observation and apply the correction to the spherical harmonic coefficients themselves rather than to the power spectra. Such a procedure will be implemented in the near future on subsequent reductions of similar observations.

5.2.4 Uncertainties

As for the high spectral resolution results, uncertainties were estimated from the r.m.s. of the residuals to the fit. Since the frequency resolution of the low-resolution spectra is an order of magnitude smaller than for the high-resolution spectra, only modes for which $\sigma_\nu < 1.5 \mu\text{Hz}$ and $\sigma_P/P < 0.05$ were kept. A selection of these modal frequencies, widths and power amplitudes are listed in Appendix C.

Alternatively, we have also estimated frequency uncertainties from the internal scatter about the ridge. Using $10\text{-}\ell$ wide portions of each ridge, a quadratic polynomial in ℓ was fitted to the corrected frequencies, using the inverse of the r.m.s. based uncertainty as weights. The scatter of the residuals to the polynomial fit was then computed as a measure of the uncertainty. Since the standard deviations of the mean computed this

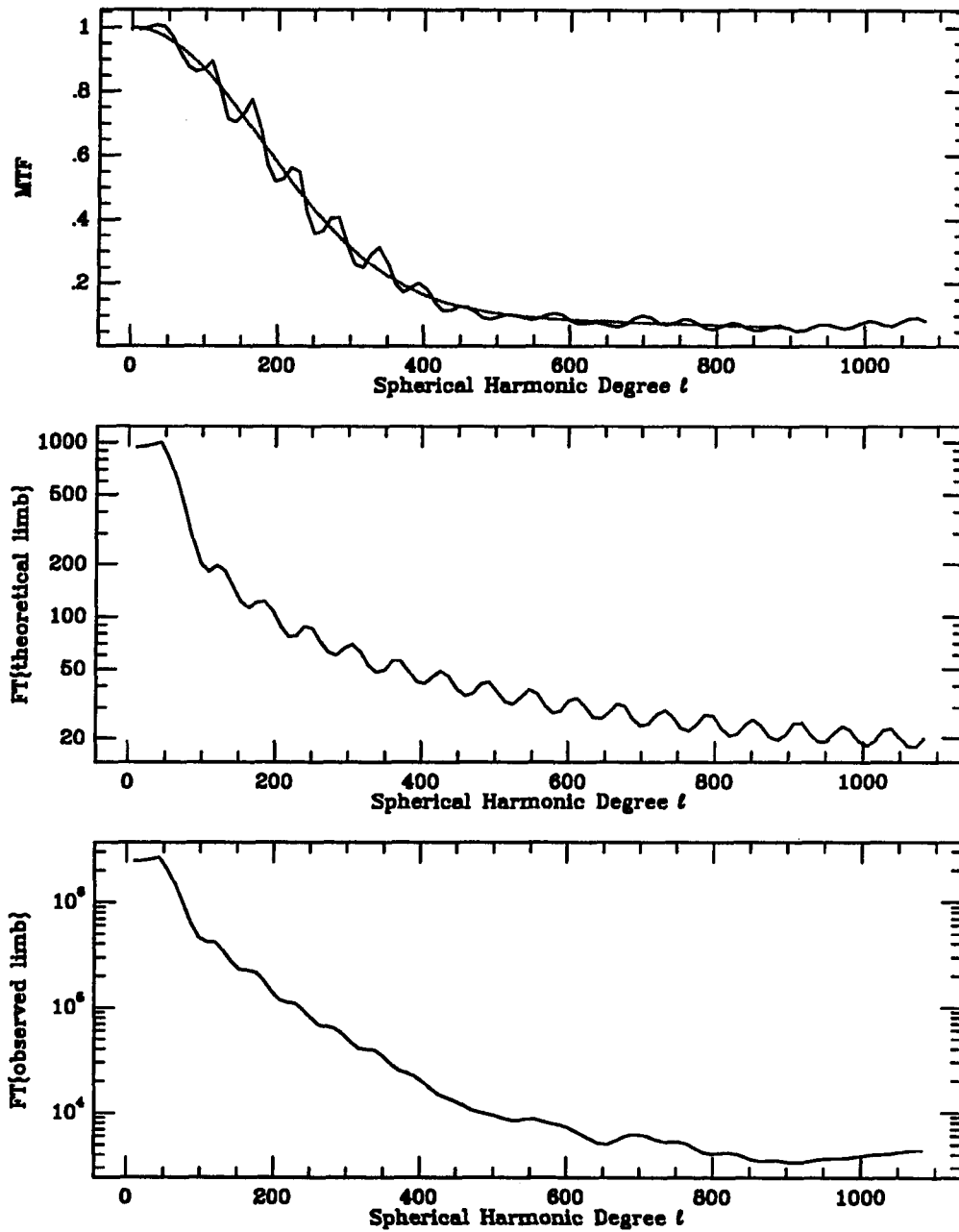


Figure 5.11: Fourier transforms of the observed limb (bottom panel), the theoretical limb (middle panel) and the resulting MTF (top panel) estimated from the ratio, and the two-Gaussian profile fitted to the ratio (dash line).

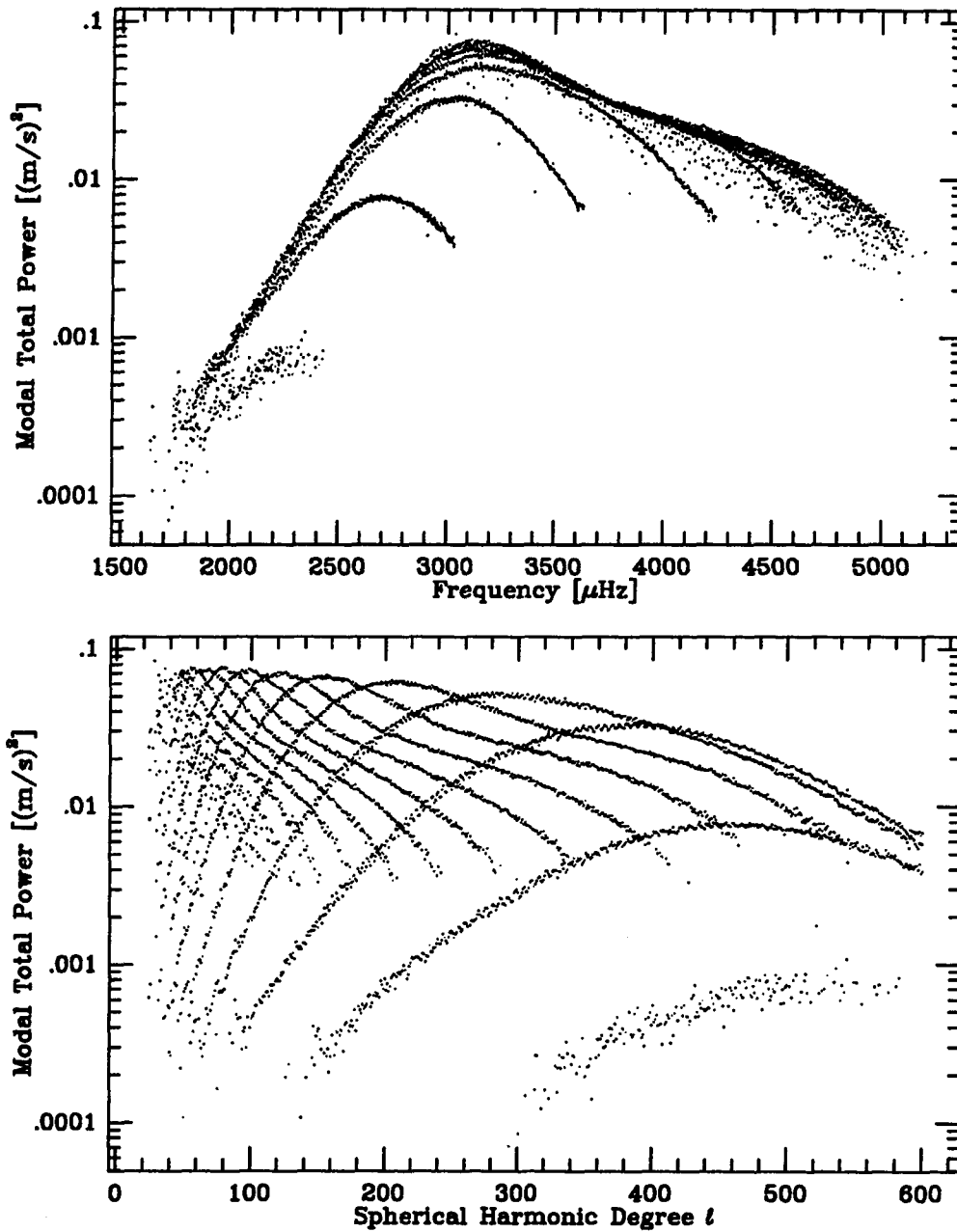


Figure 5.12: Total modal power estimated from the low-resolution spectra, as a function of degree (lower panel) and as a function of frequency (upper panel).

way were of the same magnitude as the uncertainties computed from the Lorentzian fit residuals r.m.s., the uncertainties computed from the r.m.s. of the residuals must have been underestimated by a factor $\sqrt{N} \simeq 3$, invalidating the “equipartition” assumption.

Since widths were corrected according to Equation (5.13), the uncertainty introduced by the correction should be propagated to the corrected width uncertainties. Since there is no uncertainty associated with the window function width per say, and the uncertainty on the ridge slope is itself small, let us simply consider $w_c^2 = w^2 - w_o^2$, where w_c is the corrected width, w the measured width and w_o some offset width with negligible uncertainty. Error propagation gives

$$\delta w_c = \frac{w}{w_c} \delta w \quad (5.17)$$

hence a large error magnification when $w_c \ll w$. Therefore, only when the relative error on the corrected width was smaller than 1/3 were the corrected widths considered to be valid.

Two potential sources of systematic errors in the mode width estimates should be addressed. First, any systematic errors in the frequency splitting measurements lead to corrupted FWHM. Indeed, since we measure the FWHM of the collapsed spectra, an improper collapsing due to a corrupted frequency splitting estimate will lead to a widened collapsed ridge, hence an overestimate of the modal FWHM. Secondly, the simple-minded nature of the “deconvolution” procedure will leave some residual systematic errors in the corrected FWHM. More quantitatively, an error in the frequency splitting, used for the collapsing will correspond to an error in the frequency shift of the order of $m \delta(\Delta\nu/L)$, hence a potential systematic error on the order of 2 μHz when considering $m = \ell = 500$ and $\delta(\Delta\nu/L) \approx 2 \text{ nHz}$. Similarly, since $s d\nu/d\ell$ is on the order of 10 μHz , the residual systematics associated to the leakage “deconvolution” may not be much larger than a few μHz . In both cases, the potential systematics remain an order of magnitude smaller than the FWHM, except for low-degree and low-frequency modes.

5.3 Comparisons with Previous Measurements

5.3.1 High-Resolution Results

As for the splittings, we have limited ourselves to comparing the low- and intermediate-degree, high-resolution frequency set to the most contemporary data set available, namely a preliminary release of modal frequencies based on the 1988 BBSO observations (3 month run). The frequency differences between both sets are shown Figure 5.13 and they average to 52.2 ± 197.3 nHz (mean \pm r.m.s., with a 5σ rejection). No significant dependence of the frequency differences with frequency or degree is present (regression coefficients: with frequency $\rho_\nu = -0.062$, with degree $\rho_l = -0.046$). If we compare the ratio of the differences to their uncertainties (i.e. $\Delta\nu/\sigma$, where σ is the largest uncertainty given in the two sets for each mode), then the σ -weighted differences average to 1.02 ± 3.12 .

While the intrinsic scatter and the uncertainties in our measurement is larger than in the BBSO study, as the respective observing run lengths would predict, marginally significant systematic differences between the two sets at the ~ 50 nHz level can be detected.

On a strictly qualitative level, the comparison of the modal width and total power with published values (see for instance Figure 3 in Libbrecht, 1988) shows good agreement of the overall frequency dependence between the results of the present study and these measurements.

5.3.2 Low-Resolution Results

Contrary to the low- and intermediate-degree results, there is to this date no contemporary high-degree measurements available for direct comparison. Nevertheless a set of high-degree frequencies, based on two distinct 1-day-long runs acquired in the summer of 1987, has been distributed as preliminary results and preprints by the Caltech group (Libbrecht

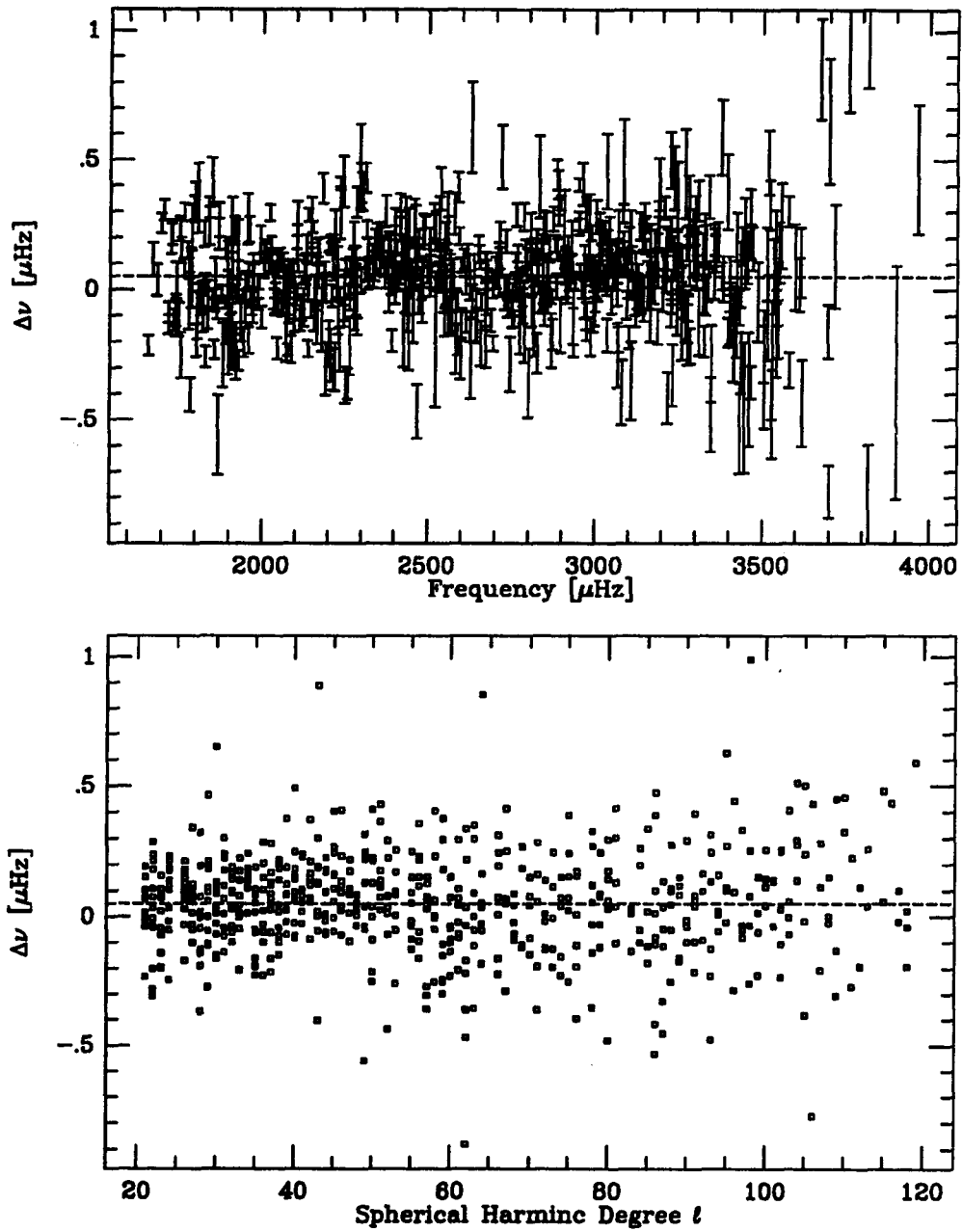


Figure 5.13: Modal frequency differences between BBSO 1988 set and the present study high-resolution modal frequencies, as a function of degree (lower panel) and as a function of frequency (upper panel).

et al., 1990). Note that the earlier analysis by the same group leading to high-degree modes ($30 \leq \ell \leq 1320$, Libbrecht and Kaufman, 1988) has been since discarded by these authors as being contaminated by systematics on the order of 10–12 μHz (Libbrecht *et al.*, 1990) and will therefore not be considered here.

Modes for $140 < \ell \leq 400$ have been measured by the Caltech group from ridge fitting to m -averaged spectra based on 9.5 hours of full-disk intensity measurements. Gaussian profiles with a background term were fitted to the ridges, and frequency centroids of the Gaussian fits corrected for power density distribution asymmetries. Image scale error correction was deemed unnecessary by the authors of that study (see further discussion in Libbrecht *et al.*, 1990). Mode frequencies were then binned over $5\text{-}\ell$ wide bins.

For $400 < \ell \leq 1860$ mode frequencies were estimated from 10 hours of doppler measurements of a portion of the solar disk. Using a plane wave approximation, a three-dimensional Fourier transform was applied to these disk-center data. The spectra were corrected for rotational frequency shifts and averaged along constant spatial frequencies, producing spectra similar to m -averaged spectra obtained with the more rigorous spherical harmonic decomposition procedure (see further details in Libbrecht *et al.*, 1990 and Hill, 1988). Ridge centroids were estimated by fitting a series of Gaussian profiles (i.e. one for each visible ridge and one as an overall background term) and a constant background term. The overlap region between $\ell \leq 140$ and $\ell \leq 400$ was used to calibrated the spatial frequency scale, and a cubic spline based interpolation was then performed to estimate modal frequencies at integral values of ℓ .

Figure 5.14 presents comparisons of our low-resolution frequencies to the BBSO results and Table 5.1 presents the average and the r.m.s. of these differences. Note that an ℓ -binning comparable to the BBSO set was not performed for our data set⁶.

⁶Considering the amplitude of the differences, such binning would not modify significantly the comparison

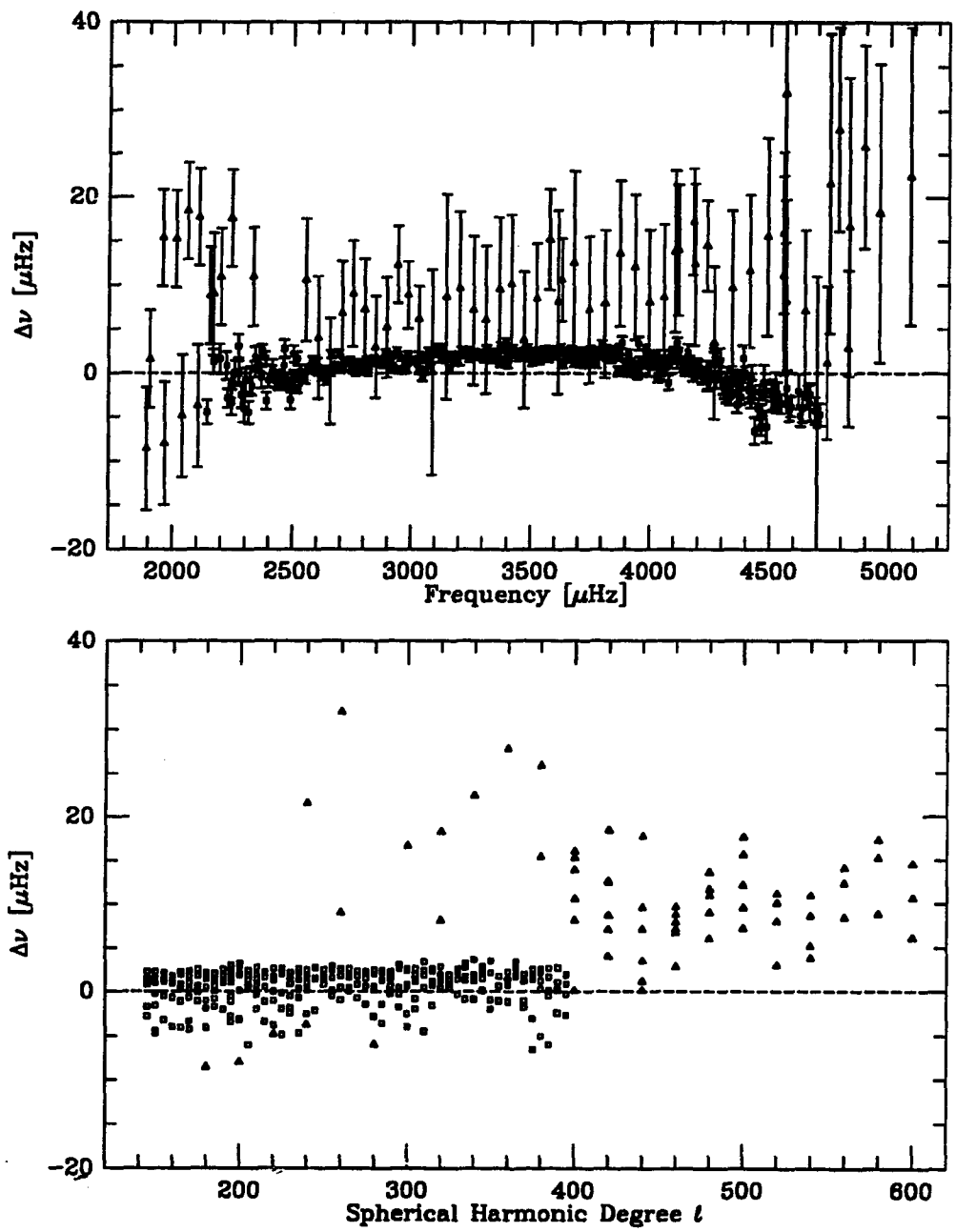


Figure 5.14: Modal frequency difference between BBSO high-degree measurements based on two distinct one-day-long observation runs at intermediate (squares) and high spatial resolution (triangles) and the high-degree, low-resolution frequencies from the present study. Notice that the frequency scale is some 30 times larger than it was in Figure 5.13.

	set a	set b	both sets
$\Delta\nu$ (μHz)	0.60 ± 1.95	9.82 ± 7.69	2.00 ± 4.51
$\Delta\nu/\sigma$	2.13 ± 3.85	1.26 ± 1.60	1.89 ± 3.57

average \pm r.m.s., with a 5σ rejection

set a: Full-disk intensity measurements, 318 overlapping modes ($145 \leq \ell \leq 400$)

set b: Disk-center doppler measurements, 67 overlapping modes ($180 \leq \ell \leq 600$)

Table 5.1: Comparison of high-degree modal frequencies with BBSO measurements

Figure 5.14 and Table 5.1 indicate clearly that significant differences between both sets are present. When comparing our results to the the intermediate spatial resolution full-disk measurements, a definite frequency dependent pattern of the differences is present, of some $8\ \mu\text{Hz}$ peak to peak in amplitude, while overall the differences average to some $0.6\ \mu\text{Hz}$, and no significant trend with ℓ can be observed. Since this frequency dependent pattern is similar to the frequency dependence of one of the terms used in the power distribution asymmetry correction (namely $\partial \log P / \partial \nu$ since the Caltech group used the approximation $d \log P / d \ell \approx \partial \log P / \partial \nu \times \partial \nu / \partial \ell + \partial \log P / \partial \ell$ and this term was estimated using an *ad hoc* procedure), we are tempted to attribute these difference to some incompleteness of the power distribution asymmetry correction performed on the BBSO set.

When comparing our results to the disk-center measurements, a systematic difference of some $9\ \mu\text{Hz}$ is observed. This difference is consistent with the quoted potential systematic errors present on the BBSO set and is on the order of the quoted uncertainties. Notice also that a less pronounced frequency dependence, similar in shape but with opposite curvature, can be observed. As for the BBSO full-disk measurements we are tempted to attribute this discrepancy to uncorrected systematics in the BBSO set. Moreover, the fact that these frequency-dependent discrepancies present opposite curvatures when our unique set of frequencies is compared to two distinct sets of measurements confirms that the source of these differences lies with remaining systematics which are not accounted for adequately in the BBSO sets.

Finally let us point out that the comparison for the overlapping range in ℓ of our low

spectral resolution estimates with our high spectral resolution measurements indicated residual differences on the order of $0.08 \mu\text{Hz}$, while the comparison of our high resolution measurements with independent contemporaneous measurements indicated a remarkable agreement between the two sets down to the $0.05 \mu\text{Hz}$ level, with in both cases no significant trends with frequency. Therefore, the source of the discrepancies at intermediate and high degrees is on that basis also most likely due to remaining systematic errors that we believe are present in the BBSO frequency sets.

In contrast to all previous estimates of intermediate- and high-degree modal frequencies, we were able in the present study to derive from the same set of observations resolved modal frequencies at low and intermediate degrees as well as estimates of modal frequencies at intermediate and high degrees. Moreover, our measurements are based on a significantly longer observing run than are all of the previous similar observations. Therefore, we are confident that any remaining systematic errors present in our set of intermediate- and high-degree frequency estimates is most likely to be below some $0.2 \mu\text{Hz}$.

5.4 Comparison with Theory

Figure 5.15 compares the observed modal frequencies to theoretical frequencies computed from a standard solar model (Korzennik and Ulrich, 1989) where the difference between the theoretical modal frequencies and the observed ones is plotted as a function of mode frequency and as a function of spherical harmonic degree, ℓ , respectively. The extension of such a comparison to high-degree modes indicates that on one hand the overall trend of the dependency with frequency of the differences between observation and theory is extended to higher frequencies, namely an increase of the differences with frequency that reaches some $30\text{--}50 \mu\text{Hz}$ around $5000 \mu\text{Hz}$. On the other hand, the comparison indicates that at high degree and high frequency the differences increase with degree as well. Notice

that the differences corresponding to the f-mode present the opposite trend as a function of degree, namely a decrease with ℓ , while the trend with frequency is not very different that for the p-modes.

Despite the fact that the disagreement between theoretical and observed solar oscillations is significant when compared to the observational uncertainties, these discrepancies are small in relative terms since they remain on the order of one to two percent. By contrast, there is no definite theoretical predictions of solar oscillation amplitudes and linewidths since the excitation and damping mechanisms themselves have not yet been unambiguously identified. While the discussion of the possible excitation and damping mechanisms is beyond the scope of this study, we will now present some related results, namely the total energy per mode and the mode lifetimes.

The mode energy can be estimated from the product of the corrected modal total power by the mode mass, $M_{n,\ell}$, since the mode mass is defined as to represent the mode kinetic energy divided by the mode mean square surface velocity, hence

$$M_{n,\ell} = \frac{1}{v_{\text{surf}}^2} \int \frac{1}{2} (\rho v^2 + \frac{c^2 \rho'}{\rho_o}) dV \quad (5.18)$$

where v is the mode radial velocity eigenfunction, ρ' the density perturbation eigenfunction and ρ_o the unperturbed density. The surface normalization, (i.e. the location of v_{surf}), has been selected as to represent the height in the atmosphere where the contribution functions of the sodium D lines are the most significant (Schleicher, 1976), namely 500 km (or $\tau_{5000} = 3 \times 10^{-4}$). The resulting estimates of the modal energy based on the low-resolution total modal power as a function of frequency and as a function of degree are shown in Figure 5.16. Figure 5.16 indicates that the total energy per mode decreases with degree, by a factor ~ 7 between $\ell = 100$ and $\ell = 400$. This result is not very dissimilar from an estimate based on disk-center measurements, obtained of Kaufman (1988), who measured a decrease by a factor ~ 5 between $\ell = 200$ and $\ell = 700$. Such a decrease would invalidate energy equipartition between the modes and the convective turbulence eddies,

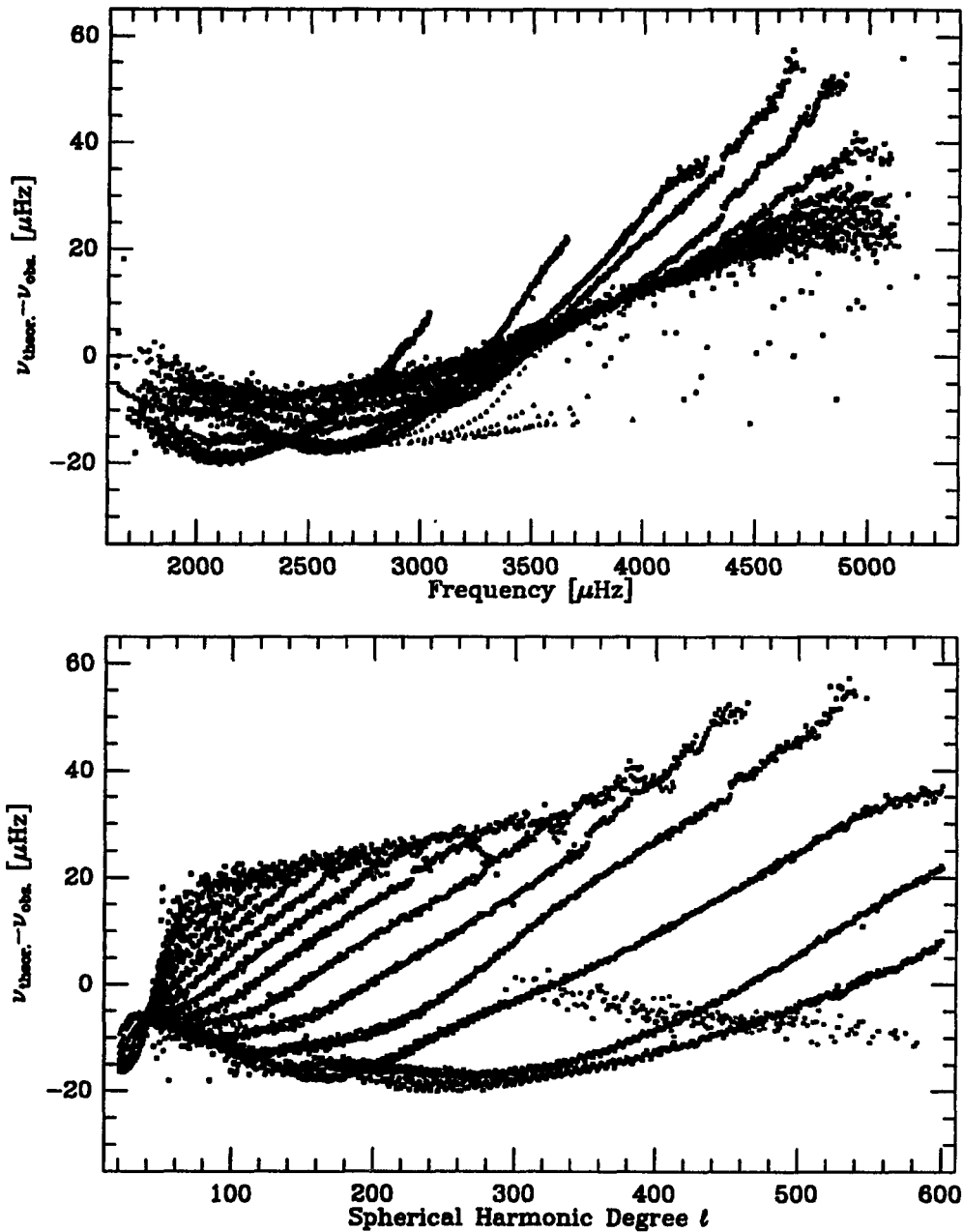


Figure 5.15: Comparison of observed frequencies with theoretical frequencies computed with a standard solar model. The differences based on the low- and intermediate degree modes computed from the high-resolution spectra are indicated by triangles, while the differences based on the intermediate- and high-degree frequencies computed from the low-resolution spectra are indicated by squares. The differences corresponding to the f-mode are indicated by filled squares. The upper panel shows these differences as a function of frequency while the lower panel shows them as a function of spherical harmonic degree.

since the energy equipartition would imply an modal energy independent of degree.

The mode lifetime (i.e. the e-folding decay time) is simply given by

$$T_{n,\ell} = \frac{2}{w_{n,\ell}} \quad (5.19)$$

and provides some measure of the cavity quality factor. Therefore, we have attempted to correlate the observed modal lifetimes to potential indicators of the cavity quality factor. We have used as potential indicators of the cavity quality factor the modal frequency, the inner turning point, the mode mass, and the turbulent pressure overlap integral.

We have defined a “turbulent pressure overlap integral” as

$$X_c = \frac{\int \rho_o v_{\text{turb}}^2 \rho_o \xi_r^2 r^2 dr}{\int \rho_o \xi_r^2 r^2 dr} \quad (5.20)$$

where $\rho_o v_{\text{turb}}^2$ represents the turbulent pressure in the solar convection zone. If turbulent pressure were the main source of mode excitation we would expect to see some correlation between this overlap integral and the modal lifetime.

Quality factors for acoustic modes in equilibrium with turbulence, under different turbulence excitation conditions and under different regimes, have been derived by Goldreich and Kumar (1988). These expressions are, for free turbulence

$$Q(\nu) \sim \frac{2\pi\nu\tau_H}{\mathcal{M}^2 f} \quad 2\pi\nu\tau_H \lesssim Re^{3/4} \quad (5.21)$$

for forced turbulence

$$Q(\nu) \sim \frac{2\pi\nu\tau_H}{f} \quad 2\pi\nu\tau_H \lesssim 1 \quad (5.22)$$

$$Q(\nu) \sim \frac{(2\pi\nu\tau_H)^3}{f} \quad 1 \lesssim 2\pi\nu\tau_H \lesssim \mathcal{M}^{-1} \quad (5.23)$$

$$Q(\nu) \sim \frac{2\pi\nu\tau_H}{\mathcal{M}^2 f} \quad \mathcal{M}^{-1} \lesssim 2\pi\nu\tau_H \lesssim Re^{3/4} \quad (5.24)$$

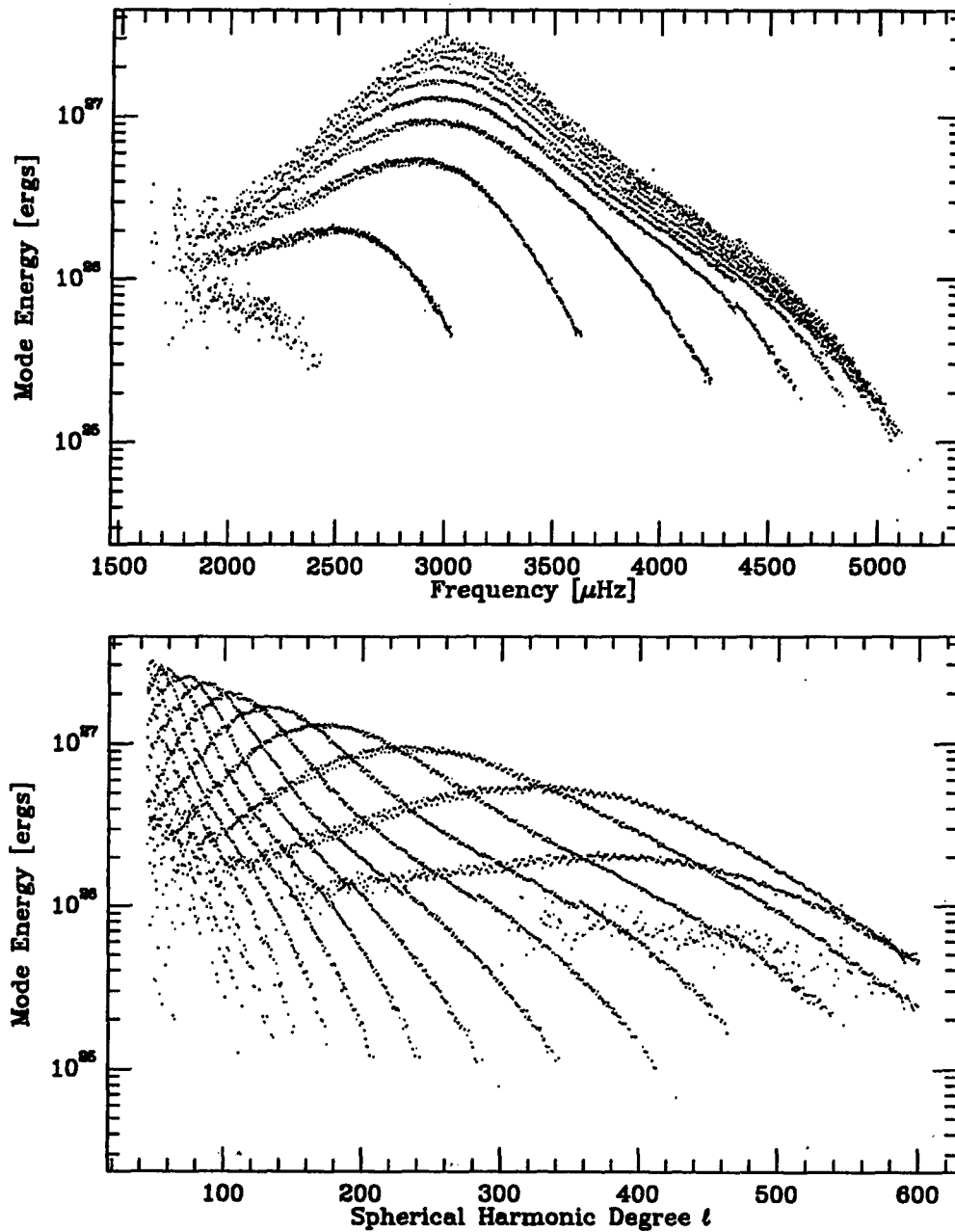


Figure 5.16: Total energy per mode, estimated from the product of the low-resolution modal total power by the mode mass computed at an altitude of 500 km, as a function of frequency (upper panel) and degree (lower panel).

and for turbulent pseudoconvection

$$Q(\nu) \sim \frac{2\pi\nu\tau_H}{\mathcal{M}^2 f} \qquad 2\pi\nu\tau_H \lesssim Re^{3/4} \qquad (5.25)$$

where τ_H represent the eddies lifetime and f the fraction of the volume that is maintained in a steady state of homogeneous, isotropic turbulence ($f \leq 1$), while \mathcal{M} is the Mach number. Note that in each case the quality factor increases with frequency, with different power laws for different regimes.

Modal lifetimes, estimated from the intermediate- and high-degree, low-resolution FWHM are presented Figure 5.17 as a function of frequency, ν , inner turning point, r_t , the mode mass, M , and the turbulent pressure overlap integral, X_c , in bi-logarithmic plots (except for the frequency and inner turning point).

Several remarkable features can be noticed in Figure 5.17. First, for none of our indicators does the low-frequency, long-lifetime modes present any form of correlation. While these are the modes which are the most susceptible to residual systematic errors, since the associated corrections were the largest for these modes, they may indicate the presence of two distinct regimes, which may in turn explain the significant difference of modal width between the low-degree and the high-degree modes. Secondly, the short-lived (i.e. less than 20 h) and high-frequency (i.e. above 3 mHz) modes present significant trends with the frequency and the turbulent pressure overlap integral, and a remarkable correlation with the mode mass. As for the low-degree modes, we observe a decrease of the mode lifetime with frequency, but with a less pronounced frequency dependence, since for low-degree modes (i.e. $\ell \sim 20$) the observed linewidths increase by a factor ~ 10 between 3 and 4 mHz (Libbrecht, 1988), while we observe a drop of the modal lifetimes for high-degree modes ($\ell > 100$) by only a factor ~ 5 , a value more consistent with the variation observed at low ℓ above 4 mHz. In both cases, the observed lifetime decreases with frequency, in contradiction to the prediction based on the quality factors mentioned above.

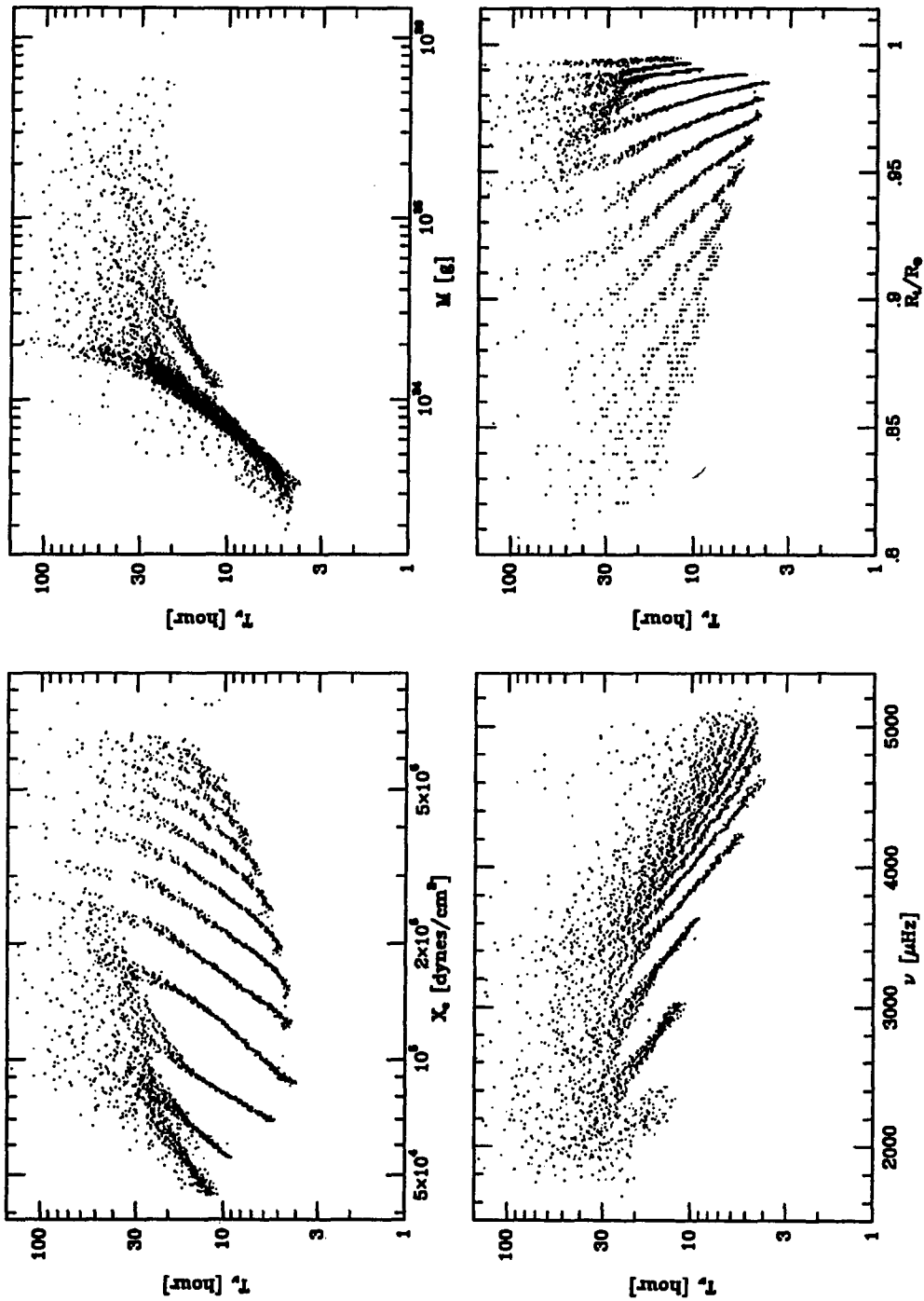


Figure 5.17: Lifetime correlations plots: modal lifetimes as a function of frequency (lower left panel), inner turning point (lower right panel), turbulent pressure overlap integral (upper left panel), and mode mass (upper right panel).

The overall trend of the modal lifetimes as a function of X_c indicates a qualitative agreement with the assumption that the turbulent pressure may be exciting the oscillations, namely an increase of the mode lifetime for larger values of the overlap integral. Nevertheless, Figure 5.17 do not really indicates a correlation per say, between T and X_c , hence this qualitative agreement may be purely fortuitous. On the other hand, a remarkable correlation of the mode lifetime with the mode mass can be observed in that figure. Indeed, for these short-lived, high-frequency modes, the observed lifetimes vary proportionally to the mode mass. This almost linear dependency with the mode mass of the modal lifetime can be interpreted in simple terms as follows: for a uniform excitation mechanism and a uniform damping mechanism near the surface, the energy stored in each mode would be proportional to the mode mass, while the energy loss would be uniform, hence the lifetime should be proportional to the mode mass.

Chapter 6

Internal Rotation Rate

As mentioned earlier, the dominant contribution to frequency splitting of the solar p-mode frequencies is the solar rotation. We present in the following sections a more formal description of the rotationally induced frequency splittings, and the inverse problem that relates these splittings to the internal rotation rate. We then describe the inversion techniques we used to solve this inverse problem and present the resulting rotation rate as a function of depth in the equatorial regions, deduced from the frequency splittings measurements determined in the present study.

We also present inverted rotation rate profiles obtained by consolidating the present study set of frequency splittings with low- and intermediate-degree contemporary frequency splittings estimated from observations carried out at the Big Bear Solar Observatory by the Caltech group (Libbrecht *et al.*, 1990). Finally, we discuss some of the implications resulting from our inverted profile in relation to solar dynamo theory, global circulation predictions, and evolutionary models of rotating stars.

6.1 Theoretical Background

Solar rotation is the dominant perturbation that lifts the azimuthal degeneracy of the p-mode eigenfrequencies by breaking the spherical symmetry, hence inducing rotational frequency splittings. In terms of traveling waves, modes propagating in the sense of the rotation are shifted to higher frequency while mode propagating in the opposite direction are shifted to lower frequency, hence the frequency difference (i.e. the frequency splitting), is related through some integral function, to the rotation rate in the region sampled by that mode.

Since different modes sample different parts of the solar interior, the accurate measurement of frequency splittings for a large set of modes that adequately sample the solar interior allows to infer the internal solar rotation rate as a function of depth and latitude.

6.1.1 Rotational splittings

The frequency splitting of a nonradial oscillation mode, $\nu_{n,\ell}$, induced by slow differential rotation, $\Omega(r, \theta) \ll 2\pi\nu_{n,\ell}$, is given by (Hansen *et al.*, 1977)

$$\nu_{n,\ell,m} - \nu_{n,\ell,0} = -\frac{m}{2\pi} \frac{\mathcal{R}_{n,\ell,m}}{\mathcal{J}_{n,\ell,m}} \quad (6.1)$$

where

$$\mathcal{R}_{n,\ell,m} = \frac{1}{\mathcal{C}_{\ell,m}} \int_0^{R_\odot} \int_0^\pi \rho_o(r) \mathcal{F}_{n,\ell,m}(r, \theta) \Omega(r, \theta) r^2 dr d(\cos \theta) \quad (6.2)$$

$$\mathcal{F}_{n,\ell,m} = \left[-\xi_{r,n,\ell}^2(r) + 2\xi_{r,n,\ell}(r) \xi_{h,n,\ell}(r) \right] P_\ell^{m,2}(\cos \theta) \quad (6.3)$$

$$+ \xi_{h,n,\ell}^2(r) \left[2P_\ell^m \frac{dP_\ell^m}{d\theta} \frac{\cos \theta}{\sin \theta} - \left(\frac{dP_\ell^m}{d\theta} \right)^2 - \frac{m^2}{\sin^2 \theta} P_\ell^{m,2} \right] \quad (6.4)$$

$$\mathcal{J}_{n,\ell} = \int_0^{R_\odot} \left[\xi_{r,n,\ell}^2(r) + \ell(\ell+1)\xi_{h,n,\ell}^2(r) \right] \rho_o(r) r^2 dr \quad (6.5)$$

$$\mathcal{C}_{\ell,m} = \frac{2}{2\ell+1} \frac{(\ell+m)!}{(\ell-m)!} \quad (6.6)$$

and where $\xi_{r,n,\ell}$ and $\xi_{h,n,\ell}$ are respectively the radial and horizontal displacement unperturbed eigenfunctions, ρ_o the unperturbed density, P_ℓ^m associated Legendre polynomials and θ the co-latitude.

After integration by part with respect to the co-latitude, θ , (see Cuypers, 1980), $\mathcal{R}_{n,\ell,m}$ can be rewritten as

$$\mathcal{R}_{n,\ell,m} = \frac{1}{C_{\ell,m}} \int_0^{R_\odot} \int_0^\pi P_\ell^{m^2}(\cos \theta) \rho_o(r) [\mathcal{G}_{n,\ell}(r) + \mathcal{S}(r, \theta)] \Omega(r, \theta) r^2 dr d(\cos \theta), \quad (6.7)$$

where

$$\mathcal{G}_{n,\ell} = \xi_{r,n,\ell}^2(r) - 2 \xi_{r,n,\ell}(r) \xi_{h,n,\ell}(r) + (\ell^2 + \ell - 1) \xi_{h,n,\ell}^2(r) \quad (6.8)$$

$$\mathcal{S}(r, \theta) = \frac{1}{\Omega(r, \theta)} \left(\frac{3}{2} \frac{\partial \Omega}{\partial \theta} \cot \theta + \frac{1}{2} \frac{\partial^2 \Omega}{\partial \theta^2} \right) \quad (6.9)$$

If we may neglect the contribution from the nonlinear term \mathcal{S} , namely when the rotation rate varies slowly with latitude ($\partial \Omega / \partial \theta \ll \Omega$), Equation (6.1) can be rewritten as

$$\Delta \nu_{n,\ell,m} = -\frac{m}{2\pi} \int_0^R \int_{-1}^{+1} \tilde{P}_\ell^{m^2}(x) K_{n,\ell}(r) \Omega(r, x) dr dx \quad (6.10)$$

where $\Delta \nu_{n,\ell,m} = \nu_{n,\ell,m} - \nu_{n,\ell,0}$, \tilde{P}_ℓ^m are normalized associated Legendre polynomials, $x = \cos(\theta)$, and $K_{n,\ell}$ unimodular rotational kernels, defined by

$$K_{n,\ell}(r) = \frac{1}{\mathcal{J}_{n,\ell}} \mathcal{G}_{n,\ell}(r) \rho_o(r) r^2 \quad (6.11)$$

Equation (6.10) clearly indicates that the frequency splittings represent some weighted average, over depth and latitude, of the rotation rate. In other words, any frequency splitting contains information on the internal rotation rate only at the depths where the rotation kernel is significantly different from zero and at latitudes where the associated Legendre polynomial is significantly different from zero as well.

From the nature of the solar acoustic cavity, each p-mode, hence its associated rotational kernel, samples a definite region of the solar interior confined between the surface and the

inner turning point. The character of the solar stratification causes the location of the inner tuning point to be a slow function of frequency but a steep function of degree. This is illustrated in Figure 6.1, where rotational kernels, for a selection of degrees, ℓ , and radial orders, n , are presented. Notice that the larger the degree or the lower the frequency (i.e. the lower the radial order), the shallower is the region sampled by that mode.

If we consider only the sectoral splittings we can rewrite Equation (6.10) as

$$\frac{\Delta\nu|_{\text{sectoral}}}{2\ell} = \frac{\nu_{n,\ell,-\ell} - \nu_{n,\ell,+\ell}}{2\ell} = \frac{1}{2\pi} \int_0^R K_{n,\ell}(r) \bar{\Omega}(r) dr \quad (6.12)$$

where

$$\bar{\Omega}(r) = \int_{-1}^{+1} [\tilde{P}_\ell^m(x)]^2 \Omega(r, x) dx \quad (6.13)$$

and

$$P_\ell^m = (-)^m (2\ell - 1)!! (1 - x^2)^{\ell/2} \quad (6.14)$$

Notice that $\bar{\Omega}$ is an average over latitude of the rotation rate, weighted by a symmetric and sharply peaked function centered around the equator. While $\bar{\Omega}$ is not the equatorial rotation rate per say, it provides a good estimate of the equatorial value since the weighting function becomes more sharply peaked as the mode penetration decreases and since the differential rotation is not expected to extend beyond the convection zone (see Thompson, 1990 and Korzennik *et al.*, 1988). Table 6.1 provides a quantitative illustration of the azimuthal extension of $\bar{\Omega}$ as a function of degree and the typical location of the inner turning point associated to it.

6.1.2 Inversion Techniques

Solving Equation (6.10) or Equation (6.12) for the rotation rate, Ω , defines a classical inverse problem, namely that an unknown function (the rotation rate) is related through a set of integral equations to a set of observables (i.e. the frequency splittings). In a more

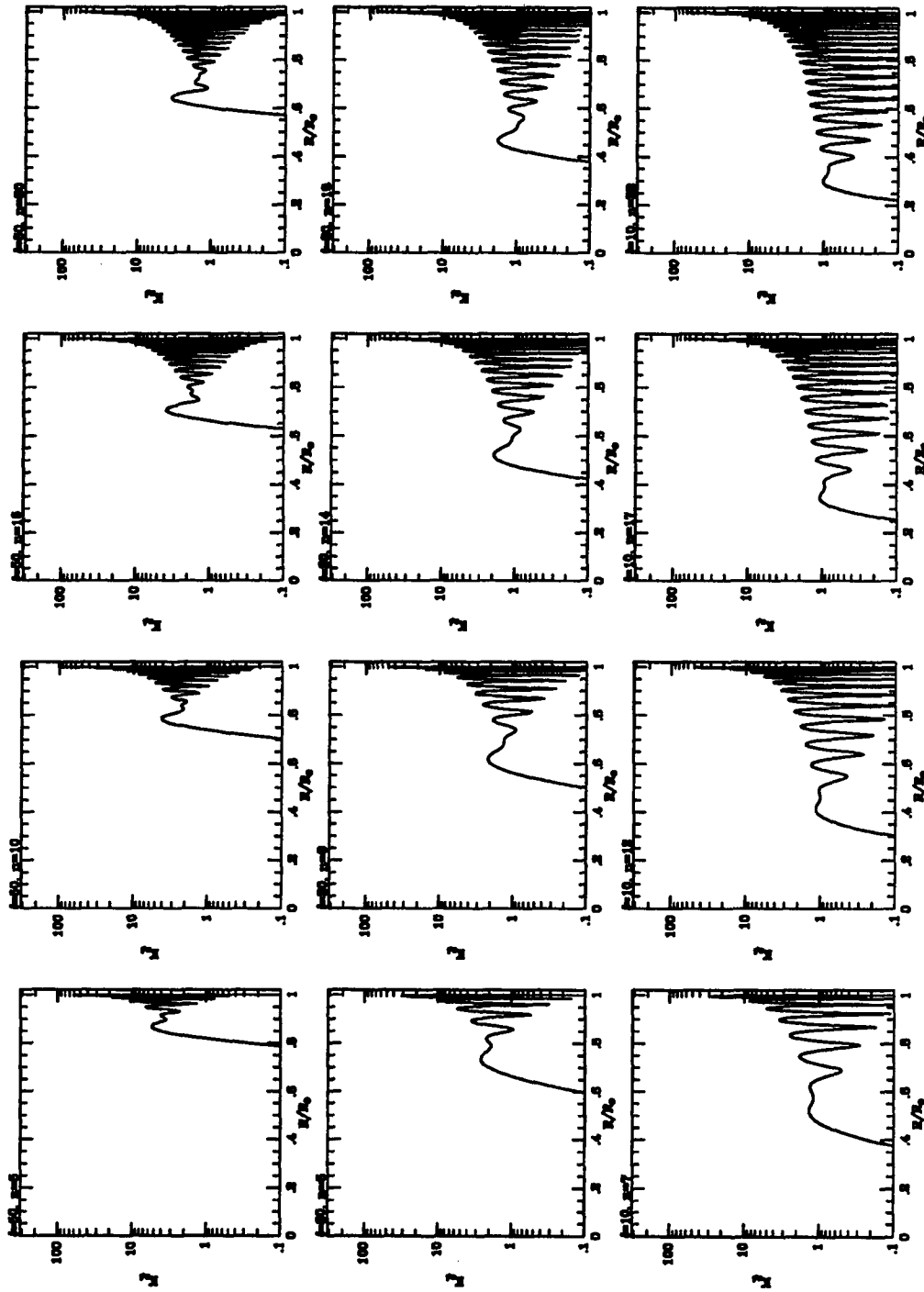


Figure 6.1: Selection of rotational kernels, $K_{n,\ell}$, as a function of radius, as defined by Equation (6.11). The corresponding spherical harmonic degree ℓ and radial order n are indicated in the upper left corner of each panel.

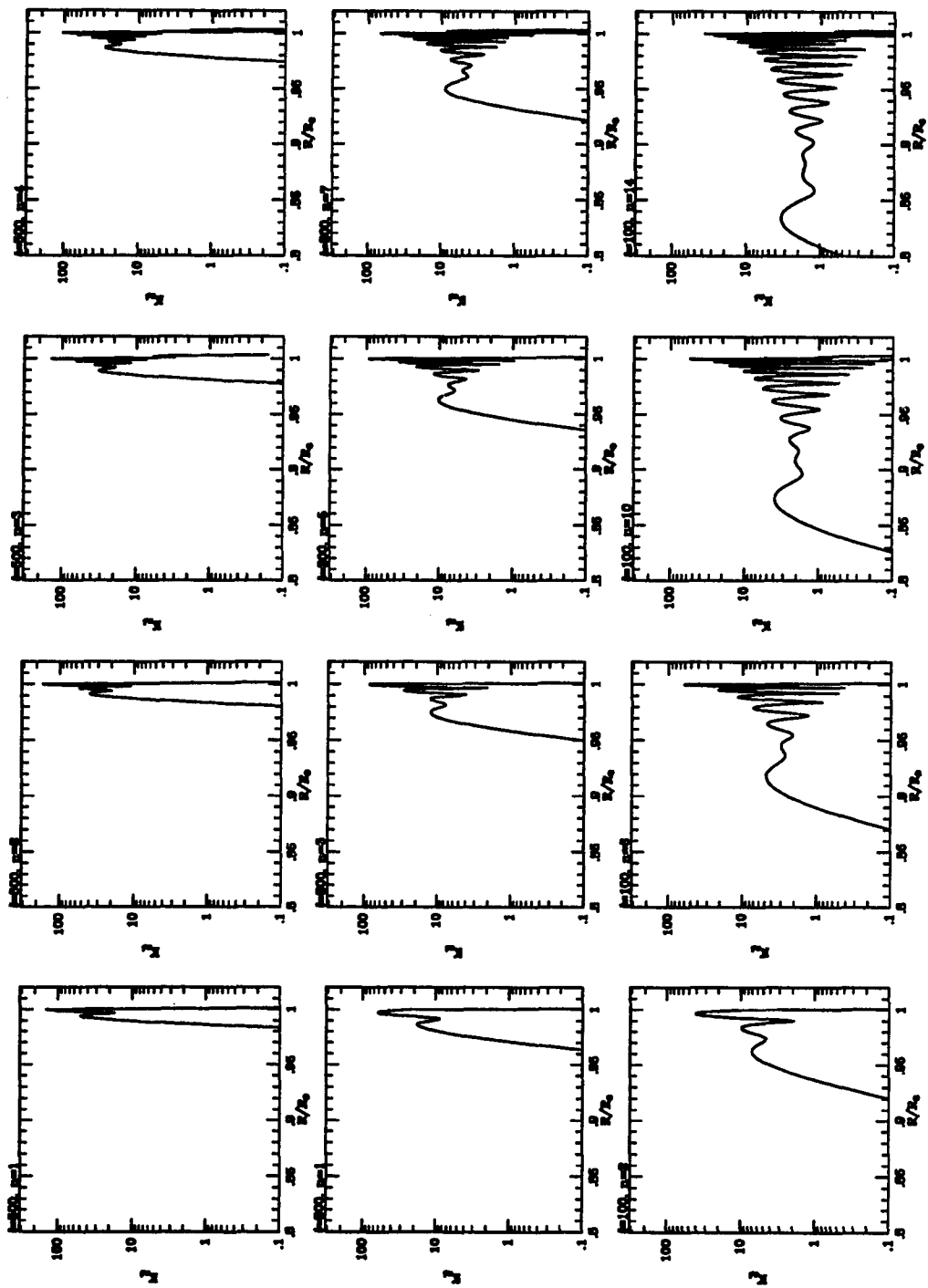


Figure 6.1 (continued)

ℓ	ϑ_{FWHM}^a	R_t/R_\oplus^b
10	15.0	0.283
20	10.6	0.443
50	6.74	0.733
100	4.77	0.880
200	3.37	0.957
500	2.13	0.989

^aangular full width at half maximum, in degree, of $(1 - x^2)^\ell$ where $x = \sin(\vartheta)$, and ϑ is the latitude

^binner turning point computed for $\nu = 3.3$ mHz

Table 6.1: Azimuthal extension of $\bar{\Omega}$ as a function of spherical harmonic degree ℓ , and typical corresponding inner turning point.

abstract formulation, for a one dimensional problem, we shall write

$$y_k \pm \sigma_k = \int_0^1 K_k(r) x(r) dr \quad \text{for } k = 1, \dots, N \quad (6.15)$$

where the y_k represent a set of observables, and σ_k their uncertainty, while $K_k(r)$ represent the associated unimodular kernels and $x(r)$ the unknown function, defined over the domain $r \in [0, 1]$.

In order to pose the problem in a dimensionless frame, let us rewrite Equation (6.15) as

$$\frac{y_k}{\sigma_k} \simeq \int_0^1 \frac{K_k(r)x_s}{\sigma_k} \frac{x(r)}{x_s} dr \quad (6.16)$$

or simply

$$y'_k \simeq \int_0^1 K'_k(r) x'(r) dr \quad \text{for } k = 1, \dots, N \quad (6.17)$$

where x_s is selected to bring $x'(r) \approx 1$. We will from now on assumed that the scaling from Equation (6.15) to Equation (6.17) has been performed and will drop the prime symbols.

Since in all practical cases the set of observables is finite and the observables are known to a finite precision, and in most cases the set of kernels associated with the available set of observables does not completely sample the domain of the unknown function, such an inverse problem is ill-posed. Indeed, on one hand, there will be a set of possible solutions x_A whose contribution to the observables is null, namely

$$\int_0^1 K_k(r) x_A(r) dr = 0 \quad \text{for all } k = 1, \dots, N \quad (6.18)$$

These functions define the annihilator space of the operator defined by our set of N integral equations. If the annihilator has a non-zero dimension there is no unique solution to the inverse problem. In more practical terms, the annihilator arises from the fact that the set of kernels associated to the the set of available observables does not sample completely the domain of the unknown function. On the other hand, since the observables are tainted by errors, there may not exist a solution that actually satisfies the set of equations exactly, hence neither the existence nor the uniqueness of the solution is guaranteed. Finally, note that the numerical implementation of the problem or the numerical estimation of the kernels may result in some cases to contribute to the actual size of the annihilator space.

Generalized inverse theory provides the framework to deal with inverse problems and has been extensively discussed in a wide variety of fields, from geoseismic analysis to image reconstruction. A complete review of inversion techniques from a terrestrial perspective can be found in Parker (1977) and references therein, and from a solar perspective in Gough (1985) and Christensen-Dalsgaard *et al.* (1990).

The general procedure to solve the linear problem defined by Equation (6.17) is based on the construction of an inverse operator H , to obtain an estimate of the solution, \hat{x} , at some targeted radius, r_t , from a linear combination of the observables y_k , namely

$$\hat{x}(r_t) = \sum_k H_k(r_t) y_k \quad (6.19)$$

it follows from the definition of the problem that

$$\hat{x}(r_t) = \int_0^1 \left(\sum_k H_k(r_t) K_k(r) \right) x(r) dr \quad (6.20)$$

$$\stackrel{\text{def}}{=} \int_0^1 A(r, r_t) x(r) dr \quad (6.21)$$

where $A(r, r_t)$ is the resolution kernel, while

$$\hat{y}_k = \int K_k(r) \hat{x}(r) dr \quad (6.22)$$

and the variance of the solution is given by

$$\sigma^2(\hat{x})|_{r_i} = \sum_k H_k^2(r_i) \quad (6.23)$$

since we consider that the problem has been rescaled according to Equation (6.16), hence $\sigma(y_k) \equiv 1$.

The procedure of determining the inverse operator, H , for a set of target radii, r_i , is specific to each inversion method, but we can in all generality state that \hat{x} will be a good estimate of the solution at or near r_i if

1. the resolution kernel is a narrow function localized around r_i , namely $A(r, r_i) \approx \delta(r - r_i)$
2. the solution represents the observables, namely $\hat{y}_k \approx y_k$ for all $k = 1, \dots, N$
3. the error magnification remains small, namely $\sigma(\hat{x}) \ll 1$.

Since the inverse problem is ill-posed, each inversion method provides an estimate of the solution based on some implicit or explicit assumption about the unknown function, $x(r)$, to condition the problem or to optimize one of the three conditions mentioned above. We have used three different methods, namely the spectral expansion method, the piecewise constant constrained least-squares method and the optimal averaging kernel method to solve the inverse problem relating the p-mode rotational splittings to the solar internal angular velocity, as defined by Equation (6.12).

The spectral expansion method (or single value decomposition method), uses a single value decomposition to compute the generalized inverse that provides the smallest-norm least-squares solution. To limit the error magnification the single value decomposition is truncated hence overestimating the size of the annihilator. This truncation performs some trade-off between resolution and error magnification.

The constrained least-squares method (or regularized method), adds to the standard least-squares method some arbitrary constraint on the unknown function $x(r)$. In practice a smoothness constraint is used to condition (or regularize) the problem. The strength of this constraint acts as a trade-off coefficient between resolution and error magnification.

The optimal averaging kernel method (or optimal resolution kernel), as its name indicates, aims at minimizing the width of the resolution kernel. Since the problem is ill-conditioned a trade-off between the resolution kernel width and the error magnification needs to be preformed in the "optimization" process.

The Spectral Expansion Method

Since only a limited resolution can be achieved, let us first discretize Equation (6.17), and consider that the solution can be written as

$$x(r) = \sum_{i=1}^M x_i \phi(r, r_i) \quad (6.24)$$

with $M \ll N$ and $\phi(r, r_i)$ a set of functions centered around $r = r_i$ (namely functions that vary linearly from 0 to 1 for $r_{i-1} < r \leq r_i$ and from 1 to 0 for $r_i < r \leq r_{i+1}$ and are zero otherwise). We can now rewrite Equation (6.17) as

$$y_k = \sum_i K_{k,i} x_i \quad \text{for } k = 1, \dots, N \quad (6.25)$$

or using matricial notation

$$\mathbf{y} = \mathbf{K}\mathbf{x} \quad (6.26)$$

where \mathbf{K} is a $N \times M$ rectangular matrix. The generalized inverse (Lanczos, 1961; Jackson, 1972) provides the smallest-norm least-squares solution by performing the single value decomposition (SVD) of \mathbf{K} , resulting from the dual eigenvalue problem

$$\mathbf{K}\mathbf{v} = \lambda\mathbf{u} \quad (6.27)$$

$$\mathbf{K}^T\mathbf{u} = \lambda\mathbf{v} \quad (6.28)$$

that defines a common set of $p \leq M \ll N$ non-zero eigenvalues, λ_i , N eigenvectors \mathbf{u}_i and M eigenvectors \mathbf{v}_i . This SVD allows the factorization of the matrix K as

$$\mathbf{K} = \mathbf{U}\mathbf{\Lambda}\mathbf{V}^T \quad (6.29)$$

where $\mathbf{\Lambda}$ is a $p \times p$ diagonal matrix whose diagonal elements are the p non-zero eigenvalues, λ_i , \mathbf{U} is a $N \times p$ matrix, whose columns are the eigenvectors \mathbf{u}_i associated with the p non-zero eigenvalues and \mathbf{V} is a $M \times p$ matrix, whose columns are the eigenvectors \mathbf{v}_i associated with the p non-zero eigenvalues.

This factorization can be inverted, since the matrices \mathbf{U} and \mathbf{V} satisfy the following relationships (see for instance Jackson, 1972)

$$\mathbf{U}^T\mathbf{U} = \mathbf{V}^T\mathbf{V} = \mathbf{I}_p \quad (6.30)$$

where \mathbf{I}_p is the $p \times p$ identity matrix, and since the inversion of the diagonal matrix $\mathbf{\Lambda}$ is trivial. The generalized inverse is thus given by

$$\mathbf{H} = \mathbf{V}\mathbf{\Lambda}^{-1}\mathbf{U}^T \quad (6.31)$$

and the smallest-norm least-square solution given by

$$\hat{\mathbf{x}} = \mathbf{H}\mathbf{y} \quad (6.32)$$

The error magnification will be given by

$$\sigma^2(\hat{\mathbf{x}}) = \mathbf{H}\mathbf{H}^T = \mathbf{V}\mathbf{\Lambda}^{-2}\mathbf{V}^T \quad (6.33)$$

or simply

$$\sigma^2(\hat{x})|_{r_i} = \sum_{j=1}^p \left(\frac{V_{i,j}}{\lambda_j} \right)^2 \quad (6.34)$$

hence small eigenvalues will introduce large error magnification. Moreover, in actual numerical implementations, the distinction between small and null eigenvalues may be blurred and the precise value of p not known.

To limit the uncertainty on the solution a trade-off between resolution and error magnification is performed by truncating the set of non-zero eigenvalues to the subset of q eigenvalues larger than some fixed threshold (where $q \leq p$) and a solution is computed from only these q largest eigenvalues and their associated eigenvectors. Such a truncation corresponds to considering the eigenvectors associated with the set of $(p - q)$ small eigenvalues which are not included in the inverse operator as actually lying in the annihilator space. By rescaling the problem according to Equation (6.17), a natural cut-off value near unity can be used to truncate the set of eigenvalues. Alternatively, the cut-off value may be chosen at each target radius to limit the error magnification below a fixed threshold.

The discretization on a given grid of the unknown function is a delicate operation that needs to be handled with caution. Indeed, the number and location of the mesh points of the discretization grid should match the resolution and the effective number of degrees of freedom of the observable data set. Since these are not known *a priori*, we have adopted an iterative approach to the definition of the discretization grid where the mesh points are redistributed according to the resolution indicated by the resolution kernels obtained at each iteration.

The Piecewise Constant Constrained Least-Squares Method

As for the spectral expansion method, let us first discretize Equation (6.17), and consider

$$x(r) = \sum_{i=1}^M x_i \varphi(r, r_i) \quad (6.35)$$

with $M \ll N$ and $\varphi(r, r_i)$ a set of functions centered around r_i respectively, and given by

$$\varphi(r, r_i) = \begin{cases} 1 & \text{if } \frac{1}{2}(r_{i-1} + r_i) \leq r < \frac{1}{2}(r_i + r_{i+1}) \\ 0 & \text{otherwise} \end{cases} \quad (6.36)$$

We can rewrite Equation (6.17) as

$$y_k = \sum_i K_{k,i} x_i \quad \text{for } k = 1, \dots, N \quad (6.37)$$

or using matricial notation

$$\mathbf{y} = \mathbf{K}\mathbf{x} \quad (6.38)$$

where \mathbf{K} is a $N \times M$ rectangular matrix. The least-squares solution to Equation (6.38), $\hat{\mathbf{x}}$, is the solution that minimizes the error function χ^2 , namely

$$\chi^2 = \frac{1}{N} \sum_k (y_k - \sum_i K_{k,i} \hat{x}_i)^2 \quad (6.39)$$

hence it is given by

$$\frac{d(\chi^2)}{d\hat{x}_j} = 0 \quad \text{for } j = 1, \dots, M \quad (6.40)$$

thus

$$\frac{2}{N} \sum_k (y_k - \sum_i K_{k,i} \hat{x}_i) K_{k,j} = 0 \quad \text{for } j = 1, \dots, M \quad (6.41)$$

or in matricial form

$$\mathbf{K}^T \mathbf{y} = \mathbf{K}^T \mathbf{K} \hat{\mathbf{x}} \quad (6.42)$$

Notice that the matrix $\mathbf{K}^T \mathbf{K}$ is a $M \times M$ square matrix, whose inverse may not exist, and in actual numerical implementations is most likely to be ill-conditioned.

To regularize the problem, let us add a constraint on the solution (i.e. a smoothness constraint) that we shall write as

$$\mathcal{F}\{\mathbf{x}\} = \sum_i (\sum_j C_{i,j} x_j)^2 \quad (6.43)$$

and compute the solution which minimizes $\chi^2 + \lambda \mathcal{F}$, where λ is an arbitrary coefficient that controls the strength of the constraint.

Introducing the constraint in Equation (6.40) leads to

$$\mathbf{K}^T \mathbf{y} = (\mathbf{K}^T \mathbf{K} + \lambda \mathbf{N} \mathbf{C}^T \mathbf{C}) \hat{\mathbf{x}} \quad (6.44)$$

It is now the matrix $\mathbf{G} = \mathbf{K}^T \mathbf{K} + \lambda \mathbf{N} \mathbf{C}^T \mathbf{C}$, a $M \times M$ square matrix whose inverse is computed. \mathbf{G} will not be any more ill-conditioned assuming λ large enough, and the inverse operator \mathbf{H} , for a given λ , is given by

$$\mathbf{H}_\lambda = \mathbf{G}_\lambda^{-1} \mathbf{K}^T \quad (6.45)$$

While the constraint can be arbitrary, as long as it can be expressed by Equation (6.43), it should be appropriate, and will influence the nature of the possible solutions. The most common and natural constraint is a smoothness constraint, namely to minimize the square of the norm of the first or second derivative. Hence by forcing the solution to be smooth, one reduces the resolution but limits the error magnification. Here it is the parameter λ that, by controlling the strength of the constraint, acts as a trade-off coefficient between resolution and error magnification.

In the first derivative implementation of the constraint, $\mathcal{F}\{x\}$ becomes

$$\mathcal{F}\{x\} = \int \left(\frac{dx}{dr} \right)^2 dr \quad (6.46)$$

where the derivative is given by a numerical estimate, namely a simple forward difference scheme, or

$$\frac{dx}{dr} = \frac{x_{i+1} - x_i}{r_{i+1} - r_i} \quad (6.47)$$

and the constraint becomes

$$\mathcal{F}\{x\} = \sum_{i=1}^{M-1} \left(\frac{x_{i+1} - x_i}{r_{i+1} - r_i} \right)^2 (r_{i+1} - r_i) \quad (6.48)$$

which in turn defines the matrix \mathbf{C} according to Equation (6.43).

In the second derivative implementation, we have this time

$$\mathcal{F}\{x\} = \int \left(\frac{d^2x}{dr^2} \right)^2 dr \quad (6.49)$$

where the derivative is also given by a numerical estimate, namely

$$\frac{d^2x}{dr^2} = \frac{x_{i+1} - 2x_i + x_{i-1}}{\left(\frac{1}{2}(r_{i+1} - r_{i-1}) \right)^2} \quad (6.50)$$

and the constraint becomes

$$\mathcal{F}\{x\} = \sum_{i=2}^{M-1} \left(\frac{x_{i+1} - 2x_i + x_{i-1}}{\left(\frac{1}{2}(r_{i+1} - r_{i-1}) \right)^2} \right)^2 \frac{1}{2} (r_{i+1} - r_{i-1}) \quad (6.51)$$

which in turn defines the matrix \mathbf{C} according to Equation (6.43).

The Optimal Averaging Kernel Method

In the optimal averaging kernel method, the emphasis is put on the resolution and the method attempts to optimize the “deltaness” of the resolution kernels (also called averaging kernels). While a complete discussion of this optimization process from a geoseismic point of view can be found in Backus and Gilbert (1970), we limit ourselves here to presenting some highlights of this process so as to illustrate the key points of the method.

Since a solution, \hat{x} , at r_t , is constructed from some linear combination of the observables, the resolution kernel is simply given by (see Equations 6.19 to 6.21)

$$A(r, r_t) = \sum_k H_k(r_t) K_k(r) \quad (6.52)$$

By minimizing the spread of $A(r, r_t)$ around r_t , the “optimal” resolution kernel will be obtained, but since the problem is ill-conditioned, a trade-off between resolution and error magnification is required.

By adopting a measure of the resolution kernel width (i.e. its spread around r_t), namely

$$s(A, r_t) = 12 \int_0^1 (r - r_t)^2 A^2(r, r_t) dr \quad (6.53)$$

and under the constraint that the resolution kernel remains unimodular, the inverse operator H is computed by minimizing the width of the resolution kernel and the error magnification. Since both minimizations cannot be achieved simultaneously, a trade-off coefficient θ is introduced, and one minimizes the quantity

$$s(A, r_t) \cos \theta + w \sigma^2(\hat{x}) \sin \theta \quad (6.54)$$

where the somewhat arbitrary scaling factor w is introduced to scale the trade-off curve (error magnification as a function of spread) with respect to the trade-off angle θ . Since the problem has been rescaled according to Equation (6.17), the spread and error magnification are on the same order of magnitude and w can be set to unity.

The inverse operator is then given by

$$\mathbf{H}_\theta = \frac{\mathbf{W}_\theta^{-1} \mathbf{u}}{\mathbf{u} \mathbf{W}_\theta^{-1} \mathbf{u}} \quad (6.55)$$

where

$$u_k = \int_0^1 K_r(\tau) d\tau \quad (6.56)$$

$$\mathbf{W}_\theta = \mathbf{S} \cos \theta + \mathbf{I}_N \sin \theta \quad (6.57)$$

\mathbf{I}_N is the $N \times N$ identity matrix and

$$S_{k,k'} = 12 \int_0^1 (r - r_i)^2 K_k(r) K_{k'}(r) dr \quad (6.58)$$

Hence, as the trade-off angle θ is increased, one reduces the error magnification by increasing the resolution kernel width.

Practical Considerations

Since we have used a cross-correlation procedure to estimate the frequency splittings, Equation (6.12) needs to be averaged over the radial order n . Hence, we have n -averaged the rotational kernels by computing for each degree, ℓ , the weighted mean of the individual kernels, using for the weight a Lorentzian profile, centered around 3.3 mHz with a FWHM of 3.0 mHz as to represent the power distribution in the 5-minute band. The individual kernels were computed using a standard solar model (Korzennik and Ulrich, 1989) with an adiabatic non-magnetic resonant analysis code based on the Ulrich formalism (Ulrich, 1970).

From a strictly numerical standpoint some significant differences between each method can be noticed. In the interactive implementation of the spectral expansion (ISE), a unique SVD for the M eigenvalues (where $M \ll N$) and their associated eigenvectors (u and v) needs to be computed for a given radial discretization. From that set of eigenvalues and eigenvectors the estimate of the solution for any given trade-off value can be computed from

a straightforward product of matrices. Since the SVD is the computationally intensive part of the procedure, the ISE presents the advantage of not requiring a lot of extra processing to explore the trade-off curve. On the other hand, since we have adopted an iterative approach for the determination of the radial discretization, the SVD needs to be recomputed at each iterative step.

One of the main advantages of the constrained least-squares method (CLS) is its numerical simplicity. Indeed, for a given discretization grid and a given trade-off parameter, only a straightforward inversion of a $M \times M$ matrix needs to be carried out. While this inversion needs to be done for any given trade-off value, the numerical burden of the CLS method is by far the smallest.

On the contrary, the optimal averaging kernel method (OAK) is the most computationally intensive method. Indeed, the matrices \mathbf{S} and \mathbf{W} need to be computed for each trade-off value and at each location, r_t , where an estimate of the solution is sought. On the other hand, since no radial discretization is required the nature of the solution for a given trade-off is guaranteed to be independent of the set of target radii selected to describe the unknown function. Note that the matrix \mathbf{S} can be written as a sum of three matrices independent of r_t by developing the square in the integral, namely

$$\mathbf{S} = r_t^2 \mathbf{S}_0 - 2r_t \mathbf{S}_1 + \mathbf{S}_2 \quad (6.59)$$

where

$$(\mathbf{S}_i)_{k,k'} = 12 \int r^i K_k(r) K_{k'}'(r) dr \quad (6.60)$$

This reduces the computation of \mathbf{S} , hence of \mathbf{W} , at each r_t to a simple matrix summation once the \mathbf{S}_i matrices have been computed. In contrast to the two other methods, the OAK method still requires a matrix inversion at each target radius for any given trade-off parameter.

Finally, let us point out that the resolution kernels, $A(r, r_t)$, are the key elements in the

interpretation of any given inverse solution. Indeed, since there is no unique solution to an ill-conditioned inverse problem, it is through the localized nature of the resolving kernel that any estimate of the solution at some target location, $\hat{x}(r_t)$, can be judged as being a good estimate of the “actual” unknown function at that location, $x(r_t)$. If the resolution kernel is reasonably localized, its centroid, r_c and its width $w(r_c)$ (i.e. the spread around the centroid), given by

$$r_c = \frac{\int_0^1 r A^2(r) dr}{\int_0^1 A^2(r) dr} \quad (6.61)$$

and

$$w(r_c) = 12 \int_0^1 (r - r_c)^2 A^2(r) dr \quad (6.62)$$

will be a good characterization of the actual location and resolution of the estimate of the solution. Therefore, we will in most cases present the resulting solutions as a function of the resolution kernel centroid, r_c , rather than the target radius, r_t .

6.2 “Equatorial” Rotation Rate

Inversions of the solar internal angular velocity from p-mode frequency splittings based on full-disk observations have been performed by various groups since reliable splitting measurements have been available while more recent and more accurate splitting measurements have prompted inversions as a function of depth and latitude (Christensen-Dalsgaard and Schou, 1988; Korzennik *et al.*, 1988). In all cases, the available splittings were restricted to low and intermediate degree ($5 \leq \ell \leq 120$) and were unable to provide reliable information in the subsurface regions ($R > 0.85R_\odot$). On the other hand, high-degree splitting measurements based on disk-center observations have prompted several attempts to infer the subsurface rotation rate (Hill *et al.*, 1988a; Hill *et al.*, 1988b) but potential systematic effects present in the splittings due to the disk-center nature of the observations have cast some doubts on these results.

The high-resolution, full-disk measurements obtained at Mt Wilson Observatory (MWO), as presented in this study, have provided the first opportunity of extending the set of splittings used for an inversion from low- to high-degree modes. In order to assess and demonstrate the specific contribution of the high-degree measurements we also present inversion results obtained by using only the low- and intermediate-degree measurements.

We have limited ourselves in this study to inverting for the equatorial rotation rate since our prime objective is to assess the contribution of the high-degree modes to the inverted profile. Since, as discussed at length in Chapter 4, the latitudinal information for high-degree splittings could not be satisfactorily estimated, we have judged it inappropriate to attempt to infer any latitudinal information from such a data set. On the contrary, the sectoral measurements have proven to be more robust and while they still may be tainted by some residual systematics, the significance of the general trends in this set is undoubtedly real. Therefore, we have used the tesseral measurements at low and intermediate degree ($20 < \ell \leq 120$), based on the high-resolution spectra, reduced to their sectoral equivalent ($a_1 + a_3 + a_5$), combined with the sectoral measurements at high degree ($\ell > 120$), based on the low-resolution spectra.

We also present inversion results obtained by consolidating the MWO frequency splittings set with the contemporary BBSO frequency splitting set graciously provided by Libbrecht prior to publication. Since the BBSO measurements are based on a singlet fitting procedure, these splittings were first reduced to n -averaged values comparable to the MWO set. Since some radial resolution may be lost through the n -averaging process, we have also inverted the unaveraged BBSO set alone and combined with the MWO set.

6.2.1 MWO Measurements Alone

We have combined the sectoral equivalent ($a_1 + a_3 + a_5$) splitting measurements obtained from the high-resolution tesseral analysis for low and intermediate degree ($20 \leq \ell < 120$) with the corrected set of high-degree, high-resolution sectoral splitting measurements estimated for $120 \leq \ell \leq 600$.

For the low- and intermediate-degree values an estimate of the uncertainty was computed from the scatter to the polynomial fit in m/L . Since errors associated with sidelobe contamination are most likely to be present (see discussion in Section 3.5.1) this value underestimates the actual uncertainty, as the internal scatter of the measurements clearly indicates. Therefore, we have simply multiplied these uncertainties by a somewhat arbitrary factor of 3 to account for all the potential sources of uncertainties.

In order to estimate uncertainties and increase the significance of the high degree measurements, we have used $10\text{-}\ell$ wide binned values for $\ell \geq 120$. The uncertainties were here estimated from the r.m.s. of the scatter around the mean in each bin. Since at high ℓ the variation with degree of the mode penetration diminishes, the ℓ -binning should not significantly decrease the radial resolution while it substantially reduces some of the computational requirements.

To demonstrate the effects on any estimate of the solution of the procedural details of each inversion procedure we will present some intermediary results that illustrate the limitations or strong points of each method. Therefore, some of the features in the rotation curves which resulted from these intermediary solutions should not be considered as valid unless they are explicitly stated as being significant.

Figure 6.2 presents inverted profiles obtained from a initial choice of radial grid for each method and for different trade-off coefficients, using the complete MWO set (namely

$\ell = 20, (1), 119$ and $\ell = 126, (10), 596$). Figure 6.3 presents the same inverted profiles, but plotted as a function of the resolution kernel centroid rather than the targeted radius, while Figure 6.4 shows a selection of resolution kernels associated with these profiles. This initial radial grid choice consisted of $r = 0, (0.1), 0.7, (0.05), 1$ for the ISE method and $r = 0, (0.05), 0.4, (0.025), 0.9, (0.0125), 1$ for the CLS and the OAK methods. These choice were justified by our *a priori* knowledge that we should not expect a good resolution in the deepest regions, and by a tendency in the ISE method for large oscillatory instabilities for dense discretization grids.

Despite our coarse discretization, the ISE (for this initial radial discretization) presents large oscillatory excursions and very poorly localized resolution kernels. It is precisely such behavior that prompted us to adopt an iterative approach to the radial discretization.

The CLS results (1st and 2nd derivative, hereafter CLS1d and CLS2d respectively) and the OAK curves present very similar features except for the innermost and outermost points. Namely a sharp variation around $r = 0.725$ followed, as we are going towards the surface, by a rapidly damped “hump” (as the trade-off coefficient increases, i.e. as the error magnification decreases) while a second “hump”, located around $r = 0.925$ persists despite the increase of the trade-off coefficients. Below $r \approx 0.6$, as indicated when using the kernel centroids to plot the inverted profiles, and by the nature of the rotation kernels themselves, none of the inversion methods were able to construct a localized resolution kernel near the targeted radius. It should be no surprise that the CLS1d “fills” the unresolved region with a flat profile since for the limit $\lambda \rightarrow \infty$ the CLS1d solution should be flat (i.e. first derivative null everywhere). Similarly, since the limit solution for $\lambda \rightarrow \infty$ of the CLS2d is a straight line, the solution in the unresolved region for the CLS2d is almost linear when plotted versus the target radii.

Above $r \approx 0.975$ the CLS and OAK solutions diverge. While a superficial inspection of the resolution kernels, based solely on the kernel centroid location, would suggest that the

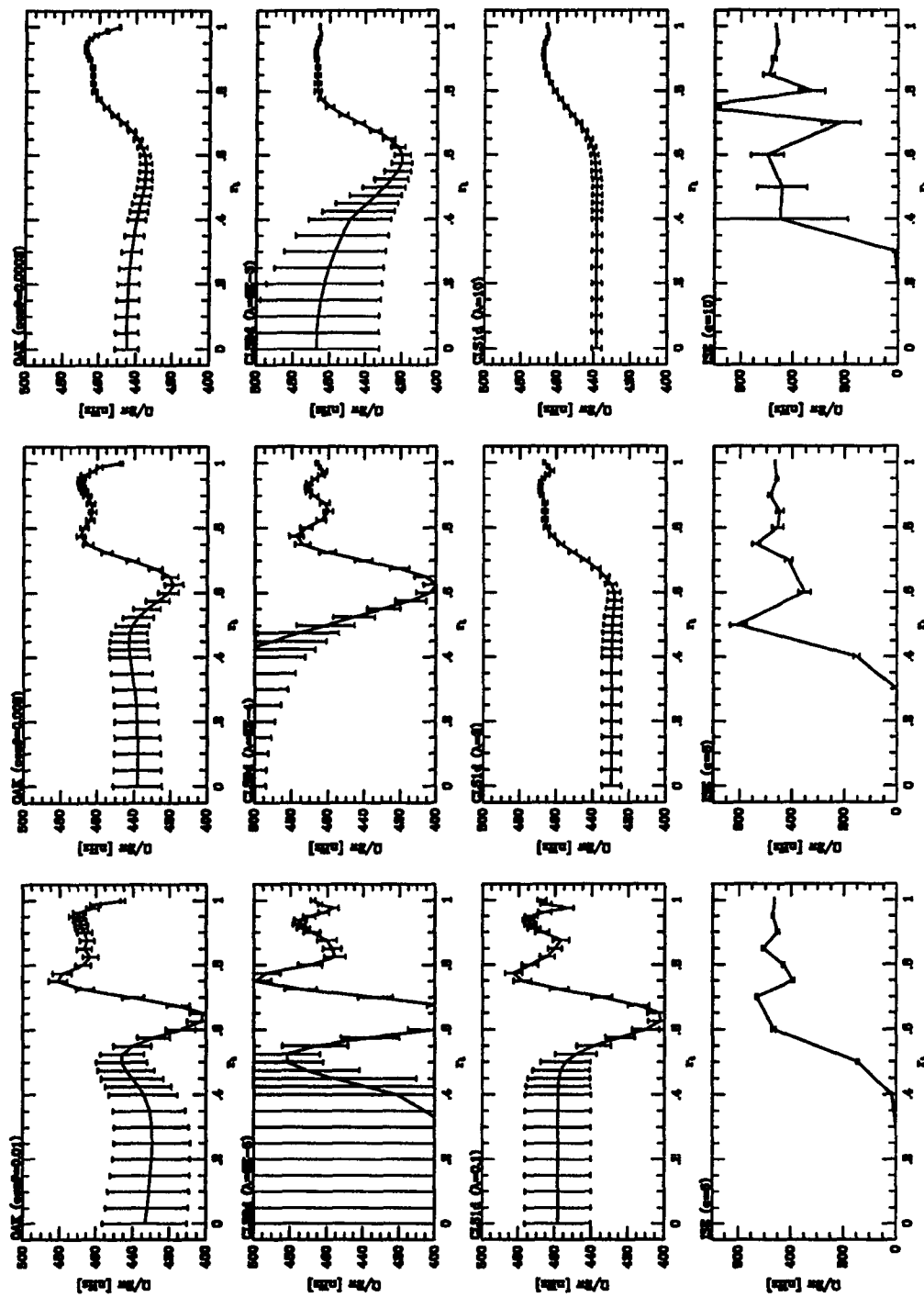


Figure 6.2: Initial inverted rotation rate profiles, function of target radii. From bottom to top profiles correspond to results from the ISE, CLS1d, CLS2d and OAK method respectively, while the trade-off coefficient increases from left to right.

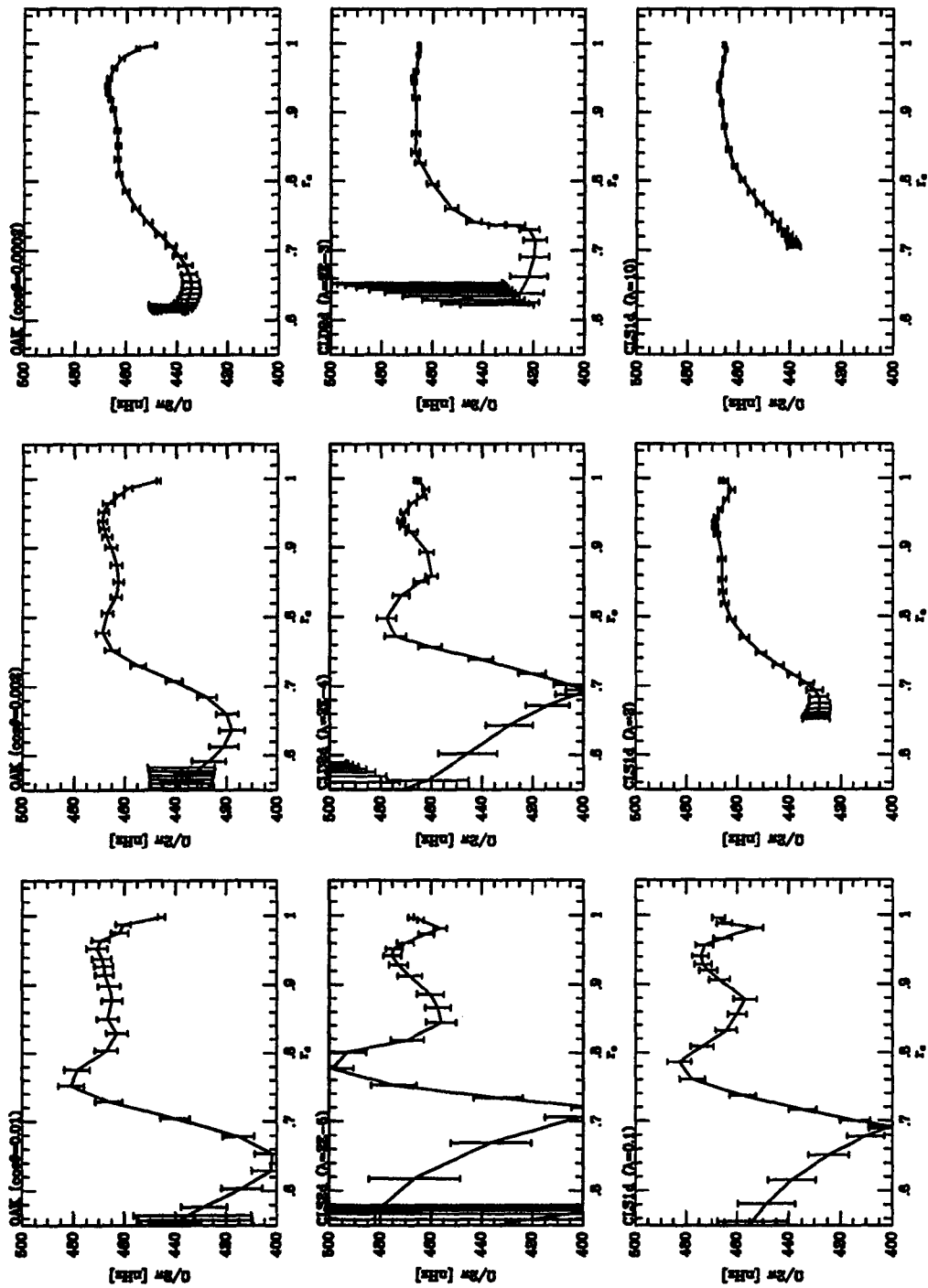


Figure 6.3: Initial inverted profiles, function of kernel centroids. As for Figure 6.2, the profiles in the panels from bottom to top correspond to results from the CLS1d, CLS2d and OAK method respectively, while the trade-off coefficient increases from left to right. Since the initial results for the ISE method presented very poorly localized kernels, we have not included them in this figure.

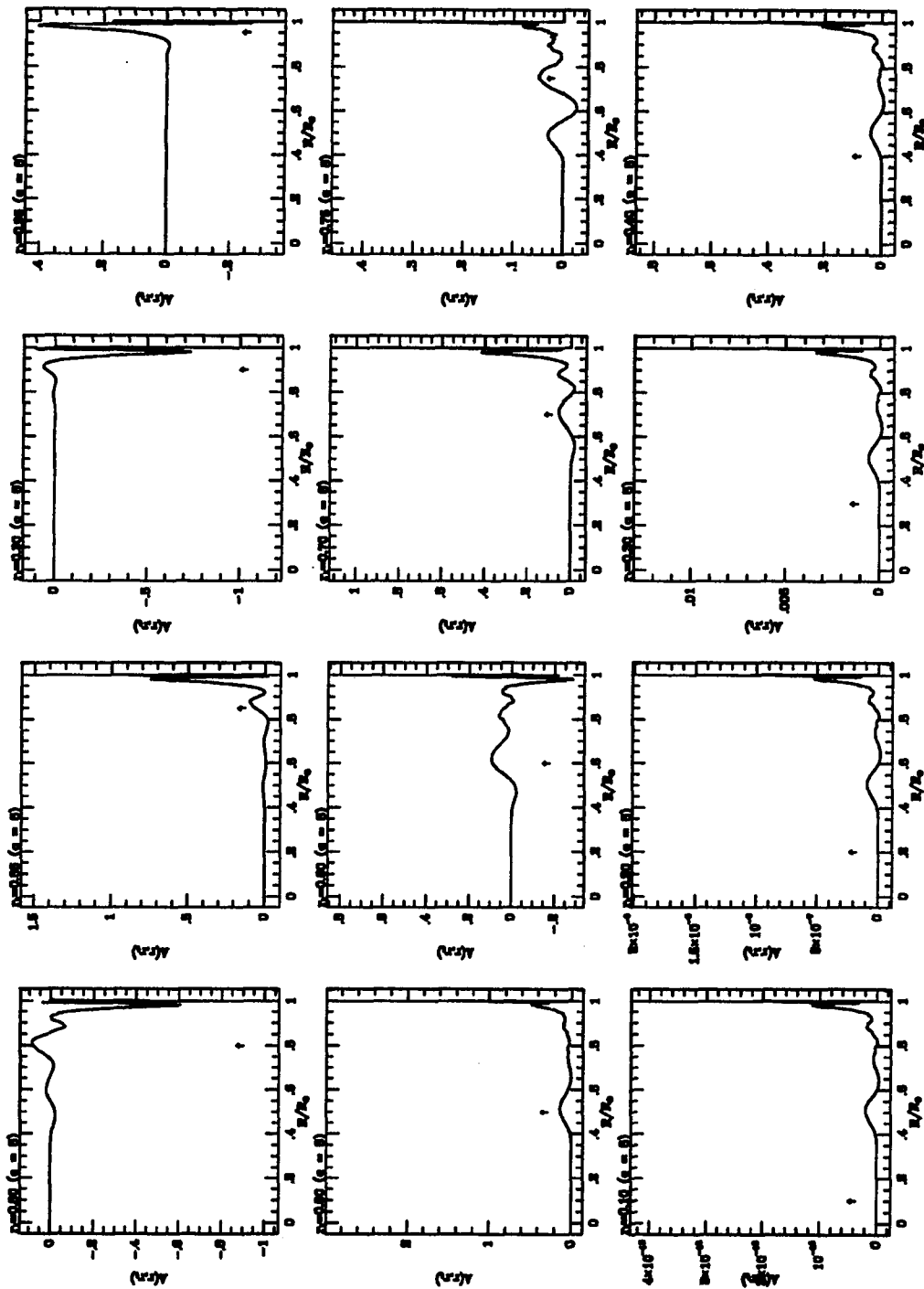


Figure 6.4: Resolution kernels corresponding to the initial inverted profiles presented Figures 6.2 and 6.3. The arrow indicates the location of the corresponding targeted radius.

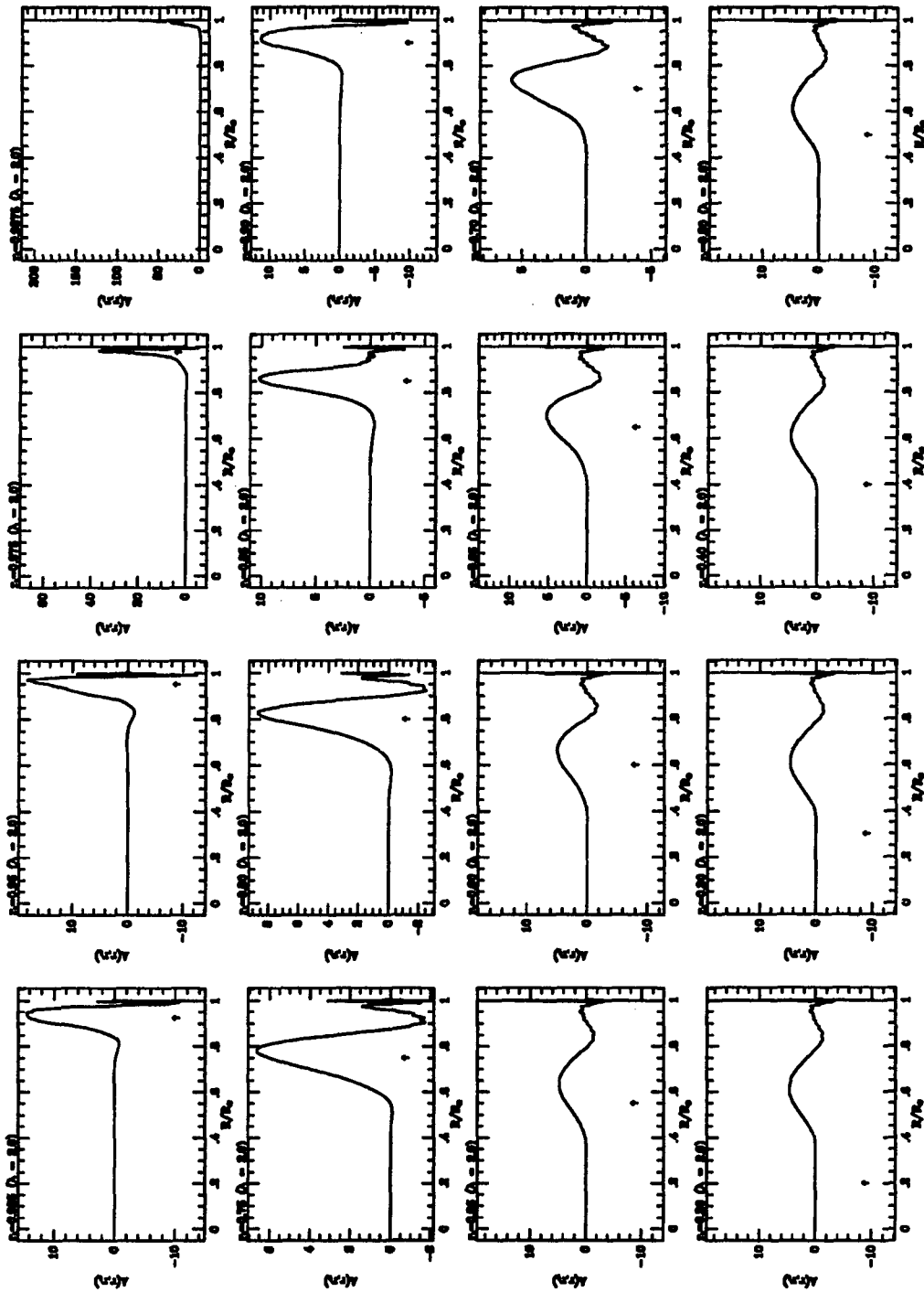


Figure 6.4 (continued)

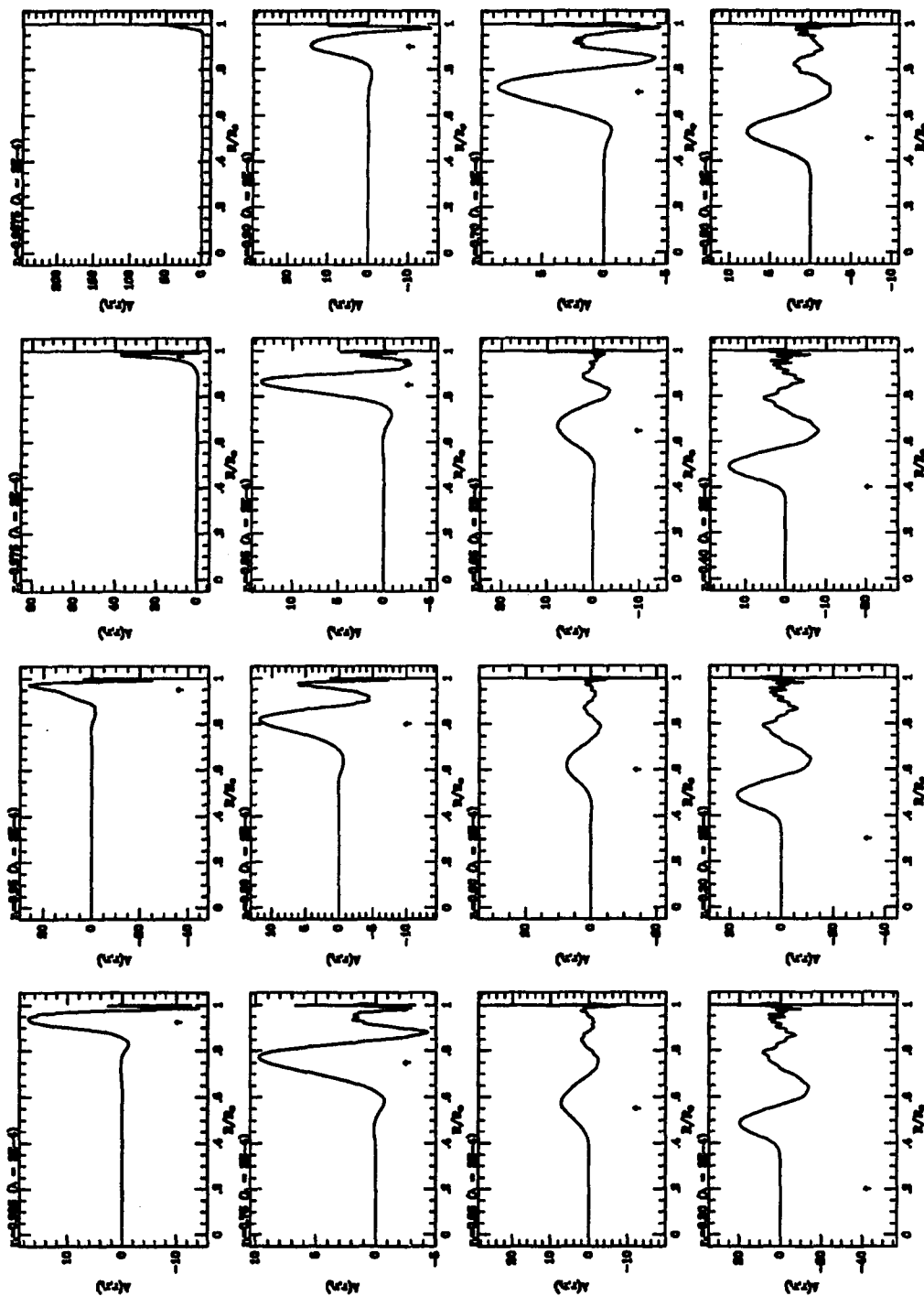


Figure 6.4 (continued)

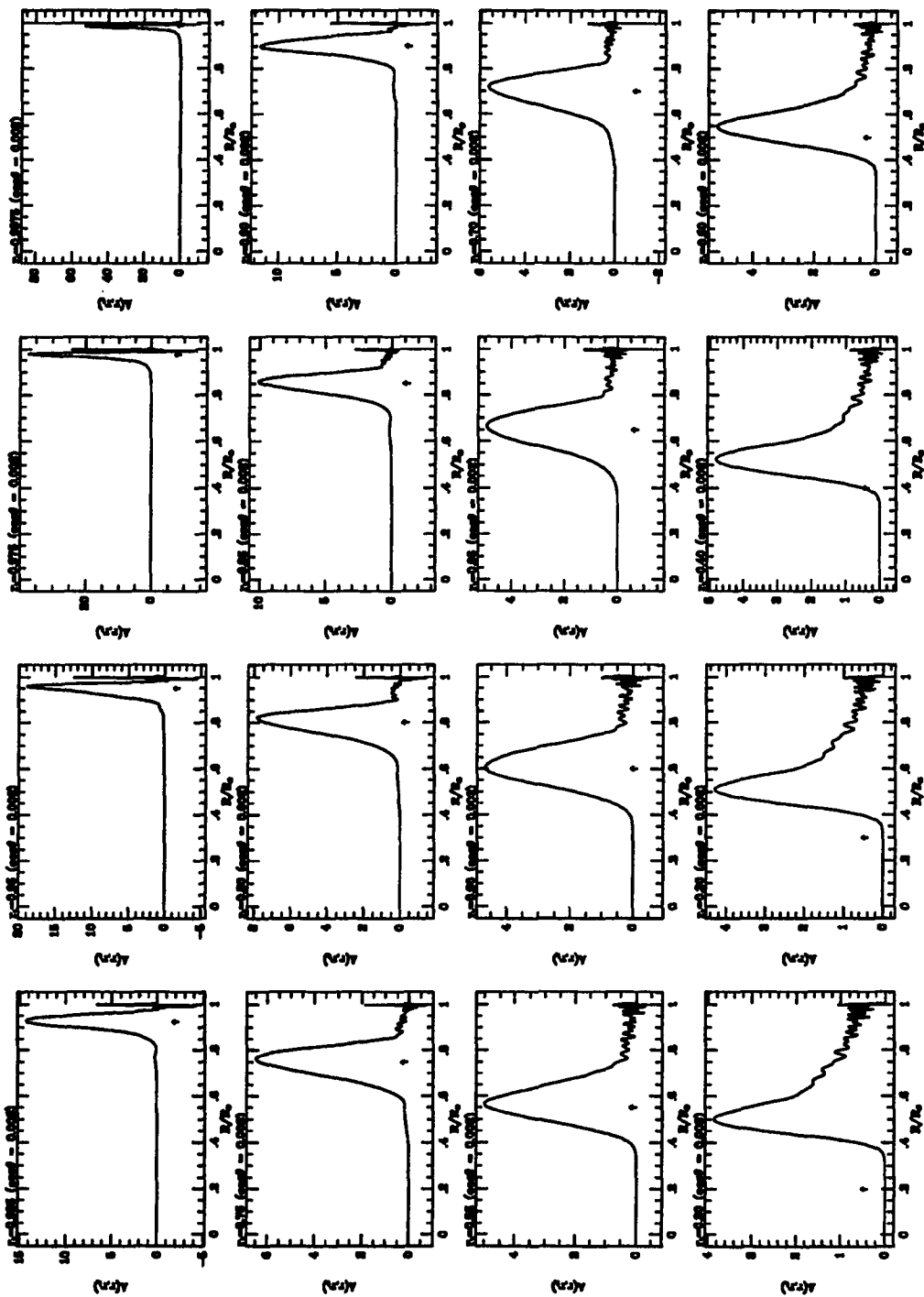


Figure 6.4 (continued)

kernels may be adequately localized, a more careful inspection of the resolution kernels themselves indicates the presence of a non-negligible secondary peak localized at the surface. The presence of such large secondary peaks indicates the inability of the methods to localize the resolution kernel near the targeted depth. This is easily explained by the nature of the rotational kernels. Indeed, since all the modes are reflected at the surface, the rotational kernels all have a significantly non-zero value just below the surface. Therefore, there exists a region near the surface where no linear combination of the available set of rotational kernels can have a small value at the surface and still be localized in that region. The depth of this region can be estimated to be on the order of the penetration depth of the shallower mode used in the inversion.

Results of the ISE with an adjusted discretization grid are shown in Figure 6.5 and a selection of corresponding resolution kernels in Figure 6.6. The SVD truncation, for each radius, was selected such as to limit the error magnification below a selected threshold (0.02 and 0.01 respectively) while keeping the largest possible number of eigenvalues. Despite several attempts to adequately distribute a larger number of discretization radii, we were unable to achieve a stable solution with more than 9 radii. Notice that the resolution kernels remain poorly localized, or when localized, still display large excursions near the surface. Therefore, the centroids of the resolution kernels do not provide a good estimate of the actual location of the inverted solution, and the interpretation of the resulting profiles becomes less straightforward. While some of the features seen with the other methods are present, their significance on the sole basis of the ISE results could not have been demonstrated.

Based on the resolution indicated by the preliminary inversion obtained for the CLS and OAK methods, we have reassessed the location of our target radii and selected a trade-off parameter that limit the error magnification without attenuating excessively the significant features present in the inverted profiles.

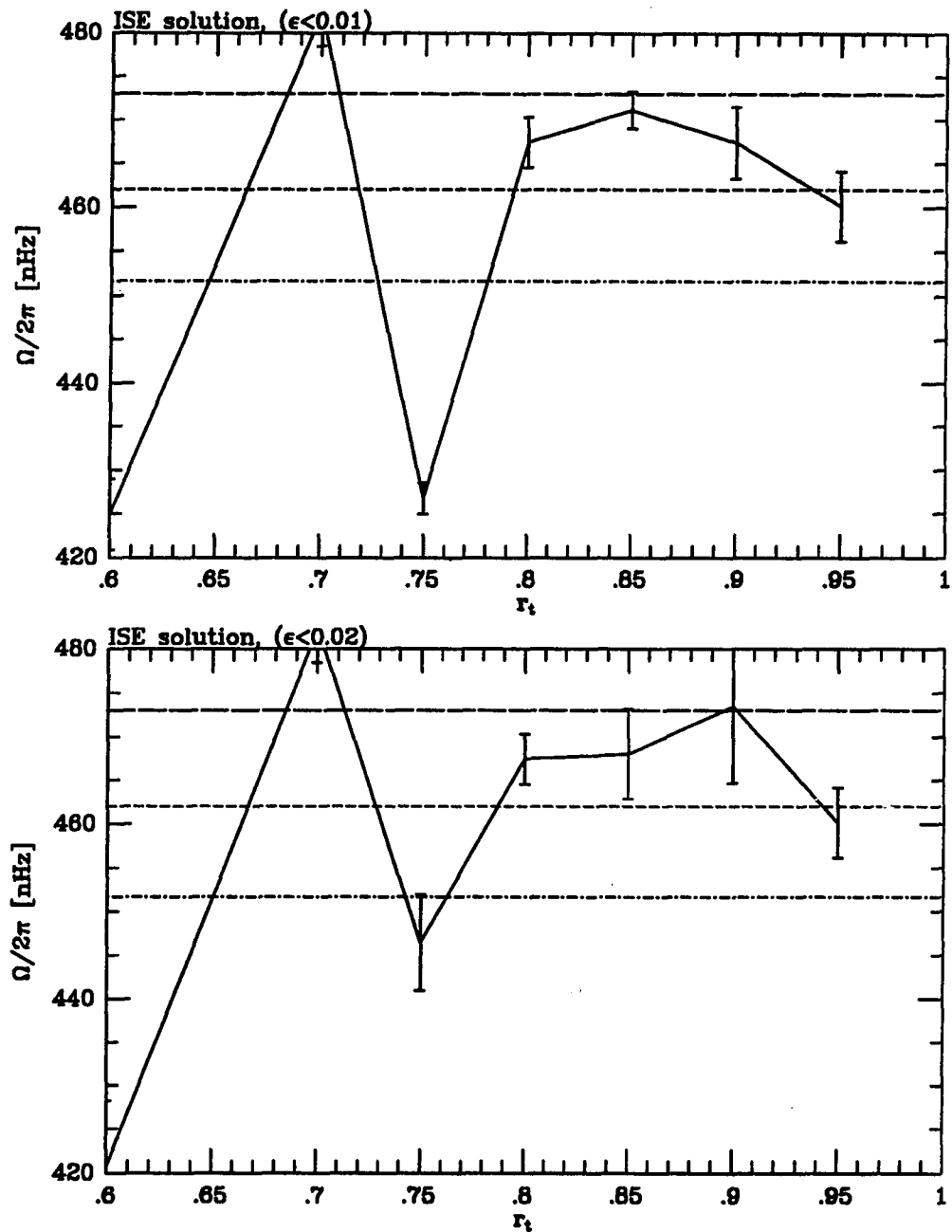


Figure 6.5: ISE solution profile after adjustment of the discretization grid through an iterative process. The SVD truncation, at each radius, was selected as to limit the relative error on the solution below 0.01 (upper panel) and 0.02 (lower panel) respectively. The non-seismic “surface” rotation rate are indicated by the long dashes, short dashes, and dot dashes lines for the doppler feature rotation rate (Snodgrass and Ulrich 1990), the magnetic feature rotation rate (Snodgrass 1983) and the spectroscopic rotation rate (Snodgrass 1985) respectively.

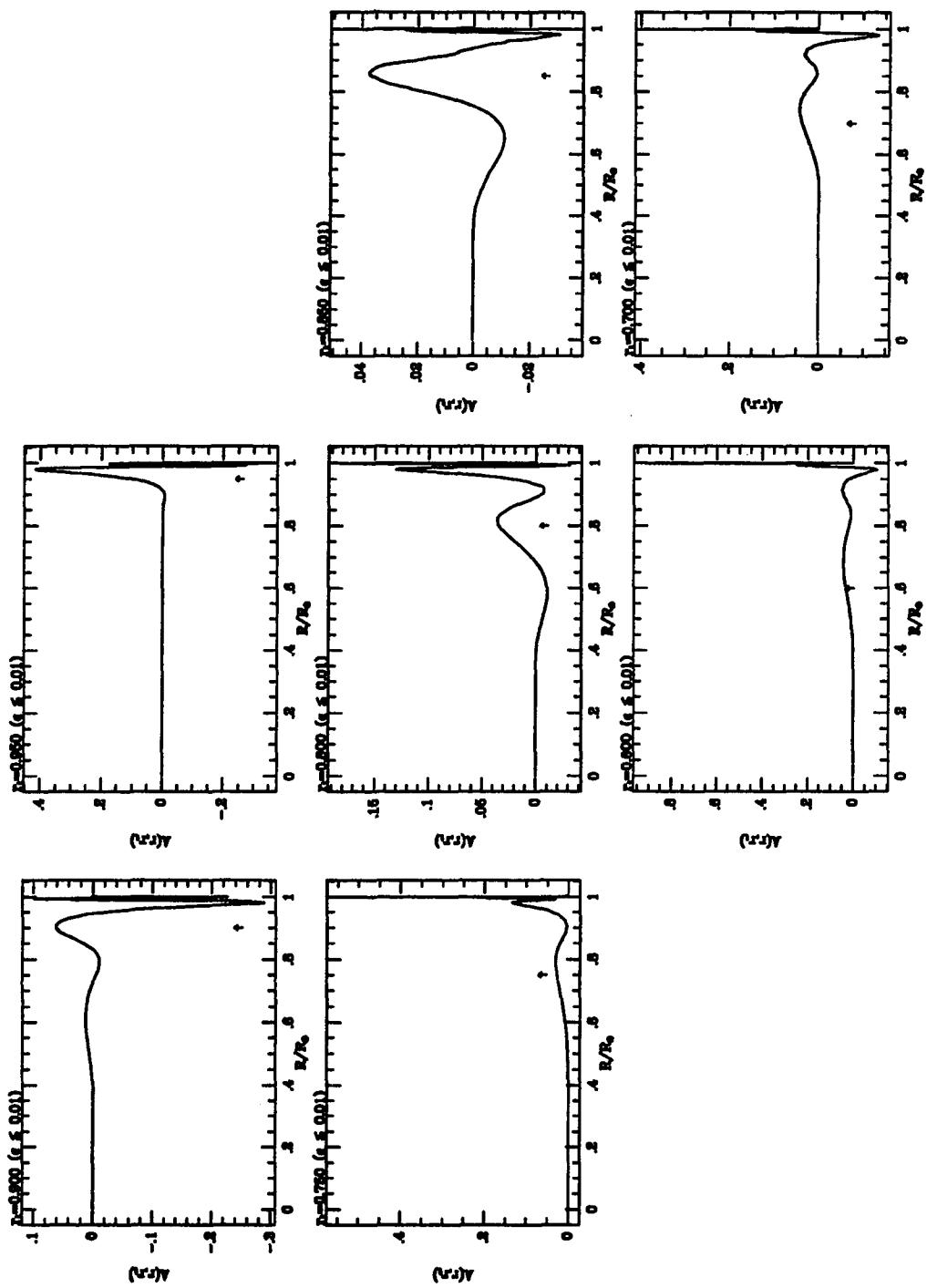


Figure 6.6: Set of resolution kernels corresponding to the ISE solutions presented Figure 6.5.

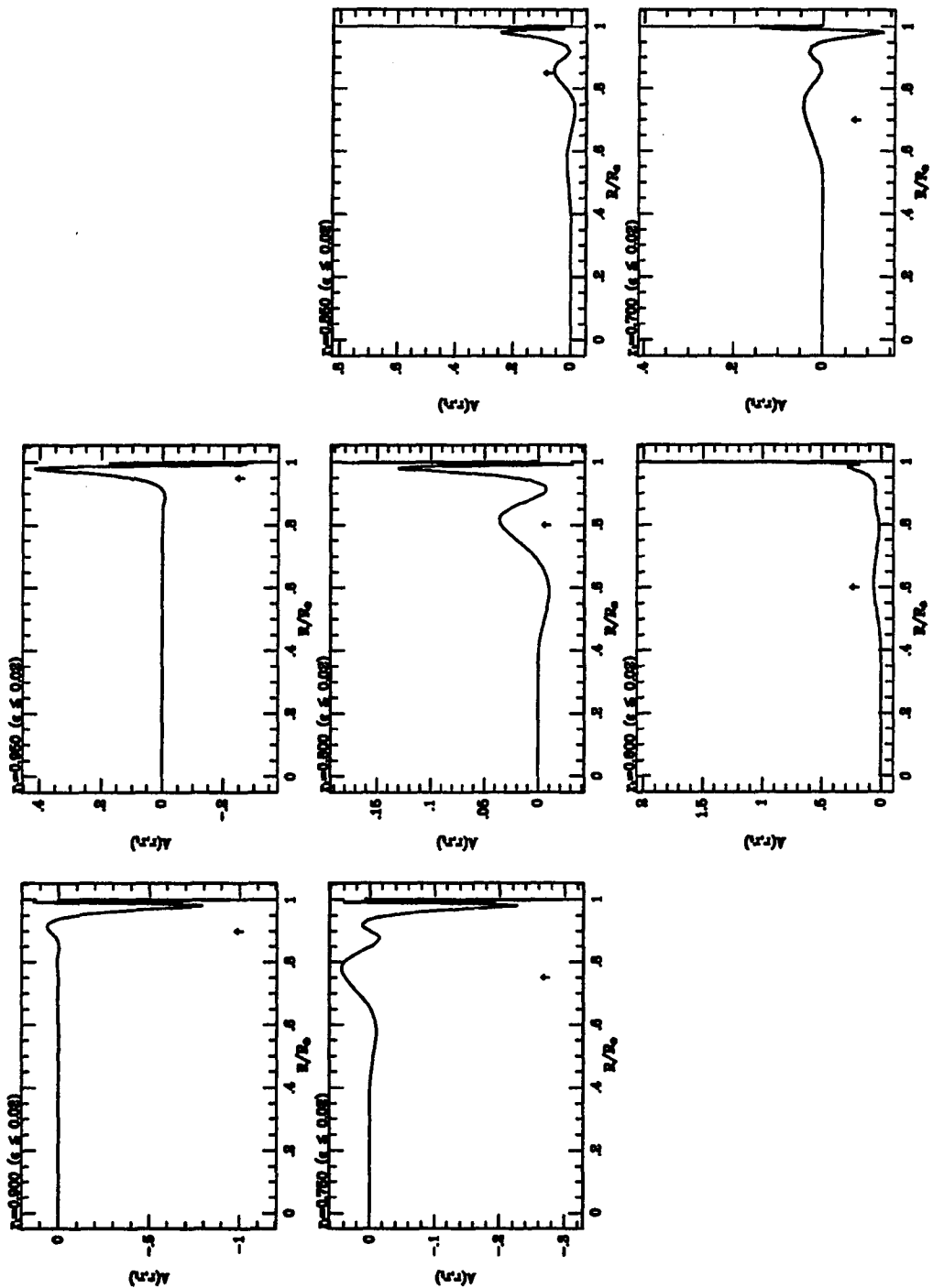


Figure 6.6 (continued)

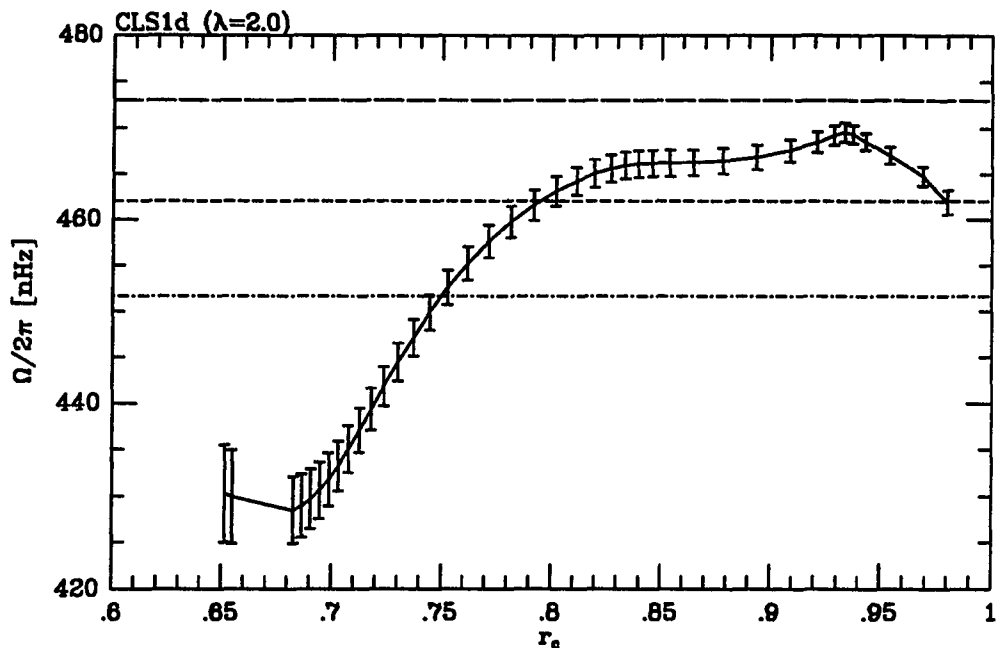


Figure 6.7: Solution obtained with the CLS1d method using MWO n -averaged splittings. As for Figure 6.5, the non-seismic “surface” determination of the rotation rate are indicated by the horizontal lines.

Figures 6.7 to 6.9 present the resulting profiles, restricted to adequately localized values, for the CLS1d, CLS2d and OAK methods, while Figures 6.10 to 6.12 present some selected resolution kernels associated with these profiles. The direct comparison of the three profiles, presented in Figure 6.13, clearly indicates that, independently of the methods used, the same features are present, with very similar amplitudes. Namely, these are a sharp increase with radius of the rotation rate from some 435 nHz to some 465 nHz between $R = 0.65R_{\odot}$ and $R = 0.80R_{\odot}$ followed by a plateau for $0.80R_{\odot} < R < 0.90R_{\odot}$, then a rise up to some 470 nHz around 0.94 followed by a decrease with radius, with a slope that can be reasonably extrapolated to a value compatible with the spectroscopic determination of the surface rotation rate (452 nHz). Despite the fact that the inner turning point for $\ell \approx 600$ is around $0.99R_{\odot}$, the present level of uncertainty of the high-degree splittings prevented us from achieving adequately localized resolution kernels with either method in the outermost 3% of the solar interior.

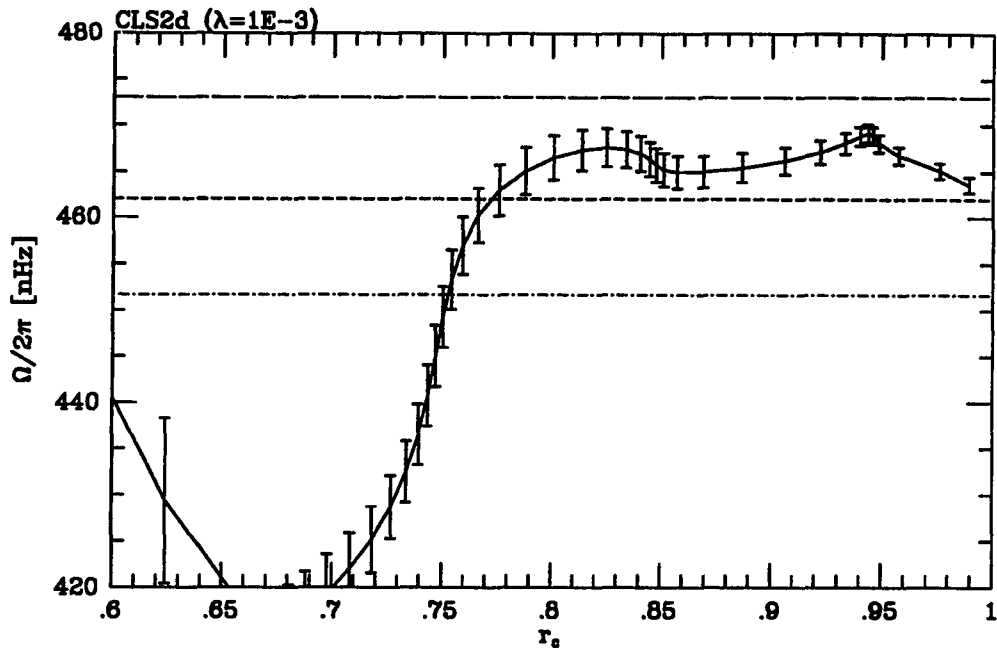


Figure 6.8: Solution obtained with the CLS2d method using MWO n -averaged splittings. As for Figure 6.5, the non-seismic "surface" determination of the rotation rate are indicated by the horizontal lines.

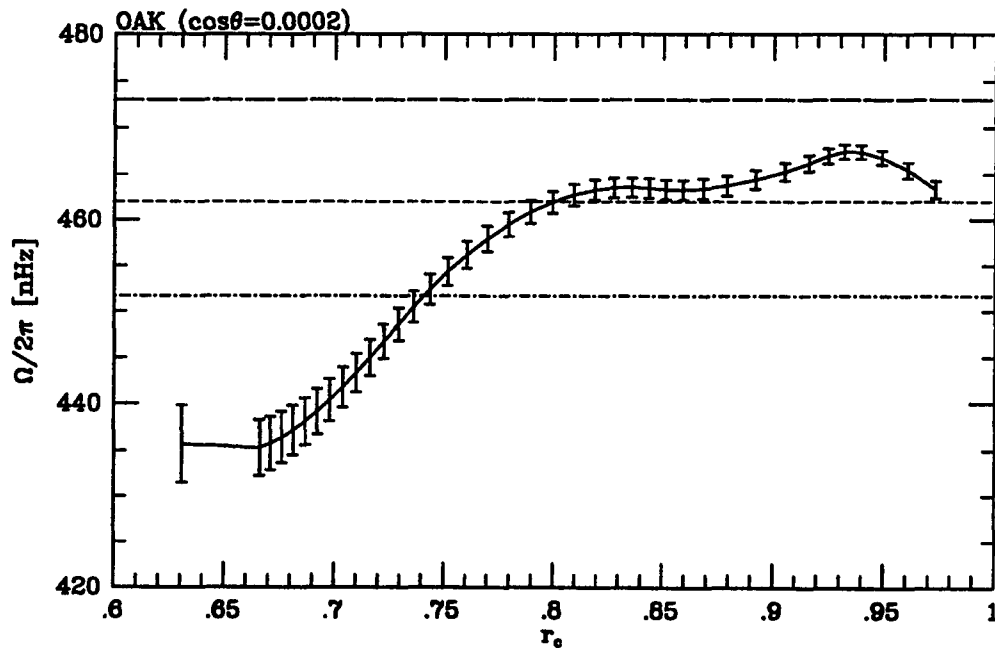


Figure 6.9: Solution obtained with the OAK method using MWO n -averaged splittings. As for Figure 6.5, the non-seismic "surface" determination of the rotation rate are indicated by the horizontal lines.

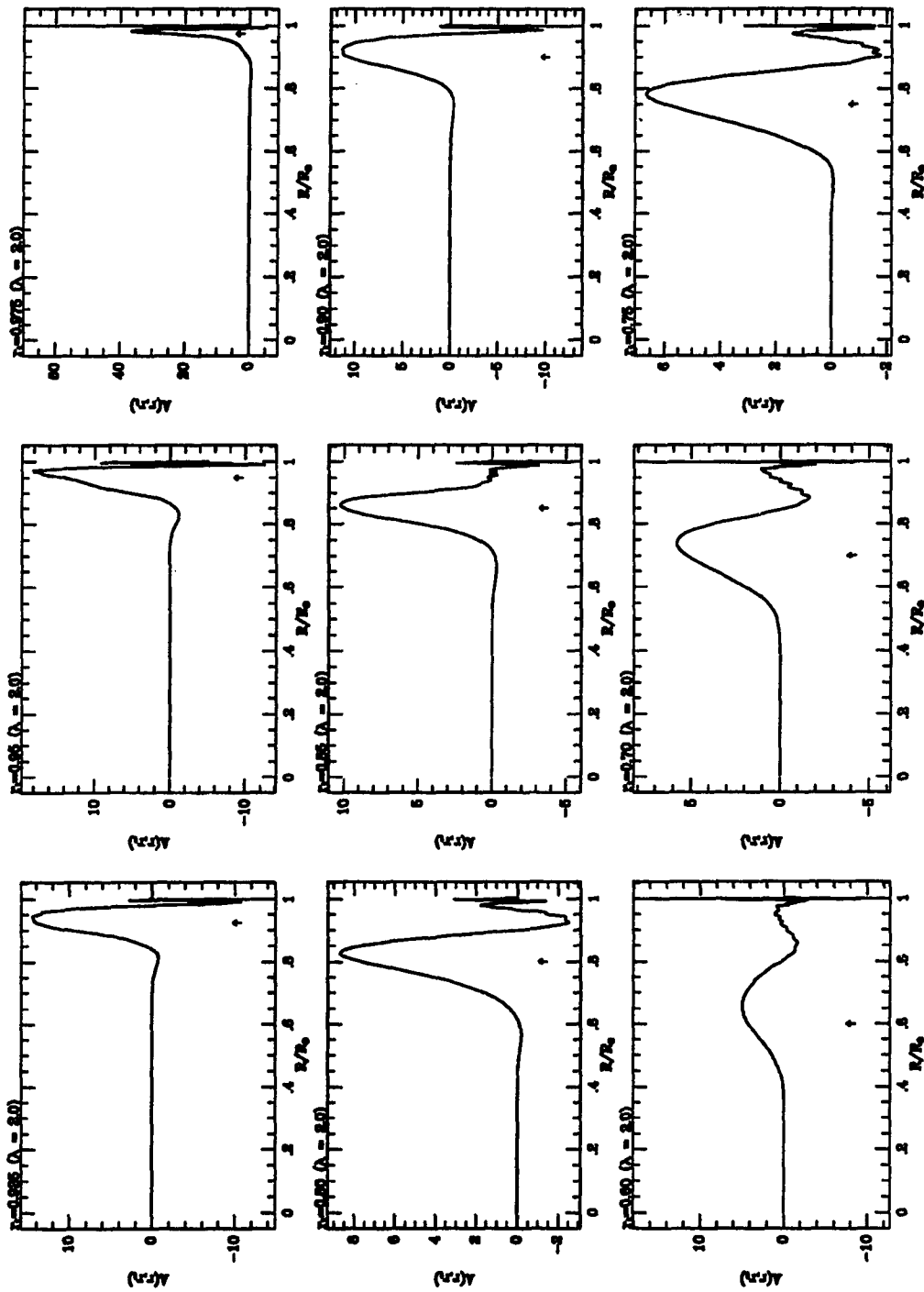


Figure 6.10: Selection of resolution kernels corresponding to the solution presented Figure 6.7, namely the CLS1d solution using the n -averaged MWO set.

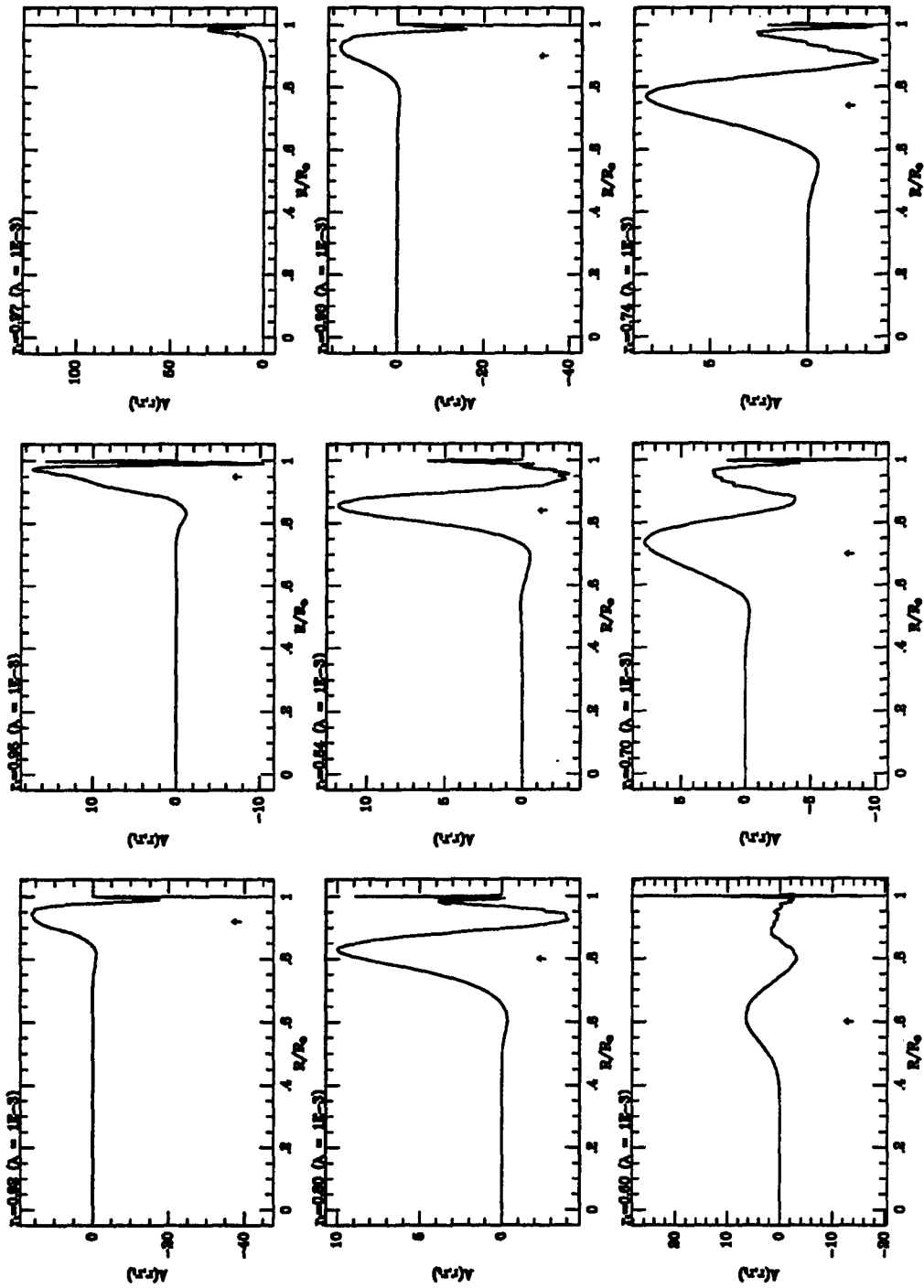


Figure 6.11: Selection of resolution kernels corresponding to the solution presented Figure 6.8, namely the CLS2d solution using the n -averaged MWO set.

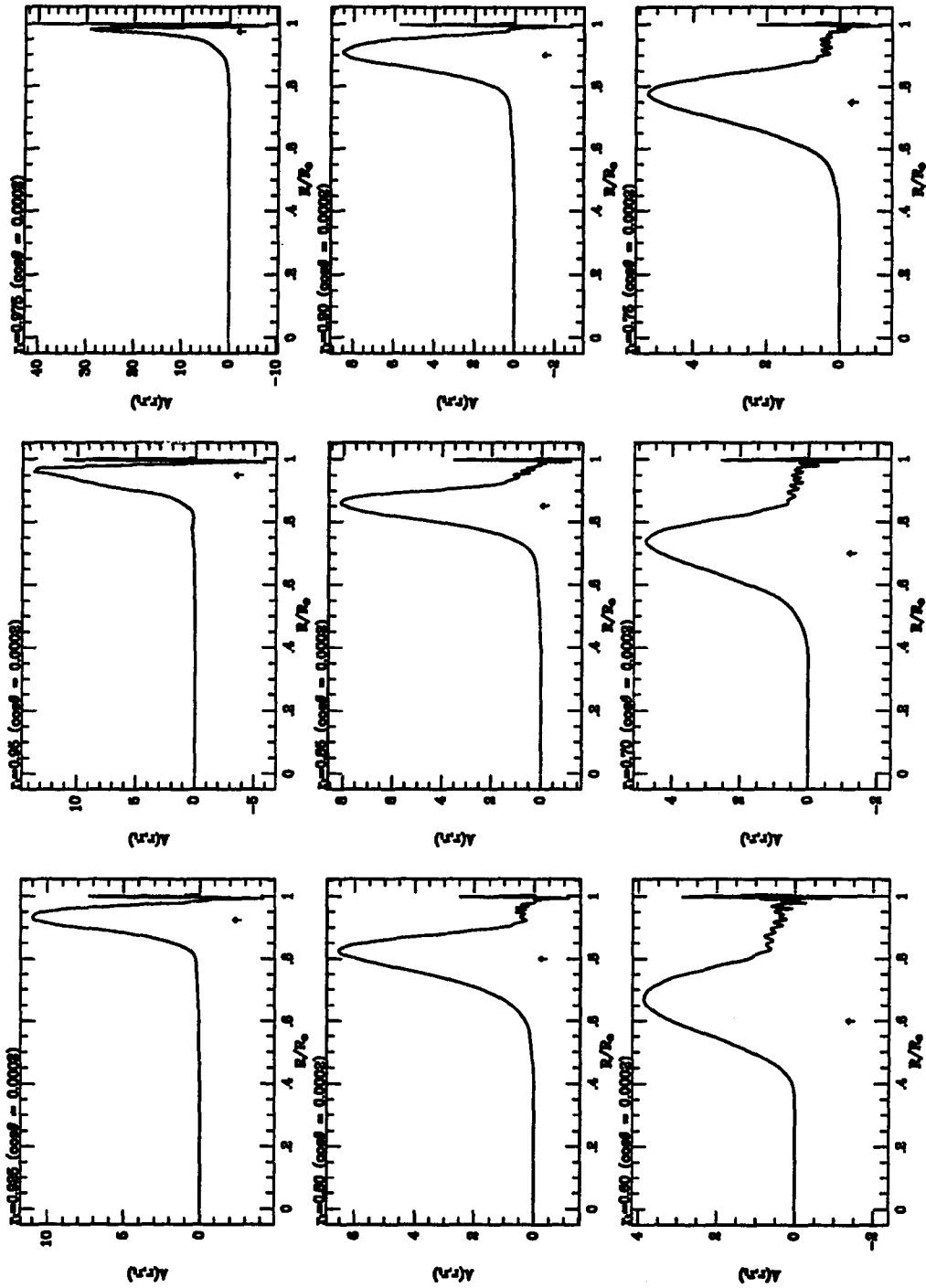


Figure 6.12: Selection of resolution kernels corresponding to the solution presented Figure 6.9, namely the OAK solution using the n -averaged MWO set.

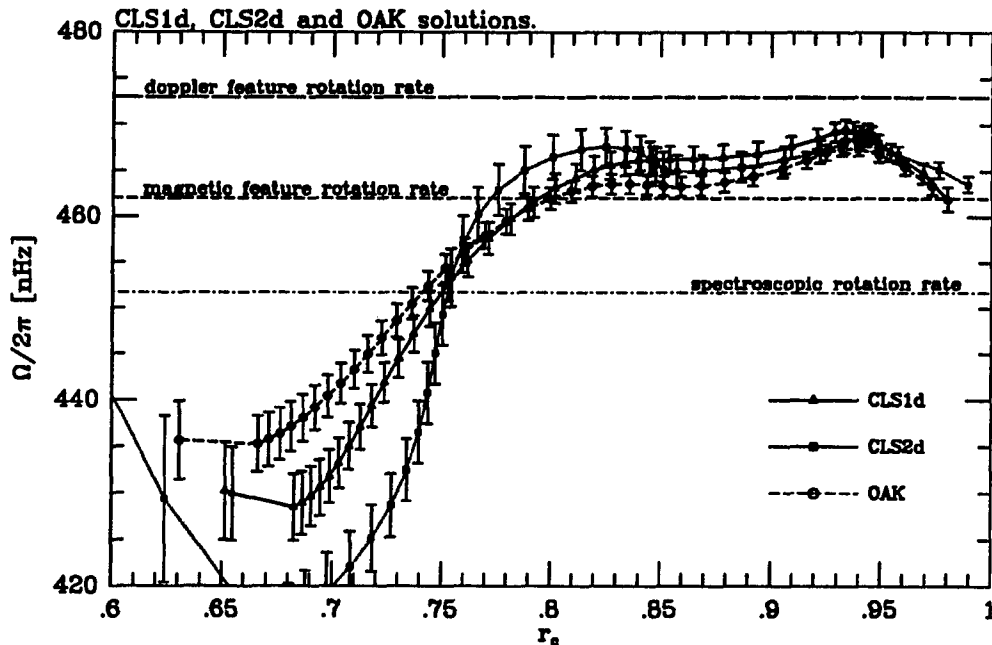


Figure 6.13: Direct comparison of inverted rotation rate profiles based on the MWO set alone, as presented Figures 6.7, 6.8 and 6.9. The non-seismic determination of the “surface” rotation rate are indicated as in Figure 6.5

In order to illustrate the specific contribution from the high-degree modes, we have also performed the inversion using only the low- and intermediate degree splittings ($20 \leq \ell < 120$). Figure 6.14 compares, for the same radial discretization and trade-off coefficient, inverted profiles obtained with and without the high-degree modes. In order to illustrate the degradation of the resolution kernels above $0.9R_{\odot}$ in the absence of high-degree modes, a selection of resolution kernels for the CLS1d solution based solely on the low- and intermediate-degree splittings is shown in Figure 6.15. Note that, as expected from the penetration depth of the highest degree mode used for these inversions (namely, since the inner turning point for $\ell = 120$ is around $0.91R_{\odot}$), no localized resolution kernels could be achieved above $0.9R_{\odot}$.

This comparison demonstrates that a) the features observed above $0.9R_{\odot}$ cannot be resolved without the high-degree modes, b) the uncertainty on the inverted profile is reduced by the inclusion of the high degree splittings even in the deeper regions and c) the am-

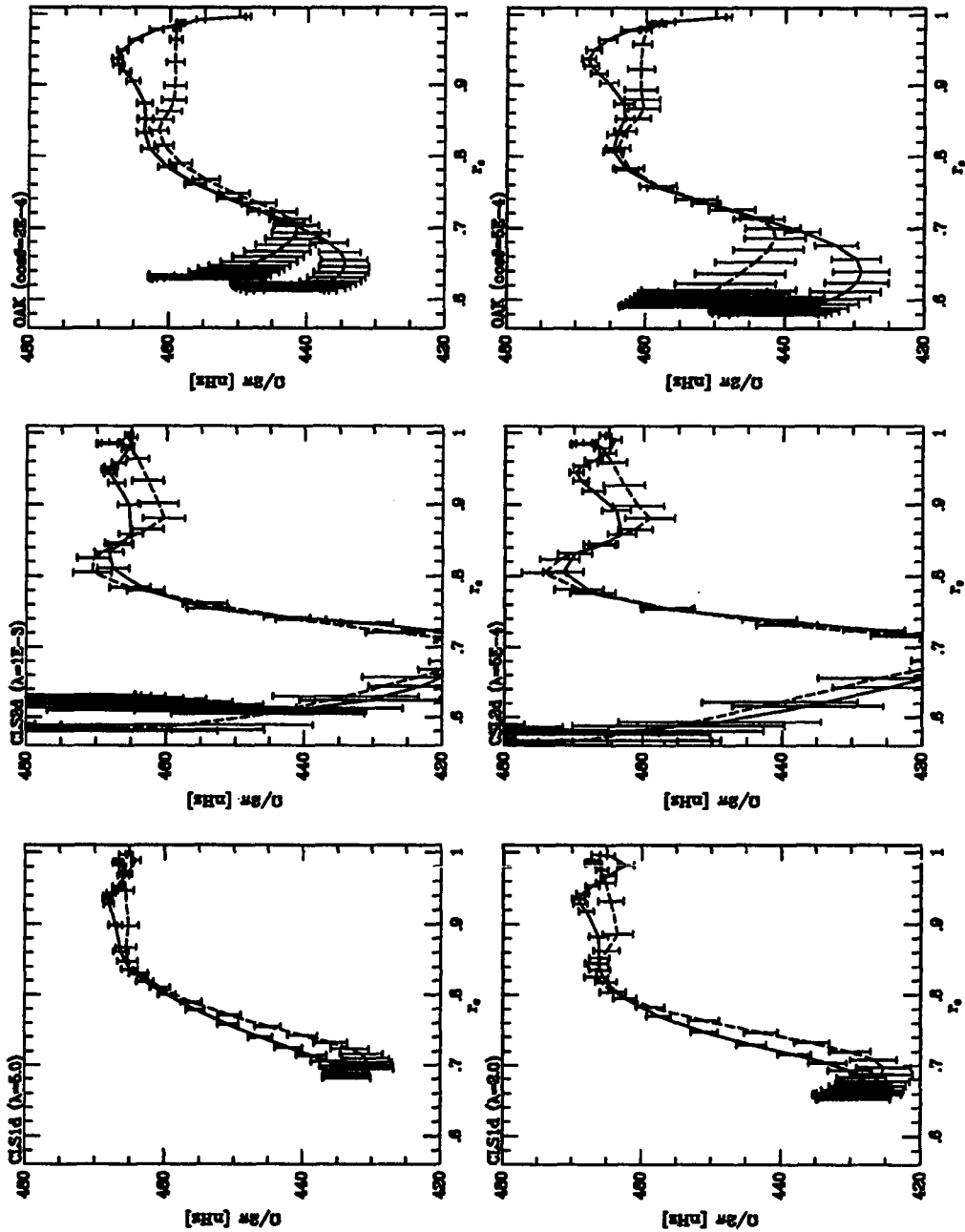


Figure 6.14: Comparison of profiles obtained using the MWO set alone, but with and without high-degree modes (i.e. $\ell > 120$), obtained with, from left to right the CLS1d, the CLS2d and the OAK methods, respectively. The solutions, at same radial discretization and trade-off parameter, obtained without the high degree modes (i.e. $20 < \ell < 120$) are connected by dashed lines. The upper panel presents solutions obtained with a larger trade-off parameter than the solutions presented in the lower panel.

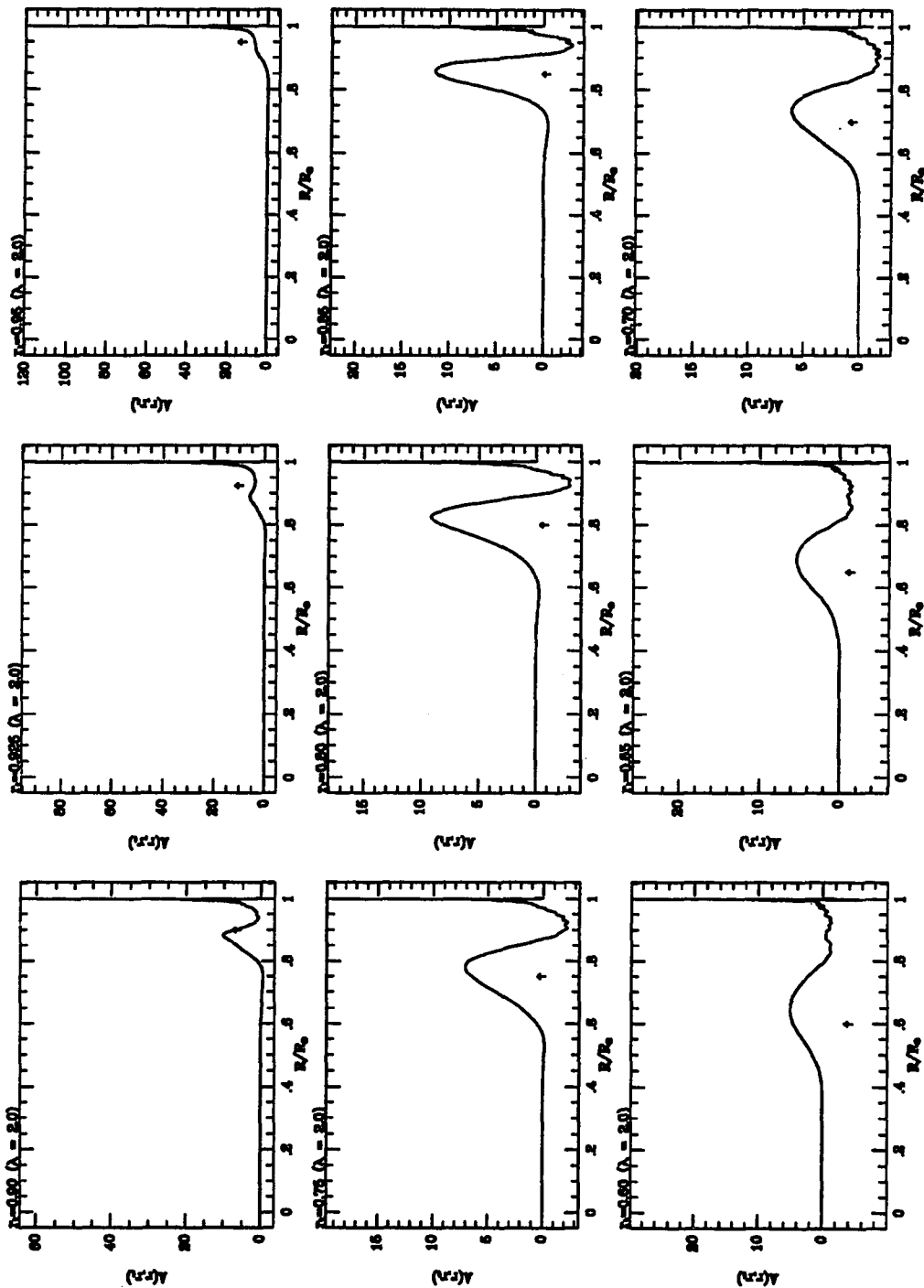


Figure 6.15: Resolution kernels corresponding to the CSL1d solution obtained using solely the MWO low- and intermediate-degree (i.e. $20 < \ell < 120$) presented in the lower left panel of Figure 6.14. Resolution kernels corresponding to the solution using the same method, radial discretization and trade-off parameter, but using the complete MWO set (i.e. $20 < \ell < 600$) are presented Figure 6.10. Notice the rapid degradation here of the resolution above $r = 0.85$.

plitude of the transition around $0.72R_{\odot}$ is underestimated by the OAK method in the absence of high-degree splittings.

The instability present near $0.72R_{\odot}$, as indicated by a large oscillatory behavior of the solution when the trade-off coefficient is reduced, suggests strongly the possibility of a discontinuity in the rotation rate at a depth very comparable to the base of the convection zone (i.e. $0.73R_{\odot}$ for the standard model, Bahcall *et al.*, 1982).

6.2.2 MWO and BBSO Measurements Combined

Since the 1988 BBSO splitting measurements are based on a longer run and potentially less contaminated by systematics, or if contaminated, are contaminated by systematics of a different nature, we have combined the MWO and BBSO set into a unique set, where below $\ell = 60$ the MWO measurements have been superseded by the BBSO values.

Results from n -averaged Splittings

The BBSO set of splittings was reduced to its sectoral equivalent (i.e. to the sum of the odd-indexed coefficients) and n -averaged as described earlier. Figures 6.16 to 6.18 compare the resulting inverted profiles for each method with the profiles based on the MWO alone data set. As expected from the agreement between the two data sets (see Section 4.3.1), these comparisons do not indicate any significant differences for the inferred profile in the outer 20% of the solar radius. The only differences present are, a) a slightly better resolution in the deeper regions as expected from the inclusion of lower degree modes, and b) a systematic shift of the location of the potential discontinuity by some 2% in radius towards the center. The magnitude of the improvement in resolution introduced by the low-degree modes is illustrated Figure 6.19 where the measure of the resolving width (as defined by Equation (6.62)) is plotted as a function of the kernel centroid for each set and

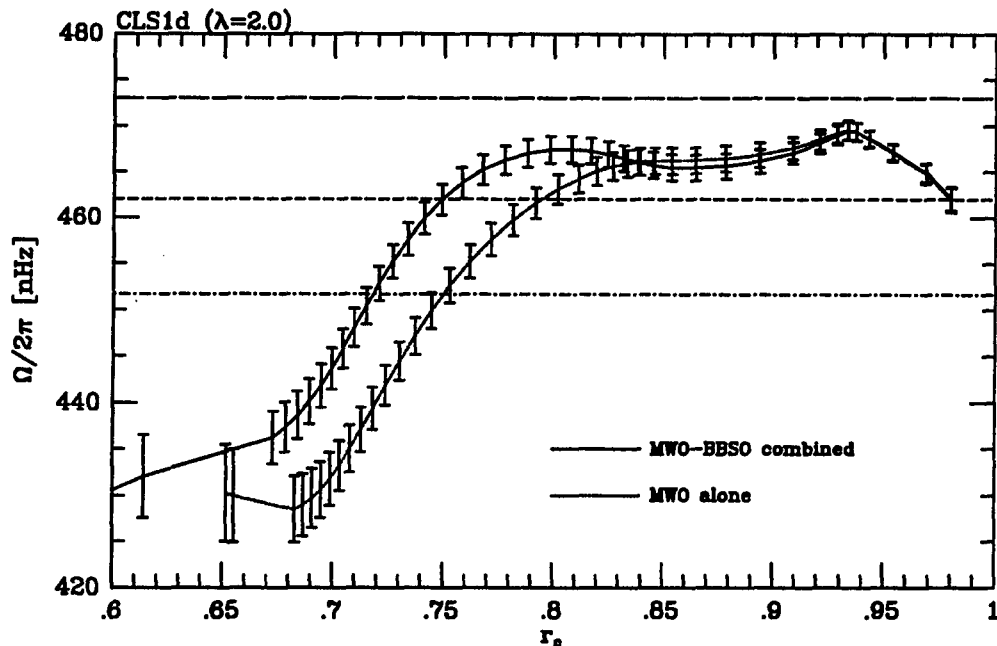


Figure 6.16: Comparison of inverted profile using MWO (dashed line) and combined n -averaged BBSO-MWO (solid line) splittings, using the CLS1d method.

each method.

Following Goode's example (Goode *et al.*, 1991), we have also attempted to allow for a discontinuity in the inverted profile. Indeed, the CLS1d method gives us the possibility to lift the constraint at any given mesh point, namely, by introducing at a selected depth a double mesh point at which no derivative is computed, hence not included in the smoothness constraint. Unfortunately, the location of this discontinuity must be defined *a priori* rather than being a free parameter fitted for. Figure 6.20 presents resulting inverted profiles when using $0.72R_{\odot}$, $0.73R_{\odot}$ and $0.74R_{\odot}$ respectively as a candidate for the location of the discontinuity. The inversions were carried out using the MWO alone and the BBSO-MWO combined sets of splittings. A selection of the associated resolution kernels for one of the resulting profile is presented Figure 6.21 where the resolution kernels are compared to the corresponding standard solution, while the resolving widths for the BBSO-MWO combined set solutions are compared to the corresponding standard solution

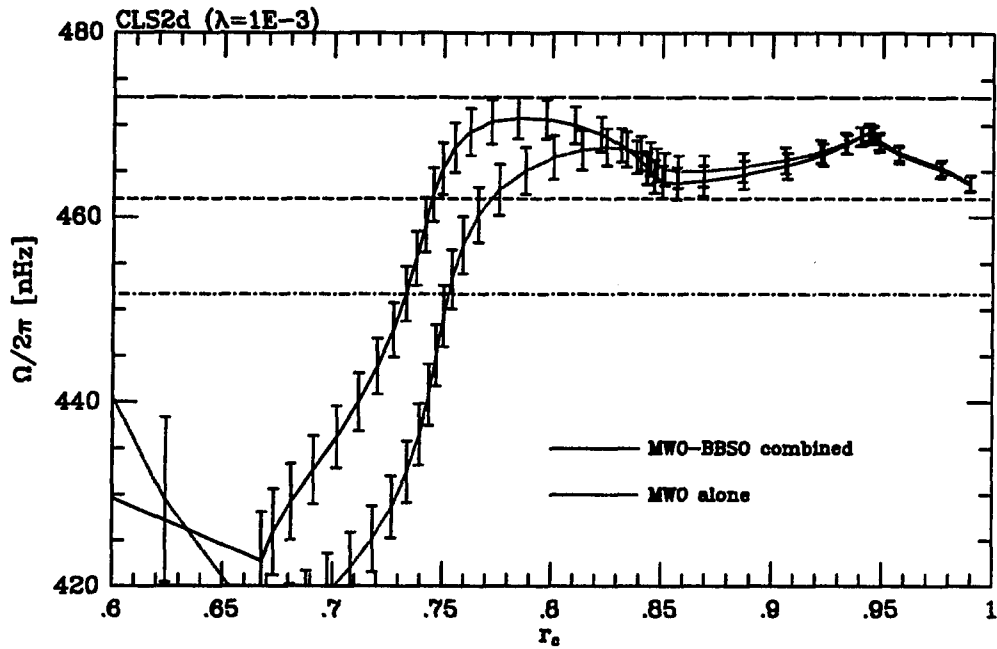


Figure 6.17: Comparison of inverted profile using MWO (dashed line) and combined n -averaged BBSO-MWO (solid line) splittings, using the CLS2d method.

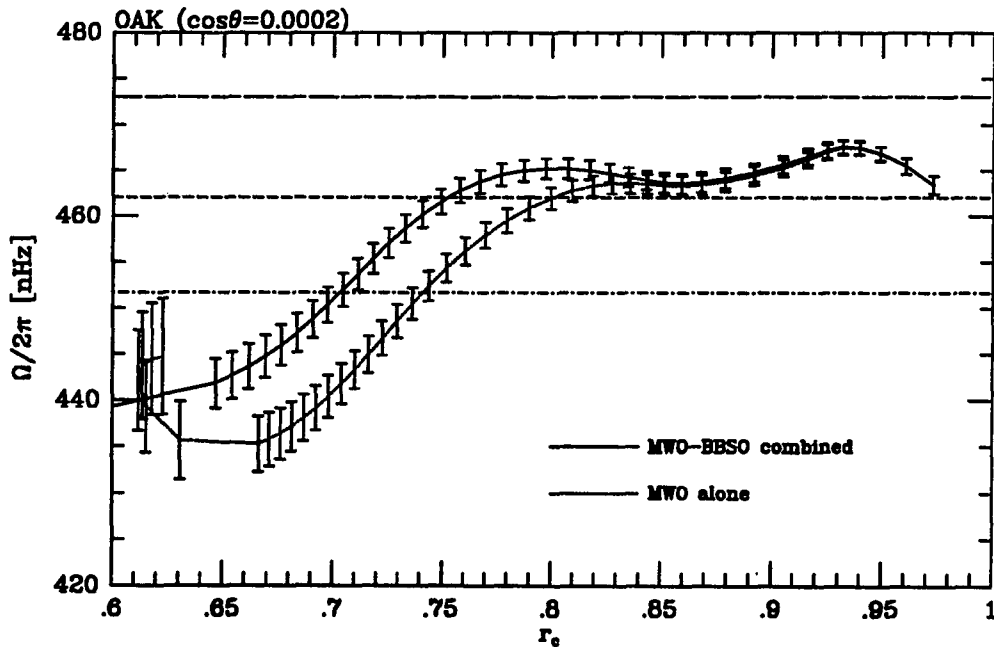


Figure 6.18: Comparison of inverted profile using MWO (dashed line) and combined n -averaged BBSO-MWO (solid line) splittings, using the OAK method.

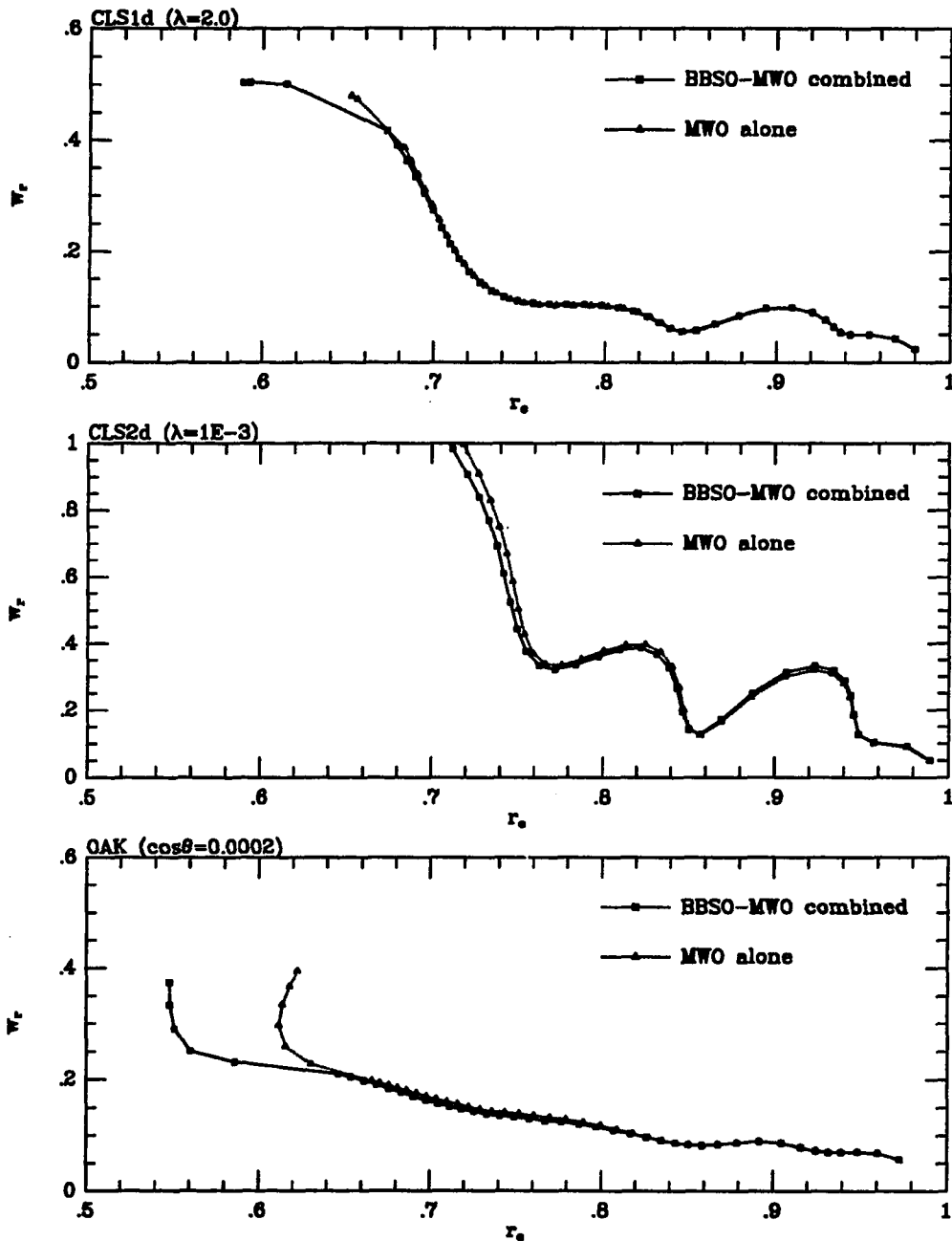


Figure 6.19: Comparison of resolving widths obtained using MWO and combined n -averaged BBSO-MWO splittings, using the CLS1d (top panel), the CLS1d (middle panel) and the OAK (bottom panel) methods, plotted versus the resolution kernel centroid location.

widths in Figure 6.22.

While very similar profiles are obtained in the outer 20% of the solar interior whether allowing or not for a discontinuity, the following points can be noticed. First, the introduction of the discontinuity leads to less well localized resolution kernels at every depth when compared to the corresponding standard solution, except for a marginal improvement in the deepest region. This degradation is concentrated around the targeted discontinuity, and leads to a skewed estimate of the resolution kernel centroids. Secondly, the amplitude of the discontinuity is a function of its *a priori* assumed location when the inverted set of splittings do not include the very low degree modes (namely when using the MWO set alone). On the contrary, when including these values, hence increasing the resolution below the most probable location of the discontinuity, the amplitude of such potential discontinuity remains fairly independent of the assumed location of the discontinuity. Nevertheless, the resolution kernels near the discontinuity remain poorly localized, and especially so for the target radii situated below the estimated location of the discontinuity. This prevents one from conclusively asserting the reality, location and amplitude of the discontinuity and indicates that such results should be interpreted with caution.

Results from Singlet and n -averaged Splittings

Since the BBSO data set provides an estimate of the frequency splittings for each individual radial overtone, and since significant differences in the rotational kernels associated with different radial overtones are present, it is highly desirable to avoid reducing the data set to n -averaged values from an inversion standpoint. Therefore we have also inverted the BBSO singlet measurements ($5 \leq \ell \leq 60$), but have consolidated that set with the intermediate- and high-degree n -averaged MWO values ($\ell = 61, (1), 119$ and $\ell = 126, (10), 596$). As previously and when required, tesseral frequency splittings were reduced to their sectoral equivalent.

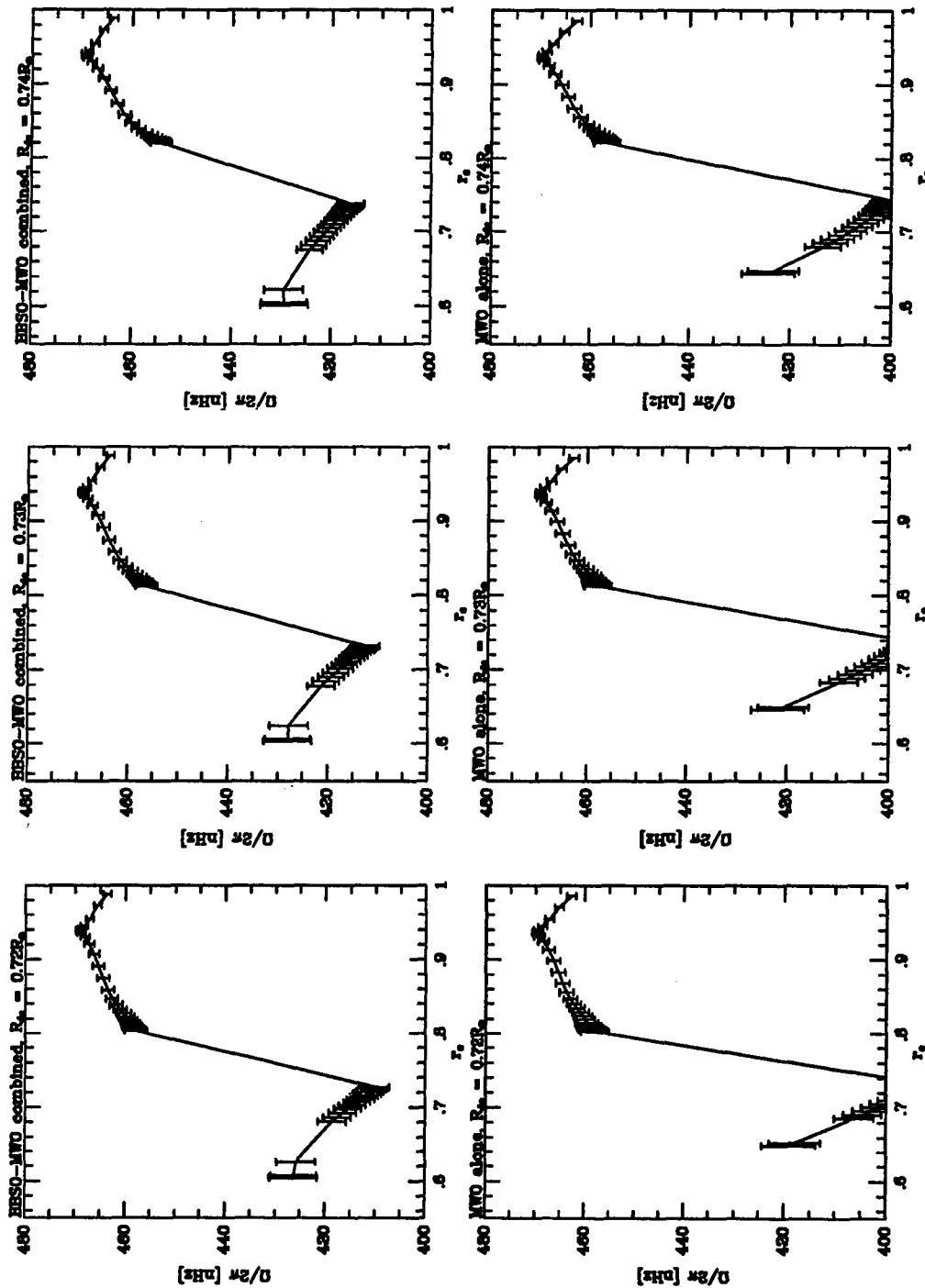


Figure 6.20: Inverted profiles using the CLS1d method modified to allow for a discontinuity. The discontinuities locations are $0.72 R_{\odot}$ (left panels), $0.73 R_{\odot}$ (middle panels) and $0.74 R_{\odot}$ (right panels) respectively. The bottom panels show solutions based on the MWO set alone while the top panels present solutions obtained with the BBSO-MWO combined set.

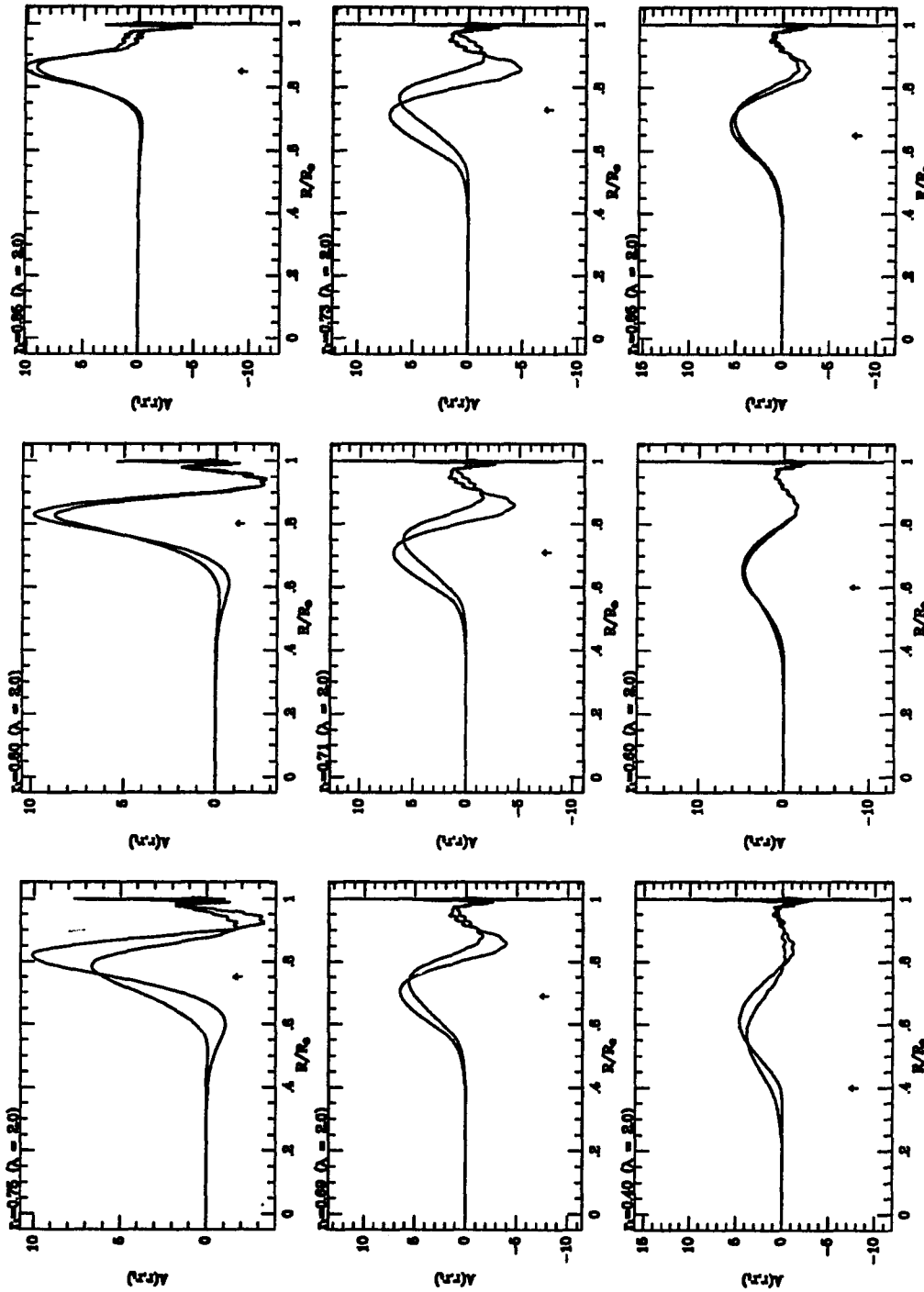


Figure 6.21: Resolution kernels associated with the profile inverted using the CLS1d method modified to allow for a discontinuity at $0.73R_{\odot}$, and based on the combined BBSO-MWO set (i.e. corresponding to the solution presented in the middle upper panel in Figure 6.20). The resolution kernels associated with the corresponding standard CLS1d solution are indicated by the dashed curves.

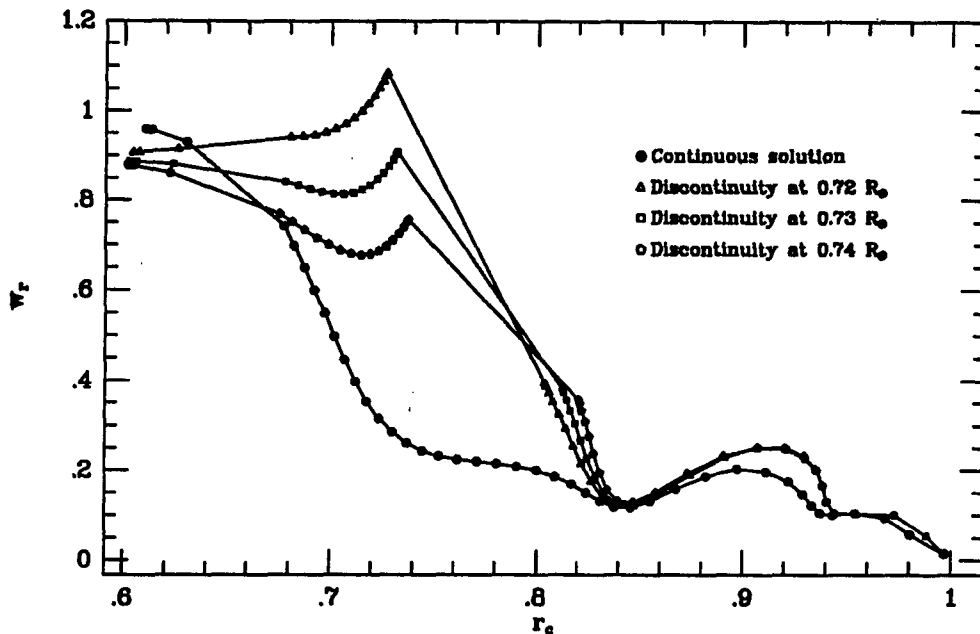


Figure 6.22: Resolving widths versus resolution kernel centroid for the solution obtained with the CLS1d method modified to allow for a discontinuity, and based on the BBSO-MWO combined set. The filled circles indicate the resolving widths associated with the corresponding standard CLS1d solution.

Figure 6.23 presents inverted profiles obtained with the OAK method using respectively the BBSO set alone (797 singlet values for $5 \leq \ell \leq 60$), the BBSO set complemented by the MWO intermediate-degree, high-resolution, n -averaged set (852 values, 797 singlet values extended by 55 n -averaged values to $\ell < 120$) and the BBSO set complemented by the intermediate-degree, high-resolution and high-degree, low-resolution sets (i.e. 900 values, 797 singlet values extended by 103 n -averaged values to $\ell \leq 596$). A selection of associated resolution kernels are shown in Figures 6.24 to 6.26, while Figure 6.27 presents the resolving width as a function of the kernel centroid for each set.

These figures indicates that a) the localization of the resolution kernels is dramatically improved by adding a small number of modes that sample uniquely the subsurface regions, and b) despite presenting similar features where the resolution kernels are localized, a systematic shift of some 10 and 5 nHz respectively is present when not including intermediate-

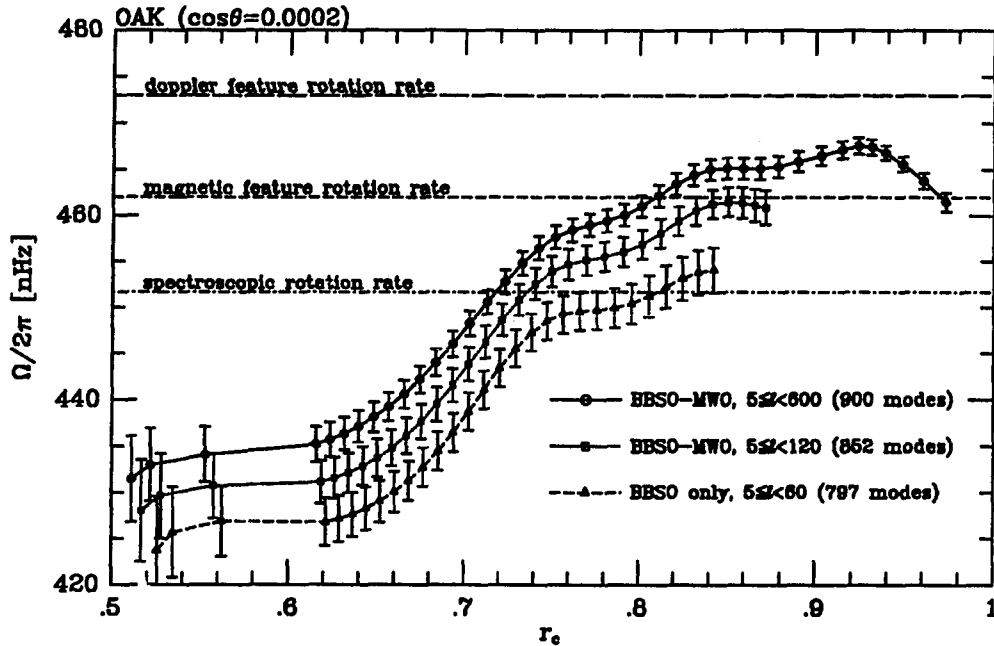


Figure 6.23: Inverted profiles computed with the OAK method and obtained using the singlet BBSO values consolidated by the MWO intermediate- and high-degree n -averaged values (i.e. 797 singlets for $5 \leq \ell \leq 60$ combined with 103 n -averaged values for $60 < \ell \leq 595$). Also plotted are solutions computed using the BBSO set alone (i.e. 797 singlets for $5 \leq \ell \leq 60$) and using the BBSO set combined with the intermediate-degree MWO set (i.e. 797 singlets for $5 \leq \ell \leq 60$ combined with 55 n -averaged values for $60 < \ell \leq 120$).

or high-degree modes¹. This systematic shift is easily explained by the residual sensitivity of the resolution kernels associated with the deeper target radii to the subsurface value.

Finally, let us point out that, while indeed the use of different radial overtones, when restricted to low-degree modes, allows us to extend the inversion beyond the typical inner turning point of the highest degree available (namely $0.85R_{\odot}$ while the inner turning point for $\ell = 60$ and $\nu = 3.3$ mHz is around $0.78R_{\odot}$), the total absence of information on the subsurface layers, to which these low-degree modes are also sensitive, introduces systematic effects associated with the limitation of any method to provide perfectly localized resolution kernels.

¹The CLS methods presented systematics of a different nature when not including the intermediate- or high-degree modes, but would in every case produce less localized kernels than the one obtained for the corresponding case with the OAK method

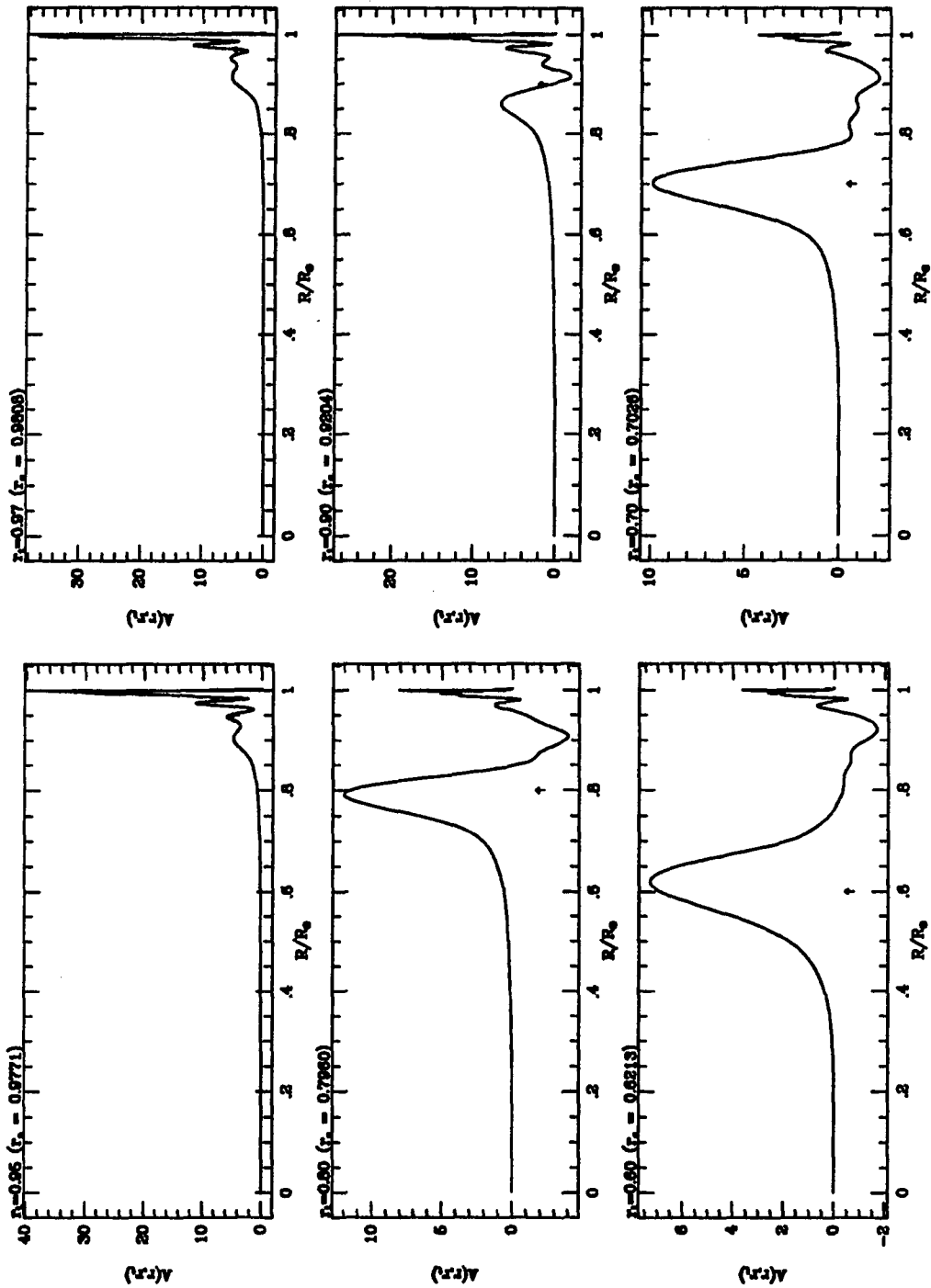


Figure 6.24: Selection of resolution kernels associated with the solution presented Figure 6.23 that uses only the singlet BBSO set

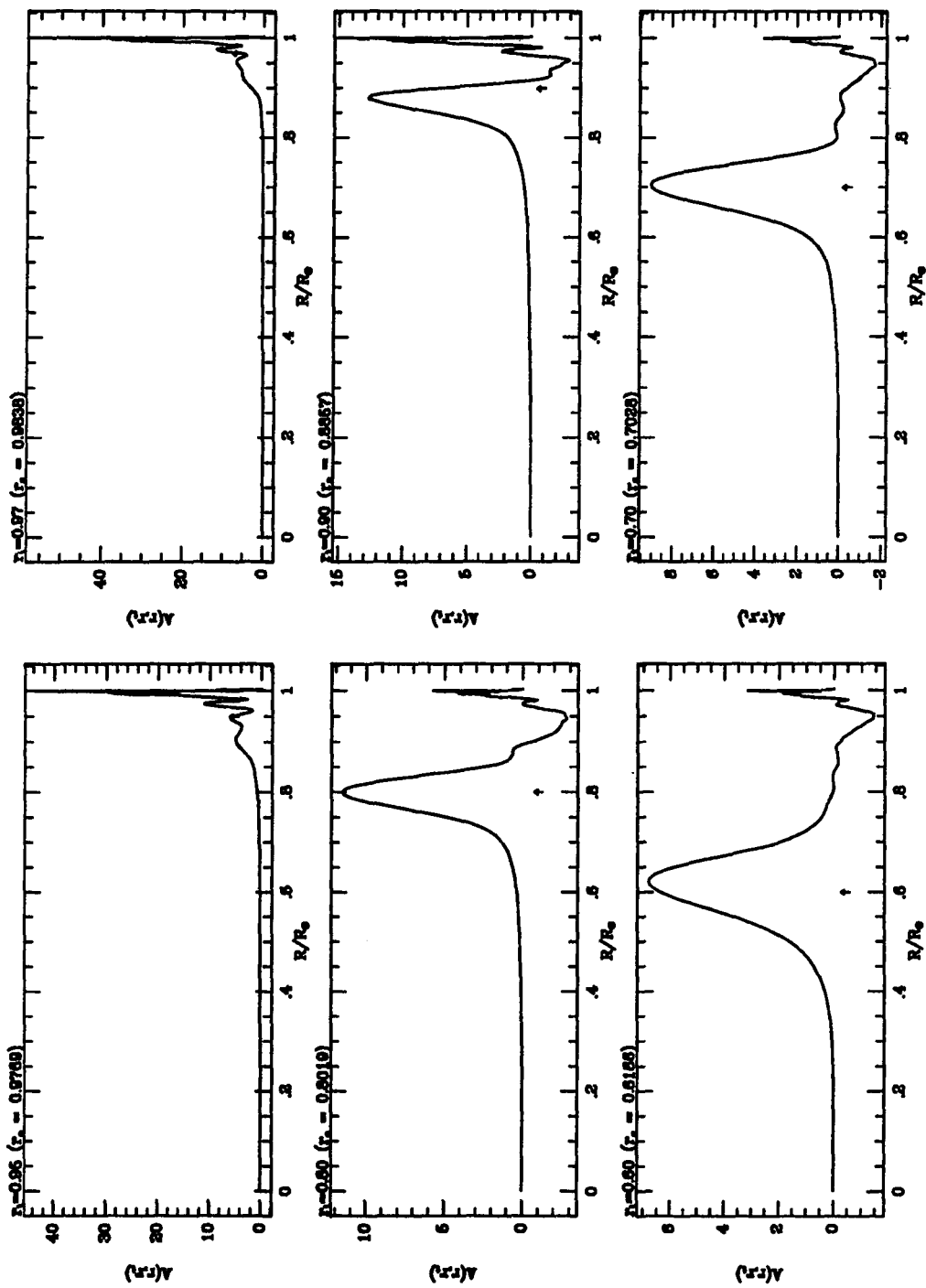


Figure 6.25: Selection of resolution kernels associated with the solution presented Figure 6.23 that uses the singlet BBSO set combined with the intermediate-degree MWO set

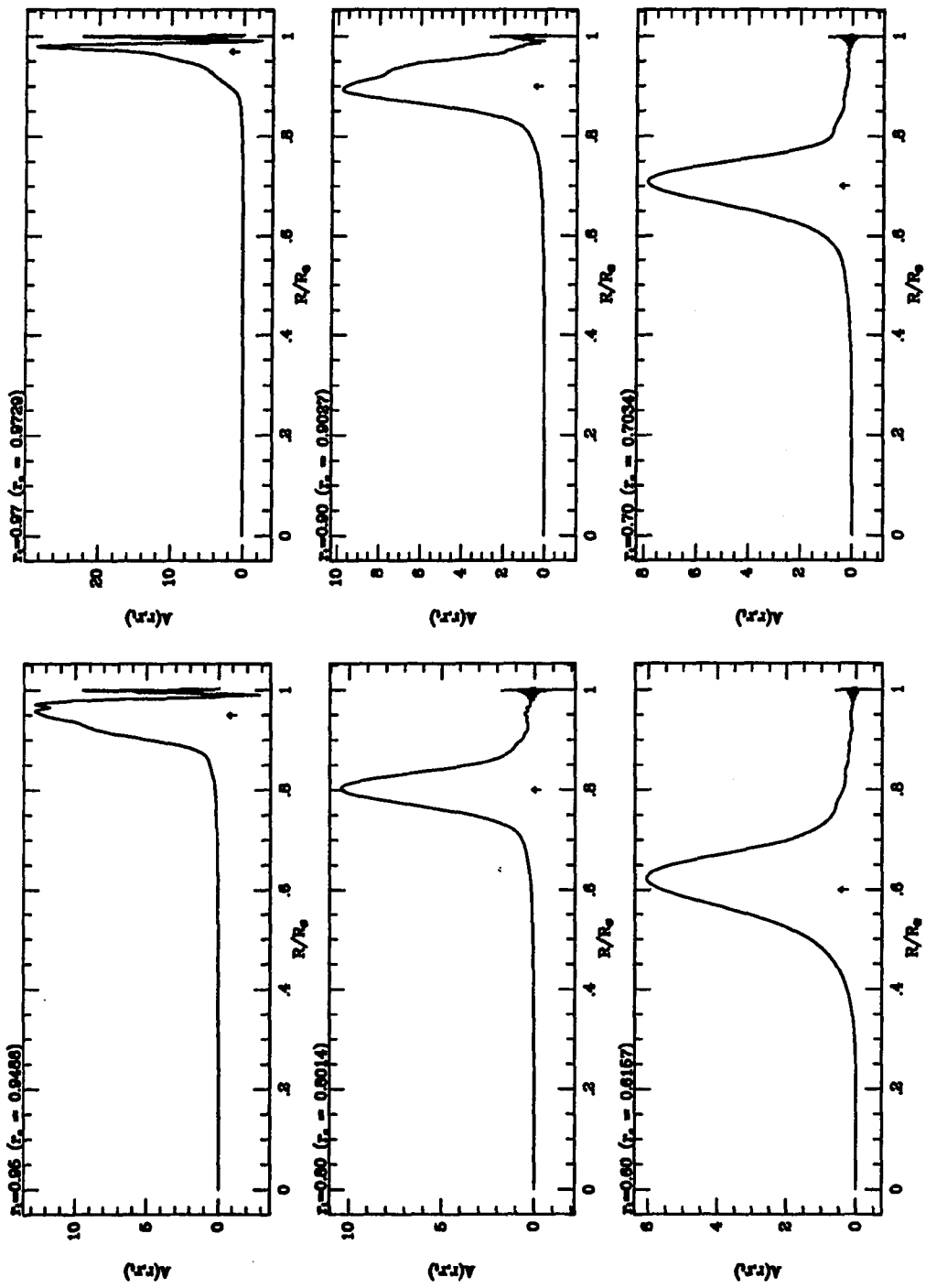


Figure 6.26: Selection of resolution kernels associated with the solution presented Figure 6.23 that uses the singlet BBSO set consolidated by the MWO intermediate- and high-degree set

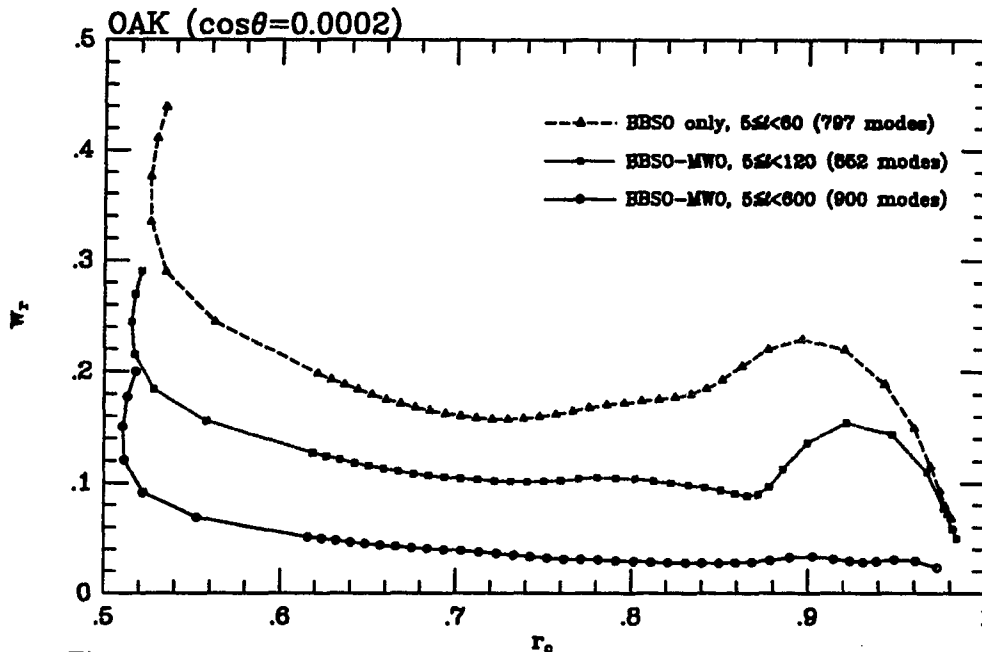


Figure 6.27: Resolving widths associated with solutions presented Figure 6.23

6.3 Conclusions

Keeping in mind that the solar internal angular velocity profile inferred in this chapter may be affected by systematic errors still present in the frequency splitting data set, the following picture for the equatorial rotation rate, as presented in Figure 6.28, emerges from the present study. First, we confirm the presence of a strong evidence for a discontinuity of the rotation rate at the base of the convection zone, but we remain unsuccessful in pinpointing its location or estimating reliably its amplitude. Second, by expanding the available splitting measurements to high-degree modes, a new picture emerges of the rotation rate in the outermost 15% of the solar radius that may reconcile the different non-seismic “surface” measurements.

While our inverted rotation profile is consistent with the spectroscopic rotation rate when extrapolated to the surface, it presents a rise with depth of the equatorial rotation rate just below the surface to reach a maximum value around $R/R_{\odot} = 0.93 \pm 0.01$. This higher-

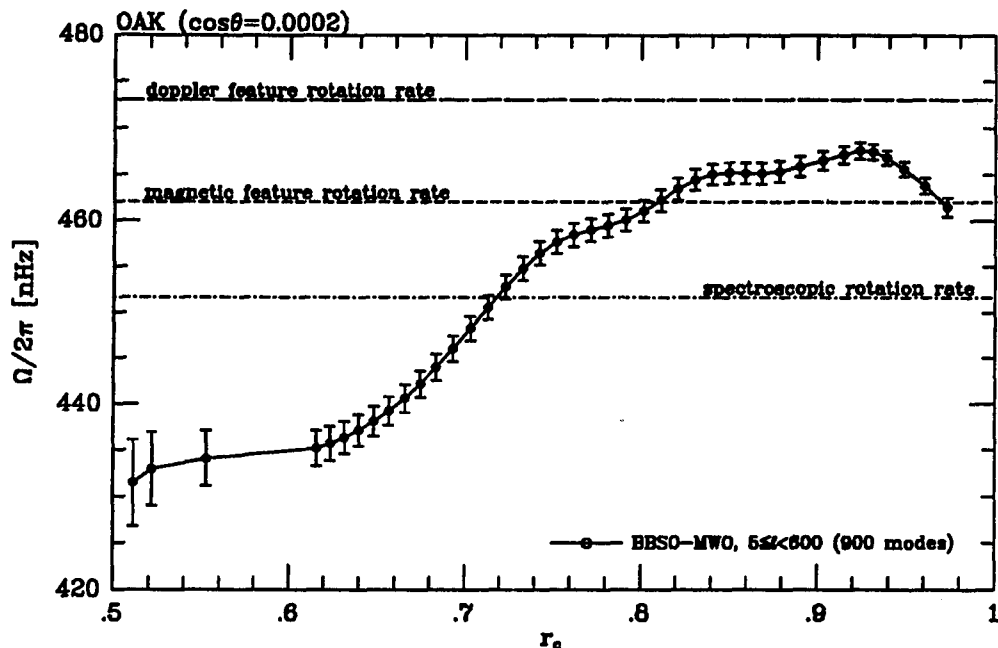


Figure 6.28: Equatorial rotation rate as a function of depth inferred from rotational frequency splittings, measured for degree $5 \leq \ell \leq 600$. Measurements based on 1988 BBSO ($5 \leq \ell \leq 60$) and on 1988 MWO ($60 < \ell \leq 600$) observations have been combined to obtain this profile.

than-surface value is consistent, in view of the actual width of the resolution kernels, with the rotation rate determined independently from cross-correlation doppler measurements (473.0 nHz, Snodgrass and Ulrich 1990) and attributed to the supergranulation network. In the deeper regions, namely, the bottom third of the convection zone, the inverted rotation rate presents a plateau around 464 nHz consistent with the magnetic feature rotation rate (462 nHz, Snodgrass 1983).

On the basis of the correspondence between the various non-seismic measurements of the “surface” rotation rate and the features present in our inverted profile of the solar rotation rate, we are tempted to speculate that the supergranulation network may be driven by a region located some 49 ± 7 Mm below the solar surface, a depth in reasonable agreement with the horizontal scale of supergranulation (~ 30 Mm). On the other hand, the surface magnetic features would be driven by a layer situated in the bottom third of the convection zone that would in turn be the seed of the surface magnetic field. This

conclusion is consistent with inversion results of even-indexed splitting coefficients showing evidence for a megagauss size toroidal field centered near the base of the convection zone (Dziembowski and Goode, 1989).

As previous inversions of p-modes frequency splittings have indicated, we see no evidence for an increase of the rotation rate with depth, as deep as $0.5 R_{\odot}$, but on the contrary, we see a definite inward decrease of some 6% in the rotation rate, concentrated at the base of the convection zone. By expanding the measure of p-mode frequency splittings to high-degree modes, we were also able to resolve the subsurface regions, and infer an increase inwards of the rotation rate by some 3% in the upper fourth of the convection zone.

In contrast, kinematic theories of solar dynamo (see Gilman, 1986) have been able to successfully represent several of the observed solar features, namely the period of the magnetic field reversal, the migration towards the equator of toroidal fields and in some cases the amplitude of the cycle, with the α - ω dynamo process, by relying on an angular velocity that increases inwards. On the other hand, global circulation models (Gilman and Miller, 1986) that attempt to explain the solar differential rotation, predict an angular velocity that decreases inwards, and is nearly constant on cylindrical surfaces parallel to the axis of rotation.

Clearly, our results are in strong disagreement with the classical kinematic dynamo theory, since our inverted profile is nearly flat in the convection zone. While we observe a 3% inward increase of the angular velocity in the outermost regions of the convection zone, the classical kinematic theory assumes that solar dynamo is seated in the bulk of the convection zone, and relies on an overall positive gradient in that region. However, as recent global circulation models have suggested, the source of the solar dynamo may instead be seated in a thin layer located at the bottom of the convection zone, rather than driven by the differential rotation in the bulk of the convection zone. In that thin layer,

the sharp inward decrease of the angular velocity, associated with the vanishing of the differential rotation and the presence of a significant magnetic field would be the driving mechanism behind the solar dynamo, hence the solar cycle. The plausibility of a dynamo mechanism in these conditions has been indicated by Gilman *et al.* (1989).

Finally, let us point out that evolutionary models of rotating stars (Pinsonneault *et al.*, 1989) predict a nearly flat rotation rate in the outer layers of the solar interior ($R > 0.6R_{\odot}$) combined with a rapidly rotating core (i.e. a rotation some 4 to 15 times the surface values at $0.2 R_{\odot}$). While the present accuracy of the low-degree p-mode frequency splittings limits the resolution of any inversion to the upper half of the solar interior, no significant hint for an inward increase of the solar rotation can be observed in our inverted profile. Thus, even though our results do not contradict the rapidly rotating core hypothesis, they do place an upper limit in the depth at which the required inward increase would begin. Hence our results favor models with either a slower or smaller rapidly rotating core.

Bibliography

- Backus, G. and Gilbert, F., 1970: "Uniqueness in the Inversion of Inaccurate Gross Earth Data," *Phil. Trans. R. Soc. London*, **266**, 123-192.
- Bahcall, J. N., Huebner, W. F., Lubow, S. H., Parker, P. D., and Ulrich, R. K., 1982: "Standard Solar Models and the Uncertainties in Predicted Capture Rates of Solar Neutrinos," *Rev. Modern Phys.*, **54**, 767-799.
- Brown, T. M., 1985: "Solar Rotation as a Function of Depth and Latitude," *Nature*, **317**, 591-594.
- Brown, T. M. and Morrow, C. A., 1987: "Depth and Latitude Dependence of Solar Rotation," *Astrophys. J. (Letters)*, **314**, L21.
- Brown, T., Mihalas, B. W., Rhodes, E. J., Jr., 1986: "Solar Waves and Oscillations," in *Physics of the Sun*, Sturrock, P. A., Holzer, T. E., Mihalas, D. M., and Ulrich, R. K. (Ed.), Dordrecht: Reidel, Chap. 7.
- Christensen-Dalsgaard, J. and Schou, J., 1988: "Differential Rotation in the Solar Interior," in *Advances in Helio- and Asteroseismology*, I.A.U. Symp. 123, J. Christensen-Dalsgaard and S. Frandsen (Ed.), Reidel: Dordrecht, 149-153.
- Christensen-Dalsgaard, J., Schou, J., and Thompson, M. J., 1990: "A Comparison of Methods for Inverting Helioseismic Data," *Mon. Not. R. astr. Soc.*, **242**, 353-369.
- Cuypers, J., 1980: "On the Calculation of the Frequency Splitting of Adiabatic Non-radial Stellar Oscillations by Slow Differential Rotation," *Astron. Astrophys.*, **89**, 207-208.
- Deubner, F. L., 1975: "Observation of Low Wavenumber Nonradial Eigenmodes of the Sun," *Astron. Astrophys.*, **44**, 371.
- Deubner, F. L., Ulrich, R. K., and Rhodes, E. J., Jr., 1979: "Solar p-Mode Oscillations as a Tracer of Radial Differential Rotation," *Astron. Astrophys.*, **72**, 177-185.
- Duvall, T. L., Harvey, J. W., and Pomerantz, M. A., 1987: "Latitude and Depth Variation of Solar Rotation," *Nature*, **321**, 500-501.
- Duvall, T. L., Harvey, J. W., Libbrecht, K. G., Popp, B. D., and Pomerantz, M. A., 1988: "Frequencies of Solar p-Mode Oscillations," *Astrophys. J.*, **324**, 1158-1171.
- Dziembowski, W. A. and Goode, P. R., 1989: "The Toroidal Magnetic Field Inside the Sun," *Astrophys. J.*, **347**, 540-550.

- Gilman, P., 1986: "The Solar Dynamo: Observations and Theories of Solar Convection, Global Circulation, and Magnetic Fields," in *Physics of the Sun*, Sturrock, P. A., Holzer, T. E., Mihalas, D. M., and Ulrich, R. K. (Ed.), Dordrecht: Reidel, Chap. 5.
- Gilman, P. A. and Miller, J., 1986: "Nonlinear Convection of a Compressible Fluid in a Rotating Spherical Shell," *Astrophys. J.*, **61**, 585-608.
- Gilman, P. A., Morrow, C. A., and DeLucas, E. E., 1989: "Angular Momentum Transport and Dynamo Action in the Sun: Implications of Recent Oscillation Measurements," *Astrophys. J.*, **338**, 528-537.
- Goldreich, P. and Kumar, P., 1988: "The Interaction of Acoustic Radiation with Turbulence," *Astrophys. J.*, **326**, 462-478.
- Goode, P. R., Dziembowski, W. A., Rhodes, E. J., Jr, and Korzennik, S. G., 1991: "What We Know about the Sun's Internal Rotation from Solar Oscillations," *Astrophys. J.*, in press.
- Gough, D., 1985: "Inverting Helioseismic Data," *Solar Phys.*, **100**, 65-99.
- Hale, G. E., 1908: "The Tower Telescope of the Mt. Wilson Solar Observatory," *Astrophys. J.*, **27**, 204-212.
- Hansen, C. J., Cox, J. P., and Van Horn, H. M., 1977: "The Effects of Differential Rotation on the Splitting of Nonradial Modes of Stellar Oscillation," *Astrophys. J.*, **217**, 151-159.
- Hathaway, D., Cacciani, A., Korzennik, S. G., and Rhodes E. J., Jr, in preparation.
- Hill, F., 1988: "Rings and Trumpets—Three-Dimensional Power Spectra of Solar Oscillations," *Astrophys. J.*, **333**, 996-1013.
- Hill, F., Gough, D., Toomre, J., and Haber, D. A., 1988: "Solar Equatorial Rotation Rate Inferred from Inversion of Frequency Splittings of High-degree Modes," in *Advances in Helio- and Asteroseismology*, I.A.U. Symp. 123, J. Christensen-Dalsgaard and S. Frandsen (Ed.), Reidel: Dordrecht, 45-48.
- Hill, F., Rust, D. M., and Appourchaux, T., 1988: "Rotation in the Solar Convection Zone Inferred from Fabry-Perot Observations of the 5-min Oscillations," in *Advances in Helios- and Asteroseismology*, I.A.U. Symp. 123, J. Christensen-Dalsgaard and S. Frandsen (Ed.), Reidel: Dordrecht, 49-52.
- Jackson, D., 1972: "Interpretation of Inaccurate, Insufficient and Inconsistent Data," *Geophys. J. Roy. astron. Soc.*, **28**, 97-109.
- Jiménez, A., Pallé, P. L., Roca Cortés, T., Domingo, V., and Korzennik, S. G., 1987: "Ground-Based Measurements of Solar Intensity Oscillations," *Astron. Astrophys.*, **172**, 323-326.
- Kaufman, J. M., 1988: "Measurements of High Degree Solar Oscillation Amplitudes," in *Seismology of the Sun and Sun-Like Stars*, E. J. Rolfe (Ed.), Paris: ESA SP-286, 31-35.
- Keys, R. G., 1981: "Cubic Convolution Interpolation for Digital Image Processing," *IEEE Trans. Acoustics, Speech, and Signal Processing*, **29**, 1153-1160.

- Korzennik, S. G., Cacciani, A., Rhodes, E. J., Jr., Tomczyk, S., and Ulrich, R. K., 1988: "Inversion of the Solar Rotation Rate versus Depth and Latitude," in *Seismology of the Sun and Sun-Like Stars*, E. J. Rolfe (Ed.), Paris: ESA SP-286, 31-35.
- Korzennik, S. G. and Ulrich, R. K., 1989: "Seismic Analysis of the Solar Interior. I. Can Opacity Changes Improve the Theoretical Frequencies?," *Astrophys. J.*, **339**, 1144-1155.
- Lanczos, C., 1961: *Linear Differential Operators*, London: van Nostrand, Chap. 3.
- Leighton, R. B., Noyes, R. W., and Simon, G. W., 1962: "Velocity Fields in the Solar Atmosphere. I. Preliminary Report," *Astrophys. J.*, **135**, 471.
- Libbrecht, K. G., 1988: "Solar p-Mode Phenomenology," *Astrophys. J.*, **334**, 510-516.
- Libbrecht, K. G., 1989: "Solar p-Mode Frequency Splitting," *Astrophys. J.*, **336**, 1092-1097.
- Libbrecht, K. G. and Kaufman, J. M., 1988: "Frequencies of High-Degree Solar Oscillations," *Astrophys. J.*, **324**, 1172-1183.
- Libbrecht, K. G., Woodard M. F., and Kaufman, J. M., 1990: "Frequencies of Solar Oscillations," *Astrophys. J. Supp.*, submitted.
- Noyes, R. W., 1982: *The Sun, Our Star*, Cambridge: Harvard University Press, 76-82.
- Pallé, P. L., Pérez, J. C., Régulo, C., Roca Cortés, T., Isaak, G. R., McLeod, C. P., and van der Raay, H. B., 1986: "The Global Oscillations Spectrum of the Sun," *Astron. Astrophys.*, **170**, 114.
- Parker, R. L., 1977: "Understanding Inverse Theory," *Ann. Rev. Earth Planet. Sci.*, **5**, 35-64.
- Pierce, K. A., and Wadell, J. H., 1961: "Analysis of Limb Darkening Observations," *Mem. R.A.S.*, **68**, 89-112.
- Pinsonneault, M. H., Kawaler, S. D., Sofia, S., and Demarque, P., 1989: "Evolutionary Models of the Rotating Sun," *Astrophys. J.*, **338**, 424-452.
- Rhodes, E. J., Jr., Ulrich, R. K., and Simon, G. W., 1977: "Observation of Nonradial p-Mode Oscillations on the Sun," *Astrophys. J.*, **218**, 901.
- Rhodes, E. J., Jr., Howard, R. F., Ulrich, R. K., and Smith, E. J., 1983: "A new System for Observing Solar Oscillations at Mt. Wilson Observatory," *Solar Phys.*, **82**, 245-258.
- Rhodes, E. J., Jr., Cacciani, A., Tomczyk, S., Ulrich, R. K., Blamont, J. E., Howard, R. F., Dumont, P., and Smith, E. J., 1984: "A Compact Dopplergraph/Magnetograph Suitable for Spaced-Based Measurements of Solar Oscillations and Magnetic Fields," *Advances in Space Research*, **4**, 103.
- Rhodes, E. J., Jr., Bursch, T. K., Ulrich, R. K., and Tomczyk, S., 1986: "A One-Megapixel Image Acquisition and Processing System for Solar Oscillations Studies," *Proceedings of Instrumentation in Astronomy VI, SPIE*, **627**, 256.
- Rhodes, E. J., Jr., Cacciani, A., Korzennik, S. G., Tomczyk, S., Ulrich, R. K., and Woodard, M. F., 1990: "Depth and Latitude Dependence of the Solar Internal Angular Velocity," *Astrophys. J.*, **351**, 687-700.

- Snodgrass, H. B., 1983: "Magnetic Rotation of the Solar Photosphere," *Astrophys. J.*, **270**, 288-299.
- Snodgrass, H. B., 1985: "Separation of Large-Scale Photospheric Doppler Patterns," *Solar Phys.*, **94**, 13-31.
- Snodgrass, H. B. and Ulrich, R. K., 1990: "Rotation of Doppler Features in the Solar Photosphere," *Astrophys. J.*, **351**, 309-316.
- Schleicher, H., 1976: Ph. D. dissertation, University of Göttingen.
- Tarbell, T., Peri, M., Frank, Z., Shine, R., Title, A., 1988: "Observation of f- and p-Mode Oscillations of High Degree ($500 < \ell < 2500$) in Quiet and Active Sun," in *Seismology of the Sun and Sun-Like Stars*, E. J. Rolfe (Ed.), Paris: ESA SP-286, 315-319.
- Thompson, M. J., 1990: "A New Inversion of Solar Rotation Splitting Data," *Solar Phys.*, **125**, 1-12.
- Tomczyk, S., 1988: Ph. D. dissertation, U.C.L.A.
- Ulrich, R. K., 1970: "The Five-Minute Oscillations on the Solar Surface," *Astrophys. J.*, **162**, 993-1002.
- Ulrich, R. K., Boyden, J. E., Webster, L., Snodgrass, H. B., Gilman, P. I., Padilla, S. P., and Shieber, T. L., 1988: "Solar Rotation Measurements at Mount Wilson," *Solar Phys.*, **117**, 291-338.
- Ulrich, R. K., Caccianni, A., Henney, C., Korzennik, S. G., Rhodes, E. J., Jr., and Wang, J., in preparation.
- Unno, W., Osaki, Y., Ando, H., Saio, H., and Shibahashi, H., 1989: *Nonradial Oscillations of Stars*, Tokyo: University of Tokyo Press, Chap. 3.
- Wittmann, A., 1977: "The Diameter of the Sun," *Astron. Astrophys.*, **61**, 225-227.
- Woodard, M. F., 1984: Ph. D. dissertation, U.C.S.D.
- Woodard, M. F. and Libbrecht, K. G., 1988: "On the Measurement of Solar Rotation using High-Degree p-Mode Oscillations," in *Seismology of the Sun and Sun-Like Stars*, E. J. Rolfe (Ed.), Paris: ESA SP-286, 67-71.
- Zirin, H., 1988: *Astrophysics of the Sun*, Cambridge: Cambridge University Press, Chap. 6.

Appendix A

Frequency Splittings

A.1 Tesseral Values from the High-Resolution Spectra

The following table lists the Legendre polynomials fitting coefficients resulting from the frequency splitting analysis of the high resolution tesseral spectra. The coefficients are listed in nHz, sidereal, with the respective 3σ uncertainties estimated from the scatter to the fit.

ℓ	a_0		a_1		a_2		a_3		a_4		a_5	
20	-0.03	1.02	434.70	1.74	0.72	2.20	17.62	2.58	0.34	2.87	1.18	3.19
21	0.07	1.49	441.20	2.70	1.86	3.56	6.78	4.45	6.83	5.05	5.94	5.88
22	0.28	1.16	436.70	1.98	-3.33	2.51	7.24	2.94	2.26	3.28	6.41	3.63
23	0.11	1.15	439.20	2.07	4.08	2.73	18.10	3.38	3.71	3.85	2.73	4.45
24	0.03	1.02	437.50	1.74	-1.12	2.21	12.73	2.59	0.20	2.89	-4.70	3.19
25	0.00	0.92	437.50	1.65	1.69	2.17	12.96	2.67	2.91	3.05	-2.64	3.50
26	-0.04	0.92	441.70	1.57	5.26	2.00	8.86	2.34	-5.11	2.61	1.70	2.88
27	0.07	0.62	436.60	1.10	-1.43	1.45	18.19	1.77	-3.10	2.02	0.66	2.32
28	0.06	0.98	438.20	1.68	3.54	2.14	11.89	2.50	-2.38	2.80	-0.68	3.08
29	-0.03	0.74	439.80	1.31	6.69	1.72	14.96	2.10	-0.86	2.41	6.16	2.75
30	0.12	0.75	438.80	1.29	-1.25	1.64	13.98	1.92	-3.05	2.14	0.69	2.36
31	0.18	0.70	438.60	1.24	2.59	1.63	14.16	1.98	-1.48	2.27	-1.97	2.58
32	-0.08	0.86	436.20	1.48	1.26	1.88	12.56	2.21	0.02	2.47	-4.05	2.72
33	0.08	0.64	439.70	1.13	3.36	1.48	13.92	1.80	3.65	2.06	-5.91	2.34
34	0.10	0.67	440.20	1.15	0.42	1.46	18.61	1.71	-3.20	1.92	-3.38	2.11
35	0.02	0.67	440.90	1.18	0.27	1.54	15.20	1.87	1.68	2.14	-2.61	2.42
36	0.44	0.64	434.70	1.28	5.72	1.81	12.98	2.14	3.37	2.39	-5.93	2.41
37	0.01	0.83	436.20	1.47	1.94	1.93	16.30	2.33	0.45	2.67	0.18	3.01
38	0.11	0.65	437.80	1.12	2.42	1.43	17.35	1.67	-1.27	1.88	0.47	2.06
39	-0.02	0.57	437.60	1.01	4.78	1.31	18.17	1.59	-2.57	1.82	-7.95	2.05

Table A.1: Legendre polynomials fitting coefficients resulting from the frequency splitting analysis of the tesseral high resolution spectra

ℓ	a_0		a_1		a_2		a_3		a_4		a_5	
40	0.08	0.60	438.30	1.04	1.09	1.32	17.49	1.55	-0.30	1.74	-3.86	1.92
41	0.02	0.54	438.20	0.94	2.38	1.23	20.47	1.49	2.11	1.70	0.45	1.92
42	0.08	0.53	436.40	0.92	0.64	1.17	18.81	1.37	-1.17	1.54	1.51	1.69
43	0.03	0.67	438.10	1.17	-0.28	1.53	20.12	1.85	4.51	2.11	-4.04	2.38
44	0.08	0.58	435.70	1.00	1.28	1.28	17.08	1.50	-0.73	1.68	1.45	1.85
45	0.01	0.29	437.50	0.51	-0.51	0.67	19.93	0.80	0.55	0.92	0.14	1.04
46	0.06	0.41	439.20	0.71	0.55	0.91	19.38	1.07	-0.69	1.20	-0.80	1.32
47	-0.08	0.43	439.40	0.75	0.23	0.98	22.51	1.18	2.65	1.35	2.45	1.51
48	0.06	0.50	440.50	0.85	0.17	1.09	20.68	1.28	-1.15	1.43	0.49	1.58
49	-0.06	0.50	438.20	0.87	3.10	1.15	17.44	1.37	1.72	1.57	-0.46	1.77
50	0.16	0.57	438.70	0.98	-0.88	1.26	21.56	1.47	-2.59	1.66	-2.14	1.82
51	-0.03	0.42	439.00	0.73	-1.45	0.95	21.08	1.14	-1.63	1.30	-1.26	1.46
52	0.07	0.42	438.70	0.73	-1.40	0.93	21.29	1.09	-4.29	1.22	0.96	1.35
53	-0.02	0.45	441.30	0.79	3.20	1.03	23.07	1.23	-1.29	1.41	-1.60	1.58
54	0.00	0.40	437.10	0.68	0.62	0.87	20.28	1.02	-0.11	1.15	-0.26	1.26
55	0.00	0.47	438.50	0.82	2.84	1.08	22.37	1.29	-0.22	1.49	-0.63	1.65
56	-0.03	0.46	440.90	0.78	-0.19	1.00	19.81	1.18	-0.41	1.33	-3.67	1.46
57	-0.02	0.41	442.50	0.73	2.68	0.94	23.98	1.13	4.01	1.29	0.10	1.45
58	-0.04	0.42	443.30	0.72	0.63	0.94	20.83	1.08	-1.16	1.21	-1.07	1.33
59	0.07	0.35	440.70	0.60	2.79	0.79	21.37	0.94	2.75	1.07	0.45	1.20
60	0.09	0.41	441.90	0.70	1.38	0.90	19.02	1.07	1.61	1.18	-2.57	1.33
61	-0.04	0.43	439.40	0.76	1.56	0.98	23.09	1.18	-3.05	1.35	-2.17	1.50
62	0.10	0.39	441.10	0.68	3.55	0.89	18.62	1.07	1.21	1.22	-5.91	1.34
63	0.02	0.39	439.50	0.68	2.23	0.88	25.66	1.05	-1.27	1.20	1.14	1.34
64	-0.06	0.40	438.60	0.68	0.78	0.87	23.80	1.02	2.12	1.15	-3.25	1.27
65	0.01	0.37	442.30	0.64	-0.44	0.84	23.34	1.00	-0.81	1.14	-0.45	1.28
66	0.02	0.32	443.40	0.56	-3.62	0.71	16.58	0.84	2.37	0.94	-0.78	1.04
67	-0.05	0.35	443.20	0.60	3.74	0.79	20.74	0.93	-0.45	1.07	-5.05	1.19
68	-0.03	0.31	443.00	0.54	-2.82	0.69	17.82	0.81	-2.15	0.91	-2.98	1.01
69	0.03	0.34	444.30	0.60	0.47	0.77	17.98	0.93	-1.13	1.06	-5.25	1.17
70	0.08	0.33	443.40	0.56	-5.16	0.72	20.19	0.83	2.46	0.96	-2.32	1.04
71	-0.06	0.37	442.10	0.64	-0.18	0.84	23.70	1.00	-0.96	1.14	-2.01	1.28
72	-0.04	0.28	442.50	0.48	0.56	0.62	20.99	0.72	1.71	0.82	-1.81	0.90
73	0.10	0.31	442.90	0.53	2.25	0.69	21.30	0.83	-0.59	0.94	-1.93	1.05
74	0.01	0.25	444.40	0.43	-1.30	0.55	20.77	0.65	-0.43	0.74	-4.58	0.81
75	0.03	0.30	443.10	0.51	-1.63	0.67	20.41	0.81	-1.59	0.92	-3.97	1.02
76	-0.02	0.35	444.10	0.59	-0.31	0.78	22.71	0.90	1.11	1.03	-6.28	1.12
77	-0.04	0.34	441.80	0.59	-0.85	0.77	20.43	0.91	-0.58	1.05	-2.22	1.16
78	0.05	0.31	441.80	0.54	-0.30	0.70	18.38	0.83	-1.05	0.96	-4.83	1.06
79	0.04	0.28	443.10	0.48	0.88	0.63	19.86	0.75	-0.24	0.84	-4.18	0.95
80	0.00	0.31	442.50	0.52	-2.12	0.68	19.66	0.80	-4.15	0.89	-2.29	0.98
81	0.06	0.28	443.00	0.47	-1.60	0.61	20.52	0.74	-0.76	0.83	-2.10	0.93
82	0.09	0.35	442.40	0.59	1.03	0.77	19.21	0.90	-0.73	1.02	-2.39	1.11
83	0.07	0.30	441.10	0.53	-2.14	0.69	20.78	0.82	-0.71	0.94	-4.13	1.04
84	-0.15	0.32	442.40	0.56	-0.94	0.71	21.61	0.84	-0.43	0.95	-3.33	1.04
85	0.03	0.33	442.70	0.57	0.84	0.74	19.92	0.90	0.85	1.01	-4.74	1.14

Table A.1 (continued)

l	a_0		a_1		a_2		a_3		a_4		a_5	
86	0.02	0.31	441.70	0.53	1.40	0.69	22.22	0.81	-3.55	0.91	-5.90	1.01
87	-0.01	0.37	442.40	0.63	-0.38	0.82	20.75	0.99	-0.31	1.12	-3.90	1.25
88	0.00	0.33	443.80	0.56	-0.03	0.72	20.78	0.85	-0.85	0.96	-3.91	1.05
89	-0.04	0.31	440.90	0.53	0.55	0.71	20.54	0.84	-1.08	0.93	-4.16	1.06
90	0.14	0.36	440.30	0.62	0.25	0.81	19.82	0.95	-1.77	1.10	-3.39	1.22
91	-0.12	0.34	441.40	0.58	-0.38	0.77	21.14	0.91	0.86	1.03	-3.03	1.13
92	-0.02	0.34	442.40	0.59	-1.81	0.76	20.04	0.90	-3.19	0.99	-4.23	1.09
93	-0.05	0.32	441.90	0.56	-0.30	0.74	24.06	0.87	0.74	0.99	-5.41	1.09
94	0.10	0.28	441.00	0.50	1.06	0.66	24.92	0.78	1.85	0.90	3.01	1.02
95	-0.07	0.30	439.90	0.52	-0.97	0.69	22.29	0.80	0.86	0.92	-4.11	1.02
96	0.03	0.36	441.10	0.60	2.73	0.80	22.32	0.95	0.95	1.06	-1.88	1.21
97	0.13	0.39	440.50	0.68	0.62	0.90	21.14	1.08	0.81	1.22	-5.00	1.37
98	-0.03	0.34	440.20	0.57	2.58	0.75	19.64	0.88	-1.33	0.98	-5.16	1.09
99	-0.06	0.29	441.90	0.50	0.63	0.65	22.35	0.76	-2.20	0.87	-3.13	0.97
100	0.08	0.31	441.10	0.54	0.40	0.70	19.35	0.82	-0.13	0.94	-3.78	1.04
101	-0.01	0.31	440.40	0.52	-0.06	0.70	22.25	0.81	0.17	0.93	-4.05	1.04
102	0.06	0.23	442.60	0.40	2.26	0.53	23.24	0.63	0.79	0.72	-2.01	0.79
103	-0.06	0.29	443.10	0.50	2.26	0.65	20.91	0.78	-1.04	0.87	-3.62	0.99
104	-0.01	0.32	441.50	0.55	0.98	0.72	22.04	0.85	-0.57	0.98	-1.46	1.09
105	0.01	0.29	440.10	0.50	3.91	0.68	19.72	0.82	0.75	0.95	-4.41	1.04
106	0.01	0.25	439.80	0.42	3.05	0.56	22.89	0.65	-0.58	0.73	0.24	0.81
107	-0.07	0.23	440.80	0.40	2.99	0.54	18.70	0.64	0.69	0.73	-5.30	0.81
108	0.04	0.24	442.60	0.41	2.63	0.53	22.00	0.63	-0.91	0.71	-2.92	0.78
109	0.02	0.22	439.90	0.37	1.03	0.49	22.36	0.57	-0.25	0.66	-4.03	0.73
110	-0.04	0.26	441.20	0.43	4.63	0.58	20.37	0.67	-1.18	0.78	0.21	0.84
111	-0.04	0.24	440.80	0.41	0.75	0.55	22.00	0.64	-1.20	0.73	-3.97	0.82
112	-0.03	0.25	440.80	0.42	2.01	0.54	21.99	0.66	-0.30	0.76	-3.45	0.82
113	0.09	0.23	443.60	0.38	-3.62	0.51	19.30	0.60	0.94	0.67	-1.64	0.76
114	-0.03	0.25	443.30	0.42	0.55	0.55	19.98	0.66	0.69	0.72	-2.45	0.81
115	-0.01	0.24	443.70	0.41	0.45	0.53	22.83	0.63	-0.47	0.72	-4.48	0.81
116	0.04	0.18	442.10	0.30	-0.66	0.41	19.87	0.47	-0.44	0.53	-3.73	0.58
117	-0.04	0.23	441.20	0.38	2.61	0.50	18.48	0.60	-4.22	0.68	-0.60	0.75
118	0.03	0.22	442.00	0.37	-1.12	0.49	19.82	0.56	0.19	0.66	-5.02	0.71
119	0.07	0.18	441.80	0.30	-1.25	0.40	20.11	0.48	1.93	0.56	-3.73	0.61

Table A.1 (continued)

A.2 Sectoral Results from the Low-Resolution Spectra

The following table lists the scaled frequency splittings $\Delta\nu/2\ell$, binned in $10\text{-}\ell$ wide bins, estimated from the sectoral high-resolution spectra. The uncertainties were estimated from the scatter in the bins. The values are listed in nHz, sidereal.

ℓ	$\Delta\nu/2\ell$	ℓ	$\Delta\nu/2\ell$
26	442.77 17.06	316	449.57 2.16
36	459.22 4.49	326	452.70 2.29
46	453.35 3.76	336	450.92 0.79
56	463.85 8.19	346	446.87 2.17
66	458.86 15.47	356	447.66 4.04
76	458.21 3.03	366	449.60 1.28
86	462.38 4.56	376	449.52 1.78
96	458.69 4.06	386	447.91 3.01
106	460.89 6.28	396	454.05 4.29
116	463.55 5.52	406	447.38 2.71
126	464.85 5.58	416	444.93 1.12
136	461.64 7.45	426	445.75 3.25
146	453.84 6.96	436	453.00 2.16
156	459.90 7.65	446	447.44 5.36
166	459.86 2.50	456	451.14 3.24
176	452.60 4.51	466	447.58 4.07
186	456.01 2.10	476	449.03 1.10
196	454.26 3.15	486	448.49 1.00
206	455.54 2.55	496	443.54 4.19
216	451.54 5.46	506	441.27 2.94
226	451.01 3.62	516	446.13 3.21
236	454.29 2.55	526	442.16 4.11
246	453.59 2.75	536	438.93 2.29
256	453.66 4.05	546	441.50 4.11
266	451.68 2.58	556	448.91 5.12
276	449.48 1.95	566	446.45 6.02
286	450.79 3.69	576	447.23 5.08
296	451.16 3.46	586	448.88 4.78
306	449.37 2.05	596	442.34 2.94

Table A.2: Scaled frequency splittings ($\Delta\nu/2\ell$) estimated from the low resolution sectoral spectra

Appendix B

Modal Frequencies, Widths and Amplitudes Estimated from the High-Resolution Spectra

The following table lists the modal frequency, width and total power estimated from the high-resolution collapsed spectra. The modal widths have been corrected for the finite window function resolution using the Gaussian approximation. No width is listed for modes sensitive to the spatio-temporal sidelobe contamination, and note also that in these cases, the total power is most likely contaminated by an overestimate of the mode's width. The frequencies (ν), FWHM, and their 1σ uncertainties are listed in μHz . The modal total power (P_{tot}) corresponds to the square of the average surface velocity, in $(\text{m/s})^2$.

ℓ	n	ν	FWHM		P_{tot}	ℓ	n	ν	FWHM		P_{tot}
21	6	1758.40	0.05	1.11 0.04	5.08E-04	22	6	1781.49	0.11	--	8.17E-04
21	7	1919.88	0.02	0.61 0.02	4.66E-04	22	7	1944.92	0.06	--	6.28E-04
21	8	2077.59	0.02	1.09 0.01	1.73E-03	22	8	2105.02	0.07	1.75 0.05	1.93E-03
21	9	2231.93	0.03	1.43 0.02	3.53E-03	22	9	2260.03	0.03	1.56 0.02	4.24E-03
21	11	2529.45	0.03	1.72 0.03	1.92E-02	22	10	2410.92	0.02	1.12 0.02	9.39E-03
21	12	2676.40	0.04	1.84 0.03	3.00E-02	22	11	2559.47	0.07	2.45 0.05	1.86E-02
21	13	2823.26	0.02	0.57 0.02	2.98E-02	22	12	2707.21	0.01	0.99 0.01	3.48E-02
21	14	2969.01	0.04	1.34 0.03	6.95E-02	22	13	2854.87	0.03	1.28 0.02	5.83E-02
21	15	3114.06	0.02	1.41 0.02	7.77E-02	22	14	3001.50	0.03	1.63 0.02	1.09E-01
21	16	3258.79	0.07	2.52 0.06	1.21E-01	22	15	3147.44	0.05	2.03 0.04	1.04E-01
21	17	3403.03	0.03	--	2.49E-02	22	16	3292.58	0.07	3.02 0.06	1.00E-01
21	18	3547.34	0.12	--	5.59E-02						

Table B.1: Modal frequency, width and total power estimated from the high resolution collapsed spectra

ℓ	n	ν	FWHM		P_{tot}	ℓ	n	ν	FWHM		P_{tot}		
22	17	3437.27	0.12	3.13	0.09	5.32E-02	27	13	3007.22	0.04	2.10	0.03	9.39E-02
22	18	3581.95	0.07	--	--	1.60E-02	27	14	3157.33	0.04	1.96	0.03	9.87E-02
23	6	1804.03	0.06	--	--	4.19E-04	27	15	3307.03	0.08	2.41	0.06	8.67E-02
23	7	1969.71	0.08	2.36	0.06	1.33E-03	27	16	3455.45	0.10	2.46	0.08	5.22E-02
23	8	2131.22	0.02	0.65	0.02	1.35E-03	28	6	1909.98	0.10	--	--	6.17E-04
23	9	2287.38	0.03	0.52	0.04	2.01E-03	28	7	2083.98	0.04	1.46	0.03	1.91E-03
23	10	2439.37	0.02	1.38	0.02	9.18E-03	28	8	2252.46	0.07	3.04	0.05	6.27E-03
23	11	2588.65	0.04	1.16	0.03	1.56E-02	28	9	2415.72	0.05	1.92	0.04	1.09E-02
23	12	2737.59	0.02	1.84	0.02	5.17E-02	28	10	2573.33	0.02	1.60	0.01	2.09E-02
23	13	2886.28	0.04	1.99	0.03	7.19E-02	28	11	2729.47	0.02	1.56	0.02	3.96E-02
23	14	3033.57	0.02	1.42	0.02	7.73E-02	28	12	2883.80	0.03	1.83	0.03	8.17E-02
23	16	3325.53	0.06	2.14	0.05	8.97E-02	28	13	3036.54	0.04	1.56	0.03	9.26E-02
23	18	3617.12	0.13	--	--	3.97E-02	28	14	3187.14	0.07	2.74	0.05	8.80E-02
24	6	1826.53	0.05	1.22	0.04	4.07E-04	28	15	3337.44	0.06	2.95	0.05	7.45E-02
24	7	1993.78	0.07	1.56	0.06	9.41E-04	28	16	3486.99	0.15	3.87	0.12	6.84E-02
24	8	2156.77	0.11	--	--	3.79E-03	29	6	1929.99	0.04	0.87	0.04	5.84E-04
24	9	2314.61	0.03	0.85	0.02	3.22E-03	29	7	2105.48	0.04	1.67	0.04	2.01E-03
24	10	2467.21	0.06	1.86	0.05	1.22E-02	29	8	2275.62	0.05	1.88	0.04	5.81E-03
24	11	2617.83	0.05	2.23	0.04	2.31E-02	29	9	2439.00	0.04	2.38	0.03	1.63E-02
24	12	2767.94	0.03	1.80	0.02	6.25E-02	29	10	2598.85	0.03	1.15	0.02	1.53E-02
24	13	2917.17	0.04	2.15	0.03	8.64E-02	29	11	2756.16	0.03	1.37	0.02	3.90E-02
24	14	3065.15	0.04	2.60	0.03	1.26E-01	29	12	2911.77	0.02	1.59	0.02	7.70E-02
24	15	3212.18	0.04	2.28	0.03	1.40E-01	29	13	3065.19	0.03	1.87	0.02	1.08E-01
24	16	3358.80	0.05	2.56	0.04	9.34E-02	29	14	3217.12	0.03	2.15	0.02	7.82E-02
24	17	3504.88	0.11	3.34	0.08	6.02E-02	29	15	3367.92	0.08	2.72	0.06	6.91E-02
26	6	1869.30	0.06	1.50	0.05	8.06E-04	29	16	3518.07	0.16	4.19	0.13	6.75E-02
26	7	2039.71	0.06	1.76	0.05	1.77E-03	29	19	3966.23	0.25	--	--	1.64E-02
26	8	2206.25	0.03	1.18	0.02	4.03E-03	30	6	1950.01	0.06	1.52	0.05	8.22E-04
26	9	2366.29	0.02	1.47	0.02	9.77E-03	30	7	2126.38	0.07	2.01	0.06	2.16E-03
26	10	2521.28	0.04	2.01	0.03	1.77E-02	30	8	2297.47	0.05	2.41	0.04	8.29E-03
26	11	2674.60	0.03	1.38	0.02	2.88E-02	30	9	2462.44	0.04	2.15	0.03	1.60E-02
26	12	2826.79	0.05	2.04	0.04	6.14E-02	30	10	2623.64	0.05	2.87	0.04	4.47E-02
26	13	2977.60	0.02	0.78	0.02	5.60E-02	30	11	2782.57	0.02	1.17	0.02	3.32E-02
26	14	3127.06	0.03	2.49	0.03	1.01E-01	30	12	2939.24	0.02	1.14	0.02	7.36E-02
26	15	3275.35	0.12	3.44	0.09	1.04E-01	30	13	3093.53	0.04	1.84	0.03	8.46E-02
26	16	3423.58	0.12	3.68	0.10	6.49E-02	30	14	3246.26	0.03	2.06	0.03	7.92E-02
26	18	3718.66	0.20	--	--	2.24E-02	30	15	3397.72	0.05	2.81	0.04	7.87E-02
27	6	1889.77	0.02	0.84	0.02	6.49E-04	30	16	3549.03	0.11	3.51	0.09	4.84E-02
27	7	2062.16	0.03	1.31	0.03	1.89E-03	30	17	3700.18	0.24	--	--	3.35E-02
27	8	2229.68	0.07	2.81	0.05	7.05E-03	31	5	1788.54	0.09	--	--	2.92E-04
27	9	2391.15	0.06	2.51	0.04	1.20E-02	31	6	1969.43	0.05	1.24	0.04	7.74E-04
27	10	2547.65	0.10	3.45	0.08	2.12E-02	31	7	2146.99	0.03	1.54	0.03	2.78E-03
27	11	2702.25	0.03	1.88	0.03	2.85E-02	31	8	2319.09	0.08	2.41	0.06	8.15E-03
27	12	2855.42	0.03	1.24	0.02	5.25E-02	31	9	2485.27	0.07	2.35	0.05	1.57E-02

Table B.1 (continued)

ℓ	n	ν	FWHM		P_{tot}	ℓ	n	ν	FWHM		P_{tot}		
31	10	2647.79	0.07	2.47	0.05	4.43E-02	35	13	3229.25	0.04	2.21	0.03	9.12E-02
31	11	2808.45	0.04	2.17	0.03	7.03E-02	35	15	3542.75	0.14	3.63	0.11	3.88E-02
31	12	2986.30	0.03	1.55	0.03	1.01E-01	35	16	3697.91	0.09	--	--	1.84E-02
31	13	3121.39	0.10	2.86	0.08	1.18E-01	36	6	2063.18	0.07	1.81	0.05	1.31E-03
31	14	3275.12	0.06	2.54	0.05	8.25E-02	36	7	2245.52	0.04	1.21	0.04	2.89E-03
31	16	3579.79	0.05	--	--	1.06E-02	36	8	2421.40	0.06	2.39	0.05	1.49E-02
32	5	1806.08	0.09	--	--	6.61E-04	36	9	2592.97	0.03	1.66	0.03	2.25E-02
32	6	1988.71	0.03	1.32	0.02	9.57E-04	36	10	2763.05	0.04	1.55	0.04	4.09E-02
32	7	2167.53	0.05	1.96	0.04	2.33E-03	36	11	2930.46	0.03	2.15	0.03	1.16E-01
32	8	2340.31	0.04	1.72	0.03	5.91E-03	36	12	3094.31	0.05	2.85	0.04	1.65E-01
32	9	2507.43	0.04	2.33	0.03	2.25E-02	36	13	3255.18	0.04	3.05	0.03	1.37E-01
32	10	2671.65	0.09	3.09	0.07	4.21E-02	36	14	3413.60	0.12	3.64	0.10	7.62E-02
32	11	2833.80	0.05	2.76	0.04	8.60E-02	37	5	1892.08	0.05	1.38	0.04	8.05E-04
32	12	2992.86	0.03	2.02	0.02	1.38E-01	37	6	2081.23	0.06	1.68	0.05	1.82E-03
32	13	3149.22	0.01	1.14	0.01	7.99E-02	37	7	2264.21	0.11	--	--	2.30E-03
32	14	3303.51	0.04	2.36	0.03	8.21E-02	37	8	2440.85	0.05	2.19	0.04	1.19E-02
33	5	1823.85	0.02	0.64	0.02	3.29E-04	37	9	2613.50	0.05	2.11	0.04	3.11E-02
33	6	2007.80	0.04	1.58	0.03	1.64E-03	37	10	2784.89	0.05	2.45	0.04	5.85E-02
33	7	2187.53	0.02	1.21	0.02	3.16E-03	37	11	2953.41	0.03	2.06	0.02	1.13E-01
33	8	2360.98	0.06	2.22	0.05	7.40E-03	37	12	3118.58	0.04	2.85	0.03	1.26E-01
33	9	2529.25	0.05	2.19	0.04	1.96E-02	37	13	3280.94	0.12	3.45	0.09	1.02E-01
33	10	2694.89	0.03	1.68	0.02	3.54E-02	37	14	3440.68	0.07	3.28	0.06	6.53E-02
33	11	2858.66	0.03	1.63	0.03	6.63E-02	37	15	3598.89	0.16	--	--	4.23E-02
33	12	3019.10	0.04	2.34	0.03	9.61E-02	38	5	1908.79	0.04	1.53	0.03	1.06E-03
33	13	3176.21	0.05	2.32	0.04	1.17E-01	38	6	2098.92	0.04	1.18	0.03	1.35E-03
33	14	3331.65	0.07	2.06	0.06	6.39E-02	38	7	2283.00	0.03	1.61	0.02	5.19E-03
34	5	1841.56	0.07	--	--	6.21E-04	38	8	2460.07	0.03	1.42	0.02	1.45E-02
34	6	2026.58	0.02	0.82	0.02	1.15E-03	38	9	2633.76	0.06	2.18	0.05	2.83E-02
34	7	2207.24	0.02	0.99	0.02	3.54E-03	38	10	2806.36	0.07	2.53	0.06	6.89E-02
34	8	2381.49	0.05	1.97	0.04	8.52E-03	38	11	2975.88	0.04	1.91	0.03	1.08E-01
34	9	2550.92	0.07	2.70	0.06	2.46E-02	38	12	3142.61	0.05	2.37	0.04	1.23E-01
34	10	2718.18	0.05	2.17	0.04	4.88E-02	38	13	3306.04	0.10	3.20	0.08	7.84E-02
34	11	2883.01	0.05	2.61	0.04	9.62E-02	38	14	3467.05	0.07	3.49	0.05	6.92E-02
34	12	3044.72	0.05	1.87	0.04	8.37E-02	39	5	1925.33	0.08	1.90	0.06	8.17E-04
34	13	3203.04	0.03	1.81	0.03	1.09E-01	39	6	2116.55	0.05	1.83	0.04	2.19E-03
34	14	3359.51	0.07	3.09	0.05	7.18E-02	39	7	2301.65	0.08	2.27	0.06	5.25E-03
35	5	1858.43	0.02	0.98	0.01	5.94E-04	39	8	2479.13	0.06	2.10	0.05	1.26E-02
35	6	2044.66	0.04	1.20	0.03	1.08E-03	39	9	2654.08	0.05	1.71	0.04	2.22E-02
35	7	2226.54	0.08	2.24	0.06	3.70E-03	39	10	2827.52	0.06	2.27	0.04	7.02E-02
35	8	2401.60	0.05	2.36	0.04	1.02E-02	39	11	2998.26	0.05	2.33	0.04	1.08E-01
35	9	2571.94	0.06	2.44	0.05	2.60E-02	39	12	3165.98	0.04	2.13	0.03	8.63E-02
35	10	2740.64	0.04	2.17	0.03	5.81E-02	39	13	3330.54	0.08	2.74	0.06	8.86E-02
35	11	2907.03	0.02	1.76	0.02	9.00E-02	40	4	1743.22	0.06	1.62	0.05	7.56E-04
35	12	3069.56	0.05	2.29	0.04	1.12E-01							

Table B.1 (continued)

ℓ	n	ν	FWHM		P_{tot}	ℓ	n	ν	FWHM		P_{tot}		
40	5	1941.41	0.03	1.25	0.02	1.01E-03	44	10	2929.83	0.04	2.28	0.03	8.36E-02
40	6	2134.18	0.05	1.91	0.04	2.23E-03	44	11	3105.14	0.08	2.97	0.06	1.15E-01
40	7	2319.47	0.06	1.93	0.05	4.85E-03	44	12	3277.47	0.05	2.70	0.04	1.05E-01
40	8	2498.06	0.04	1.91	0.04	1.42E-02	44	13	3448.26	0.17	--	--	5.17E-02
40	9	2673.93	0.05	2.06	0.04	3.68E-02							
40	10	2848.30	0.06	2.77	0.05	6.86E-02	45	4	1815.32	0.04	--	--	1.62E-04
40	11	3020.29	0.03	2.60	0.02	1.17E-01	45	5	2020.13	0.04	1.10	0.03	9.78E-04
40	12	3189.06	0.03	2.12	0.03	1.14E-01	45	6	2218.07	0.06	1.67	0.05	3.04E-03
40	13	3354.99	0.07	3.66	0.05	9.65E-02	45	7	2406.70	0.02	1.55	0.02	8.03E-03
40	14	3518.88	0.12	3.51	0.10	4.40E-02	45	9	2770.68	0.03	1.74	0.02	4.13E-02
40	15	3680.55	0.16	--	--	2.01E-02	45	10	2950.00	0.02	0.58	0.02	3.22E-02
							45	11	3125.53	0.07	2.57	0.05	8.82E-02
41	5	1957.58	0.05	1.17	0.04	7.11E-04	45	12	3299.20	0.10	3.04	0.07	9.59E-02
41	6	2151.44	0.02	0.35	0.03	8.88E-04	45	13	3470.88	0.08	2.47	0.07	3.98E-02
41	7	2337.28	0.05	1.95	0.04	6.21E-03							
41	8	2516.88	0.06	2.16	0.04	1.91E-02	46	4	1829.26	0.03	0.57	0.04	2.20E-04
41	9	2693.61	0.05	1.96	0.04	3.95E-02	46	5	2035.29	0.07	2.03	0.06	2.11E-03
41	10	2869.03	0.03	1.46	0.02	5.13E-02	46	6	2234.43	0.02	0.16	0.05	6.97E-04
41	11	3041.94	0.05	2.79	0.04	1.20E-01	46	7	2423.52	0.04	1.77	0.03	1.09E-02
41	12	3211.55	0.03	1.58	0.02	8.44E-02	46	8	2607.43	0.04	1.89	0.03	2.88E-02
41	13	3378.70	0.05	2.81	0.04	8.10E-02	46	9	2789.56	0.06	2.20	0.04	4.99E-02
							46	10	2969.10	0.04	2.00	0.03	9.01E-02
42	5	1973.29	0.04	1.60	0.03	1.28E-03	46	11	3146.15	0.04	1.98	0.03	9.08E-02
42	6	2168.20	0.06	1.89	0.05	2.60E-03							
42	7	2355.04	0.09	--	--	6.25E-03	47	6	2250.09	0.03	1.29	0.02	2.25E-03
42	8	2535.19	0.04	1.82	0.03	1.46E-02	47	7	2439.98	0.07	1.80	0.05	8.22E-03
42	9	2713.31	0.05	1.89	0.04	3.47E-02	47	8	2625.00	0.06	2.05	0.04	2.13E-02
42	10	2889.84	0.09	2.87	0.07	8.16E-02	47	9	2808.19	0.07	2.29	0.05	5.32E-02
42	11	3063.15	0.04	1.97	0.03	8.39E-02	47	10	2988.80	0.03	1.45	0.02	7.38E-02
42	12	3233.93	0.08	3.13	0.06	9.51E-02	47	11	3166.17	0.08	2.79	0.06	1.01E-01
42	13	3402.24	0.07	3.38	0.06	8.21E-02	47	13	3514.94	0.14	--	--	3.05E-02
43	4	1786.67	0.07	--	--	1.56E-04	48	4	1856.56	0.01	--	--	2.09E-04
43	5	1989.03	0.02	0.84	0.02	7.18E-04	48	5	2065.34	0.04	1.00	0.04	7.25E-04
43	6	2184.94	0.05	1.78	0.04	2.98E-03	48	6	2265.80	0.05	1.52	0.04	3.20E-03
43	7	2372.59	0.06	1.91	0.05	6.57E-03	48	7	2456.59	0.02	1.17	0.02	9.30E-03
43	8	2553.47	0.08	2.24	0.06	1.74E-02	48	9	2826.63	0.03	1.82	0.03	4.96E-02
43	9	2732.63	0.04	2.07	0.03	3.94E-02	48	10	3007.76	0.05	1.87	0.04	7.97E-02
43	10	2909.88	0.04	1.91	0.03	6.69E-02	48	11	3186.10	0.08	2.33	0.06	7.71E-02
43	11	3084.27	0.03	1.49	0.03	7.82E-02	48	13	3536.59	0.14	--	--	3.39E-02
43	12	3255.85	0.04	2.08	0.03	7.44E-02							
43	15	3758.47	0.20	--	--	1.54E-02	49	4	1869.47	0.15	--	--	1.93E-03
							49	5	2080.02	0.06	1.37	0.05	1.04E-03
44	5	2004.73	0.05	1.27	0.04	1.13E-03	49	6	2281.55	0.03	1.30	0.03	2.85E-03
44	6	2201.63	0.03	1.49	0.02	3.26E-03	49	7	2472.88	0.05	1.55	0.04	9.43E-03
44	7	2389.54	0.03	1.75	0.02	8.95E-03	49	8	2659.79	0.03	1.71	0.03	2.68E-02
44	8	2571.52	0.06	2.03	0.05	1.98E-02	49	9	2845.12	0.06	2.28	0.05	5.60E-02
44	9	2751.60	0.09	2.46	0.07	2.91E-02	49	10	3027.06	0.04	1.79	0.03	7.38E-02

Table B.1 (continued)

ℓ	n	ν	FWHM		P_{tot}	ℓ	n	ν	FWHM		P_{tot}		
49	11	3206.12	0.04	2.25	0.03	9.25E-02	55	10	3137.86	0.07	2.12	0.06	7.65E-02
49	12	3382.72	0.09	2.42	0.07	4.23E-02	55	11	3321.36	0.06	2.30	0.05	5.87E-02
49	13	3558.18	0.17	--	--	3.06E-02							
50	3	1661.41	0.04	--	--	2.78E-04	56	3	1732.21	0.05	--	--	6.89E-04
50	4	1883.05	0.12	--	--	2.00E-03	56	4	1960.85	0.05	--	--	2.15E-03
50	6	2297.25	0.08	1.79	0.06	3.31E-03	56	5	2179.36	0.14	--	--	6.93E-03
50	7	2489.32	0.06	1.62	0.05	1.10E-02	56	6	2386.09	0.06	--	--	1.96E-03
50	8	2677.14	0.04	1.87	0.03	2.63E-02	56	7	2583.25	0.16	--	--	1.51E-02
50	9	2863.03	0.05	2.17	0.04	5.82E-02	56	8	2777.66	0.04	1.55	0.03	3.65E-02
50	10	3045.87	0.06	2.21	0.05	6.89E-02	56	9	2968.89	0.05	1.68	0.04	5.56E-02
50	11	3225.60	0.07	2.09	0.05	6.92E-02	56	11	3340.41	0.08	2.20	0.06	4.66E-02
50	12	3403.04	0.12	3.48	0.09	4.53E-02							
51	3	1673.80	0.07	--	--	7.46E-04	57	3	1743.24	0.07	--	--	9.20E-04
51	4	1896.54	0.11	--	--	1.94E-03	57	4	1973.29	0.07	--	--	2.04E-03
51	6	2312.51	0.06	--	--	2.43E-03	57	5	2192.83	0.10	--	--	8.20E-03
51	7	2505.22	0.11	--	--	1.19E-02	57	6	2400.32	0.18	--	--	2.11E-02
51	9	2881.25	0.03	1.71	0.03	6.01E-02	57	7	2598.37	0.07	2.16	0.06	2.01E-02
51	10	3064.65	0.06	2.20	0.05	6.68E-02	57	8	2794.13	0.03	1.67	0.02	4.06E-02
51	11	3245.22	0.13	--	--	7.24E-02	57	9	2985.95	0.06	1.86	0.04	5.82E-02
51	12	3423.50	0.09	2.72	0.07	5.68E-02	57	10	3173.72	0.03	1.89	0.03	7.47E-02
							57	11	3358.77	0.06	2.28	0.05	4.74E-02
							57	12	3541.99	0.15	--	--	1.77E-02
							57	14	3902.98	0.03	--	--	1.70E-03
52	3	1685.67	0.06	--	--	4.35E-04	58	3	1754.50	0.05	--	--	8.47E-04
52	4	1909.64	0.11	--	--	1.69E-03	58	4	1985.59	0.06	--	--	2.32E-03
52	7	2521.25	0.07	1.84	0.06	1.04E-02	58	5	2206.37	0.10	--	--	7.63E-03
52	8	2711.16	0.04	1.92	0.03	3.35E-02	58	6	2414.43	0.04	--	--	3.53E-03
52	9	2898.93	0.03	1.88	0.03	6.51E-02	58	8	2810.20	0.09	--	--	3.47E-02
52	10	3083.31	0.04	1.60	0.03	6.98E-02	58	9	3002.89	0.04	1.54	0.03	7.05E-02
52	11	3264.11	0.04	2.01	0.03	7.99E-02	58	10	3191.71	0.10	--	--	7.40E-02
52	13	3620.81	0.17	--	--	1.30E-02							
53	3	1697.71	0.04	--	--	7.02E-04	59	3	1765.54	0.03	--	--	4.61E-04
53	4	1922.27	0.09	--	--	1.71E-03	59	4	1997.76	0.04	--	--	2.98E-03
53	5	2137.80	0.05	1.04	0.04	1.48E-03	59	5	2219.60	0.09	--	--	7.20E-03
53	6	2342.14	0.03	0.92	0.03	3.65E-03	59	6	2428.28	0.15	--	--	2.12E-02
53	7	2536.91	0.07	1.59	0.05	8.66E-03	59	7	2628.67	0.17	--	--	2.89E-02
53	8	2727.97	0.03	1.62	0.02	2.53E-02	59	8	2826.02	0.08	1.90	0.06	2.63E-02
53	9	2916.58	0.06	2.28	0.04	8.69E-02	59	9	3019.89	0.05	1.56	0.04	6.39E-02
53	10	3101.65	0.07	2.35	0.06	7.95E-02	59	11	3395.75	0.14	--	--	3.34E-02
53	12	3463.76	0.13	--	--	3.03E-02							
55	3	1720.54	0.04	--	--	6.28E-04	60	3	1776.23	0.03	--	--	8.53E-04
55	4	1948.01	0.09	--	--	2.07E-03	60	4	2010.20	0.04	--	--	3.16E-03
55	5	2165.56	0.08	--	--	2.11E-03	60	5	2232.86	0.08	--	--	1.04E-02
55	7	2568.02	0.08	--	--	1.52E-02	60	6	2442.20	0.17	--	--	1.74E-02
55	8	2761.38	0.05	1.75	0.04	3.43E-02	60	7	2643.84	0.10	2.73	0.08	2.85E-02
55	9	2951.77	0.02	1.53	0.02	6.38E-02	60	8	2842.24	0.04	1.89	0.03	4.49E-02
							60	9	3036.46	0.08	1.81	0.06	6.28E-02

Table B.1 (continued)

ℓ	n	ν	FWHM		P_{tot}	ℓ	n	ν	FWHM		P_{tot}		
60	10	3226.21	0.05	1.97	0.04	7.40E-02	67	5	2321.94	0.05	--	8.89E-03	
60	11	3413.73	0.06	1.93	0.05	3.32E-02	67	6	2536.68	0.06	--	4.36E-02	
61	3	1786.97	0.11	--	--	1.07E-03	67	7	2745.51	0.10	--	8.03E-02	
61	4	2022.45	0.03	--	--	2.44E-03	67	9	3150.12	0.03	1.29	0.03	4.75E-02
61	5	2246.15	0.10	--	--	7.90E-03	68	3	1859.24	0.08	--	--	1.39E-03
61	6	2456.04	0.12	--	--	2.95E-02	68	4	2104.12	0.04	--	--	3.52E-03
61	7	2658.53	0.09	--	--	1.76E-02	68	5	2334.21	0.08	--	--	1.50E-02
61	9	3053.03	0.07	1.97	0.05	8.45E-02	68	6	2549.64	0.09	--	--	3.89E-02
61	10	3243.73	0.05	1.71	0.04	5.51E-02	68	9	3165.53	0.13	--	--	8.15E-02
61	11	3431.73	0.07	--	--	2.36E-02	68	12	3747.80	0.07	--	--	3.02E-03
62	3	1797.83	0.08	--	--	1.10E-03	69	3	1869.40	0.07	1.68	0.05	8.47E-04
62	4	2034.14	0.04	--	--	2.91E-03	69	4	2115.36	0.04	--	--	4.78E-03
62	5	2258.77	0.06	--	--	1.14E-02	69	5	2346.40	0.07	--	--	1.51E-02
62	6	2469.36	0.10	--	--	3.14E-02	69	6	2562.51	0.07	--	--	4.78E-02
62	7	2673.26	0.08	--	--	1.64E-02	69	7	2773.82	0.13	--	--	9.00E-02
62	8	2873.64	0.06	1.58	0.05	4.13E-02	70	4	2126.76	0.05	--	--	3.79E-03
62	9	3069.67	0.09	--	--	3.69E-02	70	5	2358.36	0.09	--	--	1.70E-02
62	10	3260.91	0.06	1.94	0.05	5.35E-02	70	6	2575.64	0.07	--	--	4.31E-02
62	13	3819.80	0.02	--	--	7.08E-04	70	7	2787.78	0.13	--	--	9.69E-02
63	3	1808.33	0.13	--	--	1.19E-03	70	8	2995.20	0.08	--	--	2.59E-02
63	4	2046.03	0.04	--	--	2.81E-03	71	3	1889.08	0.03	0.85	0.03	5.49E-04
63	5	2272.02	0.07	--	--	1.17E-02	71	4	2138.10	0.03	--	--	3.64E-03
63	6	2483.39	0.13	--	--	3.13E-02	71	5	2370.15	0.05	--	--	1.63E-02
63	8	2889.67	0.05	1.40	0.04	3.64E-02	71	6	2588.32	0.06	--	--	4.91E-02
63	10	3277.80	0.09	--	--	4.51E-02	71	7	2801.50	0.13	--	--	1.18E-01
63	11	3467.14	0.02	--	--	3.06E-03	72	3	1898.55	0.20	--	--	1.31E-03
64	3	1818.41	0.06	1.99	0.05	9.47E-04	72	4	2149.02	0.04	--	--	5.26E-03
64	4	2057.83	0.05	--	--	3.19E-03	72	5	2381.77	0.07	--	--	1.78E-02
64	5	2284.65	0.07	--	--	1.23E-02	72	6	2600.99	0.06	--	--	4.88E-02
64	7	2702.74	0.02	0.63	0.02	9.53E-03	72	7	2815.47	0.14	--	--	1.27E-01
64	9	3101.78	0.04	0.97	0.04	4.06E-02	72	9	3227.54	0.07	--	--	1.81E-02
64	10	3295.11	0.10	--	--	3.74E-02	73	3	1908.56	0.11	--	--	1.44E-03
64	12	3674.19	0.01	--	--	1.89E-03	73	4	2159.83	0.05	--	--	5.06E-03
66	3	1839.31	0.01	--	--	1.79E-04	73	5	2393.25	0.04	--	--	1.92E-02
66	4	2081.20	0.05	--	--	3.20E-03	73	6	2613.72	0.04	--	--	6.00E-02
66	5	2309.60	0.04	--	--	1.21E-02	73	9	3242.98	0.07	--	--	1.69E-02
66	6	2523.23	0.23	--	--	2.57E-02	74	3	1917.72	0.08	--	--	1.41E-03
66	8	2935.22	0.09	--	--	3.82E-02	74	4	2170.85	0.05	--	--	5.32E-03
66	9	3134.30	0.05	--	--	3.19E-02	74	5	2405.07	0.05	--	--	1.60E-02
66	10	3328.86	0.10	--	--	2.98E-02	74	6	2626.23	0.04	--	--	6.37E-02
67	3	1849.53	0.09	--	--	1.46E-03	74	7	2842.95	0.12	--	--	1.17E-01
67	4	2092.74	0.05	--	--	2.84E-03							

Table B.1 (continued)

ℓ	n	ν	FWHM	P_{tot}	ℓ	n	ν	FWHM	P_{tot}				
74	12	3848.22	0.16	--	7.54E-03	83	7	2961.25	0.05	--	1.44E-01		
						83	10	3595.41	0.03	--	3.57E-03		
75	3	1927.56	0.12	--	1.27E-03	84	2	1728.80	0.06	--	3.15E-04		
75	4	2181.83	0.06	--	6.00E-03	84	5	2516.26	0.07	--	3.12E-02		
75	5	2416.74	0.06	--	2.14E-02	84	6	2748.09	0.05	--	8.70E-02		
75	6	2638.90	0.07	--	5.84E-02	84	7	2973.93	0.05	--	1.62E-01		
75	7	2856.40	0.11	--	1.16E-01								
75	8	3067.39	0.12	--	2.14E-01	85	2	1736.19	0.04	--	2.06E-04		
						85	4	2284.50	0.06	--	8.05E-03		
76	3	1936.83	0.09	--	5.10E-04	85	6	2759.95	0.05	--	8.38E-02		
76	4	2192.08	0.06	--	6.10E-03	85	7	2986.51	0.07	--	1.73E-01		
76	5	2428.07	0.03	--	2.47E-02								
76	6	2651.40	0.05	--	6.71E-02	86	2	1743.79	0.07	--	3.13E-04		
76	7	2869.72	0.10	--	1.34E-01	86	3	2028.35	0.04	0.85	0.03	1.02E-03	
76	8	3081.41	0.12	--	1.86E-01	86	4	2294.39	0.16	--	6.12E-03		
						86	5	2537.74	0.08	--	2.92E-02		
78	3	1955.93	0.10	--	1.41E-03	86	6	2771.63	0.06	--	8.46E-02		
78	4	2213.36	0.09	--	7.71E-03	86	7	2999.15	0.06	--	1.62E-01		
78	5	2450.44	0.05	--	2.21E-02	86	8	3218.44	0.10	--	1.53E-01		
78	6	2675.92	0.07	--	6.79E-02	86	9	3432.59	0.17	--	1.13E-01		
78	7	2896.16	0.10	--	1.32E-01								
78	8	3109.51	0.15	--	1.70E-01	87	2	1751.37	0.06	--	5.18E-04		
78	10	3522.31	0.05	--	1.05E-02	87	3	2037.04	0.05	1.21	0.04	1.07E-03	
						87	5	2548.00	0.06	--	3.30E-02		
79	3	1964.91	0.02	0.61	0.03	3.12E-04	87	6	2783.21	0.08	--	1.01E-01	
79	4	2223.71	0.12	--	5.86E-03	87	7	3011.76	0.04	--	1.91E-01		
79	5	2461.72	0.08	--	2.31E-02	87	8	3231.84	0.12	--	1.56E-01		
79	6	2688.01	0.04	--	6.99E-02	87	9	3446.86	0.25	--	1.08E-01		
79	7	2909.61	0.07	--	1.12E-01								
						88	2	1758.73	0.09	--	3.62E-04		
80	3	1974.17	0.07	2.26	0.05	1.34E-03	88	3	2045.96	0.05	1.23	0.04	8.93E-04
80	4	2234.22	0.10	--	6.89E-03	88	5	2558.58	0.10	--	3.35E-02		
80	5	2472.70	0.06	--	2.43E-02	88	6	2794.99	0.05	--	8.45E-02		
80	6	2700.29	0.03	--	5.88E-02	88	7	3024.14	0.05	--	1.49E-01		
80	7	2922.67	0.07	--	1.50E-01	88	8	3245.16	0.12	--	1.47E-01		
80	9	3346.64	0.14	--	1.13E-01								
80	10	3552.91	0.12	--	1.13E-02	89	2	1766.49	0.03	--	3.64E-04		
						89	3	2054.72	0.04	1.25	0.03	8.79E-04	
81	2	1705.38	0.04	--	1.60E-04	89	6	2806.58	0.04	--	9.88E-02		
81	4	2244.57	0.10	--	8.50E-03	89	7	3036.29	0.06	--	1.82E-01		
81	5	2483.53	0.07	--	2.78E-02	89	8	3258.21	0.11	--	1.50E-01		
81	6	2712.42	0.05	--	8.22E-02								
81	7	2935.45	0.11	--	1.46E-01	90	3	2063.19	0.09	--	5.74E-04		
						90	5	2579.43	0.08	--	3.17E-02		
83	2	1720.75	0.04	--	2.18E-04	90	7	3048.66	0.05	--	1.75E-01		
83	4	2264.46	0.10	--	7.35E-03	90	8	3271.42	0.10	--	1.56E-01		
83	5	2505.29	0.06	--	3.11E-02								
83	6	2736.30	0.04	--	6.68E-02								

Table B.1 (continued)

ℓ	n	ν	FWHM		P_{tot}	ℓ	n	ν	FWHM		P_{tot}		
91	2	1781.10	0.04	1.51	0.03	4.63E-04	99	7	3155.89	0.09	--	1.69E-01	
91	3	2071.70	0.18	--	--	1.33E-03							
91	5	2589.79	0.06	--	--	3.81E-02	100	3	2147.24	0.10	--	1.23E-03	
91	6	2829.30	0.06	--	--	9.61E-02	100	4	2423.75	0.07	--	3.67E-03	
91	7	3060.95	0.06	--	--	2.01E-01	100	6	2929.07	0.12	--	1.20E-01	
91	8	3284.29	0.07	--	--	1.27E-01	100	7	3167.52	0.09	--	1.68E-01	
92	3	2080.37	0.03	0.75	0.03	6.51E-04	101	2	1850.76	0.04	1.24	0.03	6.06E-04
92	6	2840.75	0.05	--	--	1.13E-01	101	4	2432.38	0.22	--	--	1.09E-02
92	7	3073.06	0.05	--	--	1.49E-01	101	7	3179.12	0.09	--	--	1.75E-01
93	2	1795.70	0.05	1.03	0.04	2.16E-04	102	2	1857.31	0.02	0.91	0.01	4.47E-04
93	3	2088.73	0.05	1.27	0.04	6.76E-04	102	3	2163.06	0.11	--	--	9.78E-04
93	6	2852.06	0.05	--	--	1.14E-01	102	4	2441.37	0.06	--	--	5.28E-03
93	7	3085.14	0.05	--	--	1.92E-01	102	6	2950.55	0.04	--	--	1.42E-01
93	8	3310.05	0.13	--	--	1.20E-01	102	7	3190.68	0.09	--	--	1.45E-01
93	9	3529.71	0.17	--	--	4.48E-02	102	8	3422.89	0.15	--	--	7.43E-02
94	3	2097.33	0.10	--	--	1.05E-03	103	2	1864.11	0.04	0.91	0.04	4.18E-04
94	6	2863.22	0.05	--	--	1.15E-01	103	6	2961.37	0.08	--	--	1.28E-01
94	7	3097.02	0.05	--	--	1.70E-01	103	7	3201.82	0.08	--	--	1.79E-01
94	8	3322.94	0.10	--	--	1.29E-01	103	8	3435.22	0.13	--	--	8.77E-02
95	2	1809.61	0.05	1.00	0.04	2.28E-04	104	4	2458.41	0.07	--	--	6.36E-03
95	3	2106.06	0.07	1.83	0.05	1.21E-03	104	5	2719.40	0.12	--	--	3.60E-02
95	4	2378.91	0.04	--	--	2.95E-03	104	6	2971.84	0.07	--	--	1.42E-01
95	5	2630.75	0.18	--	--	3.04E-02	104	7	3213.31	0.10	--	--	1.65E-01
95	6	2874.46	0.05	--	--	1.13E-01	105	2	1877.30	0.03	--	--	2.84E-04
95	7	3109.02	0.06	--	--	1.57E-01	105	6	2982.33	0.13	--	--	1.14E-01
96	6	2885.66	0.06	--	--	1.11E-01	105	7	3224.96	0.11	--	--	1.24E-01
96	7	3120.85	0.05	--	--	1.55E-01	105	8	3459.17	0.22	--	--	8.37E-02
96	8	3348.00	0.15	--	--	9.02E-02	106	2	1877.32	0.09	--	--	6.78E-04
97	2	1823.41	0.11	--	--	4.85E-04	106	7	3236.10	0.12	--	--	1.15E-01
97	3	2122.31	0.04	0.89	0.04	8.97E-04	106	9	3701.27	0.10	--	--	9.04E-03
97	6	2896.55	0.03	--	--	8.19E-02	107	2	1884.35	0.09	--	--	7.05E-04
97	7	3132.51	0.06	--	--	1.38E-01	107	3	2202.27	0.09	--	--	1.06E-03
98	2	1830.15	0.04	0.89	0.04	2.71E-04	107	6	3003.11	0.06	--	--	1.33E-01
98	3	2130.74	0.06	--	--	8.51E-04	107	7	3246.95	0.11	--	--	1.06E-01
98	6	2907.44	0.13	--	--	1.13E-01	108	2	1896.68	0.07	--	--	8.74E-04
98	7	3144.19	0.09	--	--	1.78E-01	108	3	2210.12	0.04	0.89	0.03	1.05E-03
98	10	3817.69	0.12	--	--	6.12E-03	108	6	3013.38	0.15	--	--	1.09E-01
99	2	1837.19	0.09	--	--	2.56E-04	109	2	1903.05	0.04	--	--	3.35E-04
99	3	2138.59	0.03	0.93	0.03	8.10E-04	109	3	2217.52	0.03	--	--	1.26E-03
99	6	2918.26	0.05	--	--	1.10E-01							

Table B.1 (continued)

ℓ	n	ν	FWHM	P_{tot}
109	7	3269.47 0.17	--	9.89E-02
109	8	3507.13 0.23	--	3.81E-02
110	2	1903.39 0.07	--	6.12E-04
110	6	3034.17 0.15	--	1.13E-01
110	7	3280.32 0.12	--	1.03E-01
111	2	1916.07 0.05	--	6.71E-04
111	8	3530.83 0.23	--	5.50E-02
112	2	1922.02 0.07	--	8.82E-04
112	7	3302.06 0.11	--	1.10E-01
113	2	1928.51 0.07	--	9.06E-04
113	4	2533.45 0.10	--	8.52E-03
115	2	1935.01 0.07	--	9.26E-04
115	4	2549.39 0.12	--	5.11E-03
115	6	3084.58 0.18	--	8.15E-02
116	5	2831.81 0.16	--	4.22E-02
117	3	2277.42 0.13	--	2.72E-03
117	7	3355.97 0.14	--	9.83E-02
118	2	1959.14 0.05	--	8.95E-04
118	3	2284.58 0.05 1.15 0.04		2.01E-03
118	8	3612.31 0.10	--	1.08E-02
119	7	3377.59 0.15	--	6.04E-02

Table B.1 (continued)

Appendix C

Modal Frequencies, Widths and Amplitudes Estimated from the Low-Resolution Spectra

The following table lists the modal frequency, width and total power estimated from the low-resolution collapsed spectra, for a selection of modes, namely for $\ell = 50, (10), 600$. Note that no averaging, binning or fitting was performed on the data, these are individual modal values. Only “valid” widths are listed, see discussion in Chapter 5. The frequencies (ν), FWHM, and their 1σ uncertainties are listed in μHz . The modal total power (P_{tot}) corresponds to the square of the average surface velocity, in $(\text{m/s})^2$.

ℓ	n	ν	FWHM	P_{tot}	ℓ	n	ν	FWHM	P_{tot}			
50	4	1884.25	0.88	--	6.02e-04	60	3	1772.29	1.15	--	4.43e-04	
50	5	2096.52	1.16	--	1.40e-03	60	4	2012.08	1.12	--	8.65e-04	
50	6	2298.47	0.94	--	3.58e-03	60	5	2232.87	0.68	--	3.31e-03	
50	7	2489.10	0.58	--	1.17e-02	60	6	2442.61	0.70	--	9.21e-03	
50	8	2678.27	0.85	--	2.61e-02	60	7	2643.89	0.69	--	2.17e-02	
50	9	2862.17	0.78	--	4.99e-02	60	8	2843.56	0.65	--	4.71e-02	
50	10	3045.69	0.88	--	7.17e-02	60	9	3036.43	0.76	--	7.12e-02	
50	11	3224.68	1.00	--	6.92e-02	60	10	3226.78	0.65	--	7.13e-02	
50	12	3401.18	1.41	--	4.76e-02	60	11	3414.16	0.87	--	5.54e-02	
50	14	3754.18	2.67	--	1.88e-02	60	12	3598.87	1.00	--	3.68e-02	
50	15	3923.89	2.15	--	1.69e-02	60	13	3781.58	2.50	--	2.20e-02	
50	16	4091.56	3.22	--	1.18e-02	60	14	3961.82	0.91	--	2.53e-02	
50	17	4265.98	2.10	--	1.08e-02							
50	20	4738.58	3.20	26.15	2.53	3.23e-03	70	3	1881.46	0.51	--	4.20e-04
							70	4	2127.28	0.44	--	1.60e-03

Table C.1: Modal frequency, width and total power estimated from the low resolution collapsed spectra

ℓ	n	ν	FWHM	P_{tot}	ℓ	n	ν	FWHM	P_{tot}				
70	5	2357.48	0.61	--	5.92e-03	100	11	4060.84	0.70	21.71	0.73	2.10e-02	
70	6	2575.31	0.59	--	1.75e-02	100	12	4273.79	0.95	26.61	0.86	1.60e-02	
70	7	2787.92	0.53	--	3.88e-02	100	13	4481.57	1.12	33.50	0.87	1.18e-02	
70	8	2996.08	0.70	--	6.44e-02	100	14	4688.73	3.67	--	--	5.63e-03	
70	9	3196.21	0.64	--	7.29e-02								
70	10	3394.98	0.71	--	5.54e-02	110	2	1909.00	0.62	15.68	0.58	6.25e-04	
70	11	3589.77	0.79	--	3.94e-02	110	3	2226.00	0.25	--	--	2.97e-03	
70	12	3782.31	0.90	--	2.73e-02	110	4	2508.94	0.36	--	--	1.25e-02	
70	13	3972.06	1.49	--	1.97e-02	110	5	2776.41	0.45	--	--	3.68e-02	
70	14	4159.46	1.17	--	1.59e-02	110	6	3034.57	0.57	--	--	6.76e-02	
						110	7	3279.49	0.54	--	--	6.68e-02	
80	3	1972.08	0.51	--	6.93e-04	110	8	3518.09	0.47	--	--	4.58e-02	
80	4	2233.26	0.48	--	3.11e-03	110	9	3752.30	0.54	12.99	0.81	3.15e-02	
80	5	2471.93	0.48	--	1.06e-02	110	10	3979.88	0.55	25.66	0.47	2.41e-02	
80	6	2700.20	0.40	--	2.68e-02	110	11	4202.82	0.60	25.22	0.54	1.80e-02	
80	7	2923.59	0.55	--	5.58e-02	110	12	4420.63	1.01	37.27	0.69	1.32e-02	
80	8	3137.27	0.57	--	7.61e-02	110	13	4636.86	1.47	39.69	0.98	8.66e-03	
80	9	3346.63	0.61	--	6.34e-02	110	14	4849.32	2.86	--	--	4.59e-03	
80	10	3552.37	0.63	--	3.98e-02								
80	11	3754.53	0.72	--	3.13e-02	120	2	1970.00	0.50	--	--	8.11e-04	
80	12	3953.78	0.98	--	2.19e-02	120	3	2298.36	0.51	8.20	0.88	4.55e-03	
80	13	4150.66	1.15	--	1.82e-02	120	4	2589.45	0.42	--	--	1.90e-02	
80	14	4344.19	2.45	--	1.14e-02	120	5	2868.15	0.53	--	--	4.72e-02	
80	15	4535.98	2.88	--	7.72e-03	120	6	3134.31	0.49	--	--	7.09e-02	
						120	7	3387.75	0.38	--	--	5.69e-02	
90	2	1769.86	1.18	25.58	0.78	4.84e-04	120	8	3635.09	0.52	17.00	0.58	3.74e-02
90	3	2062.85	0.58	--	1.22e-03	120	9	3875.46	0.51	23.83	0.44	2.60e-02	
90	4	2332.76	0.52	--	5.38e-03	120	10	4110.53	0.49	31.97	0.35	2.07e-02	
90	5	2580.26	0.49	--	1.72e-02	120	11	4338.91	0.86	41.47	0.53	1.60e-02	
90	6	2817.76	0.46	--	4.26e-02	120	12	4563.52	0.81	41.66	0.51	1.13e-02	
90	7	3048.44	0.53	--	6.93e-02	120	13	4783.99	2.18	32.38	1.65	5.98e-03	
90	8	3271.83	0.58	--	6.87e-02								
90	9	3489.53	0.53	--	4.77e-02	130	2	2031.25	0.26	--	--	1.16e-03	
90	10	3701.26	0.77	7.83	2.07	3.19e-02							
90	11	3912.68	0.75	15.23	1.10	2.52e-02	130	4	2666.99	0.20	--	--	2.38e-02
90	12	4116.85	0.84	21.29	0.95	2.00e-02	130	5	2956.37	0.42	--	--	5.63e-02
90	13	4321.03	1.07	--	1.35e-02	130	6	3227.71	0.52	--	--	6.69e-02	
90	14	4520.40	1.89	--	9.52e-03	130	7	3490.78	0.51	13.33	0.66	4.76e-02	
						130	8	3746.04	0.47	20.37	0.43	3.11e-02	
100	2	1847.15	0.52	--	3.97e-04	130	9	3993.51	0.49	30.01	0.35	2.37e-02	
100	3	2146.50	0.31	--	1.97e-03	130	10	4235.12	0.47	36.65	0.30	1.82e-02	
100	4	2424.08	0.37	--	8.16e-03	130	11	4470.51	0.53	45.98	0.30	1.34e-02	
100	5	2680.16	0.42	--	2.68e-02	130	12	4703.10	1.51	42.33	0.91	7.94e-03	
100	6	2929.68	0.35	--	5.64e-02	130	13	4931.52	3.35	17.57	4.14	3.42e-03	
100	7	3167.57	0.51	--	7.32e-02								
100	8	3397.93	0.47	--	5.45e-02	140	2	2088.70	0.50	--	--	1.37e-03	
100	9	3624.26	0.46	11.26	0.82	3.74e-02	140	3	2433.37	0.38	11.69	0.46	8.82e-03
100	10	3844.89	0.61	17.82	0.73	2.70e-02	140	4	2741.34	0.44	8.83	0.71	3.26e-02

Table C.1 (continued)

ℓ	n	ν	FWHM		P_{tot}	ℓ	n	ν	FWHM		P_{tot}
140	5	3039.49	0.38	-	6.34e-02	180	4	3011.61	0.27	-	5.48e-02
140	6	3319.83	0.27	-	6.18e-02	180	5	3338.16	0.29	8.47	5.77e-02
140	7	3589.62	0.51	20.56	4.22e-02	180	6	3652.08	0.45	24.86	3.64e-02
140	8	3853.18	0.47	29.03	2.83e-02	180	7	3953.20	0.40	35.59	2.49e-02
140	9	4107.42	0.50	38.62	2.17e-02	180	8	4243.85	0.39	48.40	1.86e-02
140	10	4354.02	0.64	47.58	1.56e-02	180	9	4524.60	0.60	62.15	1.29e-02
140	11	4596.48	0.86	49.54	1.06e-02	180	10	4797.78	1.16	71.98	7.75e-03
140	12	4834.89	2.80	42.77	5.27e-03						
150	1	1762.14	0.50	17.62	3.74e-04	190	1	1931.46	0.34	-	5.37e-04
150	2	2144.05	0.19	-	1.71e-03	190	2	2345.88	0.40	13.61	4.80e-03
150	3	2493.40	0.39	12.26	1.14e-02	190	3	2714.84	0.20	-	2.38e-02
150	4	2812.97	0.23	-	3.70e-02	190	4	3074.06	0.20	-	5.84e-02
150	5	3119.00	0.47	-	6.71e-02	190	5	3407.10	0.40	18.33	5.28e-02
150	6	3406.07	0.41	8.64	5.43e-02	190	6	3728.88	0.35	25.37	3.17e-02
150	7	3685.76	0.43	21.55	3.48e-02	190	7	4037.41	0.42	38.61	2.23e-02
150	8	3955.71	0.36	28.12	2.42e-02	190	8	4334.85	0.58	55.02	1.64e-02
150	9	4217.62	0.51	42.49	1.82e-02	190	9	4620.64	0.69	64.89	1.09e-02
150	10	4470.38	0.64	48.07	1.30e-02	190	10	4900.85	1.93	68.96	5.74e-03
150	11	4718.51	1.20	55.59	8.22e-03	200	1	1967.04	0.21	11.70	8.12e-04
150	12	4963.76	3.71	31.64	3.33e-03	200	2	2392.36	0.28	7.19	5.66e-03
160	1	1806.64	0.62	-	2.62e-04	200	3	2766.07	0.21	-	2.82e-02
160	2	2196.91	0.36	8.07	2.44e-03	200	4	3133.14	0.44	12.05	6.16e-02
160	3	2552.47	0.12	-	1.34e-02	200	5	3473.97	0.42	21.64	4.87e-02
160	4	2881.20	0.31	-	4.49e-02	200	6	3803.41	0.37	32.80	3.01e-02
160	6	3491.18	0.46	18.95	4.77e-02	200	7	4118.44	0.39	43.69	2.13e-02
160	7	3778.19	0.32	20.48	2.94e-02	200	8	4421.91	0.43	54.34	1.47e-02
160	8	4054.84	0.40	35.10	2.19e-02	200	9	4715.48	0.92	69.61	9.17e-03
160	9	4322.79	0.49	46.11	1.67e-02	200	10	5005.21	2.04	74.02	4.78e-03
160	10	4582.85	0.71	56.33	1.11e-02	210	1	2004.13	0.38	14.79	8.85e-04
160	11	4837.75	1.42	62.80	6.86e-03	210	2	2438.07	0.16	-	6.51e-03
170	1	1851.55	0.00	-	2.82e-04	210	3	2816.49	0.29	11.06	3.41e-02
170	2	2247.22	0.31	8.71	3.14e-03	210	4	3189.80	0.23	-	6.19e-02
170	3	2607.71	0.44	13.95	1.86e-02	210	5	3539.14	0.41	25.73	4.39e-02
170	4	2947.36	0.34	-	4.99e-02	210	6	3876.13	0.33	33.27	2.75e-02
170	5	3268.43	0.35	-	6.33e-02	210	7	4197.74	0.40	47.33	1.92e-02
170	6	3573.22	0.46	23.13	4.18e-02	210	8	4507.77	0.53	63.38	1.31e-02
170	7	3867.26	0.38	31.00	2.83e-02	210	9	4806.84	1.08	77.54	7.91e-03
170	8	4150.61	0.42	40.51	2.05e-02	220	1	2040.03	0.43	14.38	1.03e-03
170	9	4426.01	0.53	53.06	1.47e-02	220	2	2481.36	0.40	20.81	8.85e-03
170	10	4691.43	0.92	63.96	9.23e-03	220	3	2866.38	0.32	15.04	3.76e-02
180	1	1891.77	0.57	-	4.40e-04	220	4	3245.66	0.41	17.84	6.10e-02
180	2	2298.15	0.39	15.95	4.05e-03	220	5	3602.94	0.43	27.11	4.02e-02
180	3	2662.72	0.35	12.64	2.22e-02	220	6	3945.66	0.38	39.06	2.51e-02
						220	7	4274.96	0.51	55.32	1.85e-02
						220	8	4591.00	0.75	73.73	1.22e-02

Table C.1 (continued)

ℓ	n	ν	FWHM		P_{tot}	ℓ	n	ν	FWHM		P_{tot}		
220	9	4896.52	1.09	81.13	0.46	6.49e-03	280	1	2229.48	0.22	11.82	0.22	2.16e-03
230	1	2072.95	0.50	14.63	0.43	1.17e-03	280	2	2712.49	0.30	20.22	0.21	1.98e-02
230	2	2522.27	0.23	7.91	0.35	9.83e-03	280	3	3149.44	0.37	23.26	0.23	5.28e-02
230	3	2915.32	0.33	14.95	0.29	4.10e-02	280	4	3555.09	0.36	29.61	0.20	4.22e-02
230	4	3300.19	0.31	16.87	0.26	5.63e-02	280	5	3954.60	0.31	43.90	0.15	2.61e-02
230	5	3664.69	0.31	28.64	0.18	3.59e-02	280	6	4335.61	0.42	65.10	0.18	1.76e-02
230	6	4014.76	0.34	41.70	0.17	2.42e-02	280	7	4700.22	0.95	88.56	0.39	1.06e-02
230	7	4350.16	0.38	57.39	0.17	1.66e-02	280	8	5056.63	2.79	92.79	1.14	4.53e-03
230	8	4672.40	0.99	80.13	0.41	1.07e-02	290	1	2258.91	0.10	6.61	0.17	2.46e-03
230	9	4985.67	3.08	77.24	1.31	4.64e-03	290	2	2747.32	0.20	16.66	0.16	2.09e-02
240	1	2106.24	0.44	17.39	0.33	1.45e-03	290	3	3192.20	0.28	20.17	0.20	4.96e-02
240	2	2563.24	0.39	20.76	0.27	1.23e-02	290	4	3603.71	0.39	32.30	0.21	3.88e-02
240	3	2963.79	0.30	15.09	0.27	4.36e-02	290	5	4008.50	0.32	47.44	0.15	2.50e-02
240	4	3352.61	0.20	15.96	0.17	5.37e-02	290	6	4395.81	0.51	69.26	0.21	1.66e-02
240	5	3725.52	0.32	30.66	0.18	3.23e-02	290	7	4765.96	1.15	94.50	0.47	9.64e-03
240	6	4082.76	0.37	46.30	0.18	2.28e-02	300	1	2288.70	0.31	16.00	0.25	2.87e-03
240	7	4423.70	0.49	63.07	0.21	1.53e-02	300	2	2781.04	0.16	16.30	0.13	2.19e-02
240	8	4751.01	0.98	85.13	0.41	9.52e-03	300	3	3236.26	0.25	20.37	0.17	4.94e-02
240	9	5073.36	3.11	79.35	1.32	4.18e-03	300	4	3652.47	0.35	33.16	0.18	3.57e-02
250	1	2138.03	0.52	20.72	0.34	1.63e-03	300	5	4062.18	0.33	50.86	0.15	2.43e-02
250	2	2602.25	0.16	5.11	0.37	1.28e-02	300	6	4454.82	0.60	76.54	0.25	1.57e-02
250	3	3011.68	0.23	13.65	0.22	4.56e-02	300	7	4831.79	1.64	101.6	0.66	8.51e-03
250	4	3404.04	0.27	17.77	0.21	5.04e-02	310	1	2316.84	0.39	22.25	0.25	3.41e-03
250	5	3785.18	0.36	33.53	0.19	3.09e-02	310	2	2813.68	0.15	14.97	0.12	2.35e-02
250	6	4148.00	0.33	50.35	0.15	2.11e-02	310	3	3277.32	0.35	26.02	0.21	4.88e-02
250	7	4495.19	0.45	68.96	0.19	1.39e-02	310	4	3699.90	0.33	36.77	0.17	3.35e-02
250	8	4828.86	1.90	88.15	0.78	7.55e-03	310	5	4114.97	0.36	56.90	0.16	2.30e-02
260	1	2168.85	0.41	19.18	0.28	1.84e-03	310	6	4513.43	0.58	79.11	0.24	1.45e-02
260	2	2639.26	0.34	20.15	0.23	1.64e-02	320	1	2344.19	0.24	18.45	0.17	3.65e-03
260	3	3058.75	0.17	11.28	0.19	4.73e-02	320	2	2846.52	0.15	16.39	0.12	2.60e-02
260	4	3454.94	0.34	24.20	0.21	4.81e-02	320	3	3318.60	0.22	22.21	0.14	4.60e-02
260	5	3842.57	0.28	36.19	0.14	2.87e-02	320	4	3747.45	0.24	37.27	0.12	3.14e-02
260	6	4211.47	0.49	57.57	0.22	2.02e-02	320	5	4166.38	0.31	59.65	0.13	2.19e-02
260	7	4565.31	0.70	73.95	0.29	1.24e-02	320	6	4569.66	0.82	87.07	0.33	1.36e-02
260	8	4905.43	1.53	92.57	0.63	6.72e-03	320	7	4958.35	2.32	108.4	0.92	6.31e-03
270	1	2199.15	0.33	17.08	0.25	2.07e-03	330	0	1827.42	1.04	-	-	1.56e-04
270	2	2676.79	0.35	20.96	0.23	1.80e-02	330	1	2372.70	0.16	11.06	0.17	3.55e-03
270	3	3104.78	0.28	18.73	0.21	5.00e-02	330	2	2878.78	0.17	18.45	0.12	2.64e-02
270	4	3505.45	0.37	26.82	0.22	4.52e-02	330	3	3358.21	0.33	27.95	0.18	4.58e-02
270	5	3898.82	0.32	39.88	0.16	2.76e-02	330	4	3794.64	0.29	41.64	0.14	2.91e-02
270	6	4273.73	0.29	58.51	0.13	1.82e-02	330	5	4217.29	0.36	62.92	0.15	2.02e-02
270	7	4634.07	0.88	82.30	0.36	1.16e-02	330	6	4625.07	1.04	89.52	0.42	1.18e-02
270	8	4980.82	1.83	98.47	0.74	5.58e-03							

Table C.1 (continued)

ℓ	n	ν	FWHM		P_{tot}	ℓ	n	ν	FWHM		P_{tot}		
330	7	5022.86	2.28	111.6	0.90	5.52e-03	400	0	2013.25	0.64	13.26	0.59	4.13e-04
340	1	2399.76	0.34	23.68	0.20	4.38e-03	400	1	2557.27	0.28	26.50	0.15	6.62e-03
340	2	2910.65	0.23	22.56	0.14	2.84e-02	400	2	3089.73	0.22	28.23	0.12	3.16e-02
340	3	3397.33	0.31	29.11	0.17	4.50e-02	400	3	3614.57	0.18	37.24	0.09	3.22e-02
340	4	3841.15	0.30	45.19	0.14	2.85e-02	400	4	4105.94	0.34	64.27	0.14	2.15e-02
340	5	4268.35	0.46	66.30	0.19	1.91e-02	400	5	4559.07	1.22	99.09	0.49	1.32e-02
340	7	5084.95	4.31	104.8	1.72	4.46e-03	410	0	2033.02	0.18	-	-	4.20e-04
350	1	2426.41	0.24	21.54	0.15	4.62e-03	410	1	2583.12	0.21	26.68	0.12	7.01e-03
350	2	2941.62	0.26	23.57	0.16	3.08e-02	410	2	3118.97	0.33	31.01	0.17	3.22e-02
350	3	3435.46	0.22	27.98	0.13	4.15e-02	410	3	3648.24	0.22	40.87	0.10	3.09e-02
350	4	3886.96	0.28	46.18	0.13	2.76e-02	410	4	4146.91	0.24	66.34	0.10	1.97e-02
350	5	4317.79	0.43	71.64	0.18	1.85e-02	410	5	4605.05	1.37	101.3	0.54	1.17e-02
350	6	4733.94	1.60	106.5	0.63	1.09e-02	410	6	5050.59	3.63	121.9	1.42	4.72e-03
360	0	1905.49	0.43	17.92	0.31	3.35e-04	420	0	2061.21	1.02	11.47	1.05	4.43e-04
360	1	2453.73	0.13	18.54	0.09	5.09e-03	420	1	2608.18	0.26	29.39	0.14	7.33e-03
360	2	2971.56	0.32	26.66	0.18	3.24e-02	420	2	3147.21	0.35	32.57	0.18	3.12e-02
360	3	3472.14	0.30	33.12	0.16	4.15e-02	420	3	3681.76	0.25	43.45	0.12	2.88e-02
360	4	3931.79	0.29	50.65	0.13	2.58e-02	420	4	4187.74	0.34	72.28	0.14	1.91e-02
360	5	4366.54	0.48	76.90	0.20	1.71e-02	420	5	4648.94	1.83	105.8	0.72	1.04e-02
360	6	4788.43	2.17	107.0	0.86	8.95e-03	430	0	2086.35	0.99	26.09	0.56	6.10e-04
370	0	1934.14	0.16	13.99	0.14	3.58e-04	430	1	2633.64	0.21	28.28	0.11	7.46e-03
370	1	2479.43	0.33	24.80	0.19	5.97e-03	430	2	3175.21	0.26	31.39	0.14	2.88e-02
370	2	3001.48	0.36	28.44	0.20	3.24e-02	430	3	3715.31	0.24	46.80	0.11	2.72e-02
370	3	3509.26	0.31	35.16	0.15	3.96e-02	430	4	4228.13	0.28	75.75	0.12	1.84e-02
370	4	3976.15	0.32	54.76	0.14	2.52e-02	430	5	4697.32	2.14	110.3	0.84	9.40e-03
370	5	4414.95	0.55	84.25	0.22	1.64e-02	440	0	2108.61	0.82	15.22	0.67	5.09e-04
370	6	4841.26	2.21	113.1	0.87	8.77e-03	440	1	2657.82	0.26	31.41	0.13	7.74e-03
380	0	1957.69	1.09	10.98	1.17	3.18e-04	440	2	3204.00	0.25	32.97	0.13	2.79e-02
380	1	2505.78	0.14	22.41	0.09	5.88e-03	440	3	3747.81	0.21	48.23	0.09	2.49e-02
380	2	3031.14	0.30	28.25	0.17	3.31e-02	440	4	4267.69	0.30	81.99	0.12	1.69e-02
380	3	3544.84	0.27	36.84	0.13	3.75e-02	440	5	4739.75	3.19	119.7	1.25	8.59e-03
380	4	4020.59	0.37	58.39	0.16	2.42e-02	450	0	2132.20	0.85	25.96	0.48	6.09e-04
380	5	4464.10	0.72	86.81	0.29	1.56e-02	450	1	2682.89	0.14	30.73	0.07	7.65e-03
380	6	4894.99	2.67	118.0	1.05	7.52e-03	450	2	3232.01	0.31	34.91	0.15	2.63e-02
390	0	1985.88	0.46	23.68	0.28	5.36e-04	450	3	3780.47	0.26	52.02	0.11	2.36e-02
390	1	2532.47	0.23	23.76	0.14	6.15e-03	450	4	4307.00	0.52	83.45	0.21	1.54e-02
390	2	3060.43	0.21	25.73	0.12	3.23e-02	450	5	4785.61	3.57	123.5	1.39	7.54e-03
390	3	3580.11	0.23	36.63	0.11	3.47e-02	460	0	2156.21	1.81	26.74	1.01	6.52e-04
390	4	4063.30	0.31	60.83	0.13	2.25e-02	460	1	2707.24	0.28	33.07	0.14	7.88e-03
390	5	4511.20	0.73	89.94	0.29	1.38e-02	460	2	3259.50	0.30	34.54	0.15	2.42e-02
390	6	4945.66	3.59	126.9	1.41	6.65e-03	460	3	3812.71	0.20	55.16	0.09	2.19e-02
							460	4	4344.28	0.52	95.87	0.21	1.51e-02

Table C.1 (continued)

ℓ	n	ν	FWHM		P_{tot}	ℓ	n	ν	FWHM		P_{tot}		
460	5	4830.29	4.45	127.7	1.74	6.69e-03	530	0	2311.59	1.90	33.03	0.95	8.55e-04
470	0	2180.68	1.93	31.22	0.99	7.14e-04	530	1	2872.99	0.37	42.15	0.17	6.41e-03
470	1	2731.17	0.22	33.37	0.11	7.71e-03	530	2	3448.83	0.37	45.46	0.17	1.39e-02
470	2	3286.68	0.25	37.11	0.12	2.32e-02	530	3	4028.93	0.24	75.12	0.10	1.20e-02
470	3	3844.26	0.15	57.56	0.06	2.04e-02	530	4	4589.85	3.71	137.6	1.44	7.54e-03
470	4	4382.56	0.90	95.14	0.36	1.31e-02	540	0	2336.38	2.55	30.16	1.33	5.96e-04
480	0	2201.11	1.89	34.55	0.93	7.98e-04	540	1	2895.31	0.33	40.77	0.15	5.87e-03
480	1	2754.36	0.24	33.67	0.12	7.50e-03	540	2	3475.06	0.32	46.99	0.14	1.17e-02
480	2	3313.88	0.32	39.70	0.15	2.17e-02	540	3	4058.67	0.33	79.44	0.13	1.02e-02
480	3	3875.07	0.18	59.53	0.08	1.88e-02	550	0	2359.42	3.21	39.71	1.50	7.75e-04
480	4	4418.30	1.09	103.4	0.43	1.19e-02	550	1	2918.71	0.55	44.19	0.25	5.92e-03
490	0	2225.17	1.66	29.81	0.87	7.04e-04	550	2	3501.70	0.36	49.27	0.16	1.11e-02
490	1	2779.28	0.23	33.54	0.11	7.25e-03	550	3	4089.47	0.42	83.68	0.17	9.77e-03
490	2	3341.56	0.30	39.66	0.14	1.99e-02	560	1	2941.94	0.50	41.15	0.23	5.30e-03
490	3	3906.42	0.21	65.22	0.09	1.75e-02	560	2	3528.08	0.30	52.69	0.13	1.00e-02
490	4	4454.48	1.16	108.0	0.46	1.10e-02	560	3	4119.31	0.42	84.23	0.17	8.23e-03
500	0	2245.44	1.64	32.65	0.83	7.45e-04	570	1	2964.64	0.51	42.83	0.23	4.86e-03
500	1	2802.41	0.27	38.03	0.13	7.22e-03	570	2	3554.45	0.30	53.85	0.13	8.88e-03
500	2	3368.63	0.29	41.42	0.14	1.77e-02	570	3	4149.16	0.45	86.88	0.18	7.27e-03
500	3	3937.53	0.21	66.12	0.09	1.60e-02	580	1	2986.73	0.87	50.90	0.38	4.94e-03
500	4	4490.99	1.64	108.0	0.65	9.55e-03	580	2	3580.76	0.27	55.42	0.12	7.82e-03
510	0	2273.20	2.25	27.12	1.24	5.79e-04	580	3	4180.15	0.60	93.25	0.24	6.98e-03
510	1	2826.01	0.33	38.64	0.15	7.11e-03	590	1	3008.75	0.81	45.16	0.36	4.06e-03
510	2	3395.31	0.38	43.92	0.17	1.72e-02	590	2	3606.89	0.32	57.01	0.14	6.53e-03
510	3	3968.12	0.25	68.01	0.10	1.45e-02	590	3	4209.48	0.54	97.03	0.21	5.48e-03
510	4	4524.96	2.11	114.7	0.82	8.88e-03	600	1	3030.79	0.82	47.83	0.36	3.91e-03
520	1	2849.36	0.35	38.80	0.17	6.51e-03	600	2	3633.07	0.18	60.98	0.07	6.88e-03
520	2	3422.08	0.31	43.24	0.14	1.48e-02	600	3	4239.18	0.71	100.6	0.28	5.83e-03
520	3	3998.84	0.33	73.04	0.13	1.29e-02							
520	4	4560.09	2.53	121.3	0.99	7.74e-03							

Table C.1 (continued)